

I. Selective Probes for Cytochrome P450 17A1 Suggest a Design Strategy Toward Improved Breast and Prostate Cancer Agents

II. Spatiotemporal Control of Reactivity via Visible Light-Mediated C-H Activation Creates Chemically Patterned Carbohydrate Surfaces

III. Studies Toward Overcoming Product Inhibition in Catalysis of the Intramolecular Schmidt Reaction

By

Charlie Fehl

Submitted to the graduate degree program in Medicinal Chemistry and the Graduate Faculty of the University of Kansas in partial fulfillment of the requirements for the degree of Doctor of Philosophy.

---

Jeffrey Aubé, Chair

---

Emily E. Scott

---

Thomas E. Prisinzano

---

Paul R. Hanson

---

Burkhard König

Date Defended: September 9, 2014

The Thesis Committee for Charlie Fehl

certifies that this is the approved version of the following thesis:

I. Selective Probes for Cytochrome P450 17A1 Suggest a Design Strategy Toward Improved Breast and Prostate Cancer Agents

II. Spatiotemporal Control of Reactivity via Visible Light-Mediated C-H Activation Creates Chemically Patterned Carbohydrate Surfaces

III. Studies Toward Overcoming Product Inhibition in Catalysis of the Intramolecular Schmidt Reaction

---

Jeffrey Aubé, Chair

Date approved: September 9, 2014

## **Abstract**

**Selective Probes for Cytochrome P450 17A1 Suggest a Design Strategy Toward Improved Breast and Prostate Cancer Agents.** Sex steroids stimulate the growth of hormone-responsive breast and prostate tumors, the two most commonly diagnosed cancers in America. Inhibiting the sex steroid biosynthetic pathway is a promising strategy to halt the progression of these cancers. Cytochrome P450 17A1 (CYP17A1) is a validated target in prostate cancer, but clinical agents fail to achieve selectivity over the highly similar CYP21A2, involved in mineralocorticoid production and blood pressure regulation. In this work, we devised and confirmed a strategy to allow the selective blockade of sex steroidogenesis with the continued production of corticosteroid hormones. To rationally achieve this aim, several co-crystal structures were solved and an assay to evaluate CYP17A1/CYP21A2 selectivity was developed to guide the synthesis of new compounds. A class of these probes achieved significant gains in selectivity over the currently marketed drug abiraterone and galaterone and orteronel, still in clinical trials. This design strategy represents a step toward selectively targeting sex steroidogenesis as a chemotherapeutic tactic for prostate and possibly breast cancers.

**Spatiotemporal Control of Reactivity via Visible Light-Mediated C-H Activation Creates Chemically Patterned Carbohydrate Surfaces.** Reactivity in photochemistry can be restricted to a desired area of a reaction medium by controlling the exposure of reagents to light. This can create patterned surfaces of chemical functionality, which can be used in numerous applications in chemical biology. To demonstrate this utility, we formulated a light-mediated photo-Meerwein arylation reaction to occur on a surface encoded with the reaction substrate. In this proof-of-concept study, reactants were chosen

that would undergo a visible color change upon successful reaction. Potential surfaces to display these reactants were then tested. Paper sheets proved optimal for visualization, in which the cellulose C6-position was covalently modified by functionalized coumarin reactants. Use of a photomask allowed these surfaces to be selectively modified by exposure to visible light in the presence of various aryl diazonium reagents and a photocatalyst. These reactions resulted in a strikingly visible color change over the target area. This represents a rapid, cost-effective strategy to selectively encode desired chemical functionality on cellulose medium. This technology could be applied toward surfaces bearing protein capture resins, biosensors, or other agents for chemical biology.

**Studies Toward Overcoming Product Inhibition in Catalysis of the Intramolecular Schmidt Reaction.** Transformations that efficiently generate molecular complexity are useful in drug design, polymer chemistry, and natural product synthesis. The intramolecular Schmidt reaction allows access to amides and lactams from ketone starting materials, and has seen extensive use in the above applications. This reaction is promoted by strongly acidic conditions. Since the reaction creates amide products with increased Lewis basicity over the ketone reactants, most acids are readily sequestered upon successful reaction. In this chapter, we describe the optimization of conditions that promote the intramolecular Schmidt reaction with substoichiometric  $\text{Sc}(\text{OTf})_3$ , which turns over to allow a catalytic cycle in response to heat. The scope, temperature dependence, and kinetics of this transformation were characterized. Additionally, several strategies to expand this strategy were screened. This work, with additional results from a co-worker, ultimately led to the development of vastly improved conditions and scope for catalytic Schmidt reactions.

## **Acknowledgements**

This thesis, and indeed the willpower, training, and determination that allowed me to complete it, would have been impossible but for a long list of friends, family, and the strong support of my instructors and co-workers. I would like to deeply acknowledge these wonderful people, as best I can.

To my friends – thank you for helping to shape my personal growth, for challenging me both mentally and on icy slopes, rock faces, or wherever precipice on which we stumble, and for all of the wonderful times along the way.

To my family – you have raised me in the best way possible, and have provided the tools and advice to withstand and thrive in the toughest trials and decisions of my life. Though it has been hard to be so far from home, you have kept me close at heart.

To my instructors – this work simply would not have happened without you. Jeff, your example and guidance have pushed me far beyond whence I possibly could have imagined as I joined your group. Along the way, I have discovered a passion for our work that will guide me through the rest of my journey – I am excited to see where we will go. Emily, thank you for your careful training. It has been incredible to experience so much during my time here. And to my committee, I have learned from each of you: Tom – leadership and respect; Paul – zeal; Burkhard – heartfelt enthusiasm. Thank you.

To my collaborators Natasha DeVore, Patrick Porubsky, Elyse Petrunak, Steven Rogers, Peter Schroll, Hashim Motiwala – without your help I would still be in the lab. To the rest of the Aubé and Scott groups – thank you for providing a wonderful place to work.

Finally, Shannon. You have been so strong throughout this experience. Your support has absolutely made our journey not just manageable, but sublime. I look forward to our life of never-ending exploration.

## Table of Contents

<b>Abstract</b> .....	<b>iii</b>
<b>Acknowledgements</b> .....	<b>v</b>
<b>Table of Contents</b> .....	<b>vii</b>
<b>List of Figures</b> .....	<b>ix</b>
<b>List of Schemes</b> .....	<b>xii</b>
<b>List of Tables</b> .....	<b>xiv</b>
<b>1. Selective Probes for Cytochrome P450 17A1 Suggest a Design Strategy Toward Improved Breast and Prostate Cancer Agents</b> .....	<b>1</b>
Contributors .....	1
<b>1.1 Introduction</b> .....	<b>1</b>
1.1.1 Steroid hormone synthesis by cytochromes P450 .....	3
1.1.2 Prostate cancer and androgen deprivation therapy .....	9
1.1.3 CYP17A1 biochemical activity – a case for selective inhibitor design.....	15
1.1.4 Comparison of CYP17A1 and CYP21A2 crystal structures suggest that selectivity can be rationally designed .....	20
1.1.5 Preliminary design strategy toward CYP17A1/CYP21A2 selective inhibitors.....	25
<b>1.2 Methods</b> .....	<b>27</b>
1.2.1 Inhibitor synthesis.....	27
1.2.2 Enzyme activity assays .....	28
1.2.3 CYP17A1 purification and crystallography .....	33
<b>1.3 Results and Discussion</b> .....	<b>41</b>
1.3.1 Inhibitor synthesis.....	41
1.3.2 CYP17A1 and CYP21A2 activity assays for inhibitor profiling.....	48
1.3.3 Structural analysis of CYP17A1 inhibitors .....	66
<b>1.4 Conclusions</b> .....	<b>79</b>
<b>1.5 Experimental Section</b> .....	<b>80</b>
<b>1.6 References</b> .....	<b>126</b>
<b>2. Spatiotemporal Control of Reactivity via Visible Light-Mediated C-H activation Creates Chemically Patterned Carbohydrate Surfaces</b> .....	<b>138</b>
Contributors .....	138
<b>2.1 Introduction</b> .....	<b>138</b>
2.1.1 The photo-Meerwein arylation and its potential for controlled surface functionalization .....	141
2.1.2 Design strategy toward a surface-anchored photo-Meerwein reaction .....	142
<b>2.2 Methods</b> .....	<b>145</b>
2.2.1 Substrate synthesis and chromogenic scope of the photo-Meerwein arylation .....	145
2.2.2 Model reaction for glass resin epoxide-opening by coumarin substrates .....	146

2.2.3 Glass silylation with GOPS resin and functionalization with hydroxycoumarin substrate .....	146
2.2.4 Cellulose polymer and filter paper functionalization .....	147
2.2.5 Preliminary reactor setup for surface-anchored photo-Meerwein arylation .....	148
<b>2.3 Results and Discussion .....</b>	<b>149</b>
2.3.1 Identification of a chromogenic photo-Meerwein transformation .....	149
2.3.2 Creation of glass surfaces for coumarin-anchored photo-Meerwein arylation .....	151
2.3.3 Creation of functionalized cellulose sheets for anchored photo-Meerwein arylation .....	154
2.3.4 Preliminary conditions for surface-anchored photoreaction .....	156
<b>2.4 Conclusion .....</b>	<b>159</b>
<b>2.5 Experimental Section .....</b>	<b>160</b>
<b>2.6 References .....</b>	<b>171</b>
<b>3. Studies Toward Overcoming Product Inhibition in Catalysis of the Intramolecular Schmidt Reaction .....</b>	<b>175</b>
Contributors .....	175
<b>3.1 Introduction .....</b>	<b>175</b>
3.1.1 The Schmidt reaction, and the discovery of its intramolecular variant .....	177
3.1.2 Product inhibition hinders acid turnover for a catalytic Schmidt reaction .....	179
3.1.3 Previous work in our laboratory toward overcoming product inhibition .....	182
<b>3.2 Methods .....</b>	<b>186</b>
3.2.1 Substrate synthesis for intramolecular Schmidt reaction development .....	186
3.2.2 Reaction condition screening .....	187
3.2.3 Determination of the reaction substrate scope under optimized conditions .....	188
3.2.4 Further catalyst screening under optimized conditions .....	188
3.2.5 Additive/co-catalyst screening under ambient conditions .....	189
3.2.6 Standardized measurements of conversion for reaction characterization .....	189
3.2.7 Catalyst loading study of Sc(OTf) <sub>3</sub> in MeCN .....	191
3.2.8 Microwave intensity study of Sc(OTf) <sub>3</sub> in MeCN .....	191
3.2.9 Turnover number and turnover frequency of Sc(OTf) <sub>3</sub> in MeCN .....	191
<b>3.3 Results and Discussion .....</b>	<b>192</b>
3.3.1 Verification of preliminary substoichiometric catalytic conditions .....	192
3.3.2 Scope of the Sc(OTf) <sub>3</sub> -catalyzed intramolecular Schmidt reaction .....	194
3.3.3 Screen of catalysts and co-catalysts to lower the temperature dependence .....	197
3.3.4 Further characterization of the Sc(OTf) <sub>3</sub> -catalyzed reaction .....	203
<b>3.4 Conclusions .....</b>	<b>209</b>
<b>3.5 Experimental Section .....</b>	<b>210</b>
<b>3.6 References .....</b>	<b>222</b>

## List of Figures

### Chapter 1

<b>Figure 1-1.</b> Various structural changes to the steroid nucleus generate six major classes of hormones. ....	2
<b>Figure 1-2.</b> Type II P450 inhibitors make coordinate covalent interactions with the heme .....	7
<b>Figure 1-3.</b> Structures of CYP17A1 inhibitors .....	9
<b>Figure 1-4.</b> A brief history of androgen deprivation therapy in prostate cancer.....	11
<b>Figure 1-5.</b> Overall structure of CYP17A1 and CYP21A2 .....	21
<b>Figure 1-6:</b> Active site comparison between CYP21A2 and CYP17A1 .....	23
<b>Figure 1-7.</b> Design strategy toward improved CYP17A1 inhibitors .....	26
<b>Figure 1-8:</b> Protein purity and stability determination using UV-Vis .....	37
<b>Figure 1-9.</b> Conditions for the HPLC-based CYP17A1 progesterone 17 $\alpha$ -hydroxylation assay .....	51
<b>Figure 1-10.</b> CYP17A1 17 $\alpha$ -hydroxylation assay against previously reported agents. ..	51
<b>Figure 1-11.</b> CYP17A1 17 $\alpha$ -hydroxylation assay against initial compounds .....	52
<b>Figure 1-12.</b> CYP17A1 17 $\alpha$ -hydroxylation assay against azasteroid analogs .....	53
<b>Figure 1-13.</b> CYP17A1 17 $\alpha$ -hydroxylation assay against ketone-derived analogs.....	54
<b>Figure 1-14.</b> Two trends suggested from structure-activity data were used to design further analogs .....	56
<b>Figure 1-15.</b> CYP17A1 17 $\alpha$ -hydroxylation assay against geometry-optimized series. ..	57
<b>Figure 1-16.</b> Removal of Fe-coordinating moiety drops potency significantly.....	58
<b>Figure 1-17.</b> Standard curves of CYP21A2 product detected by GC/MS .....	61
<b>Figure 1-18.</b> CYP21A2 enzymatic reaction.....	62
<b>Figure 1-19.</b> Kinetic parameters of CYP21A2 progesterone 21-hydroxylation .....	63

<b>Figure 1-20.</b> Clinical CYP17A1 agents' effect on CYP21A2 progesterone 21-hydroxylation .....	64
<b>Figure 1-21.</b> Progesterone 21-hydroxylation assay against B-ring substituted compounds .....	65
<b>Figure 1-22.</b> All five new co-crystal structures of CYP17A1 overlaid .....	68
<b>Figure 1-23.</b> Co-crystal structure of <b>19</b> with CYP17A1 at 2.25 Å resolution .....	69
<b>Figure 1-24.</b> Co-crystal structure of <b>23</b> with CYP17A1 at 2.60 Å resolution .....	71
<b>Figure 1-25.</b> Co-crystal structure of <b>33</b> with CYP17A1 at 2.65 Å resolution. ....	72
<b>Figure 1-26.</b> CYP17A1 co-crystals with <b>38</b> . Hasty growth led to poor-quality crystals. ....	73
<b>Figure 1-27.</b> Co-crystal structure of <b>38</b> with CYP17A1 at 2.60 Å resolution. ....	74
<b>Figure 1-28.</b> Co-crystal structure of <b>42</b> with CYP17A1 at 2.70 Å resolution. ....	75
<b>Figure 1-29.</b> Active site view of the five structures of CYP17A1 solved in this work ...	77
<b>Figure 1-30.</b> Additional SAR directions suggested by crystallography.....	78
<b>Figure 1-31.</b> Steroid numbering to be used for nomenclature in the Experimental Section. ....	81

## Chapter 2

<b>Figure 2-1.</b> Schematic of a surface-anchored photo-Meerwein arylation, and the challenges we faced in this work. ....	143
<b>Figure 2-2.</b> Coumarin-functionalized filter paper .....	148
<b>Figure 2-3.</b> Reactor setup .....	148
<b>Figure 2-4.</b> Substrates for photo-Meerwein arylation .....	149
<b>Figure 2-5.</b> Glass slide silanized with <b>66</b> and functionalized with <b>50</b> .....	154
<b>Figure 2-6.</b> Various materials for functionalization.....	155
<b>Figure 2-7.</b> Coumarin-modified filter paper sheets.....	156
<b>Figure 2-8.</b> Photoreaction with coumarin-functionalized sheets .....	157
<b>Figure 2-9.</b> Optimized surface patterning photo-Meerwein arylation .....	158

## Chapter 3

<b>Figure 3-1.</b> Substrates to examine the scope of the Sc(OTf) <sub>3</sub> -catalyzed intramolecular Schmidt reaction. ....	187
<b>Figure 3-2.</b> Quantitation of <b>IS</b> (R <sub>T</sub> 1.3 min), product <b>68a</b> (R <sub>T</sub> 1.59 min) and substrate <b>67a</b> (R <sub>T</sub> 2.22 min). ....	190
<b>Figure 3-3.</b> The effect of Sc(OTf) <sub>3</sub> loading on ambient turnover of the intramolecular Schmidt reaction. ....	204
<b>Figure 3-4.</b> The temperature dependence of turnover is linear for Sc(OTf) <sub>3</sub> in this reaction.....	205
<b>Figure 3-5.</b> Kinetic characterization of Sc(OTf) <sub>3</sub> turnover number in the intramolecular Schmidt reaction. ....	207
<b>Figure 3-6.</b> Kinetic characterization of Sc(OTf) <sub>3</sub> turnover frequency in the intramolecular Schmidt reaction. ....	207

## List of Schemes

### Chapter 1

<b>Scheme 1-1</b> .....	4
<b>Scheme 1-2</b> .....	6
<b>Scheme 1-3</b> .....	16
<b>Scheme 1-4</b> .....	17
<b>Scheme 1-5</b> .....	18
<b>Scheme 1-6</b> .....	41
<b>Scheme 1-7</b> .....	43
<b>Scheme 1-8</b> .....	44
<b>Scheme 1-9</b> .....	45
<b>Scheme 1-10</b> .....	46
<b>Scheme 1-11</b> .....	47
<b>Scheme 1-12</b> .....	48
<b>Scheme 1-13</b> .....	60

### Chapter 2

<b>Scheme 2-1</b> .....	139
<b>Scheme 2-2</b> .....	141
<b>Scheme 2-3</b> .....	142
<b>Scheme 2-4</b> .....	144
<b>Scheme 2-5</b> .....	145
<b>Scheme 2-6</b> .....	146
<b>Scheme 2-7</b> .....	147
<b>Scheme 2-8</b> .....	147

<b>Scheme 2-9</b> .....	152
<b>Scheme 2-10</b> .....	155
<b>Chapter 3</b>	
<b>Scheme 3-1</b> .....	176
<b>Scheme 3-2</b> .....	177
<b>Scheme 3-3</b> .....	178
<b>Scheme 3-4</b> .....	179
<b>Scheme 3-5</b> .....	180
<b>Scheme 3-6</b> .....	180
<b>Scheme 3-7</b> .....	181
<b>Scheme 3-8</b> .....	186
<b>Scheme 3-9</b> .....	194
<b>Scheme 3-10</b> .....	198
<b>Scheme 3-11</b> .....	208

## List of Tables

### Chapter 1

**Table 1-1.** X-ray statistics for new CYP17A1 co-crystal structures ..... 39

**Table 1-2.** Possible interactions from CYP17A1-steroid ligand crystal structures..... 77

### Chapter 2

**Table 2-1.** Chromogenic scope of the photo-Meerwein reaction..... 150

**Table 2-2.** Model reaction for GOPS epoxide ring-opening by hydroxycoumarin **50** .. 153

**Table 2-3.** Reaction time of the surface-anchored photo-Meerwein arylation ..... 157

### Chapter 3

**Table 3-1.** Selected substoichiometric Schmidt conditions screened by Li..... 183

**Table 3-2.** Preliminary catalyst and substrate screening in H<sub>2</sub>O by Hirt ..... 185

**Table 3-3.** Preliminary condition screening with Sc(OTf)<sub>3</sub> ..... 193

**Table 3-4.** Substrate scope of improved catalytic Schmidt conditions ..... 195

**Table 3-5.** Alternative catalysts in the improved conditons..... 197

**Table 3-6.** Effect of phosphine sdditives on Sc(OTf)<sub>3</sub>-catalyzed intramolecular Schmidt reactivity ..... 199

**Table 3-7.** Salt screen – potential ligands to destabilize the Lewis acid-product complex ..... 201

**Table 3-8.** Organic additive screen – potential ligands to destabilize the Lewis acid-product complex..... 202

# 1. Selective Probes for Cytochrome P450 17A1 Suggest a Design Strategy Toward Improved Breast and Prostate Cancer Agents

## Contributors

University of Kansas, Department of Medicinal Chemistry:

- Charlie Fehl: analog design and synthesis; CYP17A1 protein production; co-crystallography experiments; activity and selectivity characterization of compounds; GC/MS assay development.
- Elyse M. Petrunak: Human CYP17A1, P450 oxidoreductase, and CYP21A2 production.
- Patrick R. Porubsky: GC/MS detection; compound purification.
- Prof. Emily E. Scott: principal investigator; analog design; biochemistry.
- Prof. Jeffrey Aubé: principal investigator; analog design; synthetic chemistry.

## 1.1 Introduction

Hormones are powerful mediators of physiological processes, and can be defined as chemical reporters that act to signal biological commands.<sup>1</sup> Autocrine or paracrine signaling affects neighboring cells, whereas endocrine signaling affects cells distal to the site of hormone production. Both types may be powerful physiological actors. Agents that block the production of various hormones are well-validated therapies for many indications, including cancer,<sup>2</sup> cardiology,<sup>3</sup> inflammation,<sup>4</sup> and the effects of diabetes.<sup>5</sup>

This strategy ideally uses an agent that is highly selective for an intended target in a designated biosynthetic pathway. Undesired effects can arise if related but unintended pathways become affected. For example, elevated levels of circulating glucocorticoids are associated with the development of severe adverse effects such as insulin resistance,

dyslipidemia, and central adiposity, all characteristics related to the onset of type 2 diabetes.<sup>6</sup>

Several major classes of hormones contain the steroid nucleus (Figure 1-1).<sup>7</sup> Steroid hormones are involved in a diverse array of metabolic, homeostatic, and neurologic processes, as well as cellular growth and development.<sup>8</sup> From an oncologic perspective, if certain biological processes that initiate growth or metabolic enhancement become overactive, carcinogenesis and/or tumor growth may occur.<sup>9</sup> In several cases, such tumors remain dependent on these signals, creating an opportunity for therapeutic intervention.<sup>10</sup>

This chapter focuses on the design of agents that block sex steroidogenesis. This is a promising treatment for breast and prostate cancers, which derive from sex steroid-responsive tissues.<sup>11</sup> Several clinical compounds validate this approach.<sup>12</sup> Improving the selectivity for the sex steroidogenic pathway of these agents over similar targets essential for corticosteroid production, aimed at reducing adverse effects, was the challenge we faced in this work.

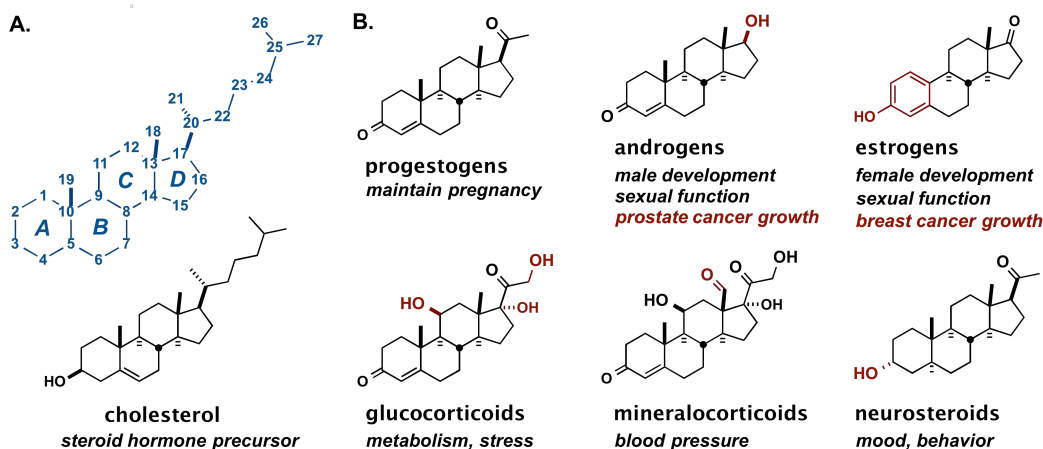


**Figure 1-1.** Various structural changes to the steroid nucleus generate six major classes of hormones. A: Steroid nomenclature: carbon skeleton numbering, ring names A-D. B: Representative steroid classes and physiological actions thereof.

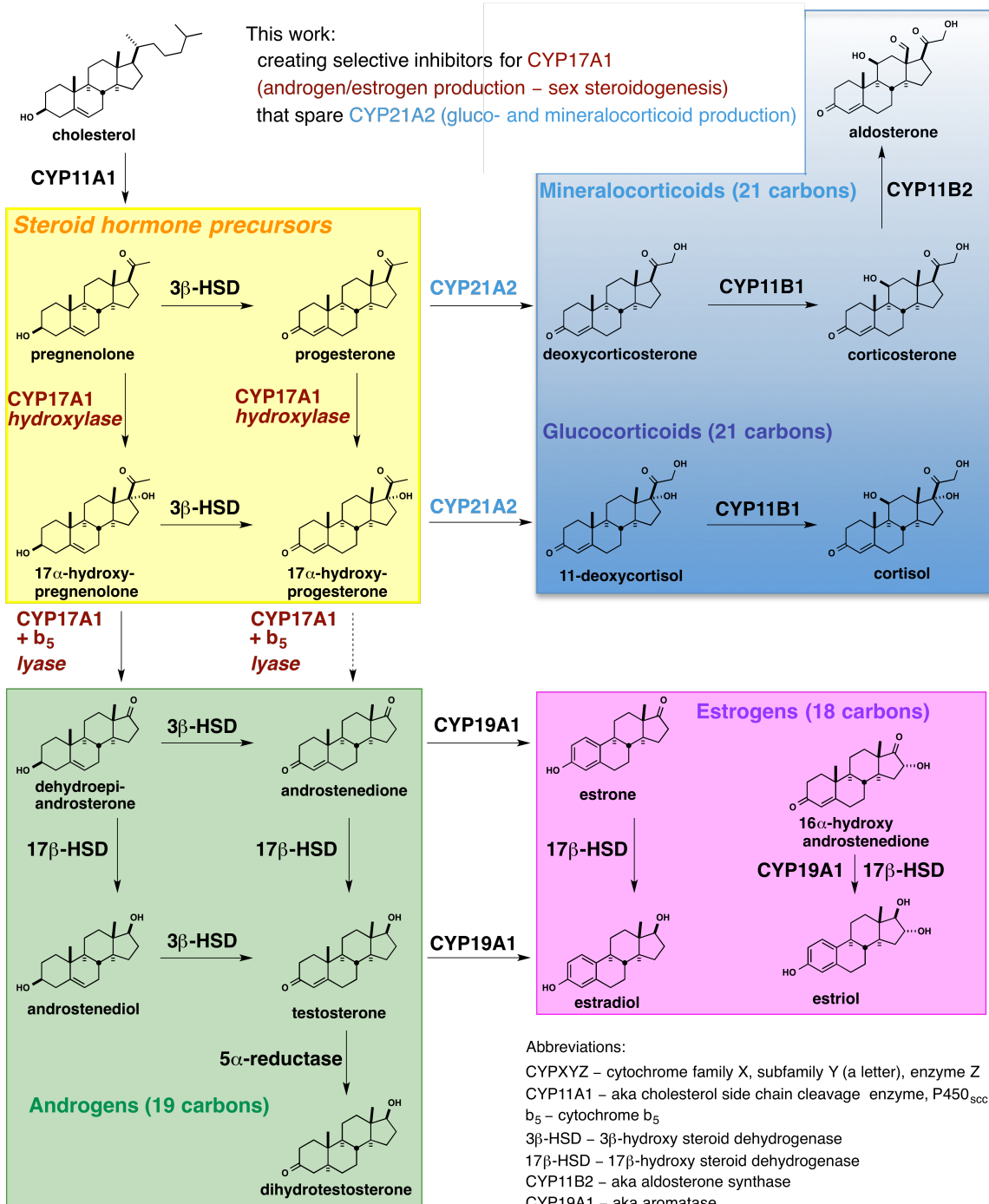
### **1.1.1 Steroid hormone synthesis by cytochromes P450**

The general pathways of steroidogenesis are shown in Scheme 1-1. Several of the enzymes involved in steroid biosynthesis belong to the cytochrome P450 superfamily, which will be described in detail shortly. The similarity between the substrates, products, and chemistry associated with these proteins can make the design of selective inhibitors for the production of a particular steroid hormone challenging.

The oxidation patterns that steroidogenic cytochrome P450 enzymes imprint on their substrates differentiate these steroid products for recognition by various steroid receptors. Steroid receptors utilize multiple mechanisms in signaling. The classically studied activities of the steroid receptors are their genomic effects.<sup>13</sup> These occur when a cytosolic steroid hormone receptor binds its cognate steroid. This complex subsequently translocates into the nucleus, where it can augment or suppress transcription. More recently, steroids have been demonstrated to additionally have nongenomic actions. For example, many steroid hormones can directly activate signaling proteins including G-protein coupled receptors or ion channels.<sup>14</sup>

Together, these modes of activation control the vast array of physiological processes mediated by the steroid hormones (Figure 1-1). This diversity of steroid action underscores the need to carefully control the selectivity of agents intended to modulate the biosynthesis of a particular steroid class.

# Scheme 1-1



Adapted from "Steroidogenesis" by David Richfield and Mikael Häggström. DOI:10.15347/wjm/2014.005

The members of the cytochrome P450 superfamily, generally referred to as P450 enzymes, are heme-containing monooxygenases that are membrane-bound in humans.<sup>15</sup> P450 enzymes are categorized into individual families, subfamilies, and enzymes based on amino acid sequence identity. For example, CYP17A1 is classified as cytochrome P450 family 17, subfamily A, enzyme 1.

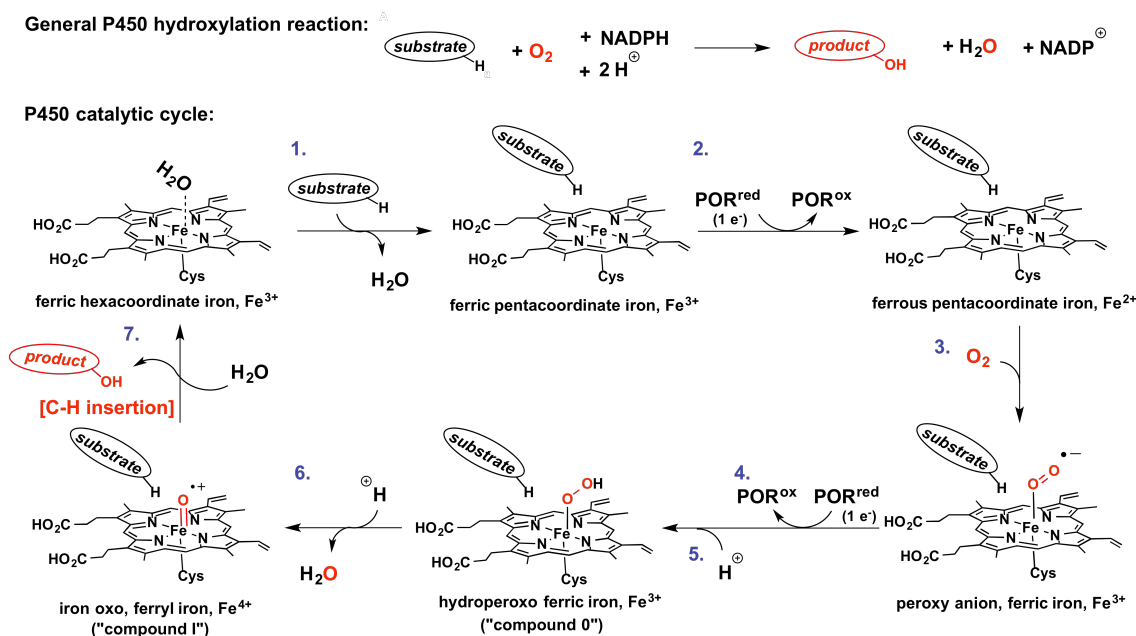
The overall tertiary structure of P450 enzymes, colloquially referred to as the P450 fold, is highly conserved across all members of the superfamily. This results in the association of a heme prosthetic group, an iron-containing porphyrin ring system, via a distinctive Fe-thiolate interaction.<sup>16</sup> P450 enzymes are able to perform various oxidative functions by utilizing the redox properties of this metal cofactor, various cellular electron donors, and oxygen. Variations in the substrate-binding active site, along with regulatory features such as protein-protein interaction sites, make each P450 enzyme unique.

P450 enzymes can be loosely generalized into xenobiotic-metabolizing enzymes and enzymes involved in endogenous metabolism. The former class typically oxidizes hydrophobic substrates to more hydrophilic metabolites, which are more readily excreted from the system. Although this metabolism is an essential aspect of drug use, it may lead to serious concerns in pharmacotherapy.<sup>17</sup> For example, drug-drug interactions or the oxidation to a reactive metabolite can cause drug-based toxicities. These enzymes typically bind and oxidize multiple chemicals with diverse substitution. In contrast, P450 enzymes associated with endogenous metabolism are often involved in the highly specific synthesis of a bioactive molecule.<sup>15</sup> Some P450 enzymes carry out both functions, such as CYP1A2, which metabolizes many drugs in addition to estrogen hormones.<sup>15</sup>

Many of the highly promiscuous xenobiotic-metabolizing P450 enzymes are in families 1, 2, and 3. CYP3A4 is a major example that can accommodate several hundred known substrates, and metabolite data has been collected among a diverse array of pharmaceutical compounds.<sup>18</sup> In contrast, CYP17A1 is a member of the endogenous biosynthetic group, and this protein conversely accepts only four very similar substrates: pregnenolone, progesterone, and their respective 17 $\alpha$ -hydroxylated versions.<sup>19</sup>

Another common feature of human P450 enzymes is that they are usually localized in the membranes of the endoplasmic reticulum or mitochondria.<sup>15</sup> This co-localizes human P450 enzymes with their redox partner protein, NADPH-cytochrome P450 oxidoreductase (POR), which reduces the substrate-heme complex to advance the catalytic cycle.<sup>20</sup> The full cycle, including POR activity, is illustrated in Scheme 1-2.

### Scheme 1-2



Inhibitors of P450 targets can be valuable therapeutic agents. The use of such agents has grown rapidly in the field of oncology as a means to short-circuit certain signaling pathways used by tumors.<sup>21</sup> In many inhibitors, properly positioned heteroatoms form a coordination complex with the heme iron and thereby deactivate P450 enzymes. These so-called Type II inhibitors typically coordinate the metal through a nitrogenous lone pair, which causes an absorbance shift in the heme system. This phenomenon may be quantitated by monitoring the visible Soret absorbance band at 424 nm upon titration with a Type II inhibitor.<sup>22</sup> An example is given using abiraterone, the first approved clinical inhibitor of CYP17A1 (Figure 1-2, data from DeVore and Scott<sup>23</sup>).

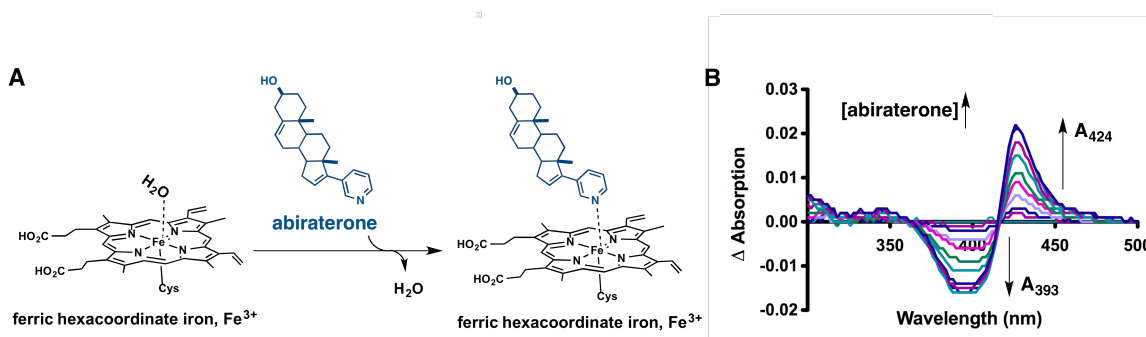


**Figure 1-2.** Type II P450 inhibitors make coordinate covalent interactions with the heme. A: Example of abiraterone-heme coordination. B: These interactions may be detected spectrophotometrically by monitoring a rise in  $A_{424}$  and a decline in  $A_{393}$  upon increasing concentration of a Type II inhibitor.

Nonspecific inhibition of xenobiotic-metabolizing enzymes is a major concern in drug discovery, since many hepatic P450 enzymes are essential for the proper excretion of drugs and other toxins.<sup>24</sup> Drugs that affect such xenobiotic-metabolizing P450 enzymes can lead to drug–drug interactions, which can modulate the pharmacokinetics of other agents co-administered with a P450 inhibitor, substrate, or inducer.<sup>24</sup>

An analogous concern for inhibitor design arises when targeting a particular P450 enzyme in a steroid biosynthetic pathway, meaning that potential agents must be screened for selectivity toward the desired target. In particular, the active sites of the steroidogenic P450 enzymes are complementary to the conserved structural features of the steroid-based substrates upon which they operate. These proteins often achieve regioselectivity through a limited set of key active site residues that position their substrates. For example, Böttner *et al.* were able to show that a three amino acid change was sufficient to engineer CYP11B2 to effecting glucocorticoid production from its role in mineralocorticoid steroid production.<sup>25</sup>

In some cases, a careful understanding of the active site structure and/or the structure–activity relationships of a compound series can enable the design of selective agents. For example, selectivity problems plagued the development of aldosterone synthase (CYP11B2) inhibitors, many of which also inhibit CYP11B1.<sup>26</sup> These complications were overcome by rigorous counter-screening against both P450 enzymes using an extensive compound library.<sup>27</sup> Useful compounds were later improved against hepatic xenobiotic-metabolizing P450 inhibition by further medicinal chemistry.<sup>28</sup>

CYP17A1 is the target of four prominent agents in advanced stages of clinical testing (Figure 1-3). The only approved CYP17A1 inhibitor, abiraterone, was revealed to cause severe perturbations of glucocorticoid and mineralocorticoid levels in most patients.<sup>29</sup> These imbalances led to side effects such as hypertension, fluid retention/swelling, and hypokalemia in the majority of patients.<sup>30</sup> The mechanisms underlying the adverse effects are still being investigated, but likely involve a combination of poor selectivity for CYP17A1 over CYP21A2 as well as the dual inhibition of CYP17A1 hydroxylase and

lyase activity.<sup>10</sup> Only CYP17A1 lyase activity is required for sex steroidogenesis, and compounds such as orteronel and VT-464 achieve some lyase selectivity.<sup>31,32</sup>

A major goal of this work is to enhance CYP17A1 selectivity over CYP21A2, which has been found to be a potential off-target of CYP17A1 inhibitors.<sup>33</sup> However, no agents have been rationally designed to attempt selective targeting of CYP17A1 over CYP21A2. Our approach toward this objective will be discussed in the following sections.

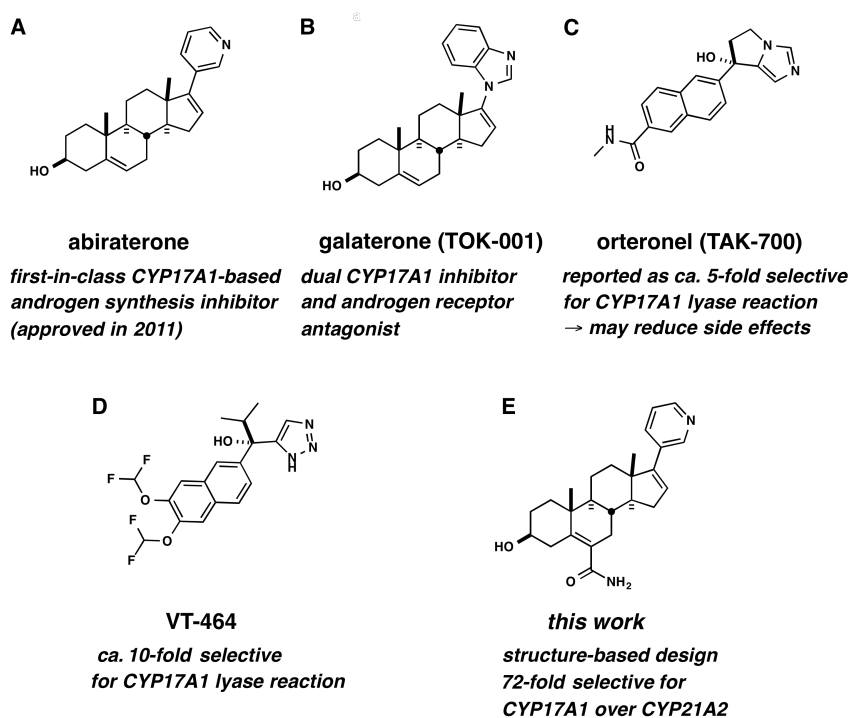


**Figure 1-3.** Structures of CYP17A1 inhibitors. A: Abiraterone, the only marketed CYP17A1-targeting drug.<sup>34</sup> B-D: Agents in clinical trials.<sup>32,31</sup> E: Outcome of this work.

### 1.1.2 Prostate cancer and androgen deprivation therapy

Prostate cancers are the most commonly diagnosed type of cancer in American men, and are second only to lung cancer in male cancer mortality.<sup>35</sup> Physiologically, prostate cancer tumors are frequently dependent on androgens for growth.<sup>36</sup> Evidence suggests

that androgens are additionally essential for prostate tumor cell survival.<sup>37</sup> Regulatory caspases initiate apoptosis in the absence of androgenic signaling in prostate tissue.<sup>38</sup> Various therapies based on lowering androgen levels have been used extensively in the treatment of this disease, and are discussed below.<sup>39</sup>

Androgens bind to the androgen receptor (AR), which is often overexpressed in prostate cancer cells.<sup>40</sup> Like the other nuclear steroid hormone receptors, the AR forms a complex with heat-shock protein chaperones. When androgens bind the AR, the heat-shock protein releases the AR, which dimerizes into its active conformation. The active AR dimer is then able to translocate from the cytosol into the nucleus, where it can associate with the androgen response element to initiate a program of transcription involved in cellular proliferation and survival.<sup>41</sup> The activated AR has also been shown to have nongenomic effects as well, including kinase signaling cascades.<sup>42</sup>

Treatment for prostate cancer typically begins with a regimen of androgen deprivation therapy (ADT), often augmented by traditional chemotherapies like docetaxel. The historic development of these therapies is outlined in Figure 1-4.<sup>39</sup> Charles Huggins and Clarence Hodges performed the original development research for ADT in the 1940s. One method of ADT is surgical castration of the androgen-producing testes.<sup>43</sup> This therapy is still used today as a treatment option (Figure 1-4 A).

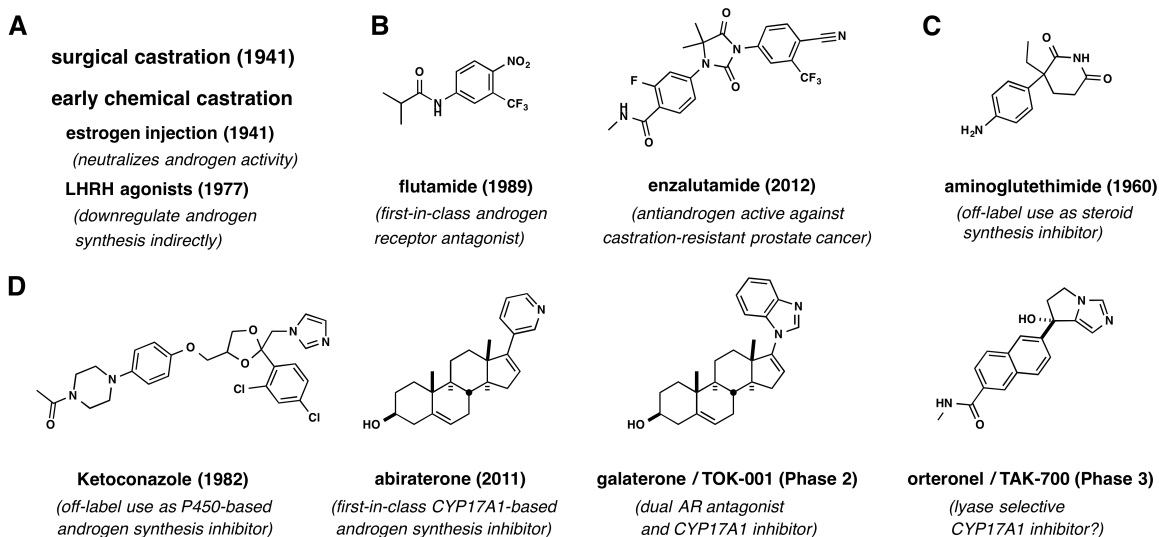


**Figure 1-4.** A brief history of androgen deprivation therapy in prostate cancer. A: Classical ADT therapy. B: Modern chemical castration – the antiandrogens. C: General steroid biosynthetic inhibitor. D: CYP17A1-targeted androgen biosynthetic inhibitors.

Chemical castration, also developed around this time by Huggins, has since overtaken surgical castration as a reversible option for ADT (Figure 1-4 A). Chemical castration historically took the form of estrogen injection, which neutralizes androgen activity, though androgen synthesis would still occur. In studies carried out between 1960 and 1980, Andrew Schally found that chronic administration of luteinizing hormone releasing hormone (LHRH) agonists down-regulated circulating levels of the androgen synthetic promoters luteinizing hormone and follicle-stimulating hormone through a negative feedback mechanism. Thus, LHRH agonists provided an indirect way to reduce androgen activity for the treatment of prostate cancer.<sup>39</sup>

Direct modulation of the AR itself, termed antiandrogen therapy, is another variant of ADT, which blocks the ability of androgens to initiate a signal through the AR (Figure 1-4 B). This approach was validated by the approval of flutamide. However, due to its

essential nature for these tumors, mutations in the AR frequently lead to antiandrogen-resistant prostate cancer.<sup>44</sup> These mutations vary, but can include a mutant AR that becomes activated by the originally antagonistic antiandrogens. Enzalutamide is a recently approved, second-generation antiandrogen that maintains efficacy in some AR-mutant cancers.<sup>45</sup> The presence of one or more types of active AR mutants is often a hallmark of castration-resistant prostate cancer (CRPC), an advanced form of this disease.<sup>46</sup>

One mechanism by which tumors progress to the CRPC state is sensitization to extremely low levels of androgens through AR overproduction or mutation.<sup>47</sup> Surgical or chemical castration fails to completely halt androgen biosynthesis, which can still occur through extra-testicular CYP17A1 activity. For instance, there is significant CYP17A1 expression in the adrenal glands, and despite relatively low adrenal levels of a protein cofactor that promotes CYP17A1-based androgen production, sufficient levels of androgens may be synthesized.<sup>48</sup> Even in castrate men, androgen-responsive CRPC tumors can utilize these low levels of circulating androgens to resume growth.<sup>49</sup> Furthermore, some CRPC tumors begin to express CYP17A1 and can fuel their own androgen-promoted growth in an autocrine fashion.<sup>50</sup>

In addition to these mutations, there are other forms of CRPC which are independent of androgens, such as those expressing a constitutively active AR.<sup>51</sup> Taken as a whole, CRPC has a low 10-year survival rate of 24%,<sup>52</sup> underscoring a pressing medical need. Inhibiting the biosynthetic pathway of the androgens results in a more extensive approach to ADT. Such a systemic and robust form of ADT is necessary for successful and lasting outcomes in patients with CRPC responsive to androgen production. To meet a

significant portion of this unmet medical need, CYP17A1 has emerged as a target for pharmaceutical intervention in androgen-responsive prostate cancers. This strategy has recently seen regulatory approval.<sup>53</sup>

In earlier clinical work, androgen and other hormone levels had been observed to drop upon administration of a high dose of the general anti-steroid aminoglutethimide, which inhibits CYP11A1/P450<sub>scc</sub> as the first step in steroidogenesis (Figure 1-4 C). This strategy was refined somewhat in the 1980s, when it was discovered that the slightly less-toxic antifungal agent ketoconazole, a relatively nonselective P450 inhibitor, had a similar effect, but did not inhibit all steroidogenic processes.<sup>39</sup> It was later determined that CYP17A1 was inhibited by ketoconazole (Figure 1-4 D). This led to the off-label use of high dose ketoconazole (HDK) as a second-line prostate cancer therapeutic, although this was wrought with side effects such as gastrointestinal toxicity, fatigue, and skin toxicities such as sticky skin and bruising.<sup>54</sup>

The first direct CYP17A1 inhibitor was abiraterone, approved as its acetate prodrug in 2011 (Figure 1-4 D).<sup>53</sup> Abiraterone was rationally designed to target CYP17A1, which performs the first enzymatic step in androgen formation, namely C17-C20 lyase. Structurally, abiraterone closely resembles the CYP17A1 substrate pregnenolone, but includes an iron-coordinating pyridyl group. This makes abiraterone a Type II P450 inhibitor (Figure 1-2). By reducing circulating testosterone to below-castrate levels, abiraterone was found to successfully prolong the overall survival of CRPC patients by ca. 3-4 months for patients post-chemotherapy with docetaxol.<sup>29</sup> Abiraterone acetate is currently undergoing evaluation for earlier stages of prostate cancer as a therapy to prevent the progression of the disease.<sup>29</sup>

In addition, CYP17A1 inhibition is a possible strategy for the treatment of estrogen receptor-positive breast cancers. Estrogen receptor-breast cancer etiology is often similar to that of androgen receptor-prostate cancer progression.<sup>55</sup> Androgen production through CYP17A1 precedes estrogen production by CYP19A1 (aromatase), and thus CYP17A1 inhibition in women would offer an earlier point of hormone biosynthesis intervention than aromatase inhibitors. Several clinical studies investigating the efficacy and safety of abiraterone treatment on various metastatic breast cancers are underway as of this writing, including trials for metastatic breast cancer,<sup>56</sup> molecular apocrine breast cancer,<sup>57</sup> and the long-term effects of abiraterone on women.<sup>58</sup>

While resistance to abiraterone has been observed in CRPC, strong evidence suggests that abiraterone-resistant tumors still remain androgen-dependent.<sup>47</sup> Thus, agents able to further improve upon abiraterone's activity, in addition to selectivity, are in clinical development. This includes galaterone, a steroid that has dual mechanisms of action in AR antagonism and CYP17A1 inhibition.

Non-steroidal compounds are also being investigated. Some promising derivatives are orteronel, which is reported to be 5.4-fold selective for the lyase reaction of CYP17A1 over the hydroxylase reaction,<sup>59</sup> and the similar agent VT-464, which reports ca. 10-fold lyase selectivity.<sup>31</sup> As of this writing, Orteronel had completed a Phase 3 study co-administered with prednisone,<sup>60</sup> which is how abiraterone is currently utilized. This agent was voluntarily terminated due to a lack of overall survival benefit.<sup>61</sup>

Orteronel is also currently undergoing a Phase 2 study without prednisone. The latter study aims to determine if the modest level of CYP17A1 lyase selectivity achieved with orteronel is able to reduce the side effects of blocking CYP17A1 hydroxylase activity,

required for glucocorticoid synthesis.<sup>62</sup> Even if this study is not ultimately successful in patients, this agent may provide important clinical data towards understanding selective CYP17A1 lyase inhibition by small molecules.

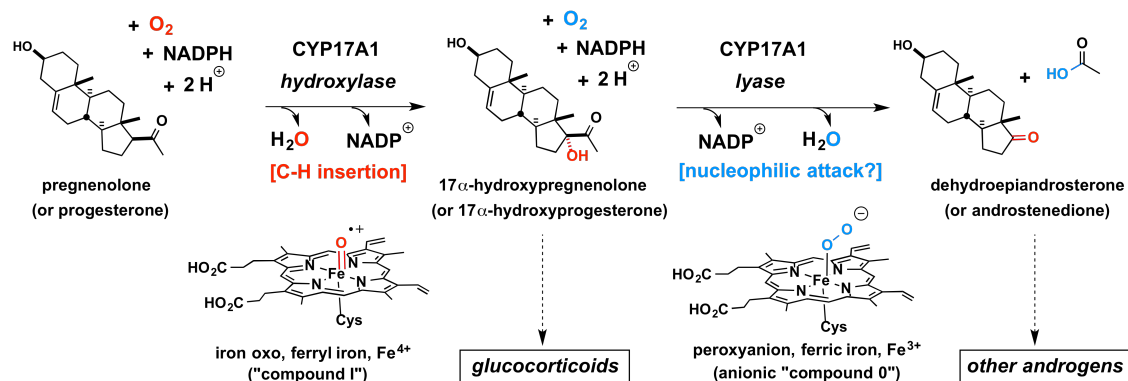
### **1.1.3 CYP17A1 biochemical activity – a case for selective inhibitor design**

As discussed above, cytochrome P450 17A1 (CYP17A1) is a key enzyme in both sex steroid and glucocorticoid production.<sup>19</sup> CYP17A1 catalyzes two discrete types of reactions (Scheme 1-3). The hydroxylase reaction creates 17 $\alpha$ -hydroxypregnenolone and 17 $\alpha$ -hydroxyprogesterone, which are precursors for the glucocorticoids. The lyase reaction, which takes place after the hydroxylase reaction, creates dehydroepiandrosterone and, to a much lesser extent, androstenedione.<sup>19</sup> This latter carbon–carbon cleavage reaction is the only source of 19-carbon sex steroids in humans.<sup>63</sup>

In CYP17A1 catalysis, it is generally accepted that the heme “compound I” is responsible for 17 $\alpha$ -hydroxylase activity (Scheme 1-3).<sup>19</sup> However, there is controversy over which stage of the P450 cycle performs the C17-C20 scission of the lyase reaction (the full cycle is shown in Scheme 1-2). Recent evidence suggests that the deprotonated form of the heme “compound 0” may be implicated in lyase chemistry, proceeding through an anionic iron-peroxo species. This nucleophile could attack the C20 ketone and form a tetrahedral intermediate, which could subsequently break down to produce the C17 ketone-bearing steroid product and acetic acid.<sup>64,65</sup> Further experimental work is needed to confirm this hypothesis, but unpublished structural data in our laboratory supports this mechanism.<sup>66</sup>

### Scheme 1-3

CYP17A1 performs two discrete reactions:



There is only one heme-containing pocket in CYP17A1, so both hydroxylase and lyase reactions necessarily occur in the same active site.<sup>67</sup> In humans, lyase activity is regulated by the protein cytochrome *b*<sub>5</sub>, which can bind CYP17A1 to enhance lyase activity by ca. 10-fold, whereas hydroxylase reactivity is only enhanced ca. 2-fold.<sup>68</sup> This is important in the tissue distribution of CYP17A1. In the testes, ovaries, and adrenal zona reticularis, CYP17A1 is co-expressed with high levels cytochrome *b*<sub>5</sub>. In the adrenal zona fasciculata, only low levels of cytochrome *b*<sub>5</sub> are present.<sup>69</sup> This provides these organ types with differential CYP17A1-product distribution, i.e. sex steroids in the testes, ovaries, and zona reticularis versus glucocorticoids in the zona fasciculata. This adrenal androgenic activity reveals why systemic and not just gonadal CYP17A1 blockade must occur for effective sex hormone deprivation therapy.

Since the CYP17A1-lyase reaction is only way to generate 19-carbon sex steroid precursors in the body, this is a potentially excellent target to block sex steroidogenesis in hormone-responsive prostate and breast cancers. However, the clinical agent abiraterone blocks CYP17A1 hydroxylase as well as lyase nearly equally effectively,<sup>70</sup> consistent with its binding to the sole active site of CYP17A1. It is unknown how the agents that are



When the activity of either class of corticoid steroid drops, feedback mechanisms signal through adrenocorticotrophic hormone (ACTH) to stimulate the production of additional steroids. This increases the flux of the steroidogenic substrates pregnenolone and progesterone from cholesterol (Scheme 1-5, steps 1, 2, and 3).<sup>73</sup> High levels of progesterone can sometimes be transformed into androgens through a biosynthetic diversion termed the “backdoor pathway” to testosterone,<sup>74</sup> which would allow tumor growth to proceed and compromise the therapeutic efficacy of abiraterone. However, CYP17A1 activity is still required for the backdoor pathway to proceed.

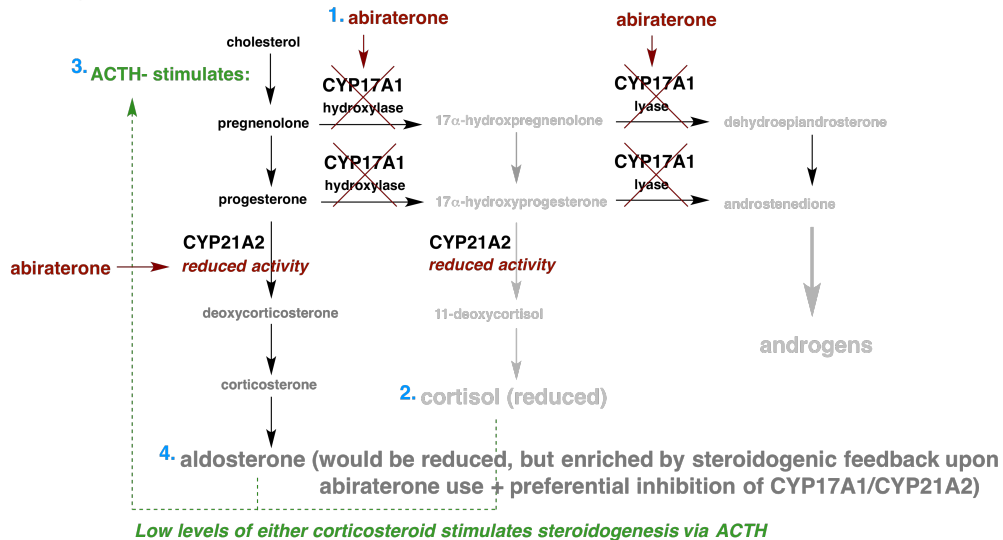
Another serious effect of ACTH-mediated increased progesterone flux is mineralocorticoid excess, since the pathways toward sex steroid and glucocorticoid synthesis are more effectively blocked by abiraterone than the pathway toward mineralocorticoid production (Scheme 1-5, step 4). Excess aldosterone increases salt and water retention, creating severe hypertension in most patients using abiraterone alone.<sup>29</sup>

### Scheme 1-5

Sequence of abiraterone-based steroid disruption:

1. ↓ 17 $\alpha$ -hydroxy steroids
2. ↓ cortisol
3. ↑ ACTH
4. ↑ aldosterone (causes hypertension)

Pathway:



→ Sparing both CYP17A1 hydroxylase and CYP21A2 is desirable to avoid ↑ steroidogenesis

Administering exogenous glucocorticoids can reduce the rise in ACTH that signals to increase steroidogenesis.<sup>73</sup> The use of glucocorticoid therapy is undesirable due to numerous side effects, including osteoporotic symptoms,<sup>75</sup> but a recent clinical evaluation by Pia *et al* concluded that this is the most effective treatment for hypertension resulting from abiraterone-induced mineralocorticoid excess.<sup>73</sup> However, there is a balance in modulating corticoid hormone levels. A phase I study of abiraterone co-administered with the glucocorticoid analog dexamethasone, which has no mineralocorticoid activity, demonstrated the desired drop in ACTH levels, but resulted in a deficiency of mineralocorticoid production.<sup>76</sup> This deficiency may be a result of abiraterone-based CYP21A2 inhibition. The most common agent co-administered with abiraterone is prednisone, a glucocorticoid with weak mineralocorticoid activity.<sup>29</sup> However, prednisone is not completely effective at relieving symptoms from mineralocorticoid excess in all patients.<sup>73</sup>

Thus, finding the optimal balance of regulating glucocorticoid activity and mineralocorticoid activity in CYP17A1-based androgen biosynthesis inhibition remains a challenge. The most effective agents will likely require selectivity for CYP17A1 lyase activity against both CYP17A1 hydroxylase and CYP21A2 activities.

This dissertation chapter focuses on designing a class of CYP17A1 inhibitors with greater selectivity relative to other P450 targets. In particular, we focus on CYP21A2, for which we have demonstrated that abiraterone also has considerable inhibitory activity. To our knowledge, this aspect of CYP17A1 drug design has not been well studied. When ultimately combined with knowledge of the basis for selectively targeting CYP17A1's lyase reaction with orteronel and VT-464, the research described here is expected to offer

additional progress toward the design of improved CYP17A1 inhibitors for sex hormone-responsive prostate and breast cancers.

#### **1.1.4 Comparison of CYP17A1 and CYP21A2 crystal structures suggest that selectivity can be rationally designed**

Structural biology can be a powerful tool for analyzing and optimizing the binding of ligands with biomolecular targets. Cytochromes P450 have been challenging to study with high-resolution biophysical techniques like X-ray crystallography and structural NMR due to their membrane-bound nature. This limits the aqueous solubility and stability of this family.<sup>77</sup> For this reason much of our early understanding of P450 structure and function arose from the study of soluble bacterial P450 enzymes.<sup>78</sup>

Removing the ca. 20 amino acids that compose the single N-terminal transmembrane helix greatly enhances P450 solubility and expression level while maintaining catalytic activity.<sup>79</sup> Natasha DeVore, a previous lab member, used this technique to solve the first crystal structures of CYP17A1, which were co-crystallized with the clinical agents abiraterone and galaterone.<sup>23,67</sup> An important finding of this work corrected previous assumptions of the abiraterone binding modes with CYP17A1, which were based on homology models. These models predicted a bi-lobed active site for the two reactions of CYP17A1,<sup>80</sup> which has not been observed in inhibitor-bound crystal structures nor in unpublished structures of CYP17A1 substrates for either reaction.<sup>66</sup>

Cytochromes P450 have a highly conserved P450 fold, but have nevertheless evolved a myriad of different, often highly selective activities. Changes to the active site architecture allow this diversity. The overall P450 fold is comprised of an  $\alpha$ -helical

protein core (major helices A-L), a number of minor helices (indicated by a prime character, e.g. B'), and several  $\beta$ -sheets (numbered 1-4).<sup>15</sup> Figure 1-5 shows these features as revealed by the crystal structures of human CYP17A1 and the previously published structure of bovine CYP21A2,<sup>81</sup> the main P450 enzymes relevant to this dissertation.

Our goal was to design more selective ligands for CYP17A1 over CYP21A2. To start, we compared X-ray structures of human CYP17A1 with CYP21A2, bound with abiraterone or  $17\alpha$ -hydroxyprogesterone, respectively (Figure 1-5). Both of these ligands are steroids, which allows some degree of comparison, as discussed below. The overall fold and helix orientation are similar between the two proteins, and the secondary structures of these PDB entries were readily aligned for direct comparison.

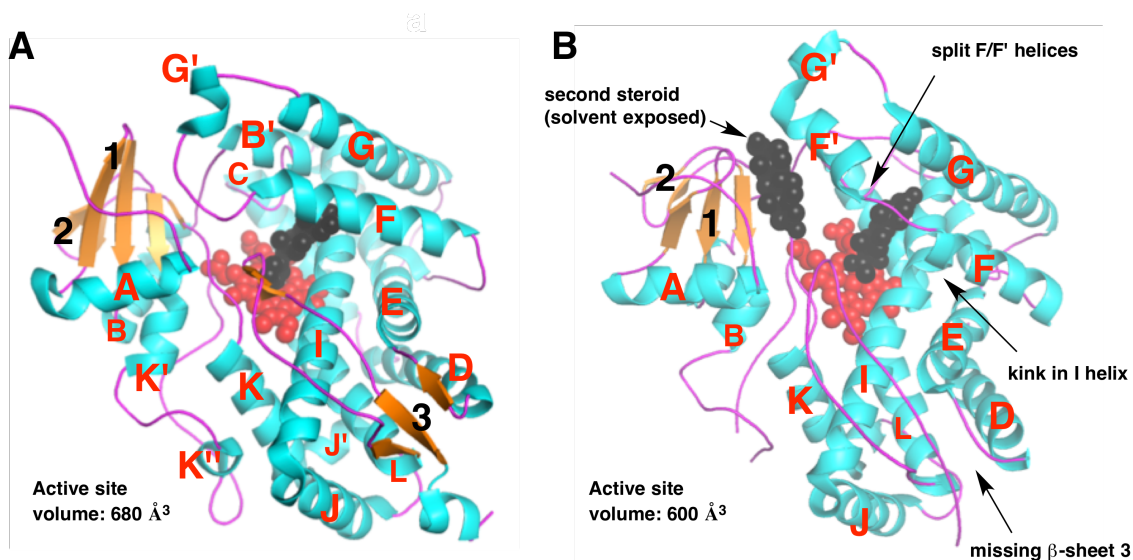


**Figure 1-5.** Overall structure of CYP17A1 and CYP21A2. A: Human CYP17A1 with abiraterone (PDB: 3RUK). B: Bovine CYP21A2 with  $17\alpha$ -hydroxyprogesterone (PDB: 3QZ1). Helices are shown as ribbons with letters and sheets as arrows with numbers. The heme, as the floor of the active site, is shown as red spheres. Steroid ligands are shown as black spheres. Key differences are indicated with arrows on the CYP21A2 structure.

Though the overall structure is generally similar, there are a few significant differences. Most strikingly, the CYP21A2 structure has two steroid ligands bound to the same protein molecule. The steroid bound nearby the heme in CYP21A2 can be compared with abiraterone in CYP17A1. The distal steroid molecule in CYP21A2 likely indicates the location of a channel through which steroids enter the active site. No second steroid has been observed in any CYP17A1 structures. Other notable changes in CYP21A2 include a distinct kink in the I-helix, which forms one wall of the active site. There is a split of the F helix into an additional F' helix, which shortens these helices. This is notable as the F-helices in each protein form key interactions with steroid ligands.

The active site volumes are roughly equal in size, though the second steroid in CYP21A2 may make this comparison less valid since it must be used as an active site “wall” for mapping the active site volume. The active site space is composed of the heme, the F (and F' in CYP21A2), G, and I helices, and several loops. Together, these make up a cavity enclosed by primarily hydrophobic residues.<sup>23</sup> The individual residues that line these cavities are important for substrate recognition, binding, and positioning.

Comparison of the active sites revealed substantial differences between the two steroid-binding active sites (Figure 1-6). Hydrogen bonding and hydrophobic interactions orient the steroid ligands, which lie at different angles from the heme plane between the two structures. In CYP21A2, the guanidinium group of Arg232 makes a hydrogen bond (H-bond) with the 3-keto group of the substrate, which directs the substrate to lie at a ca. 45° angle (where 0° would indicate the steroid core as parallel to the porphyrin ring and 90° as perpendicular). Conversely, in CYP17A1 abiraterone lies closer to perpendicularity to the heme, about 60°. This orientation is directed by an H-bond

between the C3-hydroxyl and the CYP17A1 sidechain amide of Asn202. In CYP21A2, there is a sizable cavity near the steroid 21-position, which could presumably accommodate the 21-hydroxylated products.

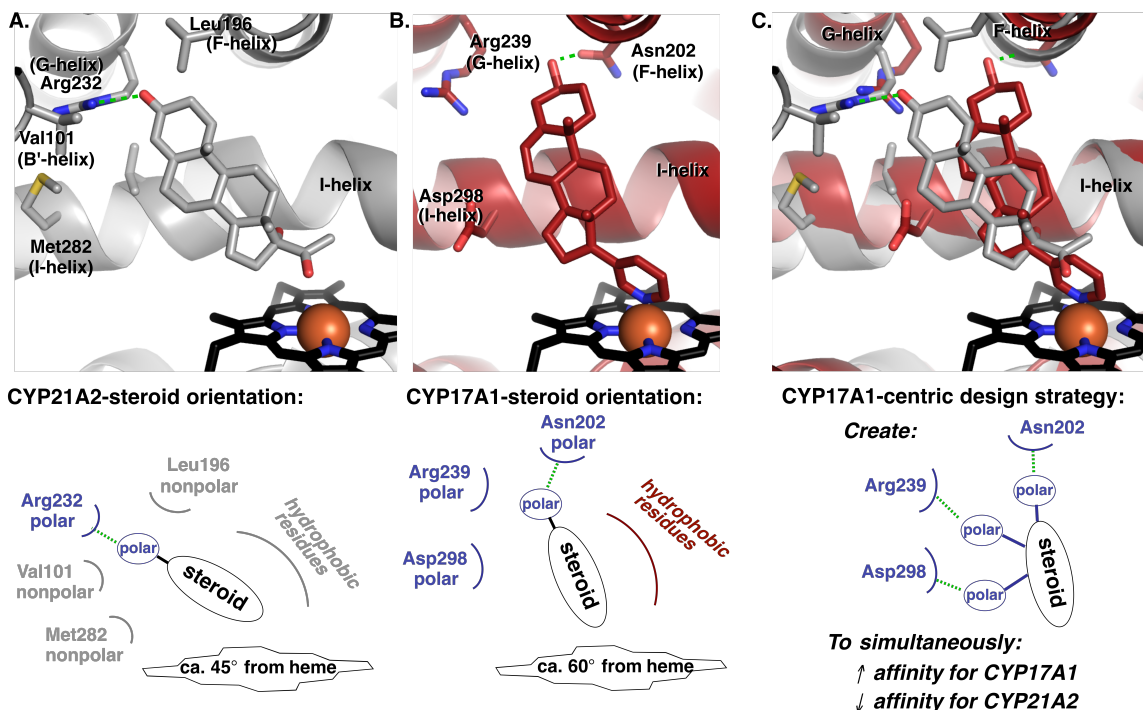


**Figure 1-6:** Active site comparison between CYP21A2 and CYP17A1. A: CYP21A2 with substrate 17 $\alpha$ -hydroxyprogesterone (PDB: 3QZ1). B: CYP17A1 with abiraterone (PDB: 3RUK). C: Overlaid. Nitrogen atoms are shown in blue, oxygen in red, and iron in an orange sphere. Hydrogen bonds are highlighted in green.

The  $\alpha$ -face of the steroid packs tightly along the I-helix in both structures. The surrounding cavity in CYP21A2 is bounded by hydrophobic residues ca. 4 Å from the steroid. In CYP17A1, only three sides of the substrate-binding cavity are composed of hydrophobic surfaces, also ca. 4 Å from the steroid. The remaining side is further from the steroid core, which leaves an approximately 6 Å-wide space flanked by the polar residues Arg239 and Asp298.

This space is the most notable difference between these structures. It is shown on the left side of the CYP17A1 active site in Figure 1-6. This polar cleft suggested that substituents to a ligand could be added to optimize binding interactions with CYP17A1. Furthermore, such substitution may clash with the nonpolar residues in similar positions in CYP21A2, Val101 and Leu196. While CYP21A2 Arg232 is roughly comparable to CYP17A1 Arg239, CYP21A2 has no analogous polar residues to CYP17A1 N202 and CYP17A1 D298.

Hence, abiraterone analogs with B-ring polar residues that maintained the CYP17A1 N202 interaction could potentially increase CYP17A1 potency while decreasing CYP21A2 potency. Thus, these features formed our general design strategy to test the hypothesis that key groups in this region could increase CYP17A1/CYP21A2 selectivity.

It is important to recognize that protein crystallography provides a static picture of a particularly stable complex between a ligand and a protein, generally in one conformation. The P450 enzymes are a highly plastic superfamily, and are often able to adopt multiple conformations in response to ligand-binding events.<sup>82</sup> Solution-phase dynamics can present structures that are different than what is observed in the solid state.<sup>68</sup> In addition, the structures we analyzed were from different species, and contained different ligands. However, this was the information available, so we used the comparisons outlined above for initial inhibitor design while remaining cognizant that alternative conformations may be observed in response to ligand modifications. In some cases, ligand-induced pockets can provide unforeseen selectivity if other isoforms are unable to accommodate such a change.<sup>83</sup> Thus, continued structure-based design would remain an important aspect of this project.

### 1.1.5 Preliminary design strategy toward CYP17A1/CYP21A2 selective inhibitors

Numerous reports of the structure-activity relationships (SAR) of steroidal and non-steroidal CYP17A1 inhibitors have been described.<sup>84</sup> The most potent of these agents retain the full steroid core, which was observed in the crystal structure of CYP17A1 to be highly complementary to three of four “sides” of the active site. Opening the B, C, or D rings in abiraterone analogs often significantly dropped potency.<sup>85</sup> The 3-pyridyl group presented nearly optimal potency among several other heterocycles at the C17-position of the steroid.<sup>86</sup> Among polar A-ring groups, the 3 $\beta$ -OH group also maintained good potency.<sup>86</sup>

Thus, our inhibitor design strategy retained the steroid scaffold, 3 $\beta$ -OH, and C17-(3-pyridyl) features of abiraterone. However, the C6-position of the steroid scaffold has been neglected in the literature, though the crystal structure suggested that additional interactions with active site residues are possible and potentially desirable. These are outlined in Figure 1-7 A. The ca. 6 Å space available to one side of the observed CYP17A1 active site may accommodate up to 3 additional C-C, C-O, or C-N bonds without requiring protein rearrangement.

The modifications we proposed utilized the  $\Delta^5$  olefin as a building block for polar substitution. Olefins can be functionalized using a variety of reactions, and we chose those that would install groups ranging in size and polarity to probe this polar cleft (Figure 1-7 B). One aim of this project was to enhance CYP17A1 selectivity over CYP21A2 while maintaining CYP17A1 potency. Initial compounds retaining good CYP17A1 potency would then be counter-screened against human CYP21A2, which was recently expressed in our laboratory.<sup>87</sup>

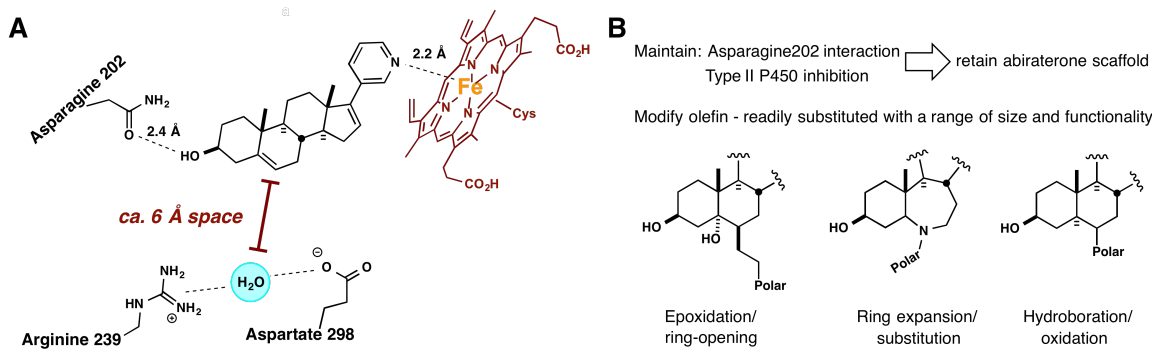


**Figure 1-7.** Design strategy toward improved CYP17A1 inhibitors. A: Schematized active site of CYP17A1. B: Features of our initial analog design strategy.

## 1.2 Methods

### 1.2.1 Inhibitor synthesis

The inhibitors synthesized in this study were prepared and characterized as described in the Experimental Section (1.5). The synthetic schemes and design aspects are examined in the Results and Discussion section (1.3.1).

Most of the compounds selected to undergo testing for biological activity were purified by preparative scale mass-directed high performance liquid chromatography (HPLC). This was performed on a Waters 2767 Mass Directed Fractionation system (2767 sample manager, 2525 Binary Pump, 515 HPLC pump) with a Waters ZQ quadrupole mass spectrometer and detected by UV (270 nm, Waters Xterra MS C-18 column, 19x150 mm, elution with the appropriate gradient of acetonitrile in pH 9.8 buffered aqueous ammonium formate at 18 mL/min flow rate).

Compound purity was determined by reverse-phase HPLC with peak area (UV) at 214 nm using a Waters Alliance 2795 system (Waters Xterra MS C-18 column, 4.6x150 mm, elution with a linear gradient of 5% acetonitrile in pH 9.8 buffered aqueous ammonium formate to 100% acetonitrile at 1.0 mL/min flow rate).

Photochemistry was performed in a Rayonet RPR-100 reactor equipped with RPR-3000 lamps,  $\lambda_{\text{max}}$  305 nm (Southern New England Ultraviolet Company, Branford, CT). Microwave reactions were carried out in a Biotage Initiator (Biotage USA, Charlotte, NC).

### 1.2.2 Enzyme activity assays

Complementary assays were utilized for the quantitative comparison of compound activity data for CYP17A1 and CYP21A2. Progesterone is a substrate for both CYP17A1 and CYP21A2, and was the substrate studied for enzyme activity, IC<sub>50</sub> determinations, and selectivity comparison. Two methods for detecting enzymatic activity were utilized. Analytical High Pressure Liquid Chromatography (HPLC) for biochemical assays was performed on a Prominence HPLC system (Shimadzu Scientific Instruments, Inc., Columbia, MD) equipped with a C18 reverse phase 100 mm Luna Column (Phenomenex, Torrance, CA). The mobile phase consisted of 40% acetonitrile, 59% water, and 1% acetic acid with a 1 mL/min flow rate at 40 °C. An injection volume of 32 µL (CYP17A1) or 45 µL (CYP21A2) was used. The presence of the CYP17A1 product 17 $\alpha$ -hydroxyprogesterone was detected with an absorption wavelength of 248 nm as reported by DeVore.<sup>23</sup> The presence of the CYP21A2 product 21-hydroxyprogesterone was detected with an absorption wavelength of 248 nm.

However, HPLC was unsuitable for CYP21A2 enzyme inhibition assays due to insufficient detection limits and the fact that since several inhibitors co-eluted with the 21-hydroxyprogesterone product under numerous HPLC conditions. Accordingly, a GC/MS detection-based protocol was developed to study CYP21A2 steady state kinetics. This is described further in section 1.3.2.

Modified constructs of human CYP17A1, human CYP21A2, and human NADPH-cytochrome P450 oxidoreductase (POR) were used. These protein constructs lack a hydrophobic N-terminal transmembrane helix. The resulting proteins are still expressed in a membrane-bound form, but can be more easily extracted and solubilized with

detergents, facilitating their crystallization and functional analysis. Specifically, this modification allows their study as purified proteins rather than as components in a less-defined preparation of microsomes. Thus, the absolute concentrations of each P450 as well as POR are known, rather than concentrations relative to total protein content as used in typical assays for CYP17A1<sup>88,89</sup> and CYP21A2<sup>90</sup> activity in the literature.

The engineering of the specific CYP17A1 construct utilized, CYP17A1 $\Delta$ 19H, is described in detail in Section 1.2.3, below. This construct was generated from the wild type sequence of human CYP17A1, as described by DeVore.<sup>23</sup> The additional  $\Delta$ 19 and H signify an N-terminal deletion of 19 amino acids for solubility (the “ $\Delta$ 19”) and a C-terminal four-histidine tag for purification (the “H”). CYP17A1H $\Delta$ 19 was overexpressed and purified by Fehl and Petrunak, as described below (section 1.2.3). Hereafter, “CYP17A1” will refer to CYP17A1H $\Delta$ 19 for simplicity. “Full-length CYP17A1” will be specifically designated when appropriate.

The CYP21A2 construct that was used, CYP21A2dH, was also engineered as originally developed by Linda Blake.<sup>87</sup> In this construct, the “d” refers to an 18 amino acid N-terminal deletion. An N-terminal solubility tag was added, in addition to a C-terminal four-histidine tag (“H”). In the present work, CYP21A2dH was overexpressed and purified by lab member Elyse Petrunak, following this reported procedure.<sup>87</sup> Hereafter, “CYP21A2” will refer to CYP21A2dH for simplicity. “Full-length CYP21A2” will be specifically designated when appropriate.

The human POR construct utilized bears an N-terminal truncation of a transmembrane helix ( $\Delta$ 27) to increase expression levels, and a K59Q mutation to prevent proteolysis.<sup>91</sup> This POR construct was overexpressed and purified by Petrunak or by the Protein

Production Group of the University of Kansas Center of Biomedical Research Excellence in Protein Structure and Function, following a reported procedure.<sup>91</sup>

GC/MS was performed on an Agilent Technologies 6850 Network GC System equipped with a 6850 series autosampler and an Agilent Technologies 5975C VL MSD with triple axis detector. The electron energy was 70 eV and the ion source temperature was 230 °C. Each sample (5 µL) was injected at an injector temperature of 280 °C and separated through an Ultra-1 capillary column (25 m × 0.2 mm inner diameter, 0.33-mm film thickness; Agilent Technologies). The oven temperature was initially 215 °C, which was ramped to 245 °C at 1 °C/min and then finally increased to 315 °C and held for 2 minutes, using a 10 °C/min ramping program. Helium was used as the carrier gas with a column head pressure of 210.3 kPa (column flow: 1.0 mL/min at an oven temperature of 215 °C). For quantitative analysis, the characteristic ions of the monitored steroids were determined as their poly-TMS derivatives. Product and starting material MS counts were normalized for analysis against a known amount of estriol internal standard.

Samples were prepared for GC/MS by solid phase extraction (SPE) using SUPELCO Supel™-Select HLB SPE tubes, bed weight 30 mg (Sigma Aldrich). Parallel evaporation was performed using a GeneVac EZ-2 plus evaporator. Poly-trimethylsilyl derivatization was accomplished using a 1000:8:4 (v/w/w) *N*-methyl-*N*-(trimethylsilyl)trifluoroacetamide:ammonium iodide:dithioerythritol mixture that had been stirred at room temperature for at least 12 hours (MSTFA).

Changes in absorbance or GC/MS counts were analyzed using Prism (GraphPad Software). Enzyme activity data was fit to the Michaelis-Menten equation to determine the steady state kinetic parameters. Product formation data was fit to the variable slope

inhibition equation  $Y=100/(1+10^{((\text{LogIC}_{50}-X)*\text{HillSlope}))}$  in Prism 5 (GraphPad, La Jolla, CA) to determine inhibitor  $\text{IC}_{50}$  values. Data from at least two replicates with 8 or more activity points each were averaged and analyzed for standard error, which is reported in the Results and Discussion section 1.3.2.

#### *Analysis of 17 $\alpha$ -hydroxyprogesterone generation by CYP17A1 using HPLC*

The assays were carried out with 50 pmol of purified CYP17A1 in a 1:4 ratio with POR. The protein stocks were gently mixed together by pipetting and incubated on ice for 20 minutes. This reconstituted protein system was added to buffer (50 mM Tris, pH 7.4 and 5 mM  $\text{MgCl}_2$ ) containing progesterone (0-50  $\mu\text{M}$ ) for a total volume of 500  $\mu\text{L}$ . For the inhibition studies, 50  $\mu\text{M}$  progesterone was used. The samples were incubated at 37° C for 3 minutes. Reactions were initiated by the addition of 1 mM NADPH. Reactions were allowed to proceed for ten minutes at 37 °C and stopped by the addition of 300  $\mu\text{L}$  of 20% TCA and placed on ice. All standards (consisting of 17 $\alpha$ -hydroxyprogesterone in assay conditions) and zero samples had 300  $\mu\text{L}$  of 20% trichloroacetic acid (TCA) added prior to the addition of NADPH. Samples and standards were centrifuged at 5000  $\times$  g for 10 minutes to pellet out the protein. The presence of 17 $\alpha$ -hydroxyprogesterone was detected with an absorption wavelength of 248 nm. 17 $\alpha$ -Hydroxyprogesterone eluted at approximately 5.5 minutes.

#### *Analysis of 21-hydroxyprogesterone generation by CYP21A2 using HPLC*

The assays were carried out as above, with 20 pmol purified CYP21A2 in 1:4 ratio with POR. For enzyme activity studies, progesterone (0-100  $\mu\text{M}$ ) was present. The

presence of 21-hydroxyprogesterone was detected with an absorption wavelength of 248 nm. 21-Hydroxyprogesterone eluted at approximately 4.1 minutes. This was used only in preliminary experiments, as discussed in Section 1.3.2.

*Analysis of 21-hydroxyprogesterone generation by CYP21A2 using GC/MS. Samples were prepared prior to analysis by solid phase extraction (SPE)*

The assays were carried out with 20 pmol of purified CYP21A1 in a 1:4 ratio with POR. The protein stocks were gently mixed together by pipetting and incubated on ice for 20 minutes. This reconstituted protein system was added to buffer (50 mM Tris, pH 7.4 and 5 mM MgCl<sub>2</sub>) containing analytes (0-2 μM) for a total volume indicated above. For the inhibition studies, 0.5 μM progesterone was used as the substrate concentration for inhibition studies. Control reactions were pre-quenched by the addition of 300 μL of 20% trichloroacetic acid [containing 34.64 μg/mL estriol internal standard] and placed on ice before the NADPH addition. Reactions were quenched 10 minutes after the addition of NADPH by the same (internal standard-containing) solution, and allowed to stand on ice for 10 minutes.

Solid phase extraction (SPE) cartridges (30 mg HLB resin, Sigma-Aldrich) were used on a parallel draining rack. SPEs were pre-equilibrated with 2 × 1 mL hexanes, 2 × 1 mL acetone, and 3 × 1 mL deionized water. Reaction samples (750 μL) were loaded onto individual SPE cartridges, allowed to drain, and then washed with 1 mL water. Glass vials (4 mL capacity) were placed under each tube, and samples were eluted with 4 × 1 mL acetone. The vials were concentrated for at least 12 hours by parallel evaporation to remove solvent and residual water. MSTFA derivatizing agent (120 μL) was added to

each sample vial, which was capped and heated to 60 °C for 60 minutes, stirring by hand intermittently.

The amount of 21-hydroxyprogesterone present was determined by GC-MS analysis using single ion monitoring (M/Z 546.35, ca. 26 min retention time), and analyzed against the estriol internal standard peak (M/Z 504.30, ca. 15 min retention time). Progesterone (M/Z 458.30, ca. 16 min retention time) was detected for quality control among reactions and standards. For instance, if a sample registered no product or standard peak as well as no progesterone peak, it was discarded from analysis due to experimental error.

### **1.2.3 CYP17A1 purification and crystallography**

The CYP17A1 construct used for assays and crystallography was identical to that described in the original CYP17A1 structural work carried out in our lab by Devore.<sup>23</sup> The original gene was synthesized by Blue Heron Biotechnology (Bothell, WA).

#### *Genetic engineering of a CYP17A1Δ19H construct*

A synthetic cDNA sequence was created that contained an N-terminal 19 amino acid truncation of the transmembrane helix, the substitution of the solubility tag Ala20-Lys21-Lys22-Thr23 for the hydrophobic sequence Arg20-Arg21-Cys22-Pro23, and a carboxy-terminal four-histidine tag to aid in purification. This cDNA, “CYP17A1Δ19H”, was cloned into the pCWori<sup>+</sup> vector for bacterial transformation, under control of an isopropyl β-D-1-thiogalactopyranoside (IPTG) inducible promoter. *Escherichia coli* JM109 cells (50 μL) were mixed with 1 μL of pCWori<sup>+</sup> CYP17A1Δ19H plasmid. The mixture was

incubated on ice for 40 min, followed by heating at 42 °C for 45 seconds. The mixture was cooled on ice for two minutes before inoculation of lysogeny broth (LB) plates containing 50 µg/mL ampicillin. Plates were incubated overnight at 37 °C. One colony was selected for growth and inoculated into 5 mL of LB with 50 µg/mL ampicillin for ca. 7 h at 37 °C, shaking at 250 rpm.

#### *Overexpression of CYP17A1*

From the culture described above, 50 µL were used to inoculate 200 mL LB, with 250 rpm shaking at 37 °C overnight. A portion of this culture (10 mL) was used to inoculate 1 liter of Terrific Broth (TB) in 2.8 L Fernbach flasks. Cultures were shaken at 250 rpm at 37 °C until the culture density reached  $OD_{600} = 0.6$ . Overexpression of CYP17A1 was induced with 0.5 mM IPTG, and the heme precursor  $\delta$ -aminolevulinic acid was added (0.61 mM) to aid heme biosynthesis. The temperature was reduced to 28 °C, and the cultures were grown with 140 rpm shaking for an additional 72 hours. The CYP17A1-containing cells were collected by centrifugation at  $6300 \times g$  for 10 min, and the thick, brown-red paste was resuspended in a 20% glycerol-containing 50 mM Tris HCl, 300 mM NaCl, pH 7.4 buffer for storage at -80 °C until purification.

#### *Purification of CYP17A1*

This cell suspension was thawed and sonicated on ice six times for 30 sec, with a 1 min recovery between each round. The lysed cells were centrifuged at  $3000 \times g$  for 15 min at 4 °C to pellet out cell debris. The supernatant was isolated and mixed with detergent (0.2% Emulgen 913, Desert Biologicals) for 2 h at 4 °C to extract CYP17A1

protein from cell membranes. The solution was centrifuged at  $100,000 \times g$  to remove cell membrane fragments. The supernatant containing the solubilized CYP17A1 was retained.

CYP17A1 was purified on an ÄKTA Fast Protein Liquid Chromatography (FPLC) system (GE Healthcare Life Sciences) using the columns and buffers listed. All purification was performed at 4 °C.

The supernatant from the cell preparation was loaded onto a nickel affinity column (NiNTA Agarose resin, Qiagen), pre-equilibrated with Ni buffer (50 mM Tris-HCl, pH 7.4, 20% glycerol, 300 mM NaCl, and 0.2% Emulgen 913). The resin was subsequently washed with 2 column volumes (CV) of Ni buffer, 6 CV of Ni buffer supplemented with 100 mM glycine to remove weakly bound contaminants, and eluted using 4 CV of Ni buffer supplemented with 100 mM glycine and 80 mM histidine. Elution fractions were collected based on absorbance of the heme Soret peak, diluted to 150 mL (~5-fold) in carboxymethyl (CM) buffer (50 mM Tris-HCl, pH 7.4, 20% glycerol, and 100 mM glycine), supplemented with 0.2% Emulgen-913, and loaded onto a 5 mL CM sepharose fast-flow column (GE Healthcare) previously equilibrated with CM buffer. The column was washed with 10 CV of CM buffer and eluted with CM buffer supplemented with 500 mM NaCl. Fractions were pooled based on the heme Soret absorbance and concentrated to ~1 mL. The concentrated protein was injected onto a Superdex 200 gel filtration column (GE Healthcare) pre-equilibrated with buffer containing 50 mM Tris-HCl, pH 7.4, 20% glycerol, 100 mM glycine, and 500 mM NaCl. Fractions with a heme absorbance peak were collected and concentrated.

For crystallization with azasteroid **19**, 10  $\mu$ M of this inhibitor was present in all buffers starting at cell resuspension. Ligand-free CYP17A1 was isolated for assays by the

above protocol with ligand-free buffers. For co-crystallization studies with compounds **23**, **32**, **37**, and **38**, ligand-free CYP17A1 was exchanged into CM buffer containing 10  $\mu\text{M}$  of the respective ligand and brought to the desired concentration for crystallization.

#### *Protein purity evaluation*

At each stage of purification, protein integrity/stability, concentration, and purity were evaluated using absolute and reduced CO difference spectra. Purity was monitored with absolute absorbance at  $A_{417}$  vs.  $A_{280}$ , to compare the heme Soret absorption band with general protein absorption. Active P450 concentrations were determined using a reduced carbon monoxide (CO) difference spectrum measurement, described below. Ultraviolet/visible (UV-vis) measurements were conducted on a UV-2101 UV-vis scanning spectrophotometer (Shimadzu Scientific Instruments, Inc., Columbia, MD).

Absolute spectra for rough concentration and purity estimation were recorded from 700-250 nm, taken in 800  $\mu\text{L}$  of the relevant buffer, to which was added 100  $\mu\text{L}$  protein sample. The absolute concentration of total P450 protein present (both active and inactive) was determined using Beer's law, by measuring the 417 nm Soret peak of the heme group ( $\epsilon = 0.100 \mu\text{M}^{-1} \text{cm}^{-1}$ ). Sample data is shown in Figure 1-8 A.

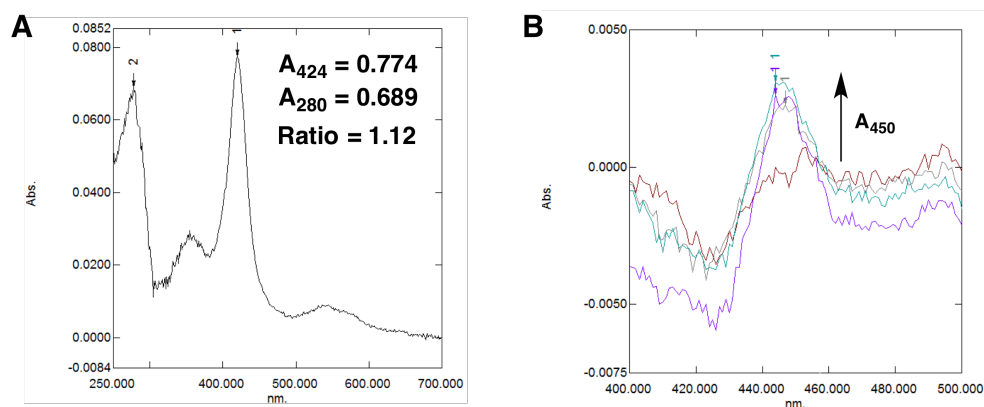


**Figure 1-8:** Protein purity and stability determination using UV-Vis. A: Absolute absorbance spectrum of P450 absorbance and protein absorbance. B: Reduced CO-difference spectrum displays concentration of active P450 species. These proteins were used for co-crystallography, in complex with compound **23** (see below).

Reduced CO difference spectra were taken to determine the concentration of active P450 enzyme. These were carried out as for the absolute spectra, but a few grains of sodium dithionite was added to fully reduce the protein. This sample was recorded as the baseline, and the sample was purged with CO for about 10 sec. The sample was mixed and spectra were recorded every three minutes until the increase in 450 nm absorbance reached its maximum. The concentration was determined using Beer's law, with the 450 nm Soret peak Soret of the heme group ( $\epsilon = 0.091 \mu\text{M}^{-1} \text{cm}^{-1}$ ). Sample data is shown in Figure 1-8 B. Here, an  $A_{450}$  peak indicated active P450 enzyme, while  $A_{420}$  indicated inactive protein.

*Protein crystallization, data collection, and structure determination:*

CYP17A1 was crystallized by hanging drop vapor diffusion. The purified protein was concentrated to  $\sim 30 \text{ mg/mL}$  (ca.  $0.54 \mu\text{M}$ ) as measured by absolute spectra in the presence of  $10 \mu\text{M}$  of one of the inhibitors, and 0.5% Emulgen-913 was added. The

precipitant solution used to crystallize CYP17A1 with these inhibitors fell into the range of 175 mM Tris-HCl, pH 8.5, 30-35% PEG 3350 (Hampton Research), 225-350 mM LiSO<sub>4</sub>, and 3-12% glycerol. Most crystals formed in 175 mM Tris-HCl, pH 8.5, 250 mM LiSO<sub>4</sub>, 3% glycerol, and 30% PEG-3350. The protein solution (1 μL) was mixed with the precipitant solution (1 μL) to form 2 μl drops. These were equilibrated against 750 μL of this precipitant solution at 20 °C (or 4 °C if crystals grew too quickly). Crystals were cryoprotected in a 7:3 mixture of mother liquor and 80% glycerol, mounted on loops, and flash cooled in liquid nitrogen.

Diffraction data were collected on beamlines 9-2 and 12-2 of the Stanford Synchrotron Radiation Lightsource and processed using XDS.<sup>92</sup> The structures were solved by molecular replacement using Phaser<sup>93</sup> in the PHENIX software suite,<sup>94</sup> using the structure of CYP17A1 with abiraterone or galaterone as the search model (PDB: 3RUK or 3SWZ, respectively). A Matthews coefficient of 2.61 suggested an asymmetric unit containing 4 molecules, with 52.8% solvent. Molecular replacement readily identified 4 molecules. Model-building and refinement were performed iteratively using Coot<sup>95</sup> and PHENIX Refine. Data collection and refinement statistics are given in Table 1-1. Four molecules of CYP17A1-ligand complex composed the asymmetric unit of each structure, as observed in the abiraterone structure (PDB 3RUK).<sup>23</sup> Figures were prepared using PyMOL (Schrodinger, LLC).

**Table 1-1.** X-ray statistics for new CYP17A1 co-crystal structures

Parameter	Ligand: 19 – azasteroid	23 – sulfonamide	33 – steroid oxime
<b>PDB Entry</b>	4RFG	4RFH	4RFI
<b>Data Collection</b>			
Beamline	SSRL BL9-2	SSRL BL12-2	SSRL BL12-2
Space group	P2 <sub>1</sub> 2 <sub>1</sub> 2 <sub>1</sub>	P2 <sub>1</sub> 2 <sub>1</sub> 2 <sub>1</sub>	P2 <sub>1</sub> 2 <sub>1</sub> 2 <sub>1</sub>
Unit cell dimensions			
a, b, c (Å)	90.1, 155.0, 169.3	92.1, 151.9, 169.0	91.9, 151.9, 168.2
$\alpha$ , $\beta$ , $\gamma$ (°)	90.0, 90.0, 90.0	90.0, 90.0, 90.0	90.0, 90.0, 90.0
Resolution (Å) <sup>a</sup>	48.82 (2.25)	39.39 (2.60)	39.31 (2.65)
Total observations <sup>a</sup>	831,922 (56,516)	483,003 (65,348)	459,623 (64,040)
Unique observations <sup>a</sup>	111,468 (8,092)	72,962 (10,195)	68,391 (9,510)
Redundancy <sup>a</sup>	7.5 (7.0)	6.6 (6.4)	6.7 (6.1)
Completeness <sup>a</sup>	99.9 (99.4)	99.3 (96.2)	99.0 (95.4)
R <sub>pim</sub> <sup>a</sup>	0.040 (0.425)	0.058 (0.580)	0.061 (0.552)
I/ $\sigma$ I <sup>a</sup>	13.4 (1.9)	13.6 (1.7)	13.1 (1.6)
<b>Refinement</b>			
Resolution (Å) <sup>a</sup>	48.82-(2.25)	39.39-(2.60)	39.31-(2.65)
No. reflections	105,768	69,084	68,391
R <sub>work</sub> / R <sub>free</sub> (%) <sup>b</sup>	19.8 / 24.6	17.9 / 24.8	17.9 / 23.8
Number of atoms /			
Average B-factor			
Protein	15,050 / 52.0	15,092 / 56.4	15,435 / 56.7
Ligand and heme	279 / 37.5	295 / 44.8	284 / 51.8
Water	281 / 43.3	85 / 44.5	144 / 50.8
R.m.s deviations			
Bond lengths (Å)	0.004	0.003	0.016
Bond angles (°)	0.881	0.821	0.817
Ramachandran angles			
Favored	96.0	96.1	96.0
Allowed	3.59	3.75	3.86
Disallowed <sup>c</sup>	0.43	0.16	0.16

<sup>a</sup>Data for highest the resolution shell are in parentheses.

<sup>b</sup>R<sub>free</sub> compared against 5% of the original data, set aside through refinement.

<sup>c</sup>Residues in disallowed Ramachandran areas were well supported by the density.

**Table 1-1 (continued)**

Parameter	Ligand: 38 – vinyl nitrile	42 – vinyl amide
<b>PDB Entry</b>	4RFJ	4RFK
<b>Data Collection</b>		
Beamline	SSRL BL12-2	SSRL BL12-2
Space group	P2 <sub>1</sub> 2 <sub>1</sub> 2 <sub>1</sub>	P2 <sub>1</sub> 2 <sub>1</sub> 2 <sub>1</sub>
Unit cell dimensions		
a, b, c (Å)	89.6, 153.4, 169.0	89.4, 154.1, 167.9
$\alpha$ , $\beta$ , $\gamma$ (°)	90.0, 90.0, 90.0	90.0, 90.0, 90.0
Resolution (Å) <sup>a</sup>	38.34 (2.60)	38.67 (2.70)
Total observations <sup>a</sup>	470,772 (59,609)	426,840 (59,546)
Unique observations <sup>a</sup>	71,754 (10,016)	64,275 (9,066)
Redundancy <sup>a</sup>	6.6 (6.0)	6.6 (6.6)
Completeness <sup>a</sup>	99.3 (96.2)	99.5 (97.6)
R <sub>pim</sub> <sup>a</sup>	0.062 (0.530)	0.054 (0.536)
I/ $\sigma$ I <sup>a</sup>	10.8 (1.7)	14.6 (1.6)
<b>Refinement</b>		
Resolution (Å) <sup>a</sup>	38.34-(2.60)	38.67-(2.70)
No. reflections	71,651	64,153
R <sub>work</sub> / R <sub>free</sub> (%) <sup>b</sup>	17.7 / 23.8	18.1 / 24.1
Number of atoms/ Average B-factor		
Protein	15,029 / 57.2	14,988 / 59.6
Ligand and heme	284 / 44.2	288 / 44.0
Water	139 / 50.8	129 / 45.7
R.m.s deviations		
Bond lengths (Å)	0.003	0.003
Bond angles (°)	0.812	0.796
Ramachandran angles		
Favored	95.4	95.9
Allowed	4.43	3.81
Disallowed <sup>c</sup>	0.16	0.32

<sup>a</sup>Data for highest the resolution shell are in parentheses.

<sup>b</sup>R<sub>free</sub> compared against 5% of the original data, set aside through refinement.

<sup>c</sup>Residues in disallowed Ramachandran areas were well supported by the density.

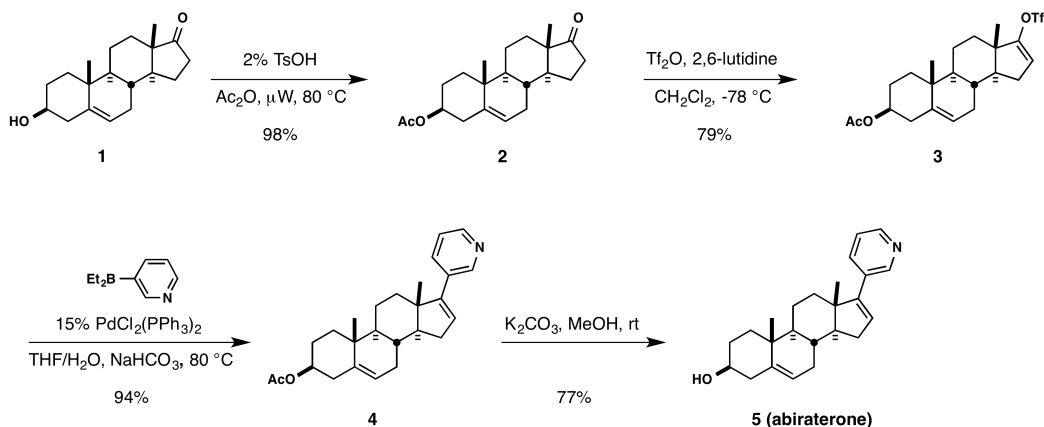
## 1.3 Results and Discussion

### 1.3.1 Inhibitor synthesis

The inhibitors prepared in this work incorporated changes to and substitution from the steroid B-ring. These changes were designed to create additional interactions with CYP17A1. As discussed in Section 1.1.5, some beneficial aspects of abiraterone, namely the C3-hydroxyl group and the 17-(3-pyridyl) group, were unchanged.<sup>86</sup> These moieties interact with Asn202 and the heme iron, respectively. Ideally, the introduction of polar groups from the steroid B-ring would also disfavor binding to CYP21A2 based on the structural elements discussed in Figure 1-6.

This work began with a resynthesis of abiraterone (Scheme 1-6). The reported synthesis<sup>70</sup> was modified to incorporate the triflate **3** as the partner for the Suzuki coupling reaction, which was found to be more synthetically accessible.

**Scheme 1-6**

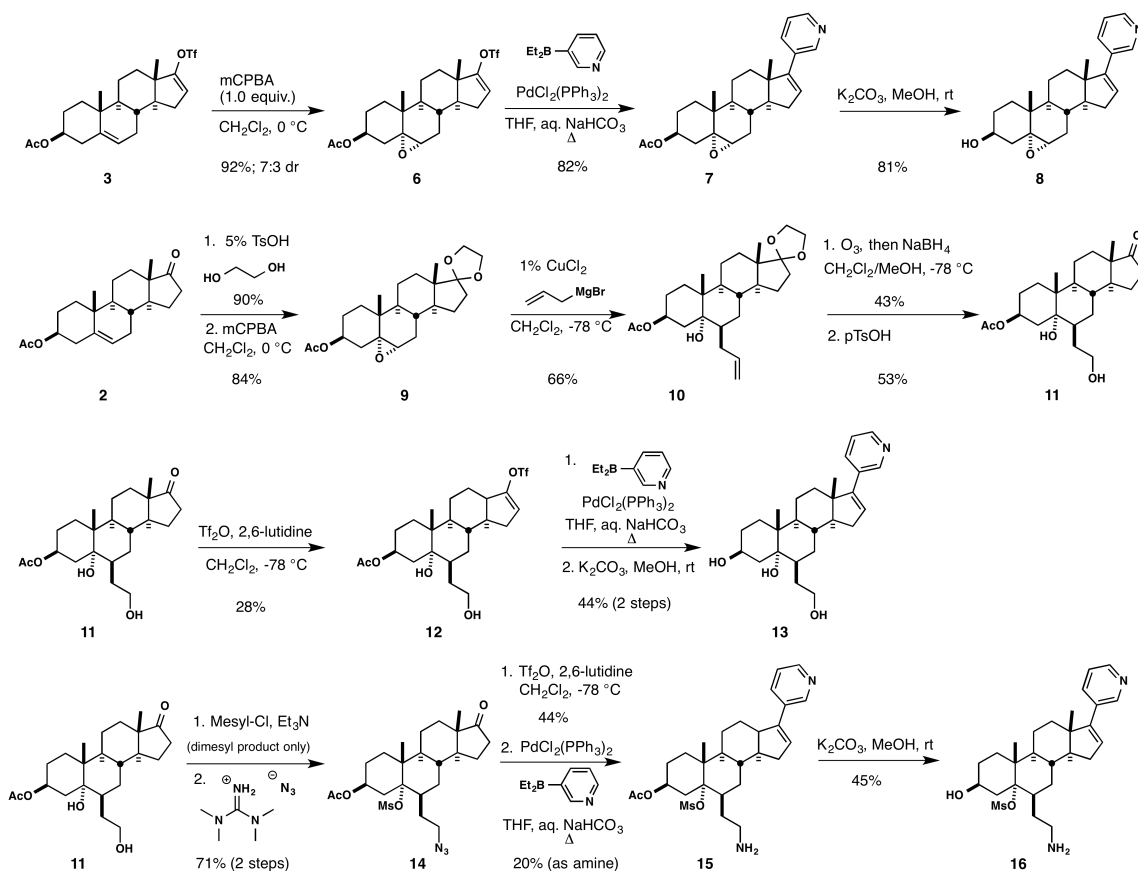


The first analog series prepared utilized the  $\Delta^5$  olefin to install an epoxide. The vinyl triflate on the  $\Delta^{16}$  olefin of **3** proved sufficiently electron-deficient to allow selective epoxidation of the  $\Delta^5$  olefin. The reaction afforded a mixture of diastereomers that was separable by preparative HPLC. In practice, the mixture was carried forward to incorporate an allyl group to provide the intermediate **10** (Scheme 1-7). The allyl group was oxidized to the corresponding aldehyde by ozonolysis. A reductive workup afforded the alcohol **11**, which was converted into trihydroxy abiraterone analog **13**.

Access to the amine-containing compound **16** proved to be more difficult. A variety of methods were attempted, including reductive amination of the aldehyde generated from allyl ozonolysis. A successful strategy proceeded through the mesylation and subsequent displacement, using sodium azide, of the allyl-derived alcohol. We were concerned the mesyl group in **14** might eliminate to provide the  $\Delta^5$  steroid, but this was not observed. Subsequently, transformation into the C5-mesyl, C6-ethylamine substituted abiraterone analog **16** was carried out.

We observed azide reduction during the Suzuki coupling of **14** to **15**, which afforded the amine product **15** only. Previous workers have also noted that simultaneous reductive chemistry can occur alongside palladium-mediated cross coupling reactions in the presence of excess base.<sup>96</sup>

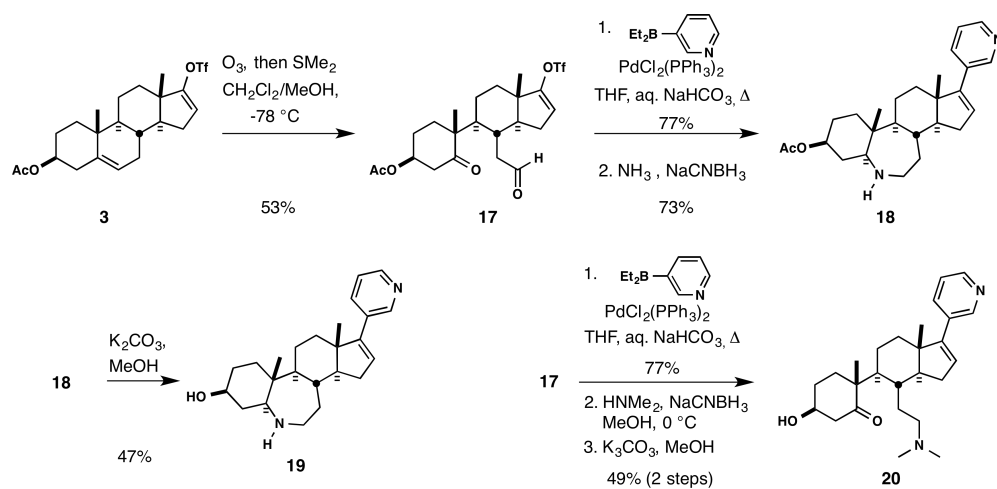
## Scheme 1-7



For additional analogs, ozonolysis was utilized to cleave the  $\Delta 5$  olefin (Scheme 1-8). The electronic difference between the triflate-substituted  $\Delta 16$  olefin and relatively electron-rich  $\Delta 5$  olefin again provided some selectivity for the oxidation. By carefully controlling the exposure to ozone through flow rate and reaction time, 1-2 gram quantities of the ring-opened steroid **17** were accessible. The resulting aldehyde was substituted via reductive amination with ammonia, which provided a primary amine that spontaneously closed onto the C5 ketone to afford the 7-membered ring **18**. Removal of the C-3 acetate provided the abiraterone analog **19**. Alternatively, the stable ring-opened

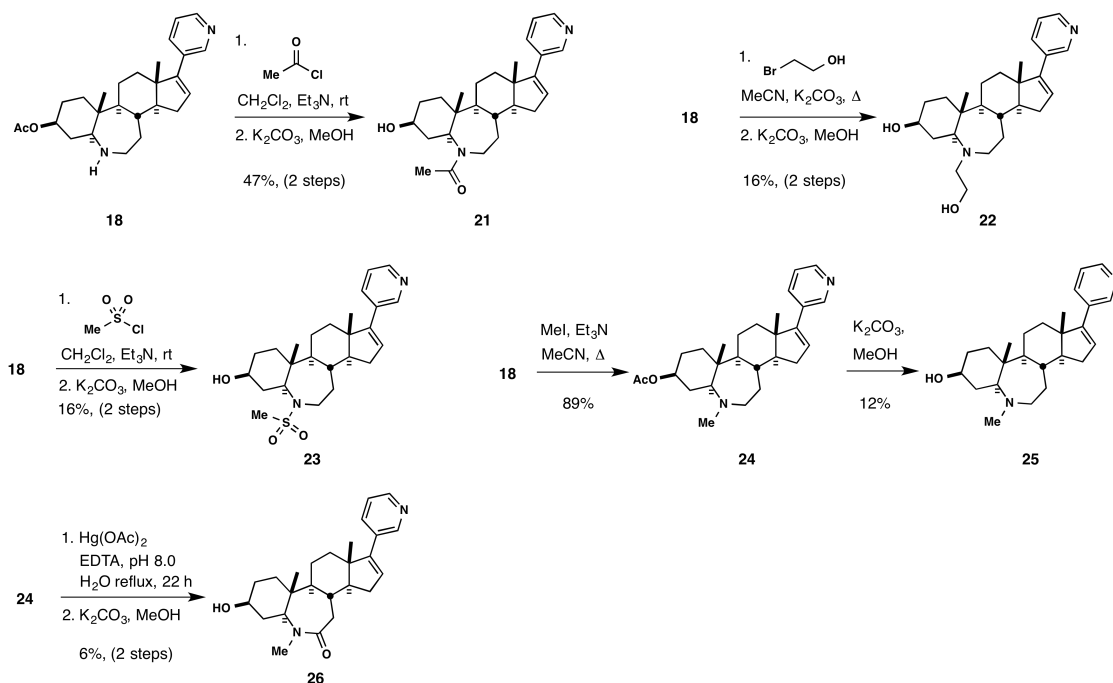
analog **20** was prepared by utilizing dimethylamine in the reductive amination step, which did not undergo subsequent reaction.

### Scheme 1-8



The amine platform of **18** served as a building block for further substitution (Scheme 1-9). A small range of electrophiles was utilized to install a variety of polar groups, including an acyl chloride, mesyl chloride, and alkyl halides (Compounds **21-24**). Oxidation of the tertiary amine of **24** with mercuric acetate<sup>97</sup> afforded the corresponding lactam **26**, albeit in low yield.

## Scheme 1-9



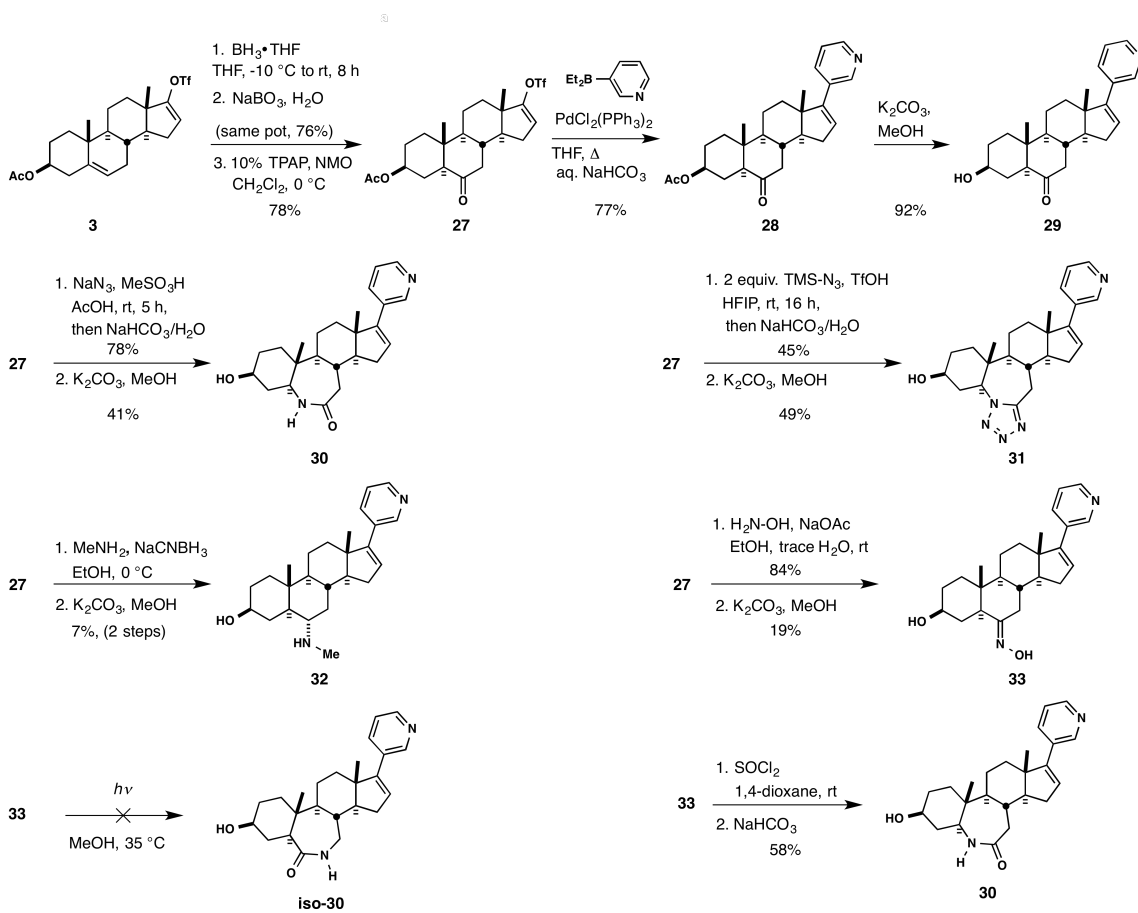
The electron-rich olefin of **3** was again subjected to a selective reaction, this time being a borane-mediated hydroboration/oxidation (Scheme 1-10). The resulting mixture of alcohols was oxidized to the ketone **27**, which could be isolated as the pure steroid isomer with a trans A/B ring junction. Presumably, the cis isomer formed during the hydroboration step, but was either not isolated alongside the major product or rapidly equilibrated under these conditions.

This C6 ketone was functionalized by a variety of means. Two variants of the Schmidt reaction afforded the secondary lactam **30** and the tetrazole **31**. In the latter case, two equivalents of azide were incorporated into the molecule. Reductive amination with methylamine afforded only the  $\alpha$ -substituted isomer **32**. This stereochemistry was assigned by comparing the H-NMR of this species to similar reported spectra, using both

the chemical shifts and coupling constants for assignment.<sup>98</sup> Attempts to achieve the other diastereomer were unsuccessful, but this was not extensively investigated.

The steroid oxime **33** was readily formed by treatment of **27** with hydroxylamine. Several attempts were made to carry out a ring expansion of this oxime to afford the isomeric lactam to **30**, **iso-30**. For example, a photo-Beckmann rearrangement was attempted on **33**, following a reported procedure for 6-keto steroids.<sup>99</sup> Unfortunately all attempts failed, affording only degradation products. To our chagrin, standard thionyl chloride-promoted Beckmann rearrangement of **33** afforded the identical product as the Schmidt reaction pathway, **30**. Thus, this route to the reversed amide was abandoned.

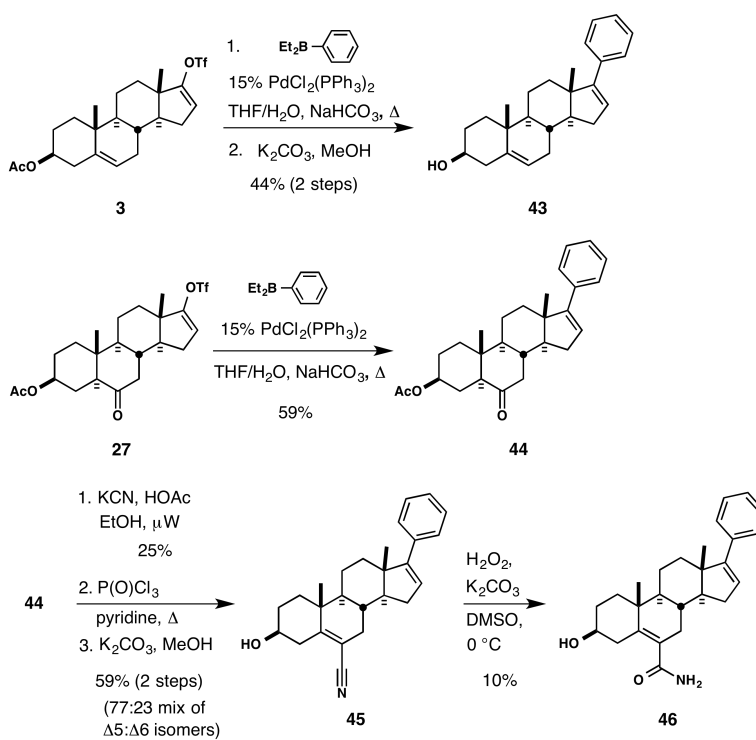
### Scheme 1-10





Two compounds were synthesized as their C17-phenyl substituted versions to study the relative effect of the pyridyl group on CYP17A1 binding (Scheme 1-12). The synthesis of **43** proceeded through **3** with the use of phenylboronic acid as the coupling agent. The vinyl amide **46** proceeded as above from **27**, again utilizing phenylboronic acid for the coupling reaction. The chemistry beyond the alternative Suzuki coupling reaction was similar in practice to that developed for the C17-pyridyl analogs.

### Scheme 1-12



### 1.3.2 CYP17A1 and CYP21A2 activity assays for inhibitor profiling

The assays performed in this work were developed for the *in vitro* characterization of CYP17A1 and CYP21A2 activity. Progesterone is a substrate for both CYP17A1-mediated  $17\alpha$ -hydroxylation and CYP21A2-mediated 21-hydroxylation. Therefore,

progesterone was utilized for all assays to simplify the comparison of selectivity values for the inhibitors tested in this work.

An additional benefit of using progesterone to study activity is its A-ring  $\alpha,\beta$ -unsaturated ketone system, which is UV-active at 248 nm. Thus, the HPLC-based detection of product formation was straightforward. DeVore had previously developed an HPLC-based activity assay which had been utilized to determine the enzyme kinetic parameters of the CYP17A1 construct.<sup>23</sup> CYP17A1 inhibitory data for the clinical inhibitors abiraterone and galaterone/TOK-001 had been also published using this procedure.<sup>67</sup>

However, steroids that lack chromophores are not detectable using this method. Notably, these include  $17\alpha$ -hydroxypregnenolone and dehydroepiandrosterone, products of the CYP17A1 hydroxylase and lyase reactions on pregnenolone, respectively. Alternative methods considered for detecting these steroids included substrate radiolabeling,<sup>90</sup> radioimmunoassay,<sup>88</sup> and mass spectrometry (MS).<sup>101</sup> Because MS-based techniques are able to accurately detect low levels of steroid metabolites,<sup>102</sup> we set out to develop a generalizable, MS-based steroid metabolism assay to extend the detection capabilities in this project.

As mentioned in section 1.2.2, the assays presented here use modified protein constructs of CYP17A1 and CYP21A2, as well as a modified form of the P450 oxidoreductase partner POR. The proteins were individually purified and the concentrations of active protein were measured. Hence, the concentration of each protein could be carefully controlled and assay components could be adjusted according to the knowledge of absolute protein concentrations.

A major practical difference between this work and the numerous reported microsomal assay preparations of full-length CYP17A1<sup>88,89</sup> and full-length CYP21A2<sup>90</sup> is that microsomal assays are measured in terms of relative activity to the “total microsomal protein content,” which includes the cytochrome P450 alongside other less-defined membrane proteins. Also, the ratio of P450:POR is unknown in microsomal assays, but was standardized herein. Thus, we chose not to compare our results quantitatively with reported literature values, which use microsomal assay data. The differences between these and our systems invalidate such comparisons. Conversely, because we know the concentrations of all assay components, the CYP17A1 and CYP21A2 assays described below can be quantitatively compared. Thus, we can describe CYP17A1/CYP21A2 selectivity factors for the compounds tested.

#### *Determination of CYP17A1 IC<sub>50</sub> values for new compounds by HPLC detection*

The previously developed HPLC-based progesterone 17 $\alpha$ -hydroxylation assay was used to characterize the inhibitors synthesized in this work for CYP17A1 inhibitory activity. The reaction and conditions utilized are shown in Figure 1-9. Using a reverse phase column, all inhibitors eluted before 4.3 minutes, allowing clean detection of the product peak at 5.5 minutes. Inhibitory activity was measured as a percentage of the maximal CYP17A1 activity. Maximal activity was determined with inhibitor-free conditions alongside each series of inhibitor concentrations. The data was processed and analyzed as described in Section 1.2.2.

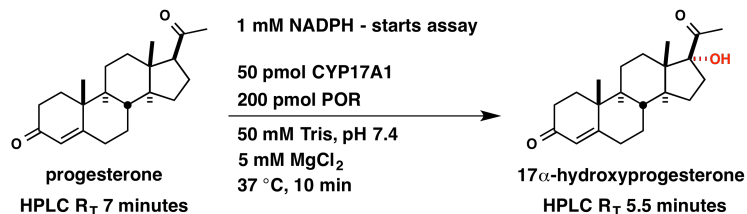


**Figure 1-9.** Conditions for the HPLC-based CYP17A1 progesterone 17 $\alpha$ -hydroxylation assay.

To establish comparative potency values for this study, the CYP17A1 progesterone hydroxylation inhibitory activities of the clinical compounds abiraterone (**5**), galaterone, and orteronel were measured. These data and fits are shown in Figure 1-10. Orteronel was significantly less potent than either **5** or galaterone, potentially due to its reported selectivity for CYP17A1 lyase over CYP17A1 hydroxylase activity.<sup>103</sup>

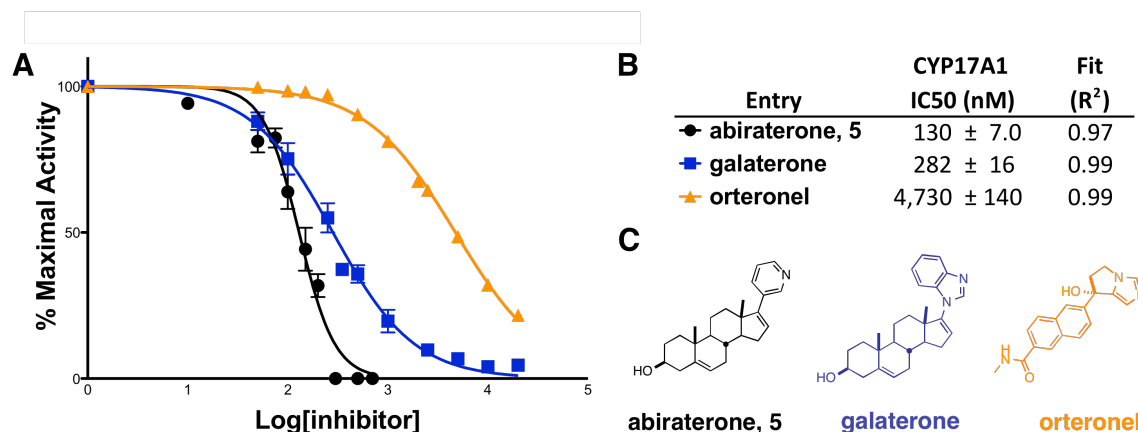


**Figure 1-10.** CYP17A1 17 $\alpha$ -hydroxylation assay against previously reported agents. A: IC<sub>50</sub> curves. The error bars for orteronel are too small to see as shown. B: Analyzed results with standard error. C: Inhibitor structures.

The CYP17A1 data for compounds **8–20** are shown in Figure 1-11. These analogs generally lost activity compared to abiraterone (**5**). Smaller structural modifications were

tolerated in the steroid B ring, such as epoxidation (**8**) as well as ring-expansion to the 7-membered azasteroid (**19**). UV-vis measurements confirmed that these act as Type II CYP17A1 inhibitors (data not shown).

Larger structural differences, such as adding multiple polar groups or opening the B-ring as in **13** and **20** significantly reduced inhibitory activity against CYP17A1. Considering the inconvenience of synthesizing **13** and **16**, these types of analogs were not pursued further. Instead, series based on more conservative changes to the steroid core, namely substituting the azasteroid **19**, became the next synthetic focus (Scheme 1-9).

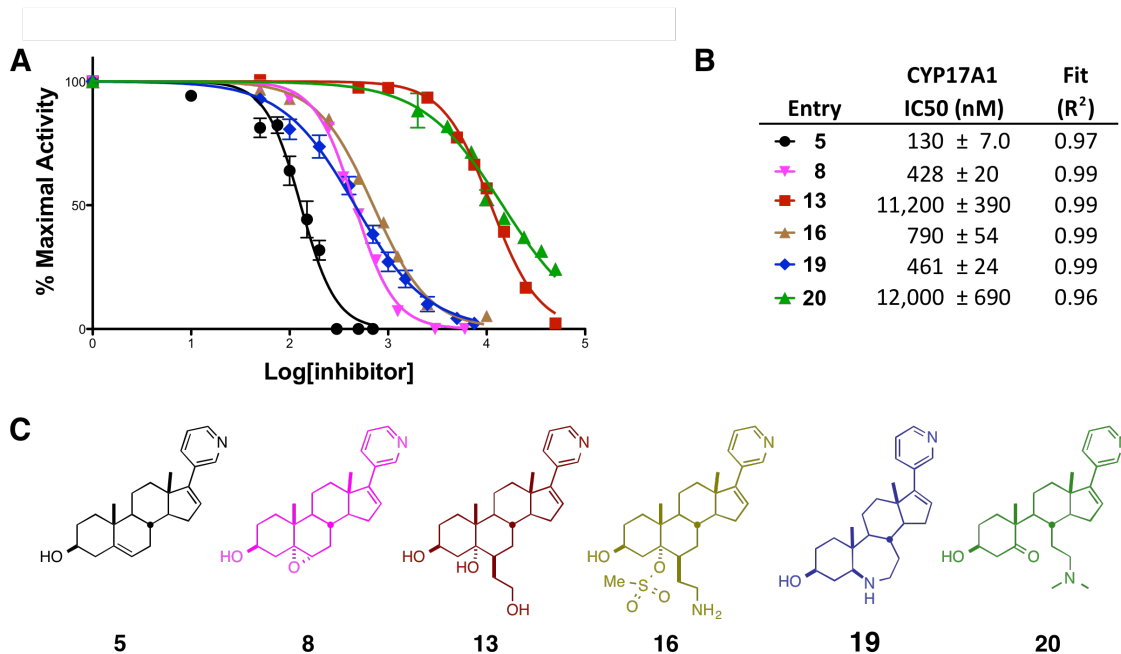


**Figure 1-11.** CYP17A1 17 $\alpha$ -hydroxylation assay against initial compounds. A: IC<sub>50</sub> curves. B: Analyzed results with standard error. C: Inhibitor structures.

The compounds derived from the substitution and functionalization of the **19** fell into a narrower activity range (Figure 1-12). As above, compounds **21-26** lost activity compared to abiraterone (**5**). The addition of an acyl group on the amine (**21**) caused the

largest drop in activity. Methylation of the amine (**25**) was unfavorable, but some activity was rescued in the tertiary lactam congener **26**, which suggested that an increase in polarity was beneficial. The hydroxyethyl-substituted amine **22** retained modest activity, but was still less potent than **19**. The only compound with increased CYP17A1 potency over the scaffold **19** in this series was the sulfonamide **23**. This moiety increases polarity, in addition to adding steric bulk. However, this volume is constrained closer to the steroid core, as opposed to than the long, flexible alkyl chains in **13**, **16**, and **22**, which displayed reduced activity.

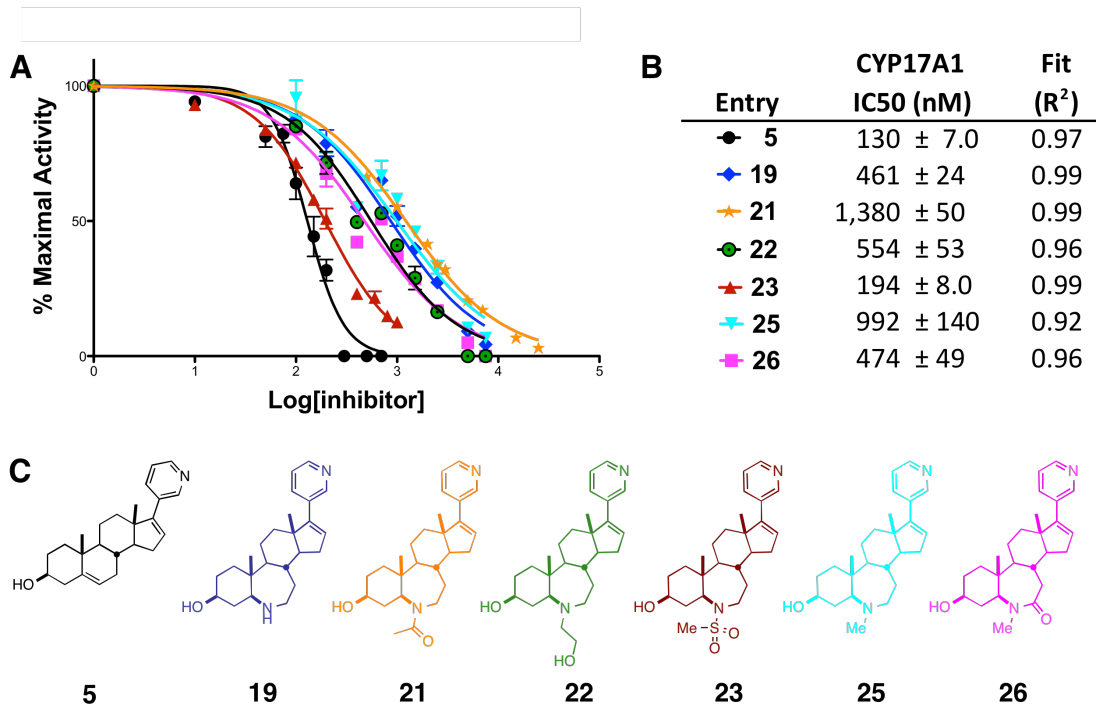


**Figure 1-12.** CYP17A1 17 $\alpha$ -hydroxylation assay against azasteroid analogs. A: IC<sub>50</sub> curves. B: Analyzed results with standard error. C: Inhibitor structures.

The information from above compounds suggested that (1) polar groups were tolerated around the steroid core and (2) too much steric bulk or conformational flexibility of substituents could be detrimental to inhibitory activity. Largely based on these initial

findings, compounds **29** to **33** were prepared as above and their CYP17A1 inhibitory activities investigated. This data is shown in Figure 1-13.

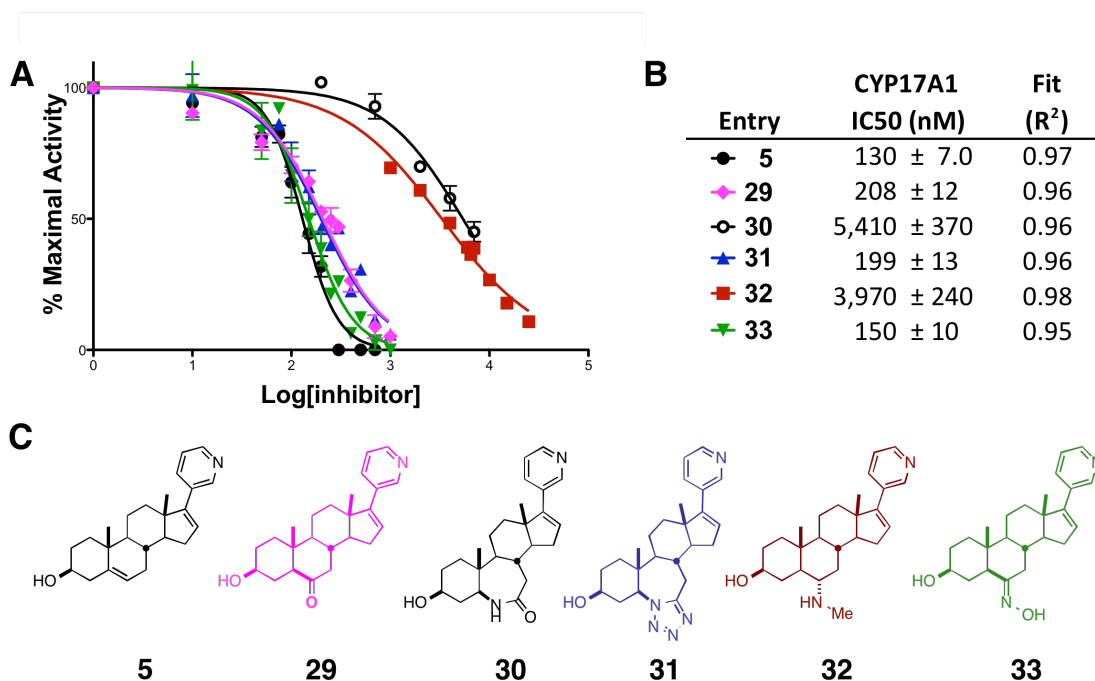


**Figure 1-13.** CYP17A1 17 $\alpha$ -hydroxylation assay against ketone-derived analogs. A: IC<sub>50</sub> curves. B: Analyzed results with standard error. C: Inhibitor structures.

The ketone **29** was nearly as potent as the sulfonamide **23**, but had a significantly smaller polar feature, suggesting that more subtle changes could also be beneficial. The SARs of the remaining derivatives were more complicated. The C6  $\alpha$ -methylamine **32** lost significant activity, despite being a relatively small structural change from the more active, especially **23**. This could be attributed to a positive charge at physiological pH, which may be incompatible with the nearby Arg239 guanidinium moiety. More surprisingly, however, was the loss of activity in the secondary lactam **30**. This was expected to be similarly potent to the tertiary lactam **26**, but was in fact an order of magnitude less active. The reasons for this difference are currently unclear.

Other analogs were more promising. The steroidal tetrazole **31**, which projects a flat polar group from the steroid B-ring, maintained relatively good potency. The activity of the C6 oxime, designed to be a synthetic precursor to the reversed lactam of **30**, was the most potent compound synthesized thus far, but still had a slightly higher IC<sub>50</sub> value than abiraterone against CYP17A1.

To help in interpreting the above data, we performed a crude structure-activity relationship analysis of various steroid substituents to help determine the next synthetic strategy. Though these compounds were not otherwise identical, there seemed to be a trend in electronic effects of B-ring substituents (Figure 1-14 A). The positively charged **32** had weak binding, which was compared with the partial negative charge of **23** and the polar H-bond-donating oxime of **33**. We reasoned that bifunctional polar groups, such as H-bond dual donor-acceptors, could improve potency by interacting with both Arg239 and Asp298.

Similarly, the geometric arrangement of the polar substituents seemed to correlate with a trend toward potency improvement through lowering the angle of substitution from the steroid core (Figure 1-14 B). For instance, the axial hydroxyethyl group of **13** should project directly over the steroid plane. From the crystal structure of CYP17A1, residues Ala105, Leu209, and Phe114 create a surface that tightly conforms to the steroid  $\beta$ -face (within 4 Å), making these residues potential candidates for a steric clash with this group.<sup>23</sup> Lowering this substituent angle with the amine-substituted hydroxyethyl group in **22**, we observed a sharp improvement in potency. Finally, the steroidal tetrazole **31**, which would project heteroatoms in a fashion roughly co-planar with the steroid core,

further improved activity. Thus, targeting substitution patterns co-planar to the steroid became another design goal.

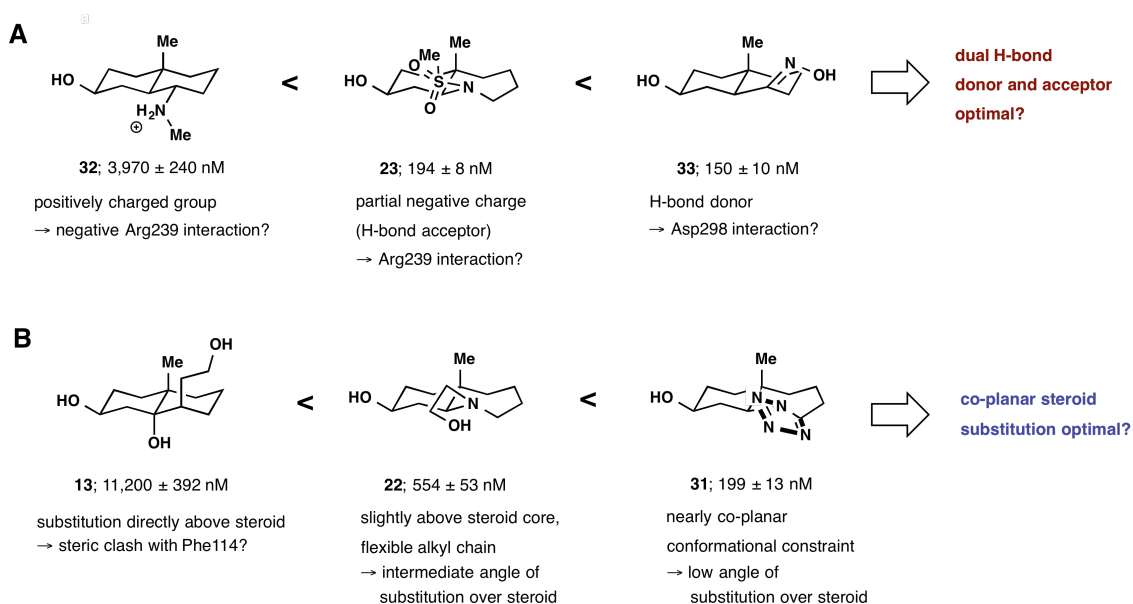


**Figure 1-14.** Two trends suggested from structure-activity data were used to design further analogs. A: Increase in activity from a positively-charged group to an H-bond donor suggested an electronic effect. B: Lowering the angle of substitution with respect to the steroid plane suggested a geometric effect on activity.

The above steric and electronic-driven rationale led to our identification of compounds **38**, **41**, and **42**, synthesized as described in Scheme 1-11. These compounds were co-planar with the steroid, and could also potentially enjoy an interaction of their polar groups with both CYP17A1 residues Arg239 and Asp298.

The inhibition data for this last set of compounds, **37-42**, is presented in Figure 1-15. These compounds were indeed improved in terms of potency over the preceding inhibitors, and all fell in a narrow activity range near the  $IC_{50}$  value of abiraterone. Though all of this series shared very similar inhibitory activities, the best compound was **42** ( $IC_{50}$  120 nM), which was approximately equipotent to abiraterone ( $IC_{50}$  130 nM).

The C6 nitro-substituted  $\Delta^5$  steroid analog **41** was only slightly less potent than abiraterone at 183 nM. Comparison between **41** and **42** suggested that the nature of the polar group affected the engagement CYP17A1 active site residues. Although both nitro and amide groups can adopt charge-separated resonance forms, the amide may be more efficient at simultaneously engaging the positive Arg239 guanidinium group and negative Asp298 acid through its partially-negative oxygen and partially-positive nitrogen, respectively. This will be discussed in the context of X-ray crystallography in the next section.

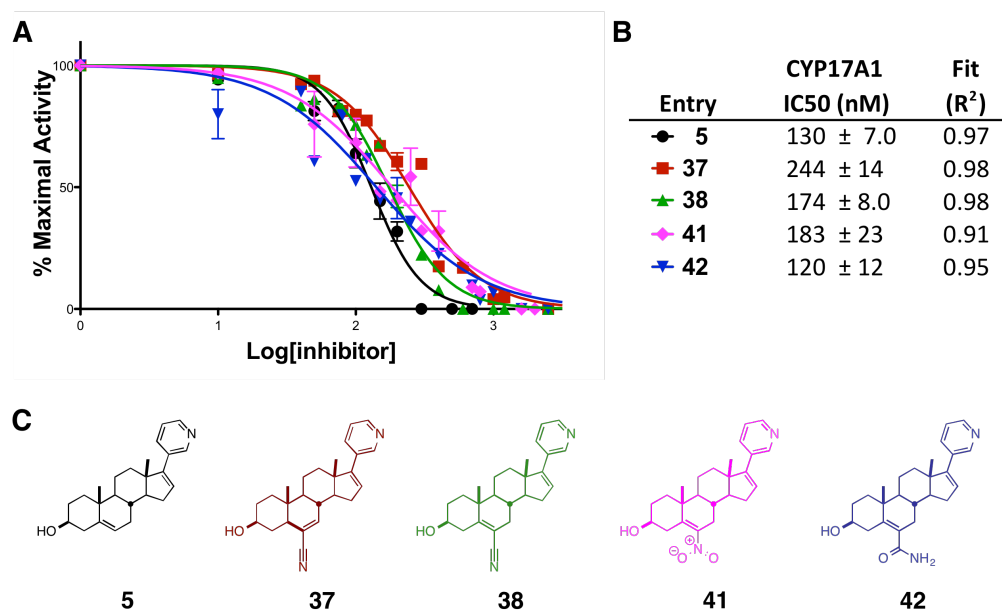


**Figure 1-15.** CYP17A1 17 $\alpha$ -hydroxylation assay against geometry-optimized series. A: IC<sub>50</sub> curves. B: Analyzed results with standard error. C: Inhibitor structures.

We were also interested in separating the effect of the heme coordination from the B-ring interactions. Thus, we might be able to design inhibitors that do not coordinate the iron, which could allow reversible binding. To do so, analogs of abiraterone and **42** in

which the C-17 3-pyridyl group was replaced with phenyl were synthesized. The activity data is shown in Figure 1-16. Though the C6 vinyl amide substitution imparted a 2-fold improvement in potency on the pregnenolone-based scaffold, these significantly weaker activities suggest that the heme-pyridyl interaction is essential for potent active site-targeted CYP17A1 inhibitors.

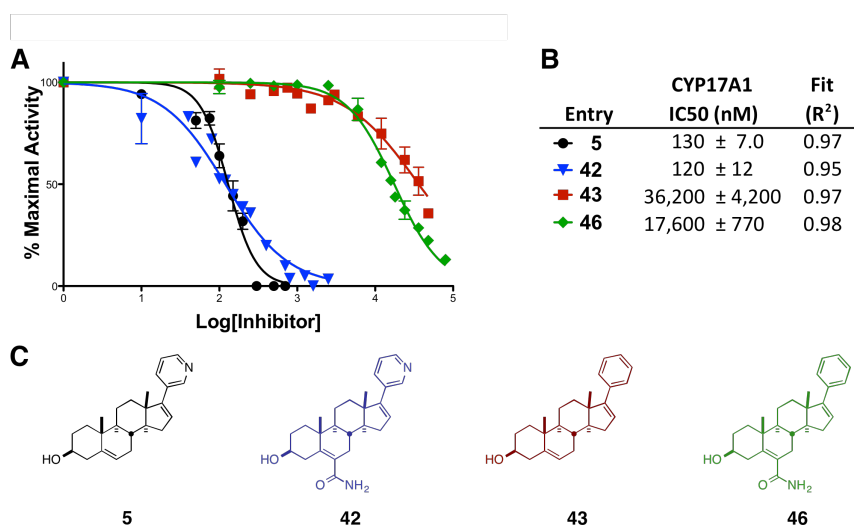


**Figure 1-16.** Removal of Fe-coordinating moiety drops potency significantly. Optimal B-ring substitution can rescue this ca. 2-fold. A: IC<sub>50</sub> curves. B: Analyzed results with standard error. C: Inhibitor structures.

#### *Determination of CYP21A2 activity by HPLC detection*

Initially, similar conditions and HPLC-detection methods as above were used to study CYP21A2 activity. Blake, who first expressed the human CYP21A2 construct described in Section 1.2.2, began the preliminary enzymology experiments with CYP21A2.<sup>87</sup> For our purposes, full kinetic characterization was necessary for the development of a comparative counter-screen of inhibitory activity. Thus, we set out to profile the

enzymology of CYP21A2 to validate this approach before moving toward screening inhibitors.

The determination of steady state kinetic parameters by the the Michaelis-Menton approach typically utilizes data from the initial phase of an enzymatic reaction.<sup>104</sup> When the substrate depletion is restricted to below ca. 10%, this initial reaction rate data is generally linear. This simplifies the analysis of  $K_m$  and  $k_{cat}$ , which are associated with the affinity for an enzyme for its substrate and the rate at which it turns over product, respectively.<sup>104</sup> Thus, it is essential to ensure that a detection method is used that is able to accurately detect the small amounts of product created during the initial activity period of the enzymatic reaction under study.

The preliminary enzymology work on CYP21A2 performed by Blake suggested that a four-fold excess of POR to CYP21A2 was the optimal system for product formation, similar to CYP17A1. Beyond this, detection issues arose when characterizing the initial activity kinetics of progesterone 21-hydroxylation. The high activity of CYP21A2 posed a challenge for finding conditions to limit substrate depletion below 10% over a 10 minute timeframe, a practical duration for an activity assay. To circumvent this, the concentrations of both CYP21A2 and substrate were reduced, but the results from HPLC-based steroid detection proved too inaccurate for this purpose.<sup>87</sup>

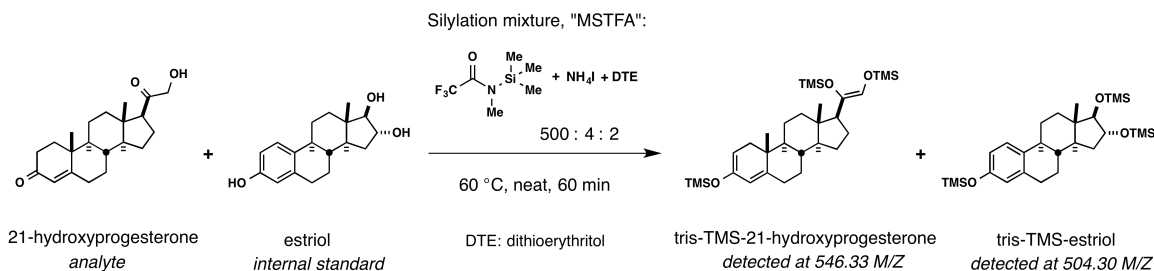
#### *Development of a mass spectrometry-based CYP21A2 activity assay*

Numerous forms of mass spectrometry-based quantitation techniques have been applied to steroid metabolites.<sup>102</sup> A previously reported gas chromatography-based separation/mass spectrometry-based detection (GC/MS) protocol served as a starting

point for our assay development and validation for CYP21A2 progesterone 21-hydroxylation.<sup>105</sup> Briefly, this protocol had been developed to analyze steroid analytes from urine samples. It used solid-phase extraction (SPE) to remove the nonpolar steroids from the aqueous matrix. The steroid analyte mixture was next subjected to silyl derivatization. These mixtures were then detected using GC/MS against internal standards for quantification.

Silylation of steroid alcohols greatly enhances the volatility of steroid samples for GC/MS detection.<sup>106</sup> In our work, we utilized a common silyl derivatization mixture, in which trimethylsilyl silane is generated from ammonium iodide and *N*-methyl-*N*-(trimethylsilyl)trifluoroacetamide (MSTFA) as outlined in Scheme 1-13. Dithioerythritol was included to increase the stability of the mixture, to prevent iodine formation and degradation of the silyl products.<sup>107</sup> An internal standard was incorporated to ensure accuracy. Estriol was eventually selected, being a steroid with M/Z orthogonal to all other components of the assay matrix. This standard was added at the reaction quench stage.

### Scheme 1-13



The first step toward assay development was to generate standard curves for 21-hydroxyprogesterone. First, 21-hydroxyprogesterone was detected for a simple standard

curve (Figure 1-17 A). Next, a full mock assay matrix was created and prepared by the SPE protocol described in Section 1.2.2 (Figure 1-17 B). Reproducible results were obtained, suggesting that this protocol was suitable for CYP21A2 activity measurements.

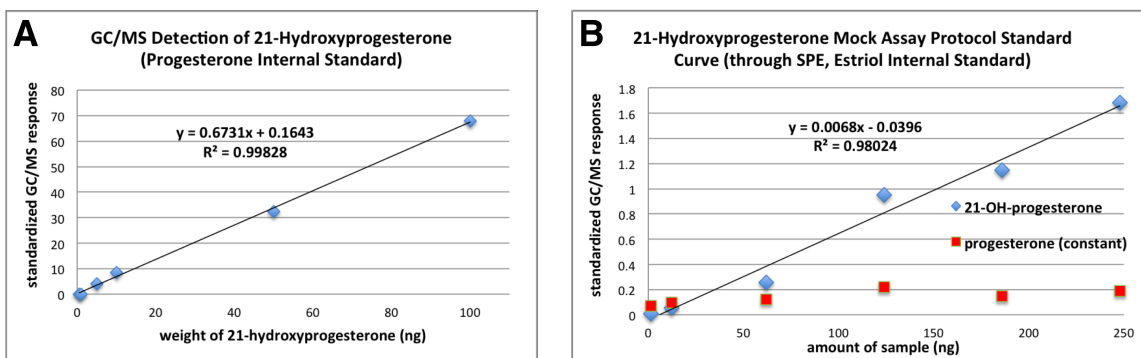


**Figure 1-17.** Standard curves of CYP21A2 product detected by GC/MS. A: 21-Hydroxyprogesterone alone. B: 21-Hydroxyprogesterone in a full assay matrix (buffer, progesterone substrate, NADPH, acid quench).

From the preliminary results from HPLC-based CYP21A2 methodology, a potential reaction sample matrix was created (Figure 1-18). The first experiment with CYP21A2 was to ensure linearity over the initial reaction time course. The batch of CYP21A2 used in this study was purified by Petrunak, who also performed the initial activity experiments to screen for a linear product formation response (Figure 1-17). She found that dropping the concentration from 50 pmol of P450, used in the CYP17A1 study, to 20 pmol provided a linear response out to 15 minutes. Less than 10% substrate depletion occurred at the 10-minute time point, which became the reaction time utilized in further activity assays.

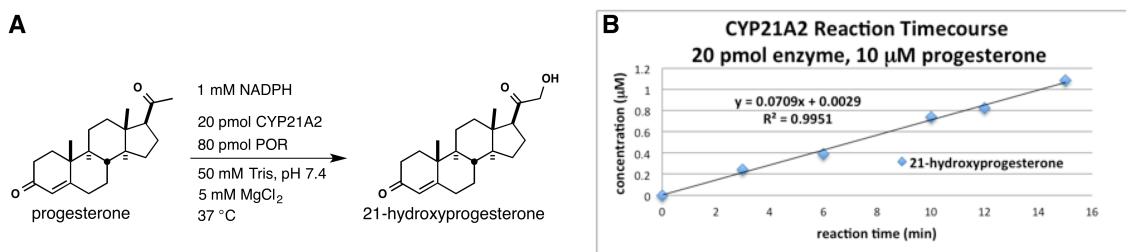


**Figure 1-18.** CYP21A2 enzymatic reaction. A: Reaction matrix. B: Timecourse. This reaction consumed less than 10% of the substrate and displayed linear conversion kinetics beyond 10 min, the time used in further assays. Data courtesy of Elyse Petrunak.

With suitable enzymatic reaction conditions in hand, I set out to characterize the kinetic parameters of CYP21A1 (Figure 1-19 A). The truncated form of the enzyme had a Michaelis constant ( $K_m$ ) of 0.527 µM and a  $k_{cat}$  of 1.26 min<sup>-1</sup> (Figure 19 B). For a rough comparison, these values were similar to the reported parameters for the full-length protein<sup>90</sup> ( $K_m$  2.21 µM and  $k_{cat}$  0.65 min<sup>-1</sup>), but as the latter results were measured in an *E. coli* microsomal assays this comparison is not precise.

To reconfirm this data, similar assays were performed using HPLC as the detection method. Since we had narrowed down the range of these enzymology parameters, we could be more confident in this form of detection. Similar data was obtained by HPLC as for GC/MS (Figure 1-19 C). Thus, HPLC was also briefly investigated as a faster assay protocol for inhibitory assays, with less sample handling to minimize error. However, several inhibitors co-eluted with 21-hydroxyprogesterone under a variety of solvent and separation conditions. This complicated inhibition assays by HPLC, and we thus returned to the GC/MS protocol for IC<sub>50</sub> determinations for CYP21A2.

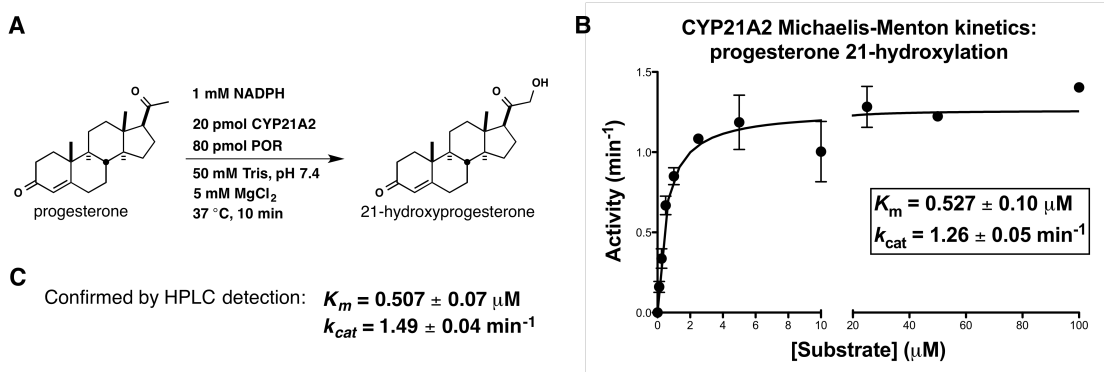


**Figure 1-19.** Kinetic parameters of CYP21A2 progesterone 21-hydroxylation. A: Assay conditions. B: GC/MS data for the enzyme activity, Michaelis-Menton parameters. C: Confirmation of activity using HPLC detection (less sample handling).

These results demonstrated that this truncated construct of human CYP21A2 was functional for progesterone 21-hydroxylation activity. Moreover, the GC/MS detection utilized was accurate in quantitating low levels of steroid analyte and suitable for inhibitory assays.

#### *Determination of CYP21A2 IC<sub>50</sub> values for new compounds by GC/MS detection*

The CYP21A2 inhibitory activity profiles of selected new compounds were determined using the conditions developed in the previous section. The substrate concentration used, 0.5 μM, was near the Michaelis constant of CYP21A2. Inhibitory activity was measured as a percentage of the maximal CYP21A2 activity, which was determined with inhibitor-free reactions run alongside each series of inhibitor concentrations. The data was processed and analyzed as described in Section 1.2.2.

The clinical compounds abiraterone (**5**), galaterone, and orteronel were profiled as shown in Figure 1-20. The selectivity factor (17A1/21A2 Sel. Factor) was calculated by dividing each compound's CYP21A2 IC<sub>50</sub> by its CYP17A1 IC<sub>50</sub>. These clinical agents

demonstrated IC<sub>50</sub> values for CYP21A2 similar to their CYP17A1 IC<sub>50</sub>. Abiraterone, which was 2.3-fold more effective in inhibiting CYP17A1 progesterone 17 $\alpha$ -hydroxylation activity than CYP21A2 progesterone 21-hydroxylation, was the most selective of these agents. Interestingly, galaterone was even less selective for CYP17A1/CYP21A2 inhibition than abiraterone. The extra nonpolar bulk of its benzimidazole C17 substituent may bind in the space near the steroid 21-position observed in the crystal structure of bovine CYP21A2, as described in Section 1.1.4.

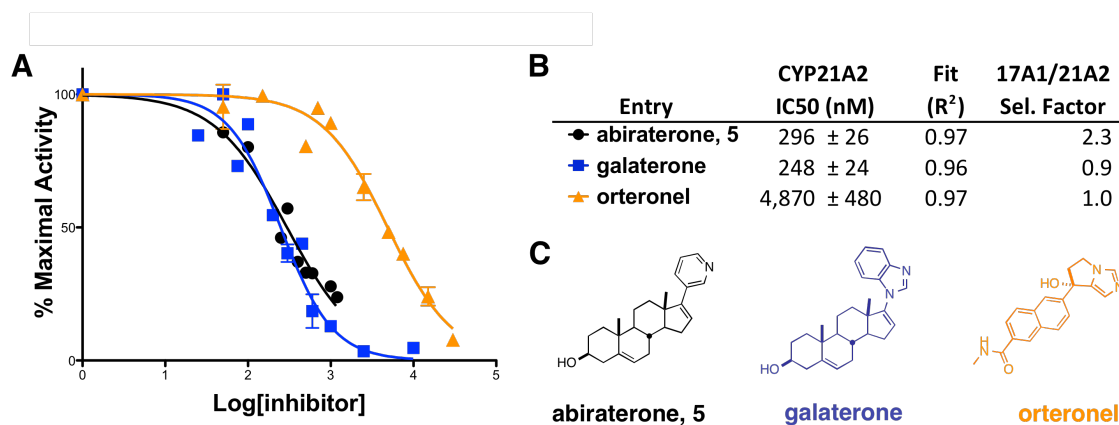


**Figure 1-20.** Clinical CYP17A1 agents' effect on CYP21A2 progesterone 21-hydroxylation. A: IC<sub>50</sub> curves. B: Analyzed results with standard error. C: Inhibitor structures.

Selected potent CYP17A1 inhibitors with suitable polar groups were selected for counter-screening against CYP21A2, to test the effect of these polar groups on CYP17A1/CYP21A2 selectivity. These data are shown in Figure 1-21. The CYP17A1 potencies of these new compounds were roughly comparable to abiraterone (IC<sub>50</sub> 120–183 nM vs. 130 nM, respectively), but a definite shift to decreasing CYP21A2 inhibition was apparent in the case of each new compound. The compounds **33** and **42** displayed a large IC<sub>50</sub> shift from CYP17A1 to CYP21A2 activity, and showed selectivity factors of

68.9 and 72.2, respectively. Notably, compound **41** was considerably less selective than **42**, despite structural similarities between the two compounds (both have a nitrogen-based polar group at C6 and a  $\Delta 5$  double bond). The least selective of these new compounds screened was **38**, which may not have sufficient bulk to provide a clash with CYP21A2 active site features.

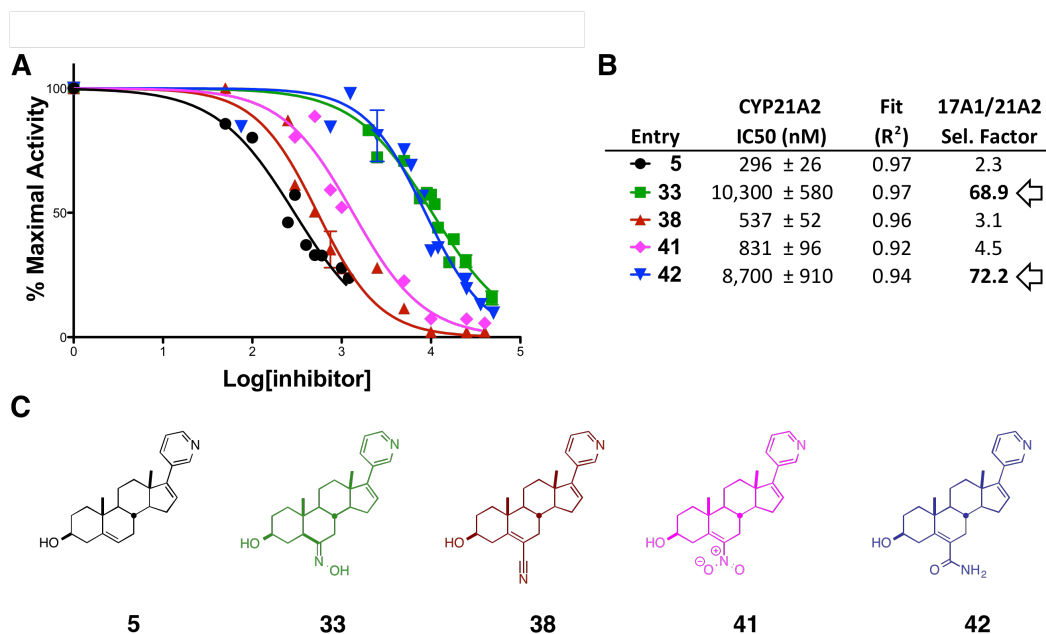


**Figure 1-21.** Progesterone 21-hydroxylation assay against B-ring substituted compounds. A: IC<sub>50</sub> curves. B: Analyzed results with standard error. C: Inhibitor structures.

Thus, this work has generated two compounds, **33** and **42**, with improved selectivity for the CYP17A1 active site over the similar CYP21A2 active site. The structural aspects of these inhibitors and their interactions with the primary target were further examined by X-ray analysis of co-crystal structures of these new compounds with CYP17A1, as discussed in the next section.

### 1.3.3 Structural analysis of CYP17A1 inhibitors

We used preliminary structural comparisons between CYP17A1 and CYP21A2 described in Section 1.1.4 to help us devise a general strategy for inhibitor design. As work proceeded, compounds with either improved potency over previous molecules or interesting structural features were co-crystallized with CYP17A1, and the complexes examined by X-ray crystallography. This analysis was used to refine the design strategy and suggest new directions in inhibitor synthesis.

The first new CYP17A1 structure was solved after the initial work on scaffold design in complex with azasteroid **19**. Though this complex was generated and maintained throughout the entire protein purification sequence, as described in Section 1.2.3, we later determined that compounds could be soaked into ligand-free CYP17A1. This was a faster method, which also required significantly less inhibitor material (i.e. < 1 mg vs. ca. 50 mg as before). The latter strategy aided in the throughput of CYP17A1-inhibitor complex formation and co-crystallization, and was utilized with compounds **23**, **33**, **38**, and **42**.

This new structural work with CYP17A1 closely followed the initial structural work performed by DeVore.<sup>67</sup> The reported initial crystallization conditions were utilized as the starting point for all of the following compound crystallization screens. Crystal growth was rapid with each compound. In all cases, the optimal conditions provided crystals visible to by eye in less than 24 hours. The morphology of successful experiments were single, rod-shaped crystals. Only two ligands did not immediately grow suitable crystals in these experiments, as described below.

X-ray data was collected at the Stanford Synchrotron Radiation Lightsource (SSRL). Structures were solved by molecular replacement using the previously determined

structures of CYP17A1 as the search model (PDB: 3RUK with abiraterone or 3SWZ with galaterone). Structural models were built in COOT and refined in PHENIX. The data collection and refinement statistics are summarized in Table 1-1 (Section 1.2.3). Like CYP17A1-abiraterone (3RUK), the asymmetric unit had four molecules of CYP17A1-ligand. The distances and conformations discussed below are representative of all four protein-ligand molecules.

The data collected from these crystals were good by standard crystallographic measures.<sup>108</sup> As indicated in Table 1-1, all structures showed a high degree of completeness and redundancy. The  $I/\sigma I$  values, which imply signal-to-noise ratios, were high, and over 1.5 for the outer shell reflections.  $R_{\text{pim}}$  ranged from 0.43 to 0.54 in the outer shell. With such cutoffs, the resolutions of these data sets ranged from 2.70 to 2.25 Å. Such resolutions allowed the unambiguous identification of the correct sidechain rotamers in nearly all cases, and permitted the observation of stable water molecules in the active site. All of these factors indicated quality data collection for membrane-associated protein structures, which have higher barriers for successful crystallography.<sup>109</sup>

The R-factors, which indicate the agreement of the original data with the model, were also reasonable. The agreements between  $R_{\text{work}}$  and  $R_{\text{free}}$  were slightly higher than optimal, with differences ranging from 5.7% to 6.5% (an  $R_{\text{free}}-R_{\text{work}}$  of < 5.0% is optimal).<sup>108</sup> Ramachandran analysis of the backbone revealed > 93% of the structure to be in preferred regions, with 1-2 outliers that were well-supported by the electron density. Overall, these crystal structures were deemed useful for structural analysis of the CYP17A1-inhibitor complexes.

### *Comparison of new CYP17A1 structures*

The global protein models of these new co-crystal structures were nearly identical. Figure 1-22 shows an overlay of the five structures, viewed along two axes. The ligands were removed for clarity. All features of CYP17A1 outlined in section 1.1.4 were maintained, with the exception of the ligand component. Thus, these crystallization conditions afford highly similar steroid-binding conformations of CYP17A1. This was more or less expected, given the similarities of these compounds to abiraterone.

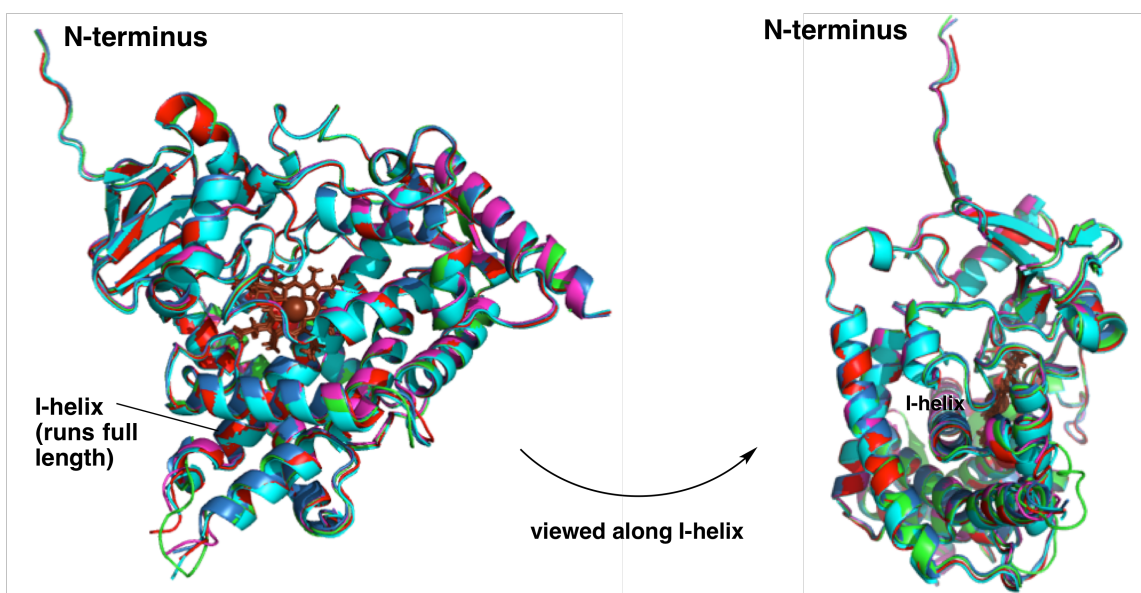


**Figure 1-22.** All five new co-crystal structures of CYP17A1 overlaid. Helices are shown with ribbons. Ligands have been removed for clarity. The heme is shown in dark red.

### *CYP17A1 co-crystallization with the azasteroid **19***

CYP17A1 was purified with **19** present at 10  $\mu$ M in all buffers from the cell resuspension/lysis stage onward. The CYP17A1-**19** complex was crystallized as described in section 1.2.3. Optimal conditions for crystal growth contained 0.175 M Tris, pH 8.5 containing 30% PEG 3350, 3% glycerol, and 0.250-0.275 M lithium sulfate. The most promising crystal diffracted to 2.25 Å, and the structure was solved by molecular

replacement using the abiraterone CYP17A1 structure as the search model (PDB: 3RUK).

The structural overview of the enzyme closely matched that observed for the complex with abiraterone, including the active site and the overall pose of steroid ligand **19**. The active site orientation of **19** is shown in Figure 1-23, along with a schematic of the structural features of interest for further compound design. Most of the binding motifs observed with abiraterone were conserved: (1) the steroid plane nestles within 4 Å of nonpolar residues of the active site such as on the I-helix (running below the steroid), (2) the C3 alcohol was 2.4 Å from Asn202, which would allow for an H-bonding interaction, and (3) the continuous electron density data between the heme iron and the pyridyl nitrogen suggested that coordination is maintained. An active site water bridging Arg239 and Asp298 was strongly supported by the electron density map, indicating that this water molecule is a feature of the CYP17A1 active site under these conditions.

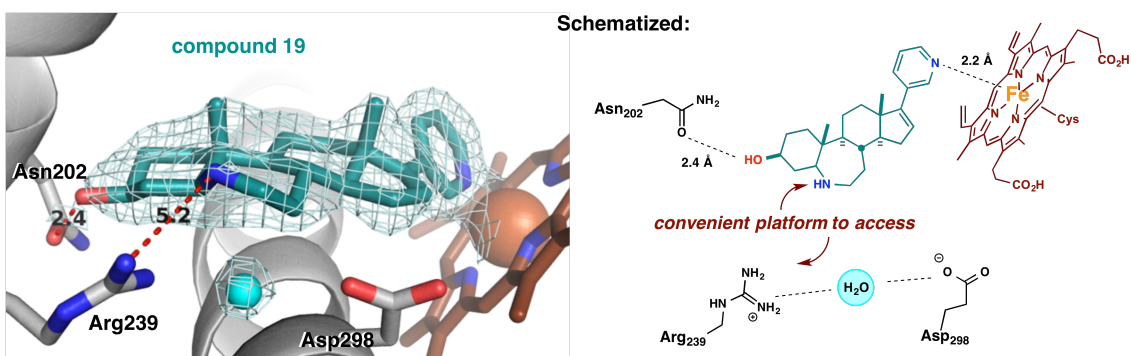


**Figure 1-23.** Co-crystal structure of **19** with CYP17A1 at 2.25 Å resolution. Electron density for the ligand and water is shown at the 1.0  $\sigma$  level of a  $|2F_o| - |F_c|$  simple composite omit map in teal mesh. A water molecule bridges the positive Arg239 and negative Asp298 side chains, shown as a light blue sphere. The heme iron is shown as a tan sphere.

These features hinted that the binding ability of **19** should be similar to abiraterone. The IC<sub>50</sub> data for abiraterone and **19** are 130 ± 7 nM and 461 ± 24 nM, respectively. The steroid core is disrupted somewhat by the ring expansion, which may be reflected in the 3.5-fold drop in potency. During our compound design planning, this structure suggested that the nitrogen in the expanded B-ring might well be able to serve as a platform for further polar substitution.

#### *CYP17A1 co-crystallization with the sulfonamide-substituted azasteroid **23***

For the second CYP17A1 co-crystal structure, purified ligand-free protein was thawed and incubated with 10 μM of compound **23** in CM elution buffer during the concentration stages. In all later respects, co-crystallization proceeded as for the CYP17A1-**19** complex. Again, optimal conditions for crystal growth contained 0.175 M Tris, pH 8.5 containing 30% PEG 3350, 3% glycerol, and 0.250-0.275 M lithium sulfate. The best crystal diffracted to 2.60 Å. The structure was solved by molecular replacement using the CYP17A1-galaterone structure as the search model (PDB: 3SWZ).

The active site data and schematic is shown in Figure 1-24. The binding mode of the azasteroid was similar to the CYP17A1-**19** complex, but significant additional electron density is observed above the azasteroid plane. When modeled with the inhibitor **23**, one carbonyl of the sulfoxide is in sufficient proximity (3.0-3.1 Å) to interact with both the guanidinyll group of Arg239 and the water bridging Arg239 and Asp298, which also displayed strong density. Thus, additional interactions were observed, potentially

accounting for the observed 2.4-fold increase in potency from  $461 \pm 24$  nM (**19**) to  $194 \pm 8$  nM (**23**).

One potentially useful strategy for increasing potency would be to prepare inhibitors able to displace the water molecule bridging Arg239 and Asp298, as this could lead to both an entropic gain from water displacement well as a potential enthalpic gain if interactions could be optimized with these polar residues. To provide complementary synthetic access to substitution that might accomplish this, the alternate scaffold of **28** was created to install polar features in different ways.

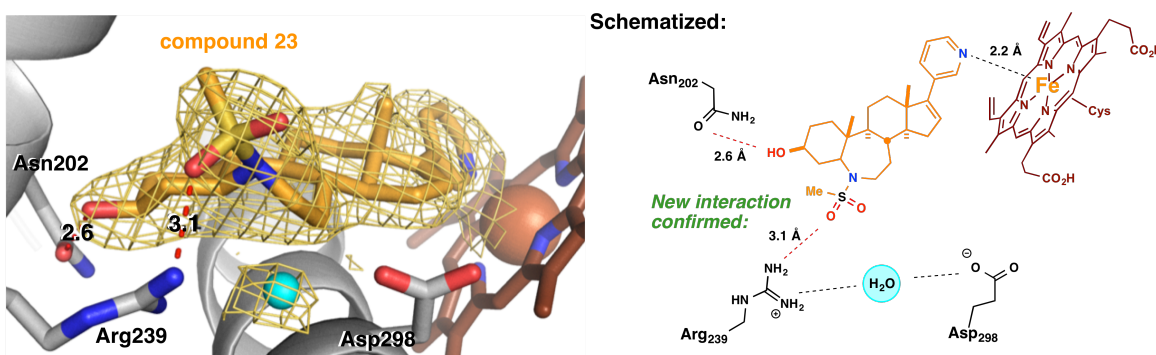


**Figure 1-24.** Co-crystal structure of **23** with CYP17A1 at 2.60 Å resolution. Electron density for the ligand is shown at the 1.0  $\sigma$  level of a  $|2F_o| - |F_c|$  simple composite omit map in orange mesh. The water was maintained as above, shown as a blue sphere. Density for the water is shown in cyan mesh at the 0.7  $\sigma$  level of the same map. The heme iron is shown as a tan sphere.

### *CYP17A1 co-crystallization with the steroidal oxime 33*

From compound **28**, the steroid oxime **33** was synthesized and then co-crystallized as described for compound **23**. The best crystal diffracted to 2.65 Å, and the structure was solved by molecular replacement using the galaterone-CYP17A1 structure as the search model (PBD: 3SWZ).

The binding motif of **33** is shown in Figure 1-25. This compound revealed a slightly increased distance between the C3 hydroxyl and Asn202 of 3.1 Å. However, the oxygen of the oxime stretches back toward the carboxylate group of Asp298 and the backbone carbonyl of Ala105. The first could form an H-bond interaction, and the later may be a dipolar interaction. These were both new potential interactions that may explain the potency of **33** ( $150 \pm 10$  nM), which maintained the activity of abiraterone ( $130 \pm 7$  nM). At the  $1.0 \sigma$  level, there was no electron density evidence for the water normally bridging Arg239 and Asp298 in three molecules in the asymmetric unit, and very weak density in the fourth at the  $0.9 \sigma$  level of the  $2F_o - 2F_c$  map. The resolution of the complex with CYP17A1-**33** was only slightly lower than the 2.60 Å for **23** in which this water was clearly apparent. Hence, this water was not modeled, but the weak density in one molecule suggested that water could still bind. Additional modifications were therefore deemed necessary to confirm the displacement of this water.

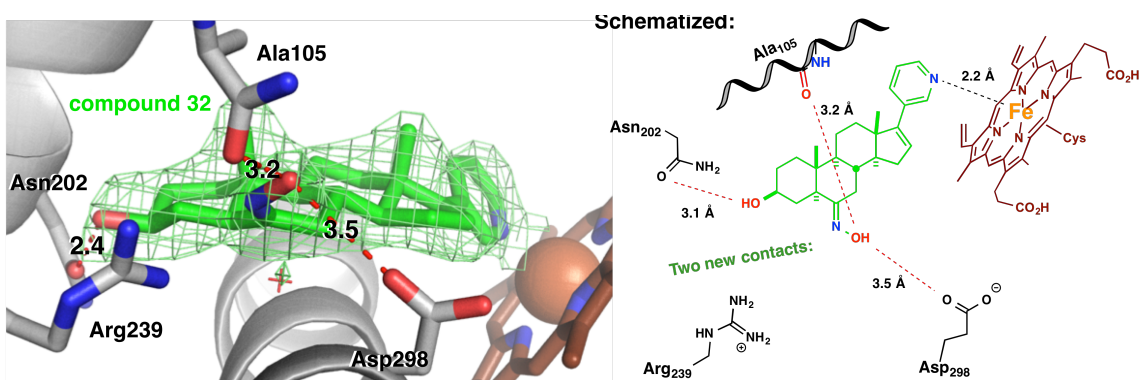


**Figure 1-25.** Co-crystal structure of **33** with CYP17A1 at 2.65 Å resolution. Electron density for the ligand is shown at the  $1.0 \sigma$  level of a  $|2F_o| - |F_c|$  simple composite omit map in green mesh. The water normally found between Arg239 and Asp298 had very weak density in only 1 of 4 molecules of the asymmetric unit (shown here as a red cross with weak electron density), and was not modeled. The heme iron is shown as a tan sphere.

*CYP17A1 co-crystallization with the steroidal nitrile 38*

The CYP17A1-**38** complex was generated as described for compounds **23** and **33**. However, when the above crystallization conditions were attempted, the majority of crystals grew in clumps, with thin crystals growing outwards (Figure 1-26). Alternatively, large hollow rods were obtained. Both results suggested that these crystals were growing faster in one dimension than others. Thick, solid rods were sought for data collection, to increase the signal and quality of the electron density diffraction data.

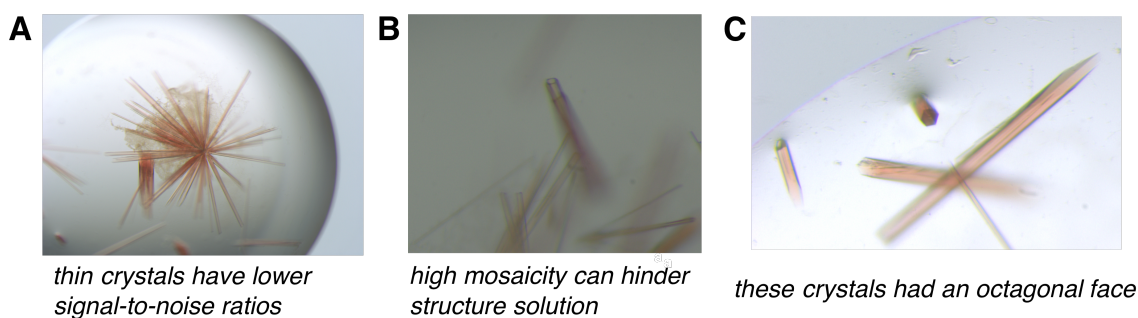


**Figure 1-26.** CYP17A1 co-crystals with **38**. Hasty growth led to poor-quality crystals. A: thin “urchins.” B: Hollow crystals. C: Optimal – solid, with defined edges.

To slow down crystal growth, the viscosity of the solution was increased by raising the concentrations of PEG3350 and/or glycerol. In addition, the temperature for crystal growth was reduced to 4 °C. The most successful strategy was found to be raising the PEG3350 concentration from 30% to 35%. Similar conditions were applied to the crystal growth of the CYP17A1-**42** complex, as described below.

Once suitable crystals were generated, these were screened and X-ray data was collected at the SSRL. The best crystal diffracted to 2.60 Å. This structure was solved by

molecular replacement using the model of CYP17A1 with galaterone (PDB 3SWZ) as the search model.

The active site features are shown in Figure 1-27. The C3 hydroxyl-Asn202 distance is maintained at 2.4 Å, as is pyridyl coordination with Fe. The nitrile projected directly from the steroid plane to interact with Arg239. This had the effect of unambiguously displacing the water from the complex by inhabiting the space normally occupied by this water molecule. The IC<sub>50</sub> data for **38** ( $174 \pm 8$  nM) was slightly weaker than abiraterone (130 nM). Thus, displacing the water may have affected other features of the protein-ligand complex, and did not augment potency. The small, linear size of the nitrile suggested that similar  $\Delta 5$ , C6 substitution could be further optimized to incorporate additional interactions.

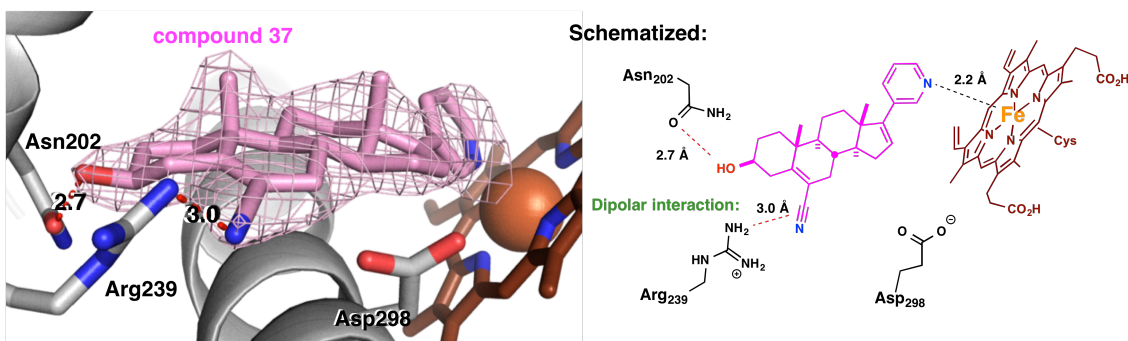


**Figure 1-27.** Co-crystal structure of **38** with CYP17A1 at 2.60 Å resolution. Electron density for the ligand is shown at the 1.0  $\sigma$  level of a  $|2F_o| - |F_c|$  simple composite omit map in pink mesh. The water bridging Arg239 and Asp298 was displaced by the ligand. The heme iron is shown as a tan sphere.

#### *CYP17A1 co-crystallization with the vinyl amide 42*

The final inhibitor to undergo co-crystallization with CYP17A1 was the coplanar amide **42**. This compound was approximately equipotent to abiraterone, with measured

IC<sub>50</sub> values of 120 ± 12 nM vs. 130 ± 7 nM, respectively. The complex generation and crystallization followed a similar procedure to the CYP17A1-**38** complex, and also required modifications of crystallization conditions designed to slow down crystal growth. A 2.70Å resolution data set was collected. The structure was solved by molecular replacement, using the CYP171-galaterone model (PDB 3SWZ) as the search model.

A representative active site is shown in Figure 1-28. This data revealed that the vinyl amido group stacked neatly between the polar residues Arg239 and Asp298. Interestingly, it twisted slightly out of conjugation, suggesting that there is some induced ligand fit. The distances between the polar atoms suggested useful interactions were possible, although the potency was within experimental error of abiraterone.

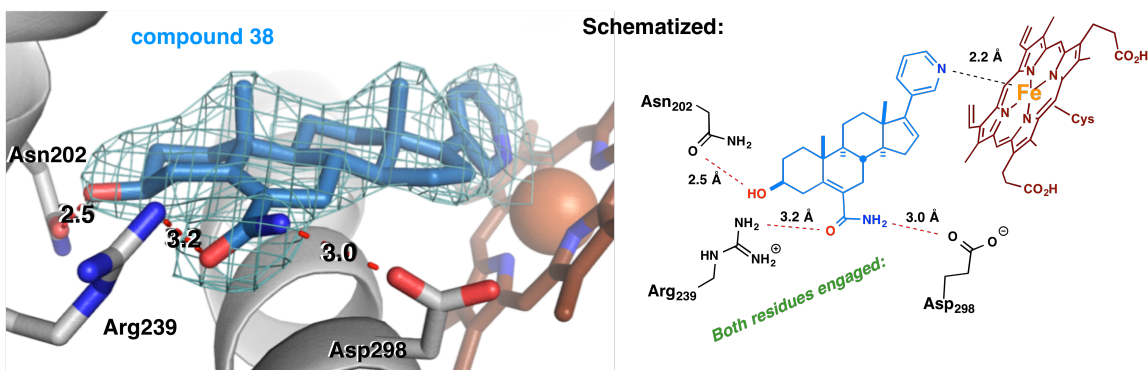


**Figure 1-28.** Co-crystal structure of **42** with CYP17A1 at 2.70 Å resolution. Electron density for the ligand is shown at the 1.0  $\sigma$  level of a  $|2F_o| - |F_c|$  simple composite omit map in blue mesh. The water was displaced by the ligand. The heme iron is shown as a tan sphere.

This structural data suggested an answer toward why compound **41**, which has a nitro group of similar size and polarity as **42**, was slightly less potent against CYP17A1. The charge-separated resonance form of the nitro group shares a negative charge over its two oxygen atoms, one of which would be expected to repel the negatively charged

carboxylate of Asp298. In contrast the amide of **42**, which can also form a charged resonance form, can interact favorably with both the positively charged guanidinium of Arg239 and the negatively charged carboxylate of Asp298. Continued optimization through the incorporation of various heterocycles may further drive down CYP17A1  $IC_{50}$ , through the tuning of these electrostatic interactions.

*Comparison of active site-inhibitor interactions:*

The active site topographies of the five new CYP17A1 protein models were also highly conserved. Figure 1-29 shows an overlay of these models. The sidechain of Asn202 held a nearly identical orientation among all structures. The B-ring partners Asp298 and especially Arg239 showed a bit of variability in this region, perhaps to accommodate new polar interactions over this ligand series. Thus, there may be a slight element of protein induced fit. This is especially apparent when comparing Asn202, which is maintained over the five structures, with Arg239, the most mobile residue. We were also vigilant for any induced structural pockets that may have been induced by an inhibitor, but no such features were observed.

The five ligands, shown in various colors, adopt a highly similar binding modality. Observed ligand-protein interactions are summarized in Table 1-2, along with the CYP17A1 progesterone hydroxylation  $IC_{50}$  values of these ligands. As one of our design goals became the displacement of the active site water between Arg239 and Asp298, this is also listed.

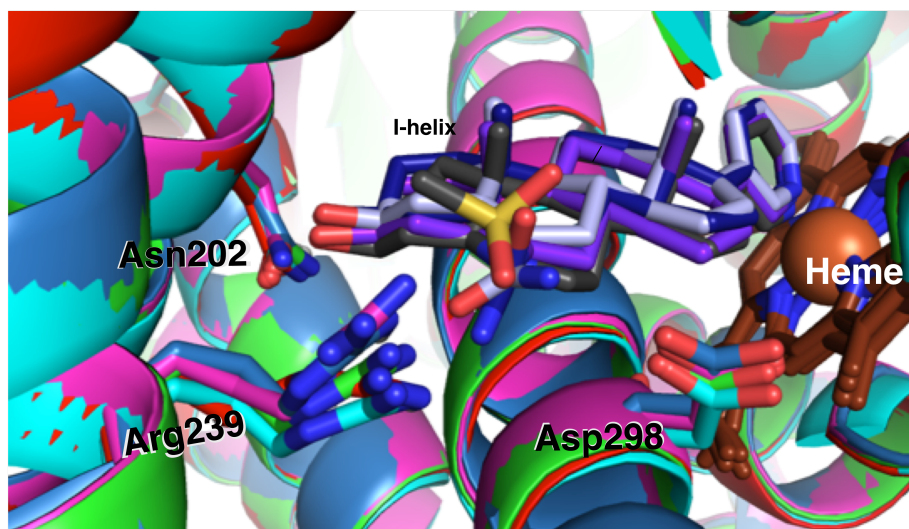


**Figure 1-29.** Active site view of the five structures of CYP17A1 solved in this work. All compounds showed a pyridine-heme coordination interaction distance of 2.2 Å.

**Table 1-2.** Observed interactions from CYP17A1-steroid ligand crystal structures

Compound	N202	Arg239	Asp298	Ala105	Active site H <sub>2</sub> O	IC <sub>50</sub> (nM)
<b>5</b> <b>abiraterone</b>	H-bond, 2.7 Å				Maintained	130 ± 7
<b>19</b> <b>azasteroid</b>	H-bond to backbone, 3.4 Å				Maintained	461 ± 24
<b>23</b> <b>sulfonamide</b>	H-bond, 2.6 Å	H-bond, 3.4 Å			Maintained	194 ± 8
<b>33</b> <b>oxime</b>	H-bond, 3.1 Å		H-bond, 3.2 Å	Dipolar interaction, 2.8 Å	Likely destabilized	150 ± 10
<b>38</b> <b>vinyl nitrile</b>	H-bond, 2.4 Å	Dipolar interactions			Displaced	174 ± 8
<b>42</b> <b>vinyl amide</b>	H-bond, 2.6 Å	H-bond, 2.4 Å	H-bond, 2.8 Å		Displaced	120 ± 12

Possible next steps to improve CYP17A1 potency are shown in Figure 1-30. The C3-amide interaction could be optimized.<sup>86</sup> The twist from conjugation seen with vinyl amide **42** may be responsible for an energetic penalty of binding and could be fixed by reducing the olefin from the  $\beta$ -face of the steroid. The distance between the amide nitrogen to Asp298 could be reduced with alternative functionality, such as heterocycles. Finally, filling the small nonpolar space near the heme, as in the benzimidazole of galaterone, may offer additional potency.

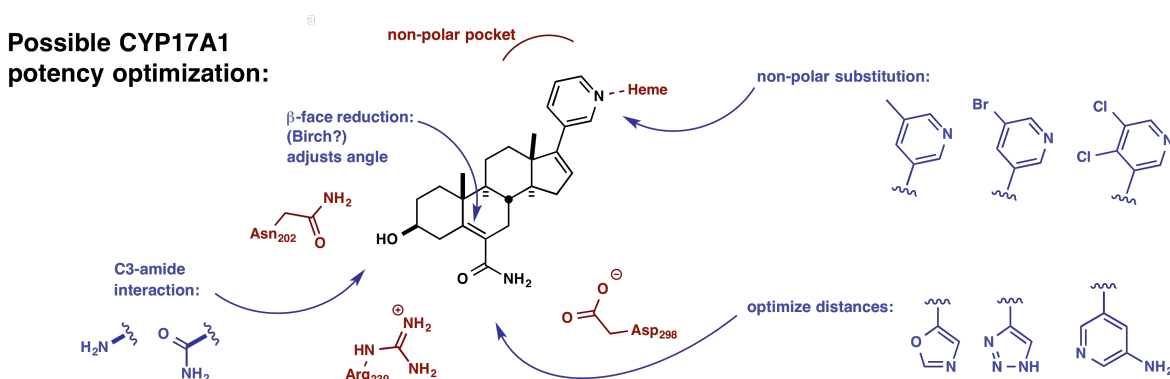


**Figure 1-30.** Additional SAR directions suggested by crystallography.

Although the CYP17A1 potency of these inhibitors did not significantly improve over that of abiraterone, the polar substitution of several of these steroid analogs provided decreased CYP21A2 inhibition, thereby augmenting CYP17A1-CYP21A2 selectivity. Co-crystallization of human CYP21A2 with a steroidal inhibitor remains an essential step to confirm the structural basis for this selectivity.

## 1.4 Conclusions

An iterative structure- and bioassay-guided sequence was used to design 24 steroid-based CYP17A1 inhibitors with the goals of improving potency and enhancing selectivity against the highly similar CYP21A2. These compounds simultaneously sought to engage polar features of CYP17A1 and clash with the hydrophobic active site of CYP21A2.

Potency for CYP17A1 inhibition was maintained, and our key findings lay in higher selectivity values over CYP21A2. Some of our compounds were up to 72-fold more selective for CYP17A1 than CYP21A2, making them 30-80 times more selective than the clinical agents abiraterone, galaterone, and orteronel. This could have practical therapeutic utility, as CYP21A2 is an essential enzyme for corticosteroid biosynthesis.

This research entailed the development of a generalizable *in vitro* P450 assay, which used GC/MS to profile an expanded range of steroid enzyme products. We are interested in using this assay to study potential CYP17A1 lyase vs. hydroxylase selectivity over our compound collection. Once we have optimized the expression of other steroidogenic enzymes such as CYP11B1 and CYP11B2, we can also use this system to test for inhibitory activity against other therapeutically-relevant enzymes.

Ultimately, we would like to combine this information from our studies with the features of the lyase-selective inhibitors orteronel/TAK-700 and VT-464. Dual CYP17A1 lyase and CYP21A2 selectivity may hold promise for the design of improved agents that achieve the selective chemotherapeutic inhibition of sex steroidogenesis. Thus far it has proven challenging to spare the highly related P450 enzymes involved in corticosteroid production as well as to properly target the CYP17A1 lyase reaction alone. This work represents one step forward toward this goal.

## 1.5 Experimental Section

*General information:*  $^1\text{H}$  and  $^{13}\text{C}$  NMR spectra were collected on a Bruker DRX-400 (400 MHz and 100 MHz, respectively) or a Bruker AM-500 (500 MHz and 125 MHz, respectively) instrument. Unless otherwise noted, all samples were dissolved in  $\text{CDCl}_3$ . A drop of MeOD was sometimes added to aid solubility. All chemical shifts are expressed in parts per million ( $\delta$ ) relative to residual  $\text{CHCl}_3$  as an internal standard ( $\delta$  7.27 ppm H NMR, 77.35 ppm C NMR). Abbreviations are: s, singlet; d, doublet; t, triplet; q, quartet; m, multiplet; dd, doublet of doublets; qd, quartet of doublets; td, triplet of doublets. The infrared (IR) spectra were recorded on Perkin-Elmer 1420 spectrometer or a Perkin-Elmer Spectrum One FT-IR and the absorption frequencies are reported in  $\text{cm}^{-1}$ . Low resolution mass spectra (MS) and high resolution mass spectra (HRMS) were recorded on a Waters LCT Premier TOF spectrometer for electrospray ionization (ESI) or a VG Instrument ZAB double-focusing mass spectrometer (FAB). Parallel Evaporations were performed using a GeneVac EZ-2 plus evaporator. Automated preparative reverse-phase HPLC purification was performed using a Waters 2767 Mass Directed Fractionation system (2767 sample manager, 2525 Binary Pump, 515 Make-up pump) with a Waters ZQ quadrupole spectrometer and detected by UV (270 nm, Waters Xterra MS C-18 column, 19x150 mm, elution with the appropriate gradient of acetonitrile in pH 9.8 buffered aqueous ammonium formate at 18 mLmin<sup>-1</sup> flow rate). Purity was determined by reverse-phase HPLC with peak area (UV) at 214 nm using a Waters Alliance 2795 system (Waters Xterra MS C-18 column, 4.6x150mm, elution with a linear gradient of 5% acetonitrile in pH 9.8 buffered aqueous ammonium formate to 100% acetonitrile at 1.0 mLmin<sup>-1</sup> flow rate). Flash chromatography was performed using Sorbent

technologies silica gel (32-63 mesh) with the reported eluent system. Automated purification was performed on a Combiflash Rf (Teledyne Isco, Lincoln, NE). Acetonitrile, methylene chloride and THF were dried by passing through two packed columns of neutral alumina using the PurSolv solvent purification system (Innovative Technology Inc.) prior to use. All chemicals were used as purchased from commercial suppliers. Dry flasks (noted) were baked in an oven overnight or were flame dried under vacuum and then placed under a positive pressure of argon. Microwave reactions were conducted with a Biotage Initiator instrument. Automated purification was performed using a Combiflash Rf 200 (Teledyne Isco, Lincoln, NE).

A note on analysis: until the pyridyl group was attached, many of these molecules ionized very poorly by electrospray-MS. Some compounds, noted, do not have sufficient MS data. None of the compounds tested for biological activity had this problem.

A simplified steroid naming convention will be used.<sup>110</sup> Steroid substitution will be indicated according to the numbering shown in Figure 1-24. For example, 17-(3-pyridyl)-androst-5,16-dien-3 $\beta$ -ol will correspond to the structure of abiraterone (**5**). Compounds that were not enumerated but were intermediates in the synthetic schemes in the body of this dissertation are named below, but not numbered.

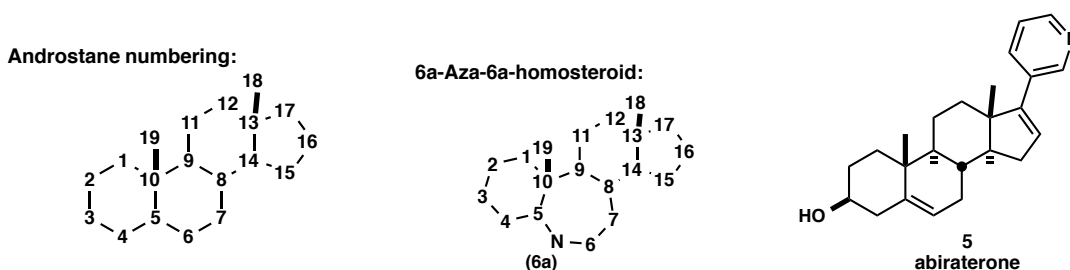
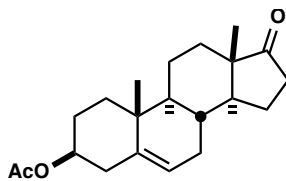
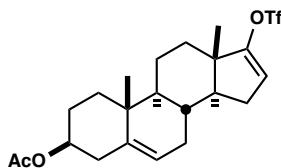


**Figure 1-31.** Steroid numbering to be used for nomenclature in the Experimental Section.



2

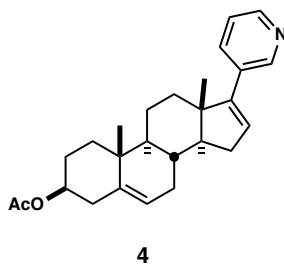
**3β-Acetoxy-androst-5-en-17-one (2).** Dehydroepiandrosterone **1** (10.0 g, 34.7 mmol) was added to a dry 20 mL microwave vial as a fine powder. Toluenesulfonic acid (0.066 g, 0.35 mmol) was added as a solid, and the mixture suspended in acetic anhydride (13.1 mL, 138 mmol). Microwave irradiation was applied to 80 °C for 6 min. Upon cooling, the resulting wet solid was dissolved in 200 mL methylene chloride, and 200 mL of a saturated aqueous solution of sodium bicarbonate was slowly added. This mixture was stirred overnight. The organic layer was separated, followed by further extraction with two portions of methylene chloride. The pooled organic layers were washed with brine, dried over sodium sulfate, and concentrated, affording 11.3 g (98% crude yield) as a white crystalline solid. The analytical data matched reported values.<sup>111</sup>



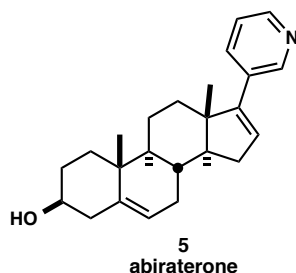
3

**3β-Acetoxy-17-triflyl-androst-5,16-diene (3).** Compound **2** (11.3 g, 34.1 mmol) was added to a dry 500 mL round bottom flask and dissolved in dry methylene chloride (227 mL, 0.15 M). The solution was cooled to -78 °C, and 2,6-lutidine (8.1 mL, 70.0 mmol) was added. Triflic anhydride (10.5 mL, 61.1 mmol) was added over 30 min. The solution was stirred at -78 °C for 2 h, then was allowed to age at -20 °C (freezer) overnight. When

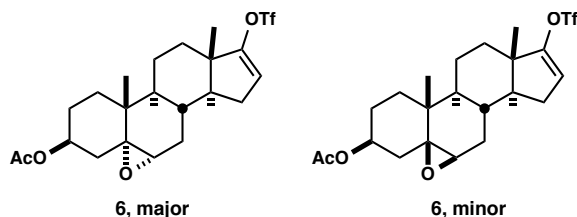
cold, the reaction was worked up with 1.0 N HCl (100 mL), extracted with methylene chloride, and dried over brine and sodium sulfate. The organic layer was concentrated onto silica and purified by silica chromatography (60 g silica, 0% to 5% to 10% ethyl acetate/hexanes) to obtain 12.3 g of a pale yellow solid (79%). The analytical data matched reported values.<sup>112</sup>



**3β-Acetoxy-17-(3-pyridyl)-andro-5,16-diene (4, abiraterone acetate).** Compound **3** (2 g, 4.3 mmol) was added to a round-bottomed flask and dissolved in a mixture of THF (29 mL, 0.15 M) and saturated aqueous sodium bicarbonate (8.6 mL, ~8.6 mmol). Bis(triphenylphosphine)palladium(II) dichloride (301 mg, 0.43 mmol) and diethyl (3-pyridyl)borane (691 mg, 4.73 mmol) were added. A condenser was attached, and the mixture heated to 60 °C for 1 h. The THF was removed under an N<sub>2</sub> stream, and water was added. The mixture was extracted with chloroform, washed with brine, and dried over NaSO<sub>4</sub>. The crude material was purified by automatic purification (40g silica, 10% to 30% to 50% EtOAc/hexanes) to yield 1.63 g of white solid (94%). The analytical data matched reported values.<sup>70</sup>

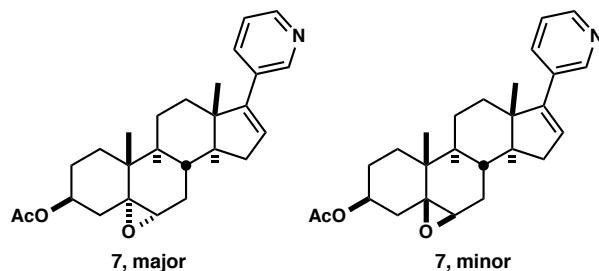


**17-(3-Pyridyl)-androst-5,16-dien-3 $\beta$ -ol (5, abiraterone).** Compound 4 (150 mg, 0.382 mmol) was dissolved in methanol (12.7 mL, 0.03 M). Solid potassium carbonate (422 mg, 3.06 mmol) was added, and the mixture stirred at rt overnight. The mixture was brought to pH ~9 with aqueous 1 N HCl, and extracted with chloroform. The organic phases were washed with brine and dried over NaSO<sub>4</sub>. The crude material was purified by automatic purification (25% to 50% EtOAc/hexanes) to isolate 103 mg as a white solid (77%). The analytical data matched reported values.<sup>70</sup>



**3 $\beta$ -Acetoxy-5 $\alpha$ ,6 $\alpha$ -epoxy-17-triflyl-androst-16-ene (6) and isomer.** Compound 3 (500 mg, 0.214 mmol) was dissolved in dry methylene chloride (2.1 mL, 0.1 M) and cooled to 0 °C. Chloroperoxybenzoic acid (77% pure, 240 mg, 0.214 mmol) was added and the mixture stirred overnight, warming to rt. Saturated aqueous sodium bicarbonate (2 mL) was added and the mixture stirred for 1 h at rt. The mixture was extracted twice more with methylene chloride, washed with brine, and dried over NaSO<sub>4</sub>. The crude material was purified by automatic purification (4g silica, 10% to 20% ethyl acetate/hexanes) to

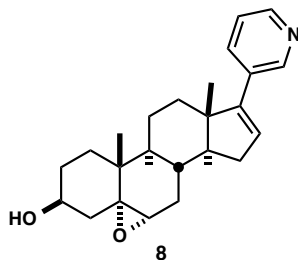
obtain 100 mg (92%) of a white solid.  $^1\text{H}$  NMR showed the isolate to be a ca. 7:3 mixture of the  $5\alpha,6\alpha:5\beta,6\beta$ -epoxide isomers. The major diastereomeric isomer was established by analogy to the related mixture observed upon mCPBA epoxidation at this position.<sup>113</sup> Major diastereomer ( $5\alpha,6\alpha$ -epoxide):  $^1\text{H}$  NMR (400 MHz,  $\text{CDCl}_3$ )  $\delta$  5.56 (dt,  $J = 3.3, 1.6$  Hz, 1H), 4.95 (tt,  $J = 11.3, 4.9$  Hz, 1H), 2.93 (d,  $J = 4.5$  Hz, 1H), 2.30–2.05 (m, 3H), 2.07–1.87 (m, 5H), 1.78–1.17 (m, 9H), 1.11 (s, 2H), 1.04 (s, 1H), 0.94 (m, 3H);  $^{13}\text{C}$  NMR (101 MHz,  $\text{CDCl}_3$ )  $\delta$  170.2, 159.0, 114.2, 71.14, 65.3, 58.5, 54.1, 44.7, 42.6, 36.0, 35.3, 32.3, 31.9, 28.4, 28.0, 27.4, 27.1, 21.3 (overlapping peaks), 19.9, 15.8, 15.0; this compound did not ionize by ESI-MS. Minor diastereomer: 4.77 (tt,  $J = 11.3, 4.9$  Hz, 1H), 3.12, (d,  $J = 4.5$  Hz, 1H).



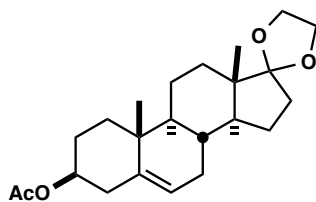
**$3\beta$ -Acetoxy- $5\alpha,6\alpha$ -epoxy-17-(3-pyridyl)- $\Delta$ 16-androst-16-ene (7) and isomer.**

Compound **6** (1.9 g, 3.97 mmol) was coupled as described for the reaction of **3** to **4** except that the temperature was reduced to 50 °C. The organic extract was purified by automatic purification to isolate 1.4 g of a pale yellow oil (82%). The isomeric ratio of 7:3 (**7, major**:**7, minor**) was maintained from the previous step. Major isomer:  $^1\text{H}$  NMR (400 MHz,  $\text{CDCl}_3$ )  $\delta$  8.59 (s, 1H), 8.53–8.37 (m, 1H), 7.62 (d,  $J = 9.3$  Hz, 1H), 7.25–7.14 (m, 1H), 5.97 (s, 1H), 5.01–4.89 (m, 1H), 2.94 (d,  $J = 4.4$  Hz, 1H), 2.10–1.91 (m, 7H),

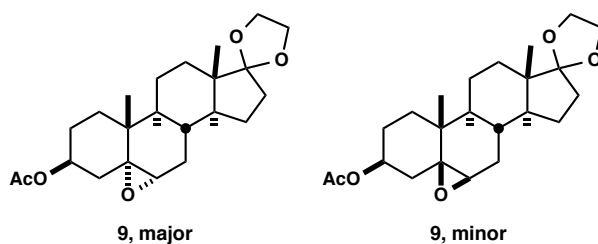
1.90–1.19 (m, 13H), 1.09 (m, 3H), 0.98 (m, 3H).  $^{13}\text{C}$  NMR (101 MHz,  $\text{CDCl}_3$ )  $\delta$  170.3, 147.7, 134.0, 132.1, 129.2, 128.7, 128.5, 123.2, 71.4, 65.4, 59.0, 57.4, 47.4, 42.6, 36.2, 35.32, 35.29, 34.9, 32.1, 31.6, 28.5, 28.4, 27.3, 21.4, 20.6, 16.5, 16.0. Minor isomer: 4.81–4.89 (m, 1H), 3.13 (d,  $J = 2.4$  Hz, 1 H).



**3 $\beta$ -Hydroxy-5,6 $\alpha$ -epoxy-17-(3-pyridyl)- $\Delta$ 16-androstane (8).** Compound **7** was deacylated as for **5**. The crude mixture was purified by silica column to isolated 21.3 mg of a white powder (81%). IR (neat) 3329, 1687, 1439, 1378.3 1250  $\text{cm}^{-1}$ ;  $^1\text{H}$  NMR (400 MHz,  $\text{CDCl}_3$ )  $\delta$  8.62 (s, 1H), 8.49 (s, 1H), 7.95 (d,  $J = 7.6$ , 1H), 7.50 (t,  $J = 6.4$ , 1H), 6.13 (s, 1H), 3.84 (s, 1H), 3.63 (d,  $J = 6.0$ , 1H), 3.38 (s, 1H), 3.04–2.86 (m, 1H), 2.30 (d,  $J = 15.9$  Hz, 2H), 1.55 (m, 7H), 1.40 (m, 9H), 1.11 (m, 3H), 0.98 (s, 3H), 0.71 (s, 1H);  $^{13}\text{C}$  NMR (101 MHz,  $\text{CDCl}_3$ )  $\delta$  151.5, 147.8, 133.7, 133.7, 132.9, 129.1, 123.0, 69.3, 68.6, 65.9, 63.6, 63.1, 59.0, 57.4, 57.2, 47.3, 42.6, 39.4, 42.2, 39.8, 37.3, 35.1, 34.9, 32.3, 31.6, 31.1, 28.5, 28.4, 20.6, 21.7, 16.5, 16.0; HRMS calculated for  $\text{C}_{24}\text{H}_{32}\text{NO}_2$  ( $\text{M}^+ + 1$ ): 366.2433, found 366.2430.



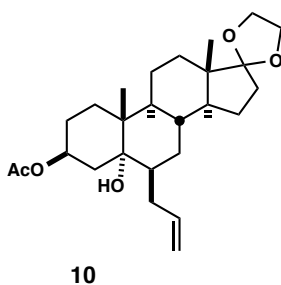
**3β-Acetoxy-androst-17-one, ethylene ketal:** Compound **2** (2.0 g, 6.03 mmol) in a dry microwave vial was dissolved in triethyl orthoformate (2.4 mL) and ethylene glycol (1.6 mL) to a concentration of 1.5 M. Toluenesulfonic acid (57 mg, 0.30 mmol) was added, and the reaction vessel was capped. The reaction was heated to 90 °C for 20 min in the microwave. The mixture was diluted with methylene chloride and washed with saturated sodium bicarbonate, water, and brine. The mixture was dried over NaSO<sub>4</sub> and purified by silica flash column chromatography (20 g silica, 20% EtOAc/hexanes) to yield 2.02 g of the title compound as a white solid (90%). The analytical data matched reported values.<sup>111</sup>



**3β-Acetoxy-5α,6α-epoxy-androst-17-one, ethylene ketal (9) and minor isomer:**

The above ketal (2.02 g, 5.44 mmol) was dissolved in methylene chloride (50 mL, 0.1 M) and cooled to 0 °C. Chloroperoxybenzoic acid (77% pure, 1.82 g, 8.16 mmol) was added and the mixture stirred overnight, warming to rt. Saturated aqueous sodium bicarbonate (50 mL) was added, and the mixture stirred for 1 h at rt. The mixture was extracted twice more with methylene chloride, washed with brine, and dried over NaSO<sub>4</sub>. The crude

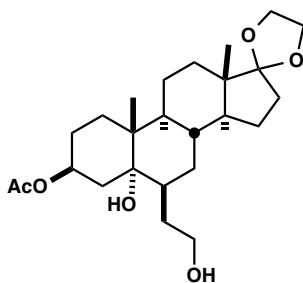
material was purified by automatic purification system (40g silica, 10% to 20% ethyl acetate/hexanes) to obtain 1.77 g (84%) of a white solid, in a ca. 10:1 mixture of the  $\alpha$ : $\beta$  epoxides. Major isomer:  $^1\text{H}$  NMR (400 MHz,  $\text{CDCl}_3$ )  $\delta$  4.99-4.88 (m, 1H), 3.98-3.72 (m, 4H), 2.88 (d,  $J = 4.4$  Hz, 1H), 2.15 (s, 1H), 2.00 (s, 3H), 1.98-1.84 (m, 3H), 1.81-1.74 (m, 1H), 1.71 (dd,  $J = 6.7, 3.0$  Hz, 1H), 1.67 (m, 1H), 1.57-1.48 (m, 2H), 1.43 (s, 3H), 1.33 (s, 5H), 1.25 (s, 1H), 1.21-1.13 (m, 1H), 1.07 (s, 3H), 0.78 (s, 3H). Minor isomer: 4.81-4.71 (m, 1 H), 3.08 (d,  $J = 2.0$  Hz, 1 H).  $^{13}\text{C}$ , IR, forthcoming.



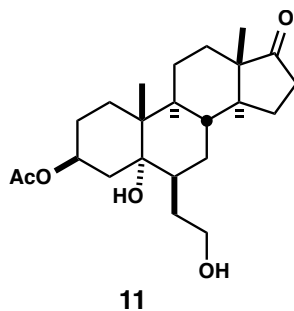
**6 $\beta$ -Allyl-3 $\beta$ -acetoxy-5 $\alpha$ -hydroxy-androst-17-one, ethylene ketal (10).** Allyl magnesium bromide (18.28 mL of a 1.0 M ethereal solution, 18.28 mmol) was cooled to 0 °C in a dry flask. Copper chloride (4.5 mg, 0.046 mmol) was added, and the mixture stirred for 20 min at 0 °C before cooling to -78 °C. The mixture **9** (1.77 g, 4.57 mmol) was added as a solution in methylene chloride (30.5 mL, 0.15 M), and the reaction stirred overnight, slowly warming to rt. The completed reaction was poured over ice, and was quenched with 50 mL of saturated aqueous ammonium chloride. The mixture was extracted with methylene chloride, washed with brine, and dried over  $\text{NaSO}_4$ . The crude material was purified by silica flash chromatography (20 g silica, 20% to 50% EtOAc/hexanes) to yield 1.3 g as a clear oil (66%), a single isomer (by NMR analysis).

$^1\text{H}$  NMR (400 MHz,  $\text{CDCl}_3$ )  $\delta$  5.66 (m, 1H), 5.31 (s, 1H), 5.00 (d,  $J = 4.4$  Hz, 1 H), 4.96 (s, 1H), 4.02–3.78 (m, 4H), 2.32–2.18 (m, 1H), 2.05 (s, 3H), 1.99–1.88 (m, 2H), 1.61 (m, 3H), 1.54–1.38 (m, 10H), 1.33–1.11 (m, 6H), 1.09–0.97 (m, 3H), 0.91–0.84 (m, 3H).

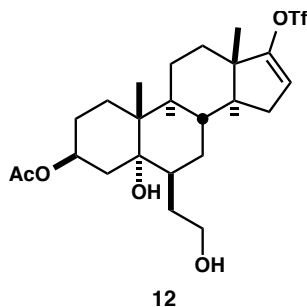
$^{13}\text{C}$ , IR forthcoming.



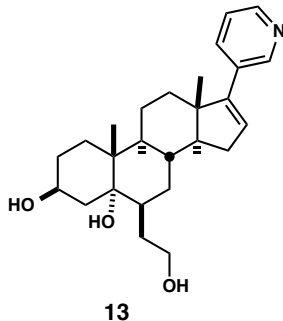
**3 $\beta$ -acetoxy-6 $\beta$ -hydroxyethyl-5 $\alpha$ -hydroxy-androst-17-one, ethylene ketal.** Compound **10** (200 mg, 0.467 mmol) was dissolved in a mixture of 14 mL methylene chloride and 1 mL methanol (0.03 M), and was cooled to  $-78$   $^\circ\text{C}$ . This was ozonized until the solution turned faintly blue, about 5 min. The solution was purged with  $\text{N}_2$  gas for 5 min, and sodium borohydride (106 mg, 2.80 mmol) was added at  $-78$   $^\circ\text{C}$ . This solution was stirred overnight, slowly warming to rt. The solvent was removed *in vacuo*, and methylene chloride and saturated aqueous sodium bicarbonate were added. This mixture was separated, then further extracted with methylene chloride. The organic layer was washed with brine, and dried over  $\text{NaSO}_4$ . The crude material was purified (4 g silica, 100% EtOAc) to obtain 86 mg of a white solid (43%).  $^1\text{H}$  NMR (400 MHz, MeOD)  $\delta$  4.15–4.02 (m, 1H), 3.98–3.78 (m, 4H), 3.56 (m, 1H), 3.47–3.40 (m, 1 H), 2.03 (s, 1 H), 2.00–1.89 (m, 2H), 1.76 (m, 3 H), 1.71 (m, 4 H), 1.58 (m, 5H), 1.46 (m, 3H), 1.41 (m, 3H), 1.32–1.22 (m, 3H), 1.05 (s, 3H), 0.87 (s, 3H).  $^{13}\text{C}$ , IR forthcoming.



**3β-Acetoxy-6β-hydroxyethyl-5α-hydroxy-17-keto-androst-17-one (11).** The above hydroxyethyl ketal (86 mg, 0.199 mmol) was dissolved in acetone (10 mL) and toluenesulfonic acid (10 mg, 0.05 mmol) was added. The mixture was stirred at rt overnight. The mixture was diluted with 60 mL of methylene chloride, washed with 10 mL of a saturated aqueous bicarbonate solution, and dried over NaSO<sub>4</sub>. The material was used without further purification, isolated as 41 mg of a white solid (53% crude yield). <sup>1</sup>H NMR (400 MHz, MeOD) δ 4.05 (m, 1H), 3.57 (m, 1H), 3.46 (m, 1H), 2.52–2.36 (m, 2H), 2.15–1.83 (m, 3H), 1.86–1.67 (m, 5H), 1.67–1.45 (m, 8H), 1.45–1.19 (m, 8H), 1.06 (s, 3H), 0.89 (s, 3H). <sup>13</sup>C, IR forthcoming.

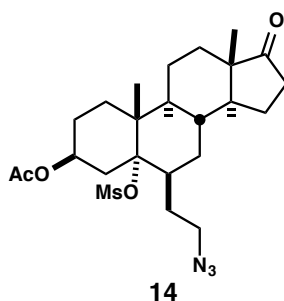


**3β-Acetoxy-6β-hydroxyethyl-5α-hydroxy-17-triflyl-androst-16-ene (12).** Compound **11** (84 mg, 0.19 mmol) was triflated as described for **3**. This mixture was purified by silica flash chromatography (25% to 50% EtOAc/hexanes) to isolate 30 mg of **12** as a yellow oil (28%). <sup>1</sup>H NMR (400 MHz, CDCl<sub>3</sub>) δ 5.59 (m, 1H), 4.52 (m, 1H), 4.07 (m, 2H), 2.50 (m, 3H), 2.20–1.90 (m, 6H), 1.90–1.68 (m, 5H), 1.66 (m, 4H), 1.29 (m, 4H), 1.06 (s, 3H), 0.99 (s, 3H). <sup>13</sup>C, IR forthcoming.



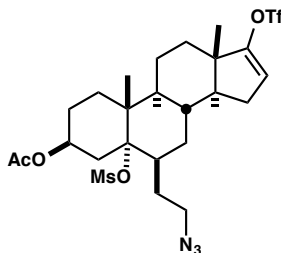
**6β-Hydroxyethyl-5α-hydroxy-17-(3-pyridyl)-androst-16-en-3β-ol (13).** Compound **12** (30 mg, 0.054 mmol) was coupled as described for **4**. The crude mixture of the above reaction (19.1 mg, ~0.039 mmol) was dissolved in methanol (0.25 mL, 0.1 M) and sodium hydroxide (0.15 mL of a 2.5 N aqueous solution) was added. The mixture was heated to 80 °C for 5 min. The mixture was neutralized with aqueous 1 N HCl and extracted with ethyl acetate. The crude material was purified (500 mg silica, 100% EtOAc) to yield 7.1 mg of a white solid (44%). IR (neat) 3319, 1449, 1410; <sup>1</sup>H NMR

(500 MHz, CDCl<sub>3</sub>) δ 8.63 (s, 1H), 8.54–8.41 (m, 1H), 7.68 (m, 1H), 7.25 (m, 1H), 6.10–5.96 (s, 1H), 3.64 (m, 2H), 3.48 (m, 1H), 2.87 (m, 1H), 2.47–2.22 (m, 3H), 2.15–1.94 (m, 3H), 1.94–1.84 (m, 2H), 1.84–1.74 (m, 2H), 1.74–1.65 (m, 3H), 1.65–1.56 (m, 3H), 1.55–1.47 (m, 2H), 1.20 (s, 2H), 1.14–0.97 (m, 6H); <sup>13</sup>C NMR (126 MHz, CDCl<sub>3</sub>) δ 151.5, 147.5, 137.1, 134.0, 129.4, 125.9, 123.2, 71.6, 61.4, 57.5, 50.3, 47.3, 37.4, 37.3, 37.1, 37.1, 35.5, 35.3, 31.8, 31.4, 30.2, 29.7, 21.0, 19.8, 19.2, 16.6; HRMS calculated for C<sub>26</sub>H<sub>36</sub>NO<sub>2</sub> (M<sup>+</sup> - OH): 394.2752, found 394.3380.

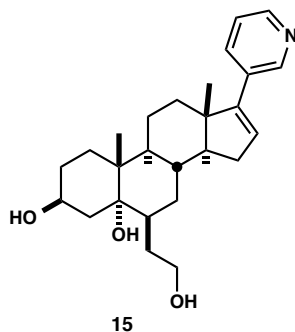


**3β-Acetoxy-6β-ethylazido-5α-mesyl-androst-17-one (14).** Compound **11** (115 mg, 0.30 mmol) was dissolved in tetrahydrofuran (3 mL, 0.1 M) and cooled to 0 °C. Triethylamine (0.18 mL, 1.3 mmol) and dimethylaminopyridine (2 mg, 5%) were added, followed by mesyl chloride (0.09 mL, 1.2 mmol). The solution was brought to rt and stirred for 25 min. When the reaction was complete, 15 mL of brine was added, and the organic layer extracted with ethyl acetate. This material was concentrated and redissolved in acetonitrile (3 mL, 0.1 M). Tetramethylguanidinium azide (95 mg, 0.6 mmol) was added, and the mixture heated to 50 °C to stir overnight. When the reaction had completed, the mixture was cooled to rt. The tetramethylguanidinium salts were filtered

off, and the filtrate was diluted with ethyl acetate and washed with brine. The crude material was purified by flash chromatography (500 mg silica, EtOAc) to yield 91 mg of a pale yellow solid (71%). IR (neat) 2099, 1733, 1664, 1235.9  $\text{cm}^{-1}$ ;  $^1\text{H}$  NMR (400 MHz,  $\text{CDCl}_3$ )  $\delta$  5.11 (m, 1H), 3.41–3.29 (m, 1H), 3.21 (m, 1H), 3.01 (s, 3H), 2.52–2.38 (m, 1H), 2.26–2.15 (m, 1H), 2.03 (s, 3H), 1.85–1.74 (m, 2H), 1.74–1.56 (m, 5H), 1.55–1.34 (m, 6H), 1.25 (m, 6H), 1.03 (s, 3H), 0.87 (s, 3H);  $^{13}\text{C}$  NMR (101 MHz,  $\text{CDCl}_3$ )  $\delta$  171.2, 80.1, 60.4, 51.1, 50.7, 47.8, 46.1, 44.7, 39.7, 38.9, 38.6, 35.8, 33.1, 31.5, 30.5, 29.6, 28.6, 28.1, 21.8, 21.1, 20.4, 17.4, 14.2, 13.9 (cyclopentanone C is out of field); this compound did not ionize by ESI-MS.

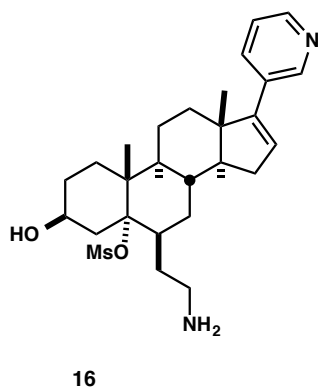


*3 $\beta$ -Acetoxy-6 $\beta$ -azidoethyl-5 $\alpha$ -mesyl-17-triflyl-androst-16-ene*. Compound **14** (91 mg, 0.211 mmol) was triflated as described for **3**. The material was purified (500 mg silica, 20% to 50% EtOAc/hexanes) to yield 52 mg of a yellow oil (44%).  $^1\text{H}$  NMR (400 MHz,  $\text{CDCl}_3$ )  $\delta$  5.59 (dd,  $J = 3.3, 1.7$  Hz, 1H), 5.14 (m, 1H), 3.37 (s, 3H), 2.28–2.18 (m, 2H), 2.05 (s, 3H), 1.90–1.83 (s, 2H), 1.77–1.63 (m, 8H), 1.51–1.44 (m, 3H), 1.28–1.25 (m, 5H), 1.06 (s, 3H), 0.99 (s, 3H).



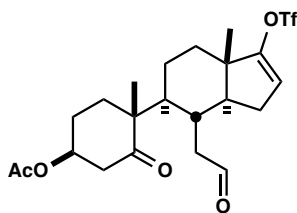
**3β-Acetoxy-6β-aminoethyl-5α-mesyl-17-(3-pyridyl)-androst-16-ene (15).**

The above material (52 mg, 0.08 mmol) was coupled as described for **4**. The amine was purified by silica flash chromatography (1 to 10% MeOH/DCM) to obtain 9.1 mg (20% crude yield) of **15** as a yellow solid. <sup>1</sup>H NMR (400 MHz, CDCl<sub>3</sub>) δ 8.54 (s, 1H), 8.38 (d, *J* = 5.0 Hz, 1H), 7.66–7.50 (m, 1H), 7.14 (t, *J* = 7.9 Hz, 1H), 5.90 (s, 1H), 5.07 (s, 1H), 3.93–3.55 (m, 2H), 2.94 (s, 3H), 2.16 (m, 5H), 1.93 (m, 4H), 1.68 (m, 7H), 1.51–1.27 (m, 7H), 1.09–0.88 (m, 6H). MS calculated for C<sub>29</sub>H<sub>42</sub>N<sub>2</sub>O<sub>5</sub>S (M<sup>+</sup>+H): 530.281, found 530.278. <sup>13</sup>C, IR forthcoming.



**6β-Aminoethyl-5α-mesyl-17-(3-pyridyl)-androst-16-en-3β-ol (16).** Compound **15** (9.1 mg, 0.017 mmol) was dissolved in methanol (0.5 mL, 0.04 M) and solid potassium carbonate was added (5.7 mg, 0.42 mmol). The mixture was stirred overnight at rt. When the reaction had completed, this was concentrated onto silica gel and purified by column

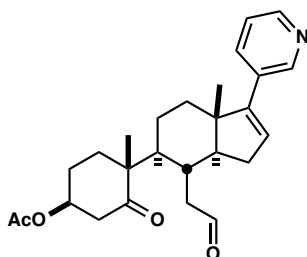
(100 mg, 1% to 2% to 5% MeOH/DCM) to isolate 3.7 mg of a clear oil (45%). IR (neat) 3328, 1567, 1475, 1341  $\text{cm}^{-1}$ ;  $^1\text{H}$  NMR (500 MHz,  $\text{CDCl}_3$ )  $\delta$  8.62 (s, 1H), 8.46 (d,  $J = 4.9$ , 1H), 7.64 (m, 1H), 7.22 (m, 1H), 5.98 (s, 1H), 5.16 (m, 1H), 3.02 (s, 3H), 2.90–2.76 (m, 1H), 2.71–2.56 (m, 1H), 2.35–2.19 (m, 2H), 2.11–1.95 (m, 3H), 1.85–1.97 (m, 2H), 1.72–1.67 (m, 3H), 1.66–1.53 (m, 7H), 1.50–1.43 (m, 4H), 1.09–0.95 (m, 6H);  $^{13}\text{C}$  NMR (126 MHz,  $\text{CDCl}_3$ )  $\delta$  151.7, 147.9, 132.9, 129.0, 126.3, 123.4, 123.0, 80.7, 77.8, 74.7, 56.7, 47.7, 46.4, 45.1, 42.4, 39.9, 39.0, 38.5, 35.3, 33.0, 31.7, 29.9, 29.4, 28.1, 21.0, 17.4, 16.9; HRMS calculated for  $\text{C}_{27}\text{H}_{41}\text{N}_2\text{O}_4\text{S}$  ( $\text{M}^+$ ): 488.2709, found 488.2709.



17

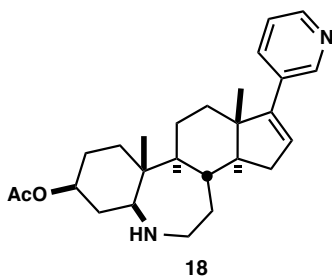
**3 $\beta$ -Acetoxy-5,6-seco-5-keto-17-triflyl- $\Delta$ 16-androstan-6-al (17).** Compound **3** (2.50 g, 5.35 mmol) was dissolved in methylene chloride (220 mL), methanol (25 mL), and pyridine (13 mL; final concentration 0.02 M) and cooled to  $-78\text{ }^\circ\text{C}$ . Ozone was bubbled through a  $0.5\text{ }\mu\text{m}$  aquarium diffuser stone for 4.5 minutes at a flow rate of 6 psi. This exposure level was found to be optimal in sparing the over-reaction of the vinyl triflate. Once ozone addition was done, the mixture was rapidly and vigorously sparged with  $\text{N}_2$ . Dimethylsulfide (2.5 mL, 42.8 mmol) was added at  $-78\text{ }^\circ\text{C}$ , and the mixture stirred for 30 min at this temperature. The mixture was allowed warmed to rt over the course of 1 h. Water was added and the organic layer was separated, washed with brine, and dried over  $\text{NaSO}_4$ . The mixture was concentrated onto silica gel *in vacuo*, careful to keep the

temperature at or below rt to avoid product decomposition, and purified by automatic purification (40 g silica, 10% to 20% to 50% EtOAc/hexanes) to yield 1.39 g of **17** as a clear oil (53%). IR (neat) 1735, 1725, 1703, 1418, 1377  $\text{cm}^{-1}$ ;  $^1\text{H}$  NMR (400 MHz,  $\text{CDCl}_3$ )  $\delta$  9.65 (s, 1H), 5.57 (t,  $J = 1.3$ , Hz, 1H), 5.39 (m, 1H), 3.03 (dd,  $J = 14.4, 4.4$  Hz, 1H), 2.60–2.20 (m, 4H), 2.19–2.05 (m, 2H), 2.04 (s, 3H), 2.02–1.73 (m, 6H), 1.75–1.55 (m, 3H), 1.55–1.39 (m, 1H), 1.08 (s, 3H), 1.02 (s, 3H);  $^{13}\text{C}$  NMR (101 MHz,  $\text{CDCl}_3$ )  $\delta$  215.4, 201.5, 170.1, 158.3, 114.2, 73.1, 52.3, 44.7, 43.3, 43.2, 42.2, 34.0, 32.8, 32.4, 29.5, 25.2, 22.4, 21.2, 17.7, 14.7, one overlapping peak; this product did not ionize by ESI-MS.



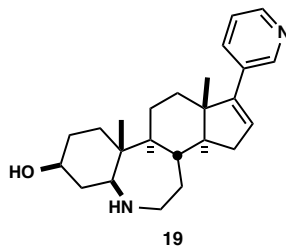
**3 $\beta$ -Acetoxy-5-keto-5,6-seco-17-(3-pyridyl)-androst-16-en-6-al.** Compound **17** (400 mg, 0.81 mmol) was coupled as described for **4**, however the temperature was reduced to 50  $^{\circ}\text{C}$ . Automatic purification (4 g silica, 25% to 60% EtOAc/hexanes) afforded 290 mg of the title compound as a clear oil (85%).  $^1\text{H}$  NMR (400 MHz,  $\text{CDCl}_3$ )  $\delta$  9.61 (s, 1H), 8.52 (s, 1H), 8.40 (d,  $J = 4.9$  Hz, 1H), 7.53–7.44 (m, 1H), 7.16 (dd,  $J = 7.9, 4.8$  Hz, 1H), 5.87 (dd,  $J = 3.0, 1.9$  Hz, 1H), 5.31 (t,  $J = 2.9$  Hz, 1H), 2.98 (dd,  $J = 14.4, 4.4$  Hz, 1H), 2.42 (dd,  $J = 6.1, 1.8$  Hz, 1H), 2.35 (m, 1H), 2.28–2.17 (m, 1H), 2.13 (m, 1H), 2.05–1.99 (m, 2H), 1.97 (s, 3H), 1.95 (m, 4H), 1.85–1.70 (m, 3H), 1.60–1.47 (m, 3H), 1.02 (s, 3H), 0.98 (s, 3H);  $^{13}\text{C}$  NMR (101 MHz,  $\text{CDCl}_3$ )  $\delta$  215.8, 202.1, 170.1, 151.2, 148.1, 147.7, 133.7, 132.0, 128.4, 123.1, 73.2, 55.5, 52.4, 47.3, 44.3, 43.2, 42.3, 35.3, 34.1, 33.0, 32.7, 25.2,

22.9, 21.2, 21.04, 17.7, 16.1; MS calculated for C<sub>26</sub>H<sub>33</sub>NO<sub>4</sub> (M<sup>+</sup>+H): 424.249, found 424.294.

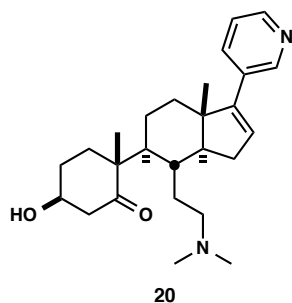


**3β-Acetoxy-6α-aza-6α-homo-17-(3-pyridyl)-androst-16-ene (18).** Compound **17** (290 mg, 0.684 mmol) was dissolved in dry methanol (11.5 mL, 0.05 M) and cooled to 0 °C. Ammonia (0.16 mL of a 7.0 M methanolic solution, 1.09 mmol) was added, followed by triethylamine (0.170 mL, 1.46 mmol). The solution was stirred for 10 min at 0 °C, then sodium cyanoborohydride (107 mg, 1.71 mmol) was added in one portion. The mixture was allowed to slowly rise to rt and was stirred for 30 h, at which point MS indicated completion. The solvent was removed, and 10 mL of aqueous 2.0 N HCl was added. Organic byproducts were extracted away in methylene chloride, then the aqueous phase was basified to pH 13 using 5 mL of aqueous 4.0 N NaOH. The product was extracted with methylene chloride. This organic layer was washed with brine and dried over NaSO<sub>4</sub>. Concentration of this layer yielded 247 mg of a white foam (88%) that was used directly in the next step. <sup>1</sup>H NMR (400 MHz, CDCl<sub>3</sub>) δ 8.56 (s, 1H), 8.42 (d, *J* = 5.7, 1H), 7.64 (d, *J* = 8.1, 1H), 7.25 (dd, *J* = 8.0, 4.8 Hz, 1H), 5.98 (m, 1H), 5.28 (s, 1H), 3.42–3.21 (m, 2H), 2.39–2.22 (m, 1H), 2.00 (m, 5H), 1.93–1.57 (m, 7H), 1.57–1.38 (m, 3H), 1.34 (m, 3H), 1.30–1.17 (m, 2H), 1.14–0.94 (m, 8H); <sup>13</sup>C NMR (101 MHz, CDCl<sub>3</sub>)

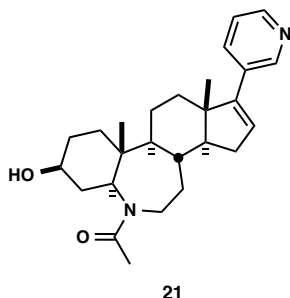
$\delta$  170.5, 151.3, 147.3, 134.1, 132.9, 132.9, 128.8, 123.4, 70.5, 62.5, 57.4, 56.4, 53.6, 46.8  
44.4, 40.3, 39.9, 36.0, 35.1, 32.9, 28.5, 24.7, 21.3, 21.0, 16.5, 13.9, 8.9; MS calculated for  
 $C_{26}H_{37}N_2O_2$  ( $M^+ + H$ ): 409.285, found 409.140.



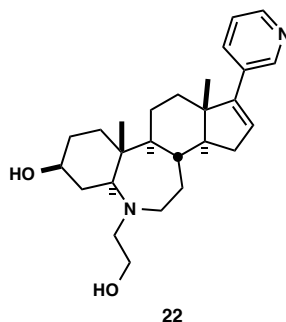
**6a-Aza-6a-homo-17-(3-pyridyl)-androst-16-en-3 $\beta$ -ol (19).** Compound **18** was deacylated as described for **5**. The mixture was purified by flash chromatography (200 mg silica, 5 to 10% MeOH/ $CH_2Cl_2$ ) to isolate 67.1 mg of **19** as a white solid (47%). IR (neat) 3306, 1456, 1411;  $^1H$  NMR (400 MHz,  $CDCl_3$ )  $\delta$  8.69–8.56 (d,  $J = 1.6$  Hz, 1H), 8.46 (dt,  $J = 4.9, 1.6$  Hz, 1H), 7.65 (dt,  $J = 7.8, 1.8$  Hz, 1H), 7.23 (m, 1H), 6.08–5.94 (m, 1H), 3.65–3.57 (m, 1H), 3.23–3.09 (m, 1H), 2.97 (td,  $J = 12.0, 5.8$  Hz, 1H), 2.66 (dd,  $J = 11.9, 4.3$  Hz, 1H), 2.38 (m, 1H), 2.17–2.03 (m, 1H), 2.05–1.90 (m, 3H), 1.90–1.78 (m, 3H), 1.70 (m, 3H), 1.64–1.36 (m, 4H), 1.34–1.17 (m, 2H), 1.05 (s, 3H), 0.96 (ds, 3H);  $^{13}C$  NMR (101 MHz,  $CDCl_3$ )  $\delta$  151.8, 147.8, 147.8, 133.7, 132.9, 128.6, 123.1, 60.5, 58.04, 56.8, 46.9, 45.2, 41.4, 39.2, 35.4, 35.3, 33.3, 32.3, 31.4, 25.8, 22.4, 21.6, 16.5, 14.0; HRMS calculated for  $C_{24}H_{35}N_2O$  ( $M^+ + H$ ): 367.2749, found 367.2740.



**6-(Dimethylamino)-5-keto-5,6-seco-17-(3-pyridyl)-androst-16-en-3 $\beta$ -ol (20).** 3 $\beta$ -Acetoxy-5-keto-5,6-seco-17-(3-pyridyl)-androst-16-en-6-al (495 mg, 1.17 mmol) was dissolved in dry methanol (15 mL, 0.08 M) and cooled to 0 °C. Dimethylamine hydrochloride (124 mg, 1.52 mmol) was added and the mixture stirred at 0 °C for 5 min. Triethylamine (0.26 mL, 1.87 mmol) was added, followed by sodium cyanoborohydride (221 mg, 3.51 mmol). The mixture was allowed to slowly warm to rt and stirred overnight. This crude mixture was diluted to 0.02 M with methanol and potassium carbonate (2.4 g, 17.6 mmol) was added. This mixture was stirred for an additional 16 h, after which the deacylation had completed. The crude mixture was purified by chromatography (4 g silica, 10% MeOH/DCM) to obtain 235 mg of **20** as a pale yellow solid (49%). IR (neat) 3351, 1715, 1674, 1458, 1410; <sup>1</sup>H NMR (400 MHz, CDCl<sub>3</sub>)  $\delta$  8.59 (dd, *J* = 2.3, 1.0 Hz, 1H), 8.46 (ddd, *J* = 5.4, 3.8, 1.6 Hz, 1H), 7.62 (ddt, *J* = 8.3, 4.2, 2.0 Hz, 1H), 7.22 (dddd, *J* = 7.5, 4.8, 2.8, 1.7 Hz, 1H), 5.95 (tt, *J* = 4.9, 2.6 Hz, 1H), 4.06–3.86 (m, 1H), 2.65 (t, *J* = 12.0 Hz, 1H), 2.49–2.16 (m, 9H), 2.16–1.86 (m, 4H), 1.86–1.25 (m, 11H), 1.18–0.91 (m, 6H); <sup>13</sup>C NMR (101 MHz, CDCl<sub>3</sub>)  $\delta$  206.8, 152.0, 148.0, 147.7, 133.8, 132.9, 129.1, 123.1, 82.5, 67.4, 63.7, 57.7, 50.1, 49.4, 46.6, 45.2, 44.9, 42.2, 35.0, 32.1, 28.4, 26.8, 21.1, 19.3, 17.0, 16.1; HRMS calculated for C<sub>26</sub>H<sub>38</sub>N<sub>2</sub>O<sub>2</sub> (M<sup>+</sup>+H): 411.3011, found 411.3006.

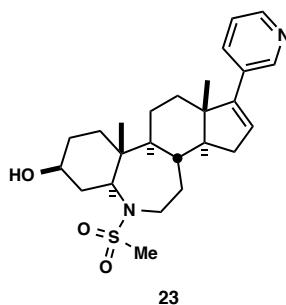


**6a-Acyl-6a-aza-6a-homo-17-(3-pyridyl)-androst-16-en-3 $\beta$ -ol (21).** Compound **18** (30 mg, 0.074 mmol) was dissolved in methylene chloride (0.75 mL, 0.1 M). Triethylamine (15.5  $\mu$ L, 0.111 mmol) was added, followed by acetic anhydride (8.4  $\mu$ L, 0.088 mmol). The mixture was stirred for 2 h, then diluted with water and methylene chloride. The was extracted with additional methylene chloride, washed with brine, and dried over NaSO<sub>4</sub>. The crude material was purified to obtain 15 mg of a white solid. This was deacylated as for **5** to obtain a residue, that was purified by preparative HPLC to yield 1.2 mg of a white solid (4%). IR (neat) 3370, 1696, 1447, 1383 cm<sup>-1</sup>; <sup>1</sup>H NMR (500 MHz, CDCl<sub>3</sub>)  $\delta$  8.63 (s, 1H), 8.49 (s, 1H), 7.74 (d, *J* = 8.3 Hz, 1H), 7.31 (m, 1H), 6.03 (dd, *J* = 3.5, 1.8 Hz, 1H), 3.59–3.47 (m, 1H), 3.37 (m, 1H), 2.31 (m, 1H), 2.13 (s, 3H), 2.07–1.87 (m, 6H), 1.85–1.75 (m, 4H), 1.65–1.58 (m, 3H), 1.52–1.40 (m, 3 H), 1.30 (s, 1 H), 1.24 (s, 3H), 1.04 (s, 3H); <sup>13</sup>C NMR (126 MHz, CDCl<sub>3</sub>)  $\delta$  169.8, 151.0, 146.6, 146.5, 134.8, 131.4, 129.5, 123.6, 70.0, 69.6, 63.7, 57.9, 57.8, 46.8, 41.0, 38.1, 36.3, 35.4, 34.2, 32.6, 31.1, 30.8, 24.1, 23.9, 16.5, 16.0; HRMS calculated for C<sub>26</sub>H<sub>36</sub>N<sub>2</sub>O<sub>2</sub> (M<sup>+</sup>+H): 409.2875, found 409.2827.

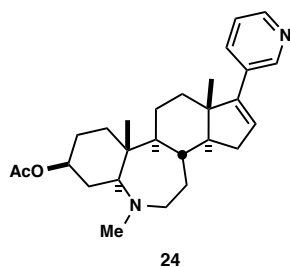


**6a-Aza-6a-homo-6a-hydroxyethyl-17-(3-pyridyl)-androst-16-en-3 $\beta$ -ol (22).**

Compound **18** (50 mg, 0.122 mmol) in a microwave vial was dissolved in acetonitrile (0.5 mL, 0.25 M). Potassium carbonate (132 mg, 0.976 mmol) was added, followed by 2-bromoethanol (10.3  $\mu$ L, 0.146 mmol). The vial was sealed, heated to 60  $^{\circ}$ C, and stirred overnight. This solution was concentrated and redissolved in methanol for the subsequent deacylation step (using the potassium carbonate present in the mixture). When this reaction was complete, the solvent was removed and the mixture suspended in chloroform and water, and extracted with chloroform. The organic layers were washed with brine, dried over NaSO<sub>4</sub>, and concentrated for purification by preparative HPLC to yield 7.8 mg as a white solid (16% over two steps). IR (neat) 3315, 1450, 1407z cm<sup>-1</sup>; <sup>1</sup>H NMR (400 MHz, CDCl<sub>3</sub>)  $\delta$  8.52 (s, 1H), 8.47–8.29 (m, 1H), 7.83 (d,  $J$  = 7.9 Hz, 1H), 7.46–7.30 (m, 1H), 6.07 (dd,  $J$  = 3.5, 1.8 Hz, 1H), 3.50 (m, 1H), 2.99 (m, 1H), 2.82 (td,  $J$  = 12.2, 5.4 Hz, 1H), 2.75–2.62 (m, 1H), 2.40 (m, 1H), 2.25–2.05 (m, 1H), 2.05–1.77 (m, 6H), 1.77–1.51 (m, 5H), 1.51–1.34 (m, 3H), 1.34–1.15 (m, 2H), 1.08 (s, 3H), 1.04 (s, 1H), 0.96 (s, 3H), 0.94 (s, 1H); <sup>13</sup>C NMR (101 MHz, CDCl<sub>3</sub>)  $\delta$  155.5, 150.5, 138.5, 137.5, 132.9, 127.5, 127.5, 72.8, 62.2, 61.3, 60.7, 50.6, 48.6, 44.4, 44.0, 43.0, 40.4, 39.1, 36.8, 36.3, 34.1, 33.4, 30.1, 26.7, 19.4, 16.5; HRMS calculated for C<sub>26</sub>H<sub>39</sub>N<sub>2</sub>O<sub>2</sub> (M<sup>+</sup>+H): 411.3011, found 411.3010.

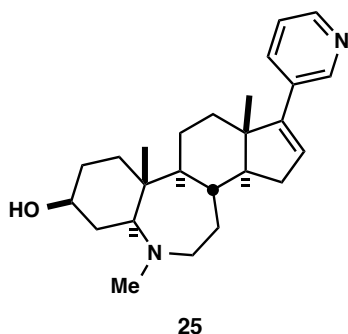


**6a-Aza-6a-homo-6a-mesyl-17-(3-pyridyl)-androst-16-en-3 $\beta$ -ol (23).** Compound **18** (50 mg, 0.122 mmol) in a microwave vial was dissolved in methylene chloride (0.5 mL, 0.25 M). Mesyl chloride (9.5  $\mu$ L, 0.122 mmol) was added, followed by triethylamine (20  $\mu$ L, 0.146 mmol). The vial was sealed and stirred overnight at rt. This solution was concentrated and redissolved in methanol (4.0 mL, 0.03 M) and potassium carbonate (136 mg, 0.976 mmol) was added for the subsequent deprotection step. When this reaction was complete, the mixture was concentrated, redissolved in chloroform and water, and extracted with chloroform. The organic layer was washed with brine, dried over NaSO<sub>4</sub>, and concentrated for purification by preparative HPLC to yield 8.4 mg of **18** as a pale oil (16% over two steps). IR (neat) 3314, 1449, 1409, 1112 cm<sup>-1</sup>; <sup>1</sup>H NMR (400 MHz, CDCl<sub>3</sub>)  $\delta$  8.53 (s, 1H), 8.47–8.36 (m, 1H), 7.83 (dt,  $J$  = 8.0, 1.4 Hz, 1H), 7.47–7.31 (m, 1H), 6.08 (dd,  $J$  = 3.4, 1.8 Hz, 1H), 3.64–3.51 (m, 1H), 3.45–3.38 (m, 1H), 2.95 (s, 3H), 2.48–2.33 (m, 1H), 2.34–2.09 (m, 3H), 2.08–1.93 (m, 4H), 1.93–1.32 (m, 10H), 1.15 (s, 3H), 1.09 (s, 3H), 1.05–0.95 (m, 1H); <sup>13</sup>C NMR (101 MHz, CDCl<sub>3</sub>)  $\delta$  162.6, 155.3, 150.5, 138.5, 133.5, 133.0, 127.5, 73.3, 67.0, 61.5, 60.7, 58.2, 50.5, 44.6, 43.4, 40.9, 39.9, 39.2, 37.9, 37.7, 36.5, 34.3, 27.3, 19.4, 18.9; HRMS calculated for C<sub>25</sub>H<sub>36</sub>N<sub>2</sub>O<sub>3</sub>S (M<sup>+</sup>): 444.2447, found 444.2447.

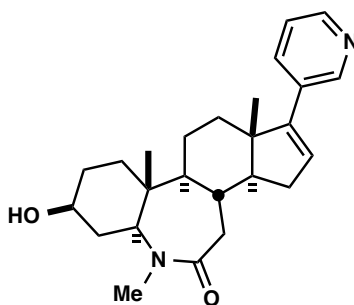


**3β-Acetoxy-6α-aza-6α-homo-6α-methyl-17-(3-pyridyl)-androst-16-ene (24).**

Compound **18** (200 mg, 0.489 mmol) in a microwave vial was dissolved in acetonitrile (2 mL, 0.25 M). Triethylamine (70  $\mu$ L, 0.489 mmol) was added, followed by methyl iodide (37  $\mu$ L, 0.587 mmol). The vial was capped, and heated to 80  $^{\circ}$ C for 2 h. The crude material was diluted with methylene chloride, adsorbed directly onto silica gel, and purified by column (1 g silica, 5% MeOH/DCM to 10% MeOH/DCM) to obtain 185 mg of a white powder (89%).  $^1\text{H}$  NMR (400 MHz,  $\text{CDCl}_3$ )  $\delta$  8.59 (d,  $J = 2.8$  Hz, 1H), 8.53–8.37 (m, 1H), 7.63 (m, 1H), 7.27–7.15 (m, 1H), 5.96 (dd,  $J = 3.4, 1.8$  Hz, 1H), 3.14–2.99 (m, 1H), 2.84–2.73 (m, 1H), 2.70–2.66 (m, 1H), 2.49–2.24 (m, 3H), 2.12–1.86 (m, 5H), 1.86–1.74 (m, 3H), 1.74–1.60 (m, 3H), 1.58–1.47 (m, 4H), 1.20 (d,  $J = 13.1$  Hz, 3H), 1.02 (s, 3H), 0.88 (s, 3H);  $^{13}\text{C}$  NMR (101 MHz,  $\text{CDCl}_3$ )  $\delta$  167.3, 151.9, 147.9, 141.1, 133.6, 133.0, 128.6, 123.0, 75.4, 59.7, 58.2, 56.8, 47.6, 46.9, 45.5, 41.8, 40.1, 39.2, 35.5, 35.0, 33.7, 33.4, 32.3, 21.8, 16.5, 14.0.



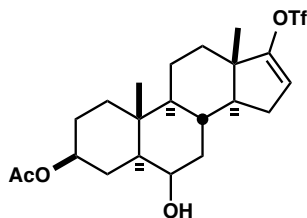
**6a-Aza-6a-homo-6a-methyl-17-(3-pyridyl)-androst-16-en-3 $\beta$ -ol (25).** Compound **18** (50 mg, 0.076 mmol) was alkylated with methyl iodide and deacylated as for **22**. This mixture was purified by silica flash chromatography (1 to 5% MeOH/CH<sub>2</sub>Cl<sub>2</sub>) to obtain 3.5 mg (12%) of **25** as a white solid. IR (neat) 3315, 1550, 1408 cm<sup>-1</sup>; <sup>1</sup>H NMR (500 MHz, MeOD)  $\delta$  8.46 (s, 1H), 8.32 (s, 1H), 7.82–7.72 (m, 1H), 7.30 (dd, *J* = 8.2, 4.7 Hz, 1H), 6.08–5.94 (m, 1H), 3.41–3.31 (m, 1H), 2.99–2.89 (m, 1H), 2.64–2.55 (m, 1H), 2.32 (m, 3H), 1.96–1.77 (m, 5H), 1.68 (m, 2H), 1.63–1.42 (m, 5H), 1.40–1.31 (m, 2H), 1.25–1.18 (m, 4H), 1.04–0.95 (m, 3H), 0.92–0.83 (m, 3H); <sup>13</sup>C NMR (126 MHz, MeOD)  $\delta$  153.5, 148.3, 136.4, 134.2, 133.5, 130.9, 130.3, 71.9, 63.1, 60.2, 58.9, 57.4, 43.3, 41.1, 38.6, 37.2, 37.1, 36.9, 34.6, 34.2, 32.4, 31.2, 24.8, 17.3, 15.4; HRMS calculated for C<sub>25</sub>H<sub>37</sub>N<sub>2</sub>O (M<sup>+</sup>+H): 381.2906, found 381.2910.



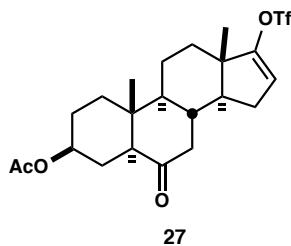
26

**6a-Aza-6a-homo-6a-methyl-7-keto-17-(3-pyridyl)-androst-16-en-3β-ol (26).**

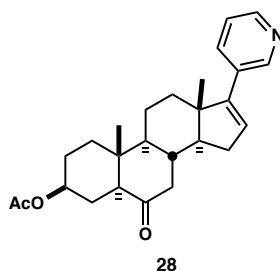
Compound **24** (185 mg, 0.437 mmol) was dissolved in an aqueous solution of 0.1 M Hg(OAc)<sub>2</sub> and 0.2 M ethylenediaminetetraacetic acid (22 mL, 2.19 mmol Hg(OAc)<sub>2</sub>) and brought to pH 8 with NaOH<sub>aq</sub>. This solution was brought to reflux and stirred for 22 h. The solution was cooled and diluted with methylene chloride, which turned this layer bright yellow. The organic layer was separated, combined with additional methylene chloride extractions, washed with brine, and dried over NaSO<sub>4</sub>. Silica flash chromatography (500 mg silica, 1 to 5% MeOH/CH<sub>2</sub>Cl<sub>2</sub>) was used to isolate 47.7 mg of a yellow solid. This material was carried directly into deacylation, as described for **5**. This material was purified by preparative HPLC to obtain 10.5 mg of a white solid (6% over two steps). IR (neat) 3315, 1668, 1449, 1411 cm<sup>-1</sup>; <sup>1</sup>H NMR (500 MHz, Methanol-*d*<sub>4</sub>) δ 8.43 (s, 1H), 8.30 (d, *J* = 5.1 Hz, 1H), 7.74 (m, 1H), 7.29 (dd, *J* = 8.0, 4.8 Hz, 1H), 5.99 (m, 1H), 3.21 (s, 3H), 3.13–2.98 (m, 1H), 2.33 (m, 1H), 2.07 (m, 1H), 1.94 (m, 2H), 1.84 (m, 2H), 1.77–1.65 (m, 3H), 1.65–1.30 (m, 5H), 1.30–1.06 (m, 4H), 1.10–0.82 (m, 6H); <sup>13</sup>C NMR (126 MHz, MeOD) δ 176.4, 152.8, 148.3, 147.9, 136.0, 133.1, 130.1, 125.0, 62.8, 58.5, 57.7, 48.0, 45.3, 41.2, 40.3, 36.8, 36.3, 33.9, 30.0, 29.6, 25.8, 23.5, 22.1, 16.8, 13.7; HRMS calculated for C<sub>25</sub>H<sub>34</sub>N<sub>2</sub>O<sub>2</sub> (M<sup>+</sup>+H): 394.2620, found 394.2604.



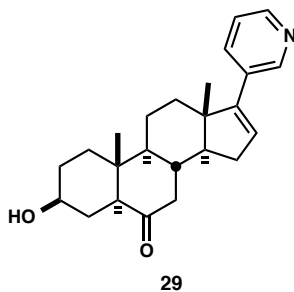
**3 $\beta$ -Acetoxy-17-triflyl-androst-16-en-6-ol.** Compound **3** (2.1 g, 4.54 mmol) was added to a dry flask, placed under inert atmosphere, and dissolved in dry tetrahydrofuran (23 mL, 0.2 M). This solution was cooled to -10 °C and a fresh bottle of borane (1.0 M in THF, 4.77 mmol) was added evenly over the course of 1 h at -10 °C. The solution was allowed to slowly rise to rt and stir over the course of 8 h. The mixture was brought to 0 °C, and water (23 mL) was very slowly added until the excess borane was quenched. Sodium perborate (768 mg, 4.99 mmol) was added in one portion, and the mixture allowed to warm to rt and stir overnight. Salt was added to facilitate separation of the phases, and the mixture was extracted twice more with tetrahydrofuran. The solution was rigorously dried with MgSO<sub>4</sub> and purified using an automatic purification system (40 g silica, 10% to 35% EtOAc/hexanes) to obtain 1.59 g of the title compound as a clear oil (76%). <sup>1</sup>H NMR (400 MHz, CDCl<sub>3</sub>)  $\delta$  5.57 (dd,  $J$  = 3.4, 1.7 Hz, 1H), 4.68 (tt,  $J$  = 11.4, 4.9 Hz, 1H), 3.44 (td,  $J$  = 10.7, 4.5 Hz, 1H), 2.33–2.13 (m, 2H), 2.11–1.96 (m, 3H), 1.87 (s, 1H), 1.81–1.57 (m, 6H), 1.57–1.39 (m, 3H), 1.39–1.17 (m, 4H), 1.17–1.05 (m, 2H), 0.96 (s, 3H), 0.87 (s, 3H); <sup>13</sup>C NMR (101 MHz, CDCl<sub>3</sub>)  $\delta$  170.6, 159.1, 114.4, 73.3, 69.1, 54.1, 53.9, 51.9, 44.9, 40.4, 36.7, 36.5, 32.5, 32.3, 28.5, 28.3, 27.1, 21.4, 20.4, 15.3, 13.3 (one carbon peak likely overlapping); this compound did not ionized by ESI-MS.



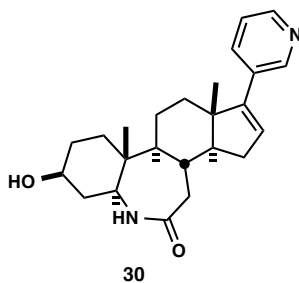
**3β-Acetoxy-17-triflyl-androst-16-en-6-one (27).** 3β-Acetoxy-17-triflyl-androst-16-en-6-ol (0.935 g, 1.95 mmol) was dissolved in dry dichloromethane (65 mL, 0.03 M). Magnesium sulfate (589 mg, 4.88 mmol) was added, followed by *N*-methyl morpholine (503 mg, 4.29 mmol). The solution was cooled to 0 °C, and tetrapropylammonium perruthenate (68.4 mg, 0.195 mmol) was added. The reaction was allowed to slowly warm to rt over the course of 1 h, then the mixture was adsorbed directly onto silica gel and purified via automated purification system (24 g, 10% to 25% EtOAc/hexanes) to obtain 729 mg of **27** as a white solid (78%). IR (neat) 1731, 1715, 1420, 1377 cm<sup>-1</sup>; <sup>1</sup>H NMR (400 MHz, CDCl<sub>3</sub>) δ 5.59 (dd, *J* = 3.4, 1.7 Hz, 1H), 4.67 (tt, *J* = 11.6, 4.8 Hz, 1H), 2.32 (m, 2H), 2.20 (m, 1H), 2.06 (s, 1H), 2.04 (s, 3H), 1.99–1.92 (m, 2H), 1.92–1.71 (m, 5H), 1.71–1.12 (m, 7H), 0.97 (s, 3H), 0.81 (s, 3H); <sup>13</sup>C NMR (101 MHz, CDCl<sub>3</sub>) δ 209.1, 170.6, 158.7, 114.4, 72.6, 56.8, 54.2, 54.1, 45.3, 45.2, 41.0, 36.1, 35.8, 32.3, 28.4, 26.8, 26.1, 21.3, 20.8, 15.2, 13.1; this compound did not ionize by ESI-MS.



**3 $\beta$ -Acetoxy-17-triflyl-androst-16-en-6-one (28).** Compound **27** (403 mg, 0.843 mmol) was coupled as described for **4**. This was purified by automatic purification systems (4g silica, 20% to 50% EtOAc/hexanes) to obtain 263 mg of **27** as a white powder (77%). IR (neat) 1730, 1710, 1444, 1371  $\text{cm}^{-1}$ ;  $^1\text{H}$  NMR (400 MHz,  $\text{CDCl}_3$ )  $\delta$  8.61 (dd,  $J = 2.4, 0.9$  Hz, 1H), 8.47 (dd,  $J = 4.8, 1.7$  Hz, 1H), 7.64 (ddd,  $J = 7.9, 2.3, 1.7$  Hz, 1H), 7.23 (ddd,  $J = 7.9, 4.8, 0.9$  Hz, 1H), 5.98 (dd,  $J = 3.3, 1.8$  Hz, 1H), 4.68 (m, 1H), 2.49–2.35 (m, 1H), 2.31 (dd,  $J = 12.6, 3.0$  Hz, 1H), 2.25–2.15 (m, 1H), 2.15–2.05 (m, 4H), 2.03 (s, 3H), 1.99–1.91 (m, 1H), 1.81 (m, 4H), 1.68–1.46 (m, 4H), 1.46–1.13 (m, 2H), 1.01 (s, 3H), 0.83 (s, 3H);  $^{13}\text{C}$  NMR (101 MHz,  $\text{CDCl}_3$ )  $\delta$  209.8, 170.6, 151.4, 148.0, 147.8, 133.8, 132.6, 128.9, 123.1, 72.7, 57.4, 56.7, 54.0, 47.8, 46.4, 41.0, 36.4, 36.2, 34.9, 31.5, 26.8, 26.1, 21.3, 16.6, 13.1; MS calculated for  $\text{C}_{26}\text{H}_{33}\text{NO}_3$  ( $\text{M}^+\text{+H}$ ): 408.254, found 408.052.

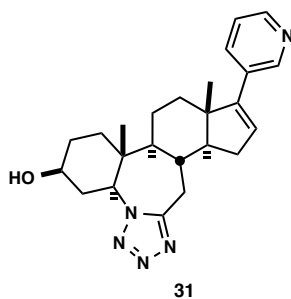


**3 $\beta$ -Hydroxy-17-(3-pyridyl)-androst-16-en-6-one (29).** Compound **28** (30 mg, 0.074 mmol) was deacylated as for **5**. 25 mg of a white solid was isolated (92%), then further subjected to preparative HPLC purification to obtain 10.5 mg of a white solid. IR (neat) 3335, 1705, 1415, 1385 cm<sup>-1</sup>; <sup>1</sup>H NMR (500 MHz, CDCl<sub>3</sub>)  $\delta$  8.62 (d, *J* = 2.3 Hz, 1H), 8.48 (dd, *J* = 4.9, 1.6 Hz, 1H), 7.65 (dt, *J* = 7.9, 2.0 Hz, 1H), 7.24 (ddd, *J* = 8.0, 4.9, 0.9 Hz, 1H), 5.99 (dd, *J* = 3.3, 1.8 Hz, 1H), 3.60 (tt, *J* = 11.2, 4.6 Hz, 1H), 2.48–2.32 (m, 1H), 2.32–2.18 (m, 2H), 2.09 (m, 3H), 1.94 (m, 1H), 1.92–1.85 (m, 1H), 1.85–1.76 (m, 3H), 1.61–1.48 (m, 2H), 1.48–1.36 (m, 2H), 1.29 (m, 1H), 1.02 (s, 3H), 0.83 (s, 3H); <sup>13</sup>C NMR (126 MHz, CDCl<sub>3</sub>)  $\delta$  210.4, 151.5, 148.1, 147.9, 133.7, 132.6, 128.9, 123.1, 70.6, 57.5, 57.0, 54.1, 47.8, 46.4, 41.1, 36.5, 36.4, 34.9, 31.5, 30.7, 30.1, 21.5, 16.6, 13.2; HRMS calculated for C<sub>24</sub>H<sub>32</sub>NO<sub>2</sub> (M<sup>+</sup>+H): 366.2433, found 366.2454.



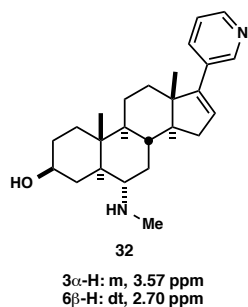
**6a-Aza-6a-homo-7-keto-17-(3-pyridyl)-androst-16-en-3 $\beta$ -ol (30).** CAUTION! This reaction generates hydrazoic acid, a known explosion hazard. Appropriate safety precautions should be observed. Compound **27** (51 mg, 0.125 mmol) was dissolved in acetic acid (glacial, 2.1 mL, 0.06 M). Sodium azide (13.4 mg, 0.26 mmol) was added, followed by methanesulfonic acid (81  $\mu$ L, 0.125 mmol). The mixture was stirred for 5 h,

then quenched with aqueous saturated sodium bicarbonate until the pH was neutral. The mixture was extracted with chloroform, washed with brine, and dried over NaSO<sub>4</sub>. The crude material (52 mg) was isolated and used without further purification. 21 mg was deacylated as described for **5** and purified by preparative HPLC to obtain 7.7 mg of a pale yellow solid (41%). IR (neat) 3286, 1648, 1444, 1388 cm<sup>-1</sup>; <sup>1</sup>H NMR (400 MHz, CDCl<sub>3</sub>) δ 8.62 (dd, *J* = 2.3, 0.9 Hz, 1H), 8.49 (dd, *J* = 4.8, 1.6 Hz, 1H), 7.65 (dt, *J* = 8.0, 1.9 Hz, 1H), 7.25 (ddd, *J* = 7.9, 4.8, 0.9 Hz, 1H), 6.00 (dd, *J* = 3.4, 1.8 Hz, 1H), 5.39 (d, *J* = 5.5 Hz, 1H), 3.65 (tt, *J* = 11.2, 4.3 Hz, 1H), 3.52–3.32 (m, 1H), 2.46–2.31 (m, 3H), 2.23 (m, 1H), 2.15–1.92 (m, 5H), 1.90 (m, 2H), 1.71 (m, 1H), 1.64–1.25 (m, 4H), 1.21–1.08 (m, 2H), 1.05 (s, 3H), 0.94 (s, 3H); <sup>13</sup>C NMR (101 MHz, CDCl<sub>3</sub>) δ 175.8, 151.5, 148.0, 147.8, 133.7, 132.6, 128.5, 123.1, 68.7, 59.0, 57.1, 56.7, 47.1, 40.6, 38.9, 38.7, 35.6, 35.4, 33.1, 32.9, 30.9, 22.8, 16.4, 12.4; HRMS calculated for C<sub>24</sub>H<sub>32</sub>N<sub>2</sub>O<sub>2</sub> (M<sup>+</sup>+H): 381.2542, found 381.2548.

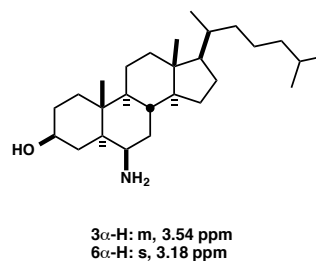
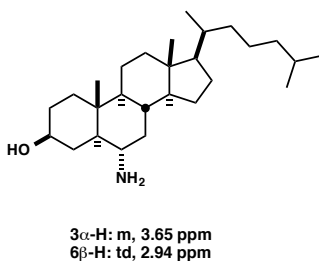


**6a-Aza-6a-homo-6a,6-tetrazolo-17-(3-pyridyl)-androst-16-en-3β-ol (31).** Compound **27** (51 mg, 0.125 mmol) was dissolved in hexafluoroisopropanol (0.3 mL, 0.4 M). Azidotrimethylsilane (41 μL, 0.250 mmol) was added, followed by triflic acid (14 μL, 0.154 mmol) and the mixture was stirred at rt overnight. The solution was neutralized

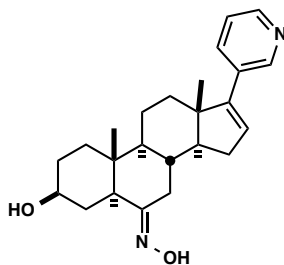
with sodium bicarbonate and extracted with chloroform. The organic layers were washed with brine, dried over NaSO<sub>4</sub>, and purified by silica flash chromatography (200 mg silica, 1 to 5% MeOH/CH<sub>2</sub>Cl<sub>2</sub>) to obtain 25 mg (45%) as a pale yellow solid. This was deacylated as for **5** and purified by preparative TLC (75% EtOAc/hexanes eluent) to obtain 11 mg of a white solid (49%). IR (neat) 3264, 1586, 1566, 1536, 1433, 1390 cm<sup>-1</sup>; <sup>1</sup>H NMR (400 MHz, CDCl<sub>3</sub>) δ 8.21 (dd, *J* = 2.3, 0.9 Hz, 1H), 8.09 (dd, *J* = 4.9, 1.6 Hz, 1H), 7.52–7.40 (m, 1H), 7.04 (ddd, *J* = 8.0, 4.9, 0.9 Hz, 1H), 5.78 (dd, *J* = 3.4, 1.7 Hz, 1H), 4.16 (dd, *J* = 10.8, 6.1 Hz, 1H), 3.46–3.27 (m, 1H), 3.10 (m, 1H), 2.48–2.31 (m, 1H), 2.30–2.13 (m, 3H), 1.97 (m, 1H), 1.87–1.67 (m, 3H), 1.61 (m, 2H), 1.45 (m, 1H), 1.35–0.90 (m, 5H), 0.71 (s, 3H), 0.31 (s, 3H); <sup>13</sup>C NMR (101 MHz, CDCl<sub>3</sub>) δ 159.3, 154.9, 151.0, 150.7, 138.6, 136.9, 132.7, 127.6, 71.9, 67.8, 62.2, 60.1, 50.7, 42.7, 39.7, 40.0, 39.4, 38.1, 36.7, 34.3, 31.0, 26.9, 19.9, 15.2; HRMS calculated for C<sub>24</sub>H<sub>36</sub>N<sub>5</sub>O (M<sup>+</sup>+H): 406.2607, found 406.2578.



assigned relative to: Beuchet *et al. Bioorg. Med. Chem. Lett.* **1998**, *8*, 3627.

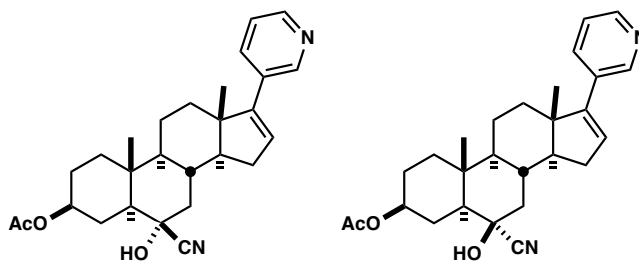


**6 $\alpha$ -Methylamine-17-(3-pyridyl)-androst-16-en-3 $\beta$ -ol (32).** Compound **27** (50 mg, 0.123 mmol) was dissolved in ethanol (1.2 mL, 0.1 M) and cooled to 0 °C. Methylamine (14.4  $\mu$ L of a 33% w/v solution in ethanol, 0.153 mmol) was added and stirred for 5 min. Sodium cyanoborohydride (12 mg, 0.185 mmol) was added in one portion, and the reaction allowed to stir for 24 h, warming to rt. This was diluted with methanol (4.0 mL, to 0.03 M), and potassium carbonate (136 mg, 0.984 mmol) was added to deacylate the C3-hydroxyl. After stirring an additional 20 h, the solution was processed as for **6**. Preparative HPLC purification furnished 3.5 mg as a white solid (7%). IR (neat) 3319, 1589, 1418, 1380  $\text{cm}^{-1}$ ;  $^1\text{H}$  NMR (500 MHz,  $\text{CDCl}_3$ )  $\delta$  8.54–8.49 (m, 1H), 8.48–8.44 (m, 1H), 7.57 (ddt,  $J = 22.1, 7.9, 2.0$  Hz, 1H), 7.13 (ddd,  $J = 8.0, 4.9, 0.9$  Hz, 1H), 5.88 (dd,  $J = 3.3, 1.8$  Hz, 1H), 3.57 (s, 1H), 2.78–2.61 (dt,  $J = 14.0, 5.5$  Hz, 1H), 2.19–2.13 (m, 1H), 2.11–1.74 (m, 7H), 1.74–1.45 (m, 6H), 1.45–1.22 (m, 5H), 1.21–1.01 (m, 2H), 0.99–0.90 (m, 3H), 0.71 (s, 3H);  $^{13}\text{C}$  NMR (126 MHz,  $\text{CDCl}_3$ )  $\delta$  151.6, 149.9, 149.2, 136.6, 133.7, 129.0, 123.0, 71.0, 70.0, 62.0, 59.5, 57.0, 54.5, 47.7, 46.7, 45.0, 43.4, 42.7, 31.3, 28.9, 27.3, 20.9, 16.9, 16.1, 15.2; HRMS calculated for  $\text{C}_{25}\text{H}_{36}\text{N}_2\text{O}$  ( $\text{M}^+\text{+H}$ ): 381.2906, found 381.2867.



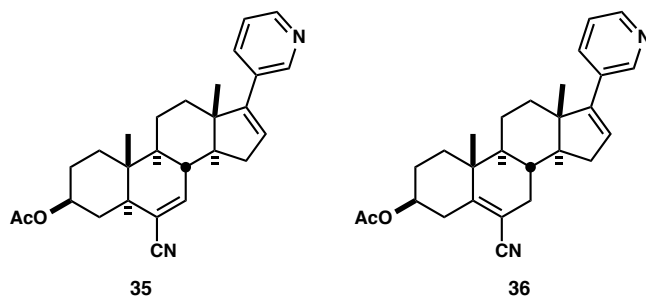
33

**6-Oxime-17-(3-pyridyl)-androst-16-en-3 $\beta$ -ol (33).** Compound **28** (50 mg, 0.114 mmol) was added to a flask along with sodium acetate (66 mg, 0.800 mmol) and hydroxylamine hydrochloride (56 mg, 0.800 mmol). Ethanol (3.8 mL, 0.03 M) was added, followed by two drops of water. The solution was stirred at rt overnight, then concentrated under a stream of N<sub>2</sub>. The mixture was dissolved in chloroform, washed with water and brine, and dried over NaSO<sub>4</sub> to obtain 43 mg of a white solid (84%). This was further purified by preparative HPLC to obtain 7.8 mg of a white solid. IR (neat) 3270, 1730.2, 1651, 1441, 1376 cm<sup>-1</sup>; <sup>1</sup>H NMR (400 MHz, CDCl<sub>3</sub>)  $\delta$  8.59 (d,  $J$  = 2.1 Hz, 1H), 8.54–8.38 (m, 1H), 7.88 (dt,  $J$  = 8.0, 1.9 Hz, 1H), 7.51–7.35 (m, 1H), 6.14 (dd,  $J$  = 3.4, 1.8 Hz, 1H), 3.65–3.54 (m, 1H), 2.40 (m, 1H), 2.23 (m, 1H), 2.18–2.05 (m, 2H), 2.00 (dq,  $J$  = 13.3, 2.5 Hz, 1H), 1.96–1.75 (m, 5H), 1.54 (s, 3H), 1.51–1.32 (m, 3H), 1.32–1.15 (m, 2H), 1.11 (s, 3H), 0.88 (s, 3H). <sup>13</sup>C NMR (101 MHz, CDCl<sub>3</sub>)  $\delta$  162.9, 155.1, 150.4, 138.8, 137.5, 133.6, 127.6, 100.0, 74.4, 61.4, 58.5, 53.6, 42.7, 39.9, 38.9, 38.2, 35.3, 34.9, 34.2, 33.1, 32.0, 25.2, 20.0, 15.9; HRMS calculated for C<sub>24</sub>H<sub>32</sub>N<sub>2</sub>O<sub>2</sub> (M<sup>+</sup>+H): 381.2542, found 381.2522.



34

**3 $\beta$ -Acetoxy-6-cyano-6-hydroxy-17-(3-pyridyl)-androst-16-ene (mixture of C6 isomers) (34).** Compound **27** (220 mg, 0.540 mmol) was added to a microwave vial and dissolved in ethanol (1.5 mL, 0.5 M). To this was added potassium cyanide (620 mg, 9.52 mmol) and acetic acid (0.674 mL, 13.3 mmol) and the vial was quickly capped. The vial was heated to 90 °C for 20 min in the microwave reactor. The solid material was removed by filtration, and the filtrate adsorbed directly onto silica gel as an acidic solution. This was purified by automatic purification system (4 g, 1% MeOH/DCM) to obtain 210 mg of a white solid (66%). IR (neat): 3175, 2211, 1727  $\text{cm}^{-1}$ ;  $^1\text{H}$  NMR (400 MHz,  $\text{CDCl}_3$ )  $\delta$  8.61 (dd,  $J = 2.3, 0.9$  Hz, 1H), 8.48 (dd,  $J = 4.9, 1.6$  Hz, 1H), 7.69 (dt,  $J = 7.9, 1.9$  Hz, 1H), 7.28 (dd,  $J = 4.8, 0.9$  Hz, 1H), 6.01 (dd,  $J = 3.3, 1.8$  Hz, 1H), 4.74 (tt,  $J = 11.1, 5.0$  Hz, 1H), 2.41 (m, 2H), 2.27 (m, 1H), 2.17 (m, 1H), 2.07 (s, 3H), 2.04–1.85 (m, 2H), 1.85–1.62 (m, 4H), 1.62–1.35 (m, 5H), 1.16 (s, 3H), 1.06 (s, 3H), 0.91 (s, 1H);  $^{13}\text{C}$  NMR (101 MHz,  $\text{CDCl}_3$ )  $\delta$  170.7, 151.3, 147.3, 134.2, 133.0, 129.1, 123.4, 121.8, 72.8, 68.7, 56.3, 53.7, 52.5, 47.5, 45.0, 38.1, 36.6, 35.0, 31.67, 31.62, 26.88, 26.84, 21.4, 20.8, 16.8, 14.2; MS calculated for ( $\text{M}^+\text{+H}$ ): 435.265, found 435.212.



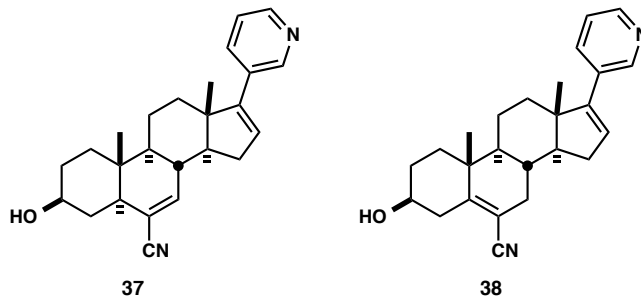
**3β-Acetoxy-6-cyano-17-(3-pyridyl)-androst-6,16-diene (35, minor product) and 3β-acetoxy-6-cyano-17-(3-pyridyl)-androst-5,16-diene (36, major product).** The mixture of compounds **34** (210 mg, 0.484 mmol) was added to a microwave vial and dissolved in pyridine (0.48 mL, 1.0 M). Fresh phosphorus oxychloride (90 μL, 0.967 mmol) was added and was heated to 115 °C for 1 h. The solution was cooled, and quenched with cold aqueous 1.0 N HCl (2.5 mL). This was basified with 3.5 mL of aqueous saturated sodium bicarbonate and extracted with chloroform. The pooled organic layers were washed with brine and dried over NaSO<sub>4</sub>, then purified by automatic purification system (4g silica, 0% to 2% MeOH/DCM) to obtain 113 mg of a mixture of **35** and **36** as a pale yellow foam (56%). The mixture was determined to be ca. 1:5 (**35:36**) by <sup>1</sup>H-NMR analysis.

For the mixture: IR (neat) 2212, 1733, 1439, 1371 cm<sup>-1</sup>; <sup>1</sup>H NMR (400 MHz, CDCl<sub>3</sub>) δ 8.54 (s, 1H), 8.41 (s, 1H), 7.57 (d, *J* = 7.9 Hz, 1H), 7.17 (dd, *J* = 7.9, 4.5 Hz, 1H), 6.05–5.84 (m, 1H), 4.71, 4.61 (tt, *J* = 11.8, 4.6 Hz, 1H), 2.45–2.18 (m, 3H), 2.18–2.04 (m, 2H), 2.03–1.96 (m, 3H), 1.96–1.83 (m, 2H), 1.83–1.69 (m, 2H), 1.69–1.29 (m, 7H), 1.27–1.14 (m, 1H), 1.08 (s, 3H), 1.05–0.85 (m, 3H), 0.79 (s, 1H); <sup>13</sup>C NMR (101 MHz, CDCl<sub>3</sub>) δ 170.1, 157.7, 151.3, 148.2, 147.9, 147.3, 133.8, 129.0, 123.2, 118.6, 107.3, 72.0, 56.7,

49.0, 47.2, 38.4, 36.2, 36.0, 34.9, 33.5, 31.6, 29.7, 27.2, 21.3, 20.6, 19.6, 16.5; MS

calculated for  $C_{27}H_{32}N_2O_2$  ( $M^+ + H$ ): 416.254, found 416.249.

Diagnostic  $^1H$ -NMR peaks for minor isomer **35**: 6.49 (s, 1H), 4.85 (td,  $J = 11.1$  Hz, 1 H).



**6-Cyano-17-(3-pyridyl)-androst-6,16-dien-3β-ol (37) and 6-Cyano-17-(3-pyridyl)-**

**androst-5,16-dien-3β-ol (38).** The mixture of isomers (20 mg; 1:5 **35** to **36**) was

deacylated as described for **5**. The resulting mixture (12 mg, 67%) was purified by

preparative HPLC to obtain 1.2 mg of **37** and 1.5 mg of **38**, both as white solids. Data for

**37**: IR (neat) 3322, 2210, 1465, 1445, 1420, 1378  $cm^{-1}$ ;  $^1H$  NMR (500 MHz,  $CDCl_3$ )  $\delta$

8.63 (s, 1H), 8.50 (s, 1H), 7.72 (dt,  $J = 8.1, 1.9$  Hz, 1H), 7.32 (d,  $J = 6.6$  Hz, 1H), 6.56 (t,

$J = 2.7$  Hz, 1H, the diagnostic peak of 7-H), 6.12–5.94 (m, 1H), 3.70 (tt,  $J = 10.6, 4.9$  Hz,

1H), 2.39 (m, 2H), 2.30–2.15 (m, 2H), 2.15–2.00 (m, 2H), 1.91–1.76 (m, 2H), 1.69 (m,

2H), 1.59 (m, 1H), 1.53–1.36 (m, 2H), 1.28–1.18 (m, 1H), 1.18–1.09 (m, 1H), 1.05 (s,

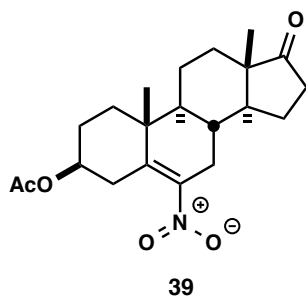
3H), 0.86 (s, 3H);  $^{13}C$  NMR (126 MHz,  $CDCl_3$ )  $\delta$  151.1, 149.0, 147.0, 146.7, 134.8,

129.5, 124.1, 123.5, 118.1, 116.2, 70.7, 54.5, 51.5, 48.4, 44.7, 41.0, 37.5, 34.9, 34.4, 33.5,

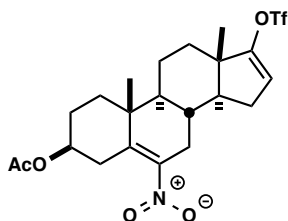
31.3, 30.6, 20.8, 16.7, 11.7; HRMS calculated for  $C_{25}H_{30}N_2O$  ( $M^+ + H$ ): 375.2436, found

375.2414.

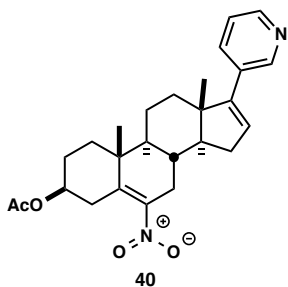
Data for **38**: IR (neat) 3318, 2211, 1454, 1445, 1412, 1376  $\text{cm}^{-1}$ ;  $^1\text{H}$  NMR (500 MHz,  $\text{CDCl}_3$ )  $\delta$  8.63 (s, 1H), 8.50 (s, 1H), 7.74 (dt,  $J = 8.0, 1.9$  Hz, 1H), 7.32 (dd,  $J = 8.0, 4.9$  Hz, 1H), 6.06 (dd,  $J = 3.3, 1.8$  Hz, 1H), 3.65 (tt,  $J = 11.1, 4.5$  Hz, 1H), 3.14 (m), 2.45–2.25 (m, 3H), 2.22–2.03 (m, 3H), 2.03–1.91 (m, 3H), 1.83 (m, 2H), 1.71 (m, 1H), 1.67–1.58 (m, 3H), 1.58–1.46 (m, 1H), 1.15 (s, 3H), 1.06 (s, 3H);  $^{13}\text{C}$  NMR (126 MHz,  $\text{CDCl}_3$ )  $\delta$  159.0, 150.9, 146.7, 146.5, 134.9, 133.2, 129.9, 123.6, 118.9, 106.4, 70.5, 56.8, 49.1, 47.2, 41.0, 40.3, 36.3, 34.9, 33.5, 31.7, 30.6, 29.7, 20.7, 19.6, 16.5; HRMS calculated for  $\text{C}_{25}\text{H}_{30}\text{N}_2\text{O}$  ( $\text{M}^+ + \text{H}$ ): 375.2436, found 375.2424.



**3 $\beta$ -Acetoxy-6-nitro- $\Delta$ 5-androst-5-en-17-one (39).** Compound **2** (150 mg, 0.453 mmol) was dissolved in dry diethyl ether and cooled to 0 °C under inert atmosphere. Fuming nitric acid was slowly added over 1 h (2.25 mL, 5% w/v). After stirring an additional 1.5 h at 0 °C, cold water (4 mL) was slowly added. The mixture was diluted with ether (15 mL), the organic layer separated and washed with water, two washes of saturated aqueous sodium bicarbonate, brine, and dried over  $\text{NaSO}_4$ . The crude material was purified by automated purification system (4 g silica, 10% to 35% EtOAc/hexanes) to yield 61 mg of a yellow powder (36%). This analytical data matched that reported for this compound.<sup>100</sup>

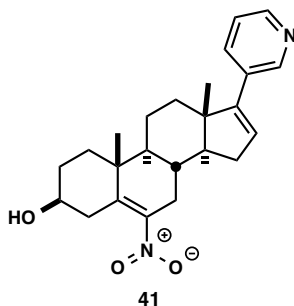


**3 $\beta$ -Acetoxy-6-nitro-17-triflyl-androst-5,16-diene**. Compound **39** (61 mg, 0.163 mmol) was triflated as described for **3**. This material was purified by silica flash chromatography (300 mg silica, 20% EtOAc/hexanes) to obtain 57 mg of **39** as a white solid (48%).  $^1\text{H}$  NMR (400 MHz,  $\text{CDCl}_3$ )  $\delta$  5.63 (dd,  $J = 3.4, 1.7$  Hz, 1H), 4.67 (tt,  $J = 11.6, 4.5$  Hz, 1H), 2.85 (m, 1H), 2.57 (m, 1H), 2.38–2.19 (m, 3H), 2.11 (m, 1H), 2.06 (s, 3H), 2.03–1.96 (m, 2H), 1.98–1.83 (m, 2H), 1.82–1.47 (m, 6H), 1.32 (m, 1H), 1.21 (s, 3H), 1.03 (s, 3H);  $^{13}\text{C}$  NMR (101 MHz,  $\text{CDCl}_3$ )  $\delta$  170.1, 158.6, 145.8, 138.2, 114.4, 71.7, 53.5, 49.2, 44.6, 38.0, 36.0, 32.4, 32.1, 31.2, 29.7, 28.5, 26.9, 21.2, 20.1, 19.6, 15.0 (there should be a duplicate peak somewhere).

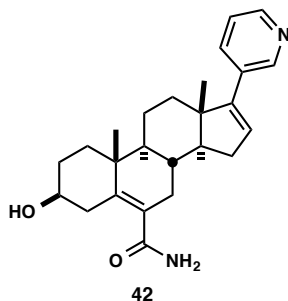


**3 $\beta$ -Acetoxy-6-nitro-17-(3-pyridyl)-androst-5,16-diene (40)**. The above compound (57 mg, 0.113 mmol) was coupled as described for **4**. This material was purified by silica flash chromatography (200 mg silica, 50% EtOAc/hexanes) to isolate 27 mg of **40** as a white solid (51%). IR (neat): 1742, 1631, 1518, 1456, 1363  $\text{cm}^{-1}$ ;  $^1\text{H}$  NMR (400 MHz,  $\text{CDCl}_3$ )  $\delta$  8.71–8.58 (m, 1H), 8.51 (dd,  $J = 4.8, 1.6$  Hz, 1H), 7.68 (dt,  $J = 8.0, 2.0$  Hz,

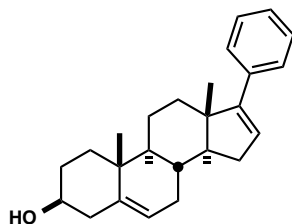
1H), 7.29–7.24 (m, 1H), 6.04 (dd,  $J = 3.3, 1.8$  Hz, 1H), 4.69 (tt,  $J = 11.6, 4.5$  Hz, 1H), 2.85 (m, 1H), 2.61 (m, 1H), 2.32 (m, 4H), 2.21–2.10 (m, 2H), 2.06 (s, 3H), 2.04–1.88 (m, 3H), 1.86–1.45 (m, 6H), 1.43–1.26 (m, 2H), 1.23 (s, 3H), 1.08 (s, 3H);  $^{13}\text{C}$  NMR (101 MHz,  $\text{CDCl}_3$ )  $\delta$  170.1, 151.2, 147.9, 147.6, 146.3, 137.9, 134.0, 132.7, 129.1, 123.2, 71.8, 56.7, 49.1, 47.3, 38.0, 36.1, 34.9, 33.0, 31.6, 31.2, 30.2, 27.0, 21.2, 20.8, 19.7, 16.5; MS calculated for  $\text{C}_{26}\text{H}_{32}\text{N}_2\text{O}_4$  ( $\text{M}^+\text{+H}$ ): 437.244, found 437.300.



**6-Nitro-17-(3-pyridyl)-androst-5,16-dien-3 $\beta$ -ol (41).** Compound **40** (27 mg, 0.061 mmol) was deacylated as for **5**. 15 mg (82%) was isolated by chromatography (50% EtOAc/hexanes). This was further purified by preparative HPLC to obtain 6 mg. IR (neat): 3330, 1547, 1518, 1440, 1376, 1351  $\text{cm}^{-1}$ ;  $^1\text{H}$  NMR (500 MHz,  $\text{CDCl}_3$ )  $\delta$  8.56 (s, 1H), 8.43 (s, 1H), 7.65 (dt,  $J = 8.0, 1.7$  Hz, 1H), 7.24 (s, 1H), 5.97 (dd,  $J = 3.3, 1.8$  Hz, 1H), 3.57 (tt,  $J = 11.3, 4.6$  Hz, 1H), 2.74 (m, 1H), 2.32–2.15 (m, 2H), 2.15–1.79 (m, 6H), 1.66 (m, 1H), 1.64–1.37 (m, 4H), 1.23–1.16 (m, 1H), 1.12 (s, 3H), 0.99 (s, 3H);  $^{13}\text{C}$  NMR (126 MHz,  $\text{CDCl}_3$ )  $\delta$  150.94, 145.82, 138.90, 134.64, 132.14, 129.66, 128.56, 128.46, 123.45, 70.16, 56.77, 49.22, 41.01, 37.96, 36.52, 35.17, 34.86, 32.94, 31.67, 30.50, 30.17, 20.78, 19.60, 16.50; HRMS calculated for  $\text{C}_{24}\text{H}_{30}\text{N}_2\text{O}_3$  ( $\text{M}^+\text{+H}$ ): 395.2334, found 395.2343.

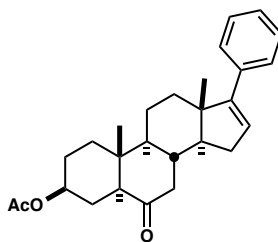


**3β-Hydroxy-17-(3-pyridyl)-androst-5,16-dien-6-amide (42).** Compound **38** (30 mg, 0.079 mmol) was added to a microwave vial, dissolved in dimethylsulfoxide (2.6 mL, 0.03 M), and cooled to 0 °C. Potassium carbonate (109 mg, 0.788 mmol) was added, followed by hydrogen peroxide (0.5 mL of 30% aqueous solution). The mixture was immediately capped and stirred for 48 h, warming to rt. The base was quenched with aqueous 2 N HCl and the DMSO/H<sub>2</sub>O frozen and lyophilized off. The resulting solid was redissolved in water and extracted with chloroform, washed with brine, and dried over NaSO<sub>4</sub>. The crude mixture was purified by column (250 mg silica, 1% MeOH/DCM to 5% MeOH/DCM) to obtain 12.1 mg of a white solid (39%). This was further subjected to preparative HPLC to obtain 3.5 mg of a fluffy white powder. IR (neat) 3344, 1658, 1597, 1426, 1408, 1377, 1335 cm<sup>-1</sup>; <sup>1</sup>H NMR (500 MHz, CDCl<sub>3</sub>) δ 8.57 (s, 1H), 8.44 (s, 1H), 7.82 (dd, *J* = 16.3, 7.2 Hz, 1H), 7.39 (s, 1H), 6.11–6.01 (m, 1H), 3.45 (ddt, *J* = 11.3, 8.3, 4.2 Hz, 1H), 3.40–3.29 (m, 1H), 2.24 (dtd, *J* = 14.9, 8.8, 7.7, 4.7 Hz, 2H), 2.16–1.94 (m, 3H), 1.94–1.70 (m, 4H), 1.70–1.32 (m, 7H), 1.18 (s, 5H), 1.10–1.02 (m, 3H), 0.98 (d, *J* = 3.7 Hz, 3H), 0.94–0.67 (m, 4H); <sup>13</sup>C NMR (126 MHz, CDCl<sub>3</sub>) δ 175.3, 151.0, 146.9, 139.8, 134.5, 132.3, 131.0, 129.8, 128.4, 123.5, 70.6, 57.1, 47.2, 40.4, 37.4, 36.8, 35.0, 33.3, 31.7, 30.5, 29.8, 29.7, 20.7, 19.4, 16.5; HRMS calculated for C<sub>25</sub>H<sub>33</sub>N<sub>2</sub>O<sub>2</sub> (M<sup>+</sup>+1): 393.2537, found 393.2525.



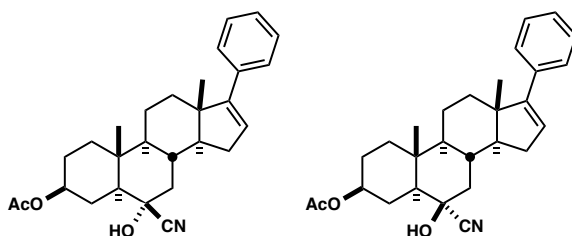
43

**17-Phenyl-androst-5,16-dien-3 $\beta$ -ol (43).** Compound **3** (128 mg, 0.274 mmol) was coupled with phenylboronic acid (37 mg, 0.301 mmol) under otherwise identical conditions as for **4**. 57 mg was isolated as a white solid. This was deacylated as for **5** to obtain 36 mg (44%) as a white solid. IR (neat) 3387, 1492, 1443, 1370, 1241  $\text{cm}^{-1}$ ;  $^1\text{H}$  NMR (400 MHz,  $\text{CDCl}_3$ )  $\delta$  7.44–7.36 (m, 2H), 7.34–7.28 (m, 2H), 7.26–7.20 (m, 1H), 5.99–5.85 (m, 1H), 5.41 (dt,  $J = 5.2, 2.0$  Hz, 1H), 3.68–3.45 (m, 1H), 2.44–2.17 (m, 3H), 2.17–1.98 (m, 3H), 1.94–1.82 (m, 2H), 1.82–1.71 (m, 2H), 1.71–1.47 (m, 7H), 1.44 (s, 1H), 1.39–1.20 (m, 3H), 1.08 (d,  $J = 3.7$  Hz, 6H), 0.95–0.82 (m, 1H).  $^{13}\text{C}$  NMR (101 MHz,  $\text{CDCl}_3$ )  $\delta$  154.8, 141.1, 137.3, 128.1, 127.2, 126.7, 121.5, 71.8, 57.7, 50.4, 47.2, 42.3, 37.2, 36.7, 35.4, 31.7, 31.6, 30.5, 21.0, 19.4, 16.7. HRMS calculated for  $\text{C}_{25}\text{H}_{32}\text{O}$  (M): 348.2453, found 348.2552.



44

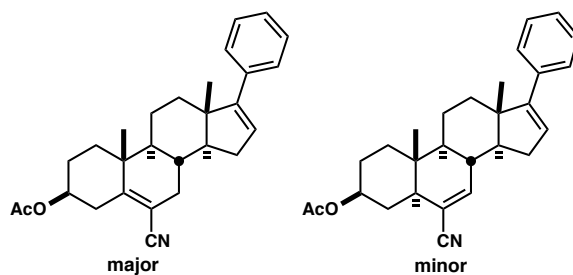
**3 $\beta$ -Acetoxy-17-phenyl-androst-16-en-6-one (44).** Compound **27** (500 mg, 1.04 mmol) was coupled as described for **43**. Column chromatography (4 g silica, 20% to 50% EtOAc:hexanes) provided 340 mg (59%) of **44** as a white solid.  $^1\text{H}$  NMR (400 MHz,  $\text{CDCl}_3$ )  $\delta$  7.44–7.23 (m, 6H), 5.92 (dd,  $J = 3.4, 1.8$  Hz, 1H), 4.71 (tt,  $J = 11.7, 4.6$  Hz, 1H), 2.54–2.38 (m, 1H), 2.38–2.28 (m, 2H), 2.28–2.15 (m, 2H), 2.10–2.06 (m, 3H), 2.04–1.95 (m, 3H), 1.94–1.75 (m, 6H), 1.75–1.47 (m, 7H), 1.47–1.19 (m, 3H), 1.05 (d,  $J = 0.9$  Hz, 3H), 0.98 (s, 2H), 0.86 (s, 2H).  $^{13}\text{C}$  NMR (101 MHz,  $\text{CDCl}_3$ )  $\delta$  210.0, 170.6, 154.6, 137.0, 128.2, 126.9, 126.7, 107.6, 72.8, 67.7, 67.4, 57.6, 56.8, 55.3, 54.2, 47.8, 46.5, 42.7, 41.1, 40.0, 38.1, 36.6, 35.6, 35.1, 31.3, 29.5, 26.8, 26.2, 23.8, 21.3, 16.7, 13.1.



**3 $\beta$ -Acetoxy-6-cyano-6-hydroxy-17-phenyl-androst-16-ene (mixture of C6 isomers).**

From **44**, the cyanohydrin was prepared as described for **34**. Column chromatography (500 mg silica, 50% EtOAc:hexanes) afforded 90 mg (25%) of this compound as a white solid. IR (neat): 3328, 2211, 1703, 1497, 1446, 1386, 1363  $\text{cm}^{-1}$ ;  $^1\text{H}$  NMR (400 MHz,

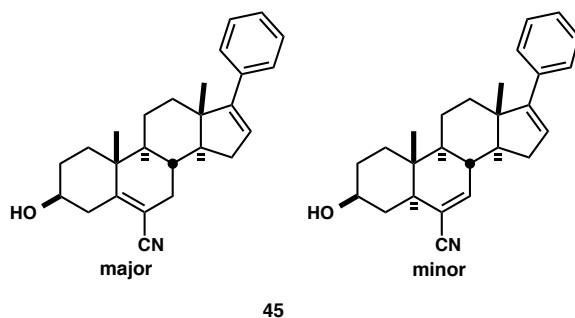
CDCl<sub>3</sub>) δ 7.44–7.22 (m, 6H), 5.92 (dd, *J* = 3.3, 1.8 Hz, 1H), 4.74 (tt, *J* = 11.4, 4.9 Hz, 1H), 3.23 (s, 1H), 2.39 (dt, *J* = 12.2, 3.3 Hz, 2H), 2.35–2.18 (m, 2H), 2.09 (s, 4H), 2.04–1.95 (m, 1H), 1.86 (ddt, *J* = 32.7, 13.3, 3.0 Hz, 3H), 1.75–1.63 (m, 4H), 1.63–1.54 (m, 2H), 1.54–1.27 (m, 5H), 1.18 (s, 3H), 1.09 (s, 4H), 0.95–0.84 (m, 1H); <sup>13</sup>C NMR (101 MHz, CDCl<sub>3</sub>) δ 170.80, 154.65, 136.95, 128.15, 126.72, 126.65, 121.40, 72.80, 69.08, 56.42, 53.72, 52.42, 47.40, 44.98, 38.01, 36.59, 35.14, 31.41, 26.87, 21.36, 20.89, 16.79, 14.20.



**3β-Acetoxy-6-cyano-17-(3-pyridyl)-androst-6,16-diene (minor product) and 3β-acetoxy-6-cyano-17-(3-pyridyl)-androst-5,16-diene (major product).** The above compound was dehydrated as for **35/36**. Column chromatography (200 mg silica, 20% to 50% EtOAc:hexanes) afforded 56 mg (60%) of the vinyl nitrile mixture, in a 23:77 ratio of Δ6:Δ5-androstane (cf. **35:36**), as determined by <sup>1</sup>H-NMR as described for **35/36**. This mixture was carried forward. <sup>1</sup>H NMR (400 MHz, CDCl<sub>3</sub>) δ 7.45–7.33 (m, 3H), 7.29–7.20 (m, 1H), 5.93 (ddt, *J* = 8.3, 3.2, 1.7 Hz, 1H), 4.88–4.65 (m, 1H), 3.14 (ddd, *J* = 13.9, 5.0, 2.1 Hz, 1H), 2.84–2.59 (m, 1H), 2.59–2.44 (m, 1H), 2.44–2.13 (m, 4H), 2.12–2.06 (m, 4H), 2.07–1.94 (m, 3H), 1.93–1.78 (m, 2H), 1.78–1.37 (m, 6H), 1.41–1.23 (m, 1H), 1.16 (d, *J* = 10.7 Hz, 3H), 1.08 (d, *J* = 2.9 Hz, 3H), 0.89 (s, 1H); <sup>13</sup>C NMR (101 MHz,

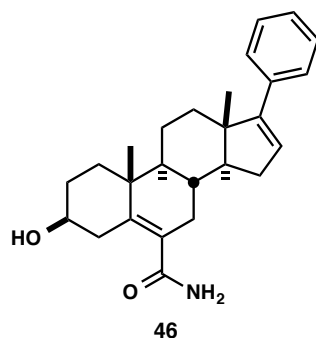
CDCl<sub>3</sub>) δ 170.1, 157.7, 154.5, 147.6, 136.9, 128.2, 126.9, 126.7, 118.7, 107.4, 72.1, 56.8, 49.1, 47.1, 38.4, 37.7, 36.2, 36.0, 35.1, 33.6, 31.4, 29.8, 27.2, 21.2, 20.7, 19.6, 16.6, 11.6.

Diagnostic <sup>1</sup>H-NMR peaks for minor isomer: 6.49 (s, 1H), 4.85 (m, 1 H).



**6-Cyano-17-phenyl-androst-6,16-dien-3 $\beta$ -ol (minor product) and 6-Cyano-17-phenyl-androst-5,16-dien-3 $\beta$ -ol (45).** The above compound was deacylated as described for **5**. Column chromatography afforded 46 mg (98%) as a white solid. IR (neat): 3377, 2211, 1632, 1494, 1442, 1374, 1360 cm<sup>-1</sup>; <sup>1</sup>H NMR (400 MHz, CDCl<sub>3</sub>) δ 7.34–7.26 (m, 2H), 7.23 (ddd, *J* = 7.6, 6.6, 1.4 Hz, 2H), 7.19–7.12 (m, 1H), 5.84 (ddd, *J* = 5.0, 3.3, 1.8 Hz, 1H), 3.68–3.48 (m, 1H), 3.05 (m, 1H), 2.42–2.20 (m, 2H), 2.10–1.94 (m, 3H), 1.96–1.80 (m, 3H), 1.80–1.65 (m, 1H), 1.65–1.27 (m, 6H), 1.06 (s, 3H), 0.98 (s, 3H), 0.77 (s, 1H); <sup>13</sup>C NMR (101 MHz, CDCl<sub>3</sub>) δ 159.3, 154.5, 147.5, 137.0, 128.2, 126.7, 126.7, 119.0, 106.5, 70.5, 56.9, 54.7, 51.6, 49.2, 47.1, 40.3, 38.3, 36.4, 35.1, 33.6, 31.4, 30.6, 29.8, 20.8, 19.6, 16.6, 11.7.

Diagnostic <sup>1</sup>H-NMR peak for minor isomer 6.56 (t, *J* = 2.9 Hz, 1H).



**3β-Hydroxy-17-phenyl-androst-5,16-dien-6-amide (46).** Compound **45** was oxidized as described for **42**. This was purified by preparative HPLC to obtain 3.0 mg of a colorless solid (10%). IR (neat): 3341, 1653, 1634, 1492, 1454, 1376, 1346  $\text{cm}^{-1}$ ;  $^1\text{H}$  NMR (500 MHz,  $\text{CDCl}_3$ )  $\delta$  7.34 (dd,  $J = 7.7, 2.9$  Hz, 2H), 7.31–7.26 (m, 3H), 7.26–7.16 (m, 1H), 6.10 (s, 1H), 5.88 (dd,  $J = 7.2, 3.0$  Hz, 1H), 3.65 (s, 1H), 3.51 (s, 1H), 2.40–2.19 (m, 3H), 2.19–1.98 (m, 3H), 1.98–1.72 (m, 4H), 1.72–1.34 (m, 6H), 1.33–1.17 (m, 2H), 1.18–1.09 (m, 3H), 1.03 (m, 3H), 0.84 (s, 3H);  $^{13}\text{C}$  NMR (126 MHz,  $\text{CDCl}_3$ )  $\delta$  175.7, 154.7, 154.5, 140.1, 137.1, 133.0, 129.1, 128.1, 126.6, 70.5, 57.2, 55.0, 51.4, 48.1, 47.1, 44.6, 37.4, 36.8, 36.0, 35.2, 34.1, 33.4, 31.5, 30.6, 29.9, 20.8, 19.4, 16.5, 12.0; HRMS calculated for  $\text{C}_{26}\text{H}_{34}\text{NO}_2$  ( $\text{M}^+ + 1$ ): 392.2584, found 392.2575.

## 1.6 References

1. Donald Voet, J. G. V. *Biochemistry, 4th Edition*. John Wiley & Sons, Inc.: 2010.
2. Ferraldeschi, R.; Sharifi, N.; Auchus, R. J.; Attard, G. Molecular pathways: Inhibiting steroid biosynthesis in prostate cancer. *Clin. Cancer Res.* **2013**, *19*, 3353-3359.
3. Dzau, V. J. Molecular biology of angiotensin II biosynthesis and receptors. *Can. J. Cardiol.* **1995**, *11 Suppl F*, 21f-26f.
4. Fleseriu, M.; Petersenn, S. Medical management of Cushing's disease: what is the future? *Pituitary* **2012**, *15*, 330-341.
5. Frank, R. N. Treating diabetic retinopathy by inhibiting growth factor pathways. *Curr. Opin. Investig. Drugs* **2009**, *10*, 327-335.
6. van Raalte, D. H.; Ouwens, D. M.; Diamant, M. Novel insights into glucocorticoid-mediated diabetogenic effects: towards expansion of therapeutic options? *Eur. J. Clin. Invest.* **2009**, *39*, 81-93.
7. Zhao, M.; Gödecke, T.; Gunn, J.; Duan, J.-A.; Che, C.-T. Protostane and Fusidane Triterpenes: A Mini-Review. *Molecules* **2013**, *18*, 4054-4080.
8. Duax, W. L.; Griffin, J. F. Steroid Hormone Structure, Receptor Binding and Activity: Empirical Drug Design. In *Structure-Based Drug Design*, Codding, P., Ed. Springer Netherlands: 1998; Vol. 352, pp 1-14.
9. Attard, G.; Reid, A. H. M.; Olmos, D.; de Bono, J. S. Antitumor Activity with CYP17 Blockade Indicates That Castration-Resistant Prostate Cancer Frequently Remains Hormone Driven. *Cancer Res.* **2009**, *69*, 4937-4940.
10. Auchus, M. L.; Auchus, R. J. Human steroid biosynthesis for the oncologist. *J. Investig. Med.* **2012**, *60*, 495-503.
11. Hirakawa, H.; Yokoyama, Y.; Yoshida, H.; Mizunuma, H. Inhibitory effects of aromatase inhibitor on estrogen receptor-alpha positive ovarian cancer in mice. *J. Ovarian Res.* **2014**, *7*, 4.

12. Ferraldeschi, R.; de Bono, J. Agents That Target Androgen Synthesis in Castration-Resistant Prostate Cancer. *Cancer J.* **2013**, *19*, 34-42  
10.1097/PPO.1090b1013e31827e31820b31826f.
13. White, R.; Parker, M. G. Molecular mechanisms of steroid hormone action. *Endocr. Relat. Cancer* **1998**, *5*, 1-14.
14. Wendler, A.; Albrecht, C.; Wehling, M. Nongenomic actions of aldosterone and progesterone revisited. *Steroids* **2012**, *77*, 1002-1006.
15. *Cytochrome P450: Structure, Mechanism, and Biochemistry*. 3rd ed.; Kluwer Academic / Plenum Publishers: New York, 2005.
16. Hasemann, C. A.; Kurumbail, R. G.; Boddupalli, S. S.; Peterson, J. A.; Deisenhofer, J. Structure and function of cytochromes P450: a comparative analysis of three crystal structures. *Structure* **1995**, *3*, 41-62.
17. Zanger, U. M.; Schwab, M. Cytochrome P450 enzymes in drug metabolism: regulation of gene expression, enzyme activities, and impact of genetic variation. *Pharmacol. Ther.* **2013**, *138*, 103-141.
18. Hayes, C.; Ansbro, D.; Kontoyianni, M. Elucidating Substrate Promiscuity in the Human Cytochrome 3A4. *J. Chem. Inf. Model.* **2014**, *54*, 857-869.
19. Porubek, D. CYP17A1: a biochemistry, chemistry, and clinical review. *Curr. Top. Med. Chem.* **2013**, *13*, 1364-1384.
20. Pandey, A. V.; Fluck, C. E. NADPH P450 oxidoreductase: structure, function, and pathology of diseases. *Pharmacol. Ther.* **2013**, *138*, 229-254.
21. Bruno, R. D.; Njar, V. C. O. Targeting cytochrome P450 enzymes: A new approach in anti-cancer drug development. *Bioorg. Med. Chem.* **2007**, *15*, 5047-5060.
22. Locuson, C. W.; Hutzler, J. M.; Tracy, T. S. Visible spectra of type II cytochrome P450-drug complexes: evidence that "incomplete" heme coordination is common. *Drug Metab. Dispos.* **2007**, *35*, 614-622.

23. Devore, N. M.; Scott, E. E. Structure and function of human cytochromes P450 enzymes: Xenobiotic metabolism by CYP2A and steroid biosynthesis by CYP17A1. University of Kansas, Lawrence, KS, 2011.
24. Lee, J. I.; Zhang, L.; Men, A. Y.; Kenna, L. A.; Huang, S. M. CYP-mediated therapeutic protein-drug interactions: clinical findings, proposed mechanisms and regulatory implications. *Clin. Pharmacokinet.* **2010**, *49*, 295-310.
25. Böttner, B.; Schrauber, H.; Bernhardt, R. Engineering a mineralocorticoid- to a glucocorticoid-synthesizing cytochrome P450. *J. Biol. Chem.* **1996**, *271*, 8028-8033.
26. Jansen, P. M.; van den Meiracker, A. H.; Jan Danser, A. H. Aldosterone synthase inhibitors: pharmacological and clinical aspects. *Curr. Opin. Investig. Drugs* **2009**, *10*, 319-326.
27. Hartmann, R. W.; Müller, U.; Ehmer, P. B. Discovery of selective CYP11B2 (aldosterone synthase) inhibitors for the therapy of congestive heart failure and myocardial fibrosis. *Eur. J. Med. Chem.* **2003**, *38*, 363-366.
28. Heim, R.; Lucas, S.; Grombein, C. M.; Ries, C.; Schewe, K. E.; Negri, M.; Müller-Vieira, U.; Birk, B.; Hartmann, R. W. Overcoming Undesirable CYP1A2 Inhibition of Pyridyl-naphthalene-Type Aldosterone Synthase Inhibitors: Influence of Heteroaryl Derivatization on Potency and Selectivity. *J. Med. Chem.* **2008**, *51*, 5064-5074.
29. Mostaghel, E. A. Abiraterone in the treatment of metastatic castration-resistant prostate cancer. *Cancer Manag Res* **2014**, *6*, 39-51.
30. Attard, G.; Reid, A. H. M.; Auchus, R. J.; Hughes, B. A.; Cassidy, A. M.; Thompson, E.; Oommen, N. B.; Folkler, E.; Dowsett, M.; Arlt, W.; de Bono, J. S. Clinical and Biochemical Consequences of CYP17A1 Inhibition with Abiraterone Given with and without Exogenous Glucocorticoids in Castrate Men with Advanced Prostate Cancer. *J. Clin. Endocrinol. Metab.* **2012**, *97*, 507-516.
31. Rafferty, S. W.; Eisner, J. R.; Moore, W. R.; Schotzinger, R. J.; Hoekstra, W. J. Highly-selective 4-(1,2,3-triazole)-based P450c17a 17,20-lyase inhibitors. *Bioorg. Med. Chem. Lett.* **2014**, *24*, 2444-2447.
32. Zhu, H.; Garcia, J. Targeting the Adrenal Gland in Castration-Resistant Prostate Cancer: A Case for Orteronel, a Selective CYP-17 17,20-Lyase Inhibitor. *Curr. Oncol. Rep.* **2013**, *15*, 105-112.

33. Dragan, C. A.; Hartmann, R. W.; Bureik, M. A fission yeast-based test system for the determination of IC50 values of anti-prostate tumor drugs acting on CYP21. *J. Enzyme Inhib. Med. Chem.* **2006**, *21*, 547-556.
34. Salem, M.; Garcia, J. A. Abiraterone acetate, a novel adrenal inhibitor in metastatic castration-resistant prostate cancer. *Curr. Oncol. Rep.* **2011**, *13*, 92-96.
35. Society, A. C. Cancer Facts & Figures 2014. In Estimates, L. N. C. C. a. D.-. Ed. National Home Office: American Cancer Society Inc. 250 Williams Street, NW, Atlanta, GA 30303, 2014.
36. Owen, C. P. 17 $\alpha$ -hydroxylase/17,20-lyase (p450(17 $\alpha$ )) inhibitors in the treatment of prostate cancer: a review. *Anticancer Agents Med. Chem.* **2009**, *9*, 613-626.
37. Zielinski, R. R.; Eigl, B. J.; Chi, K. N. Targeting the Apoptosis Pathway in Prostate Cancer. *Cancer J.* **2013**, *19*, 79-89.
38. Cornforth, A. N.; Davis, J. S.; Khanifar, E.; Nastiuk, K. L.; Krolewski, J. J. FOXO3a mediates the androgen-dependent regulation of FLIP and contributes to TRAIL-induced apoptosis of LNCaP cells. *Oncogene* **2008**, *27*, 4422-4433.
39. Denmeade, S. R.; Isaacs, J. T. A history of prostate cancer treatment. *Nat. Rev. Cancer* **2002**, *2*, 389-396.
40. Bruno, R. D.; Njar, V. C. Targeting cytochrome P450 enzymes: a new approach in anti-cancer drug development. *Bioorg. Med. Chem.* **2007**, *15*, 5047-5060.
41. Culig, Z.; Santer, F. R. Molecular aspects of androgenic signaling and possible targets for therapeutic intervention in prostate cancer. *Steroids* **2013**, *78*, 851-859.
42. Heinlein, C. A.; Chang, C. The roles of androgen receptors and androgen-binding proteins in nongenomic androgen actions. *Mol. Endocrinol.* **2002**, *16*, 2181-2187.
43. Schroder, F.; Crawford, E. D.; Axcrone, K.; Payne, H.; Keane, T. E. Androgen deprivation therapy: past, present and future. *BJU Int.* **2012**, *109 Suppl 6*, 1-12.

44. Ocana, A.; Seruga, B.; Tannock, I. F. Drug resistance in metastatic castration-resistant prostate cancer. *Nat. Rev. Clin. Oncol.* **2011**, *8*, 12+.
45. Joseph, J. D.; Lu, N.; Qian, J.; Sensintaffar, J.; Shao, G.; Brigham, D.; Moon, M.; Maneval, E. C.; Chen, I.; Darimont, B.; Hager, J. H. A clinically relevant androgen receptor mutation confers resistance to second-generation antiandrogens enzalutamide and ARN-509. *Cancer Discov* **2013**, *3*, 1020-1029.
46. Ayesha A. Shafi, A. E. Y., Nancy L. Weigel. Androgen receptors in hormone-dependent and castration-resistant prostate cancer. *Pharmacol. Ther.* **2014**, *140*, 223-238.
47. Mostaghel, E. A.; Marck, B. T.; Plymate, S. R.; Vessella, R. L.; Balk, S.; Matsumoto, A. M.; Nelson, P. S.; Montgomery, R. B. Resistance to CYP17A1 Inhibition with Abiraterone in Castration-Resistant Prostate Cancer: Induction of Steroidogenesis and Androgen Receptor Splice Variants. *Clin. Cancer Res.* **2011**, *17*, 5913-5925.
48. Nguyen, A. D.; Conley, A. J. Adrenal androgens in humans and nonhuman primates: production, zonation and regulation. *Endocr. Dev.* **2008**, *13*, 33-54.
49. Attard, G.; Reid, A. H.; Olmos, D.; de Bono, J. S. Antitumor activity with CYP17 blockade indicates that castration-resistant prostate cancer frequently remains hormone driven. *Cancer Res.* **2009**, *69*, 4937-4940.
50. Cai, C.; Balk, S. P. Intratumoral androgen biosynthesis in prostate cancer pathogenesis and response to therapy. *Endocr. Relat. Cancer* **2011**, *18*, R175-182.
51. Feldman, B. J.; Feldman, D. The development of androgen-independent prostate cancer. *Nat. Rev. Cancer* **2001**, *1*, 34-45.
52. Carles, J.; Castellano, D.; Climent, M. A.; Maroto, P.; Medina, R.; Alcaraz, A. Castration-resistant metastatic prostate cancer: current status and treatment possibilities. *Clin. Transl. Oncol.* **2012**, *14*, 169-176.
53. Institute, N. C. FDA Approval for Abiraterone Acetate.  
<http://www.cancer.gov/cancertopics/druginfo/fda-abirateroneacetate>
54. Bok, R. A.; Small, E. J. The treatment of advanced prostate cancer with ketoconazole: safety issues. *Drug Saf.* **1999**, *20*, 451-458.

55. Renoir, J. M.; Marsaud, V.; Lazenec, G. Estrogen receptor signaling as a target for novel breast cancer therapeutics. *Biochem. Pharmacol.* **2013**, *85*, 449-465.
56. Abiraterone Acetate in Treating Postmenopausal Women With Advanced or Metastatic Breast Cancer.  
<http://clinicaltrials.gov/ct2/show/NCT00755885?term=abiraterone+breast+cancer&rank=4>
57. Abiraterone Acetate in Molecular Apocrine Breast Cancer (AMA).  
<http://clinicaltrials.gov/ct2/show/NCT01842321?term=abiraterone+breast+cancer&rank=1>
58. A Study That Provides Long-term Safety Follow-up and Examines Long-term Exposure to Abiraterone Acetate.
59. Yamaoka, M.; Hara, T.; Hitaka, T.; Kaku, T.; Takeuchi, T.; Takahashi, J.; Asahi, S.; Miki, H.; Tasaka, A.; Kusaka, M. Orteronel (TAK-700), a novel non-steroidal 17,20-lyase inhibitor: effects on steroid synthesis in human and monkey adrenal cells and serum steroid levels in cynomolgus monkeys. *J. Steroid Biochem. Mol. Biol.* **2012**, *129*, 115-128.
60. Study Comparing Orteronel Plus Prednisone in Patients With Metastatic Castration-Resistant Prostate Cancer. <http://clinicaltrials.gov/show/NCT01193257>
61. Takeda Announces Termination of Orteronel (TAK-700) Development for Prostate Cancer in Japan, U.S.A. and Europe. <http://www.marketwatch.com/story/takeda-announces-termination-of-orteronel-tak-700-development-for-prostate-cancer-in-japan-usa-and-europe-2014-06-19>
62. Phase 2 Trial of TAK-700 (Orteronel) Without Prednisone for Metastatic Castration-Resistant Prostate Cancer. <https://clinicaltrials.gov/ct2/show/NCT01866423>
63. Miller, W. L. Molecular Biology of Steroid Hormone Synthesis. *Endocr. Rev.* **1988**, *9*, 295-318.
64. Gregory, M.; Mak, P. J.; Sligar, S. G.; Kincaid, J. R. Differential Hydrogen Bonding in Human CYP17 Dictates Hydroxylation versus Lyase Chemistry. *Angew. Chem., Int. Ed.* **2013**, *52*, 5342-5345.

65. Khatri, Y.; Gregory, M. C.; Grinkova, Y. V.; Denisov, I. G.; Sligar, S. G. Active site proton delivery and the lyase activity of human CYP17A1. *Biochem. Biophys. Res. Commun.* **2014**, *443*, 179-184.
66. Petrunak, E. M.; DeVore, N. M.; Scott, E. E. Structures of Human Steroidogenic Cytochrome P450 17A1 with Substrates. In *J. Biol. Chem.*, Forthcoming 2014.
67. DeVore, N. M.; Scott, E. E. Structures of cytochrome P450 17A1 with prostate cancer drugs abiraterone and TOK-001. *Nature* **2012**, *482*, 116-119.
68. Estrada, D. F.; Skinner, A. L.; Laurence, J. S.; Scott, E. E. Human Cytochrome P450 17A1 Conformational Selection: MODULATION BY LIGAND AND CYTOCHROME b5. *J. Biol. Chem.* **2014**, *289*, 14310-14320.
69. Auchus, R. J.; Lee, T. C.; Miller, W. L. Cytochrome b 5 Augments the 17,20-Lyase Activity of Human P450c17 without Direct Electron Transfer. *J. Biol. Chem.* **1998**, *273*, 3158-3165.
70. Potter, G. A.; Barrie, S. E.; Jarman, M.; Rowlands, M. G. Novel Steroidal Inhibitors of Human Cytochrome P45017.alpha.-Hydroxylase-C17,20-lyase): Potential Agents for the Treatment of Prostatic Cancer. *J. Med. Chem.* **1995**, *38*, 2463-2471.
71. Kaku, T.; Hitaka, T.; Ojida, A.; Matsunaga, N.; Adachi, M.; Tanaka, T.; Hara, T.; Yamaoka, M.; Kusaka, M.; Okuda, T.; Asahi, S.; Furuya, S.; Tasaka, A. Discovery of orteronel (TAK-700), a naphthylmethylimidazole derivative, as a highly selective 17,20-lyase inhibitor with potential utility in the treatment of prostate cancer. *Bioorg. Med. Chem.* **2011**, *19*, 6383-6399.
72. Nishizato, Y.; Imai, S.; Yabuki, M.; Kido, H.; Komuro, S. Development of relevant assay system to identify steroidogenic enzyme inhibitors. *Toxicol. In Vitro* **2010**, *24*, 677-685.
73. Pia, A.; Vignani, F.; Attard, G.; Tucci, M.; Bironzo, P.; Scagliotti, G.; Arlt, W.; Terzolo, M.; Berruti, A. Strategies for managing ACTH dependent mineralocorticoid excess induced by abiraterone. *Cancer Treat. Rev.* **2013**, *39*, 966-973.
74. Arlt, W.; Walker, E. A.; Draper, N.; Ivison, H. E.; Ride, J. P.; Hammer, F.; Chalder, S. M.; Borucka-Mankiewicz, M.; Hauffa, B. P.; Malunowicz, E. M.; Stewart, P. M.; Shackleton, C. H. Congenital adrenal hyperplasia caused by mutant P450

oxidoreductase and human androgen synthesis: analytical study. *Lancet* **2004**, *363*, 2128-2135.

75. Alesci, S.; De Martino, M. U.; Ilias, I.; Gold, P. W.; Chrousos, G. P. Glucocorticoid-induced osteoporosis: from basic mechanisms to clinical aspects. *Neuroimmunomodulation* **2005**, *12*, 1-19.

76. Ryan, C. J.; Smith, M. R.; Fong, L.; Rosenberg, J. E.; Kantoff, P.; Raynaud, F.; Martins, V.; Lee, G.; Kheoh, T.; Kim, J.; Molina, A.; Small, E. J. Phase I clinical trial of the CYP17 inhibitor abiraterone acetate demonstrating clinical activity in patients with castration-resistant prostate cancer who received prior ketoconazole therapy. *J. Clin. Oncol.* **2010**, *28*, 1481-1488.

77. Gay, S. C.; Roberts, A. G.; Halpert, J. R. Structural features of cytochromes P450 and ligands that affect drug metabolism as revealed by X-ray crystallography and NMR. *Future Med Chem* **2010**, *2*, 1451-1468.

78. Poulos, T. L.; Finzel, B. C.; Howard, A. J. High-resolution crystal structure of cytochrome P450cam. *J. Mol. Biol.* **1987**, *195*, 687-700.

79. Williams, P. A.; Cosme, J.; Ward, A.; Angove, H. C.; Matak Vinkovic, D.; Jhoti, H. Crystal structure of human cytochrome P450 2C9 with bound warfarin. *Nature* **2003**, *424*, 464-468.

80. Haider, S. M.; Patel, J. S.; Poojari, C. S.; Neidle, S. Molecular modeling on inhibitor complexes and active-site dynamics of cytochrome P450 C17, a target for prostate cancer therapy. *J. Mol. Biol.* **2010**, *400*, 1078-1098.

81. Zhao, B.; Lei, L.; Kagawa, N.; Sundaramoorthy, M.; Banerjee, S.; Nagy, L. D.; Guengerich, F. P.; Waterman, M. R. Three-dimensional structure of steroid 21-hydroxylase (cytochrome P450 21A2) with two substrates reveals locations of disease-associated variants. *J. Biol. Chem.* **2012**, *287*, 10613-10622.

82. Otyepka, M.; Berka, K.; Anzenbacher, P. Is there a relationship between the substrate preferences and structural flexibility of cytochromes P450? *Curr. Drug Metab.* **2012**, *13*, 130-142.

83. Tari, L. W.; Hoffman, I. D.; Bensen, D. C.; Hunter, M. J.; Nix, J.; Nelson, K. J.; McRee, D. E.; Swanson, R. V. Structural basis for the inhibition of Aurora A kinase by a

novel class of high affinity disubstituted pyrimidine inhibitors. *Bioorg. Med. Chem. Lett.* **2007**, *17*, 688-691.

84. Njar, V. C.; Brodie, A. M. Inhibitors of 17 $\alpha$ -hydroxylase/17,20-lyase (CYP17): potential agents for the treatment of prostate cancer. *Curr. Pharm. Des.* **1999**, *5*, 163-180.

85. Pinto-Bazurco Mendieta, M. A. E.; Negri, M.; Jagusch, C.; Müller-Vieira, U.; Lauterbach, T.; Hartmann, R. W. Synthesis, Biological Evaluation, and Molecular Modeling of Abiraterone Analogues: Novel CYP17 Inhibitors for the Treatment of Prostate Cancer. *J. Med. Chem.* **2008**, *51*, 5009-5018.

86. Purushottamachar, P.; Godbole, A. M.; Gediya, L. K.; Martin, M. S.; Vasaitis, T. S.; Kwegyir-Afful, A. K.; Ramalingam, S.; Ates-Alagoz, Z.; Njar, V. C. O. Systematic Structure Modifications of Multitarget Prostate Cancer Drug Candidate Galeterone To Produce Novel Androgen Receptor Down-Regulating Agents as an Approach to Treatment of Advanced Prostate Cancer. *J. Med. Chem.* **2013**, *56*, 4880-4898.

87. Blake, L. C.; Scott, E. E. Cytochromes P450 as therapeutic targets and counter-targets for the prevention of lung cancer and treatment of steroidogenic diseases. University of Kansas, Lawrence, KS, 2012.

88. Roelofs, M. J.; Piersma, A. H.; van den Berg, M.; van Duursen, M. B. The relevance of chemical interactions with CYP17 enzyme activity: assessment using a novel in vitro assay. *Toxicol. Appl. Pharmacol.* **2013**, *268*, 309-317.

89. Imai, T.; Globerman, H.; Gertner, J. M.; Kagawa, N.; Waterman, M. R. Expression and purification of functional human 17  $\alpha$ -hydroxylase/17,20-lyase (P450c17) in *Escherichia coli*. Use of this system for study of a novel form of combined 17  $\alpha$ -hydroxylase/17,20-lyase deficiency. *J. Biol. Chem.* **1993**, *268*, 19681-19689.

90. Dhir, V.; Ivison, H. E.; Krone, N.; Shackleton, C. H.; Doherty, A. J.; Stewart, P. M.; Arlt, W. Differential inhibition of CYP17A1 and CYP21A2 activities by the P450 oxidoreductase mutant A287P. *Mol. Endocrinol.* **2007**, *21*, 1958-1968.

91. Sandee, D.; Miller, W. L. High-yield expression of a catalytically active membrane-bound protein: human P450 oxidoreductase. *Endocrinology* **2011**, *152*, 2904-2908.

92. Kabsch, W. XDS. *Acta Crystallogr. D Biol. Crystallogr.* **2010**, *66*, 125-132.

93. McCoy, A. J.; Grosse-Kunstleve, R. W.; Adams, P. D.; Winn, M. D.; Storoni, L. C.; Read, R. J. Phaser crystallographic software. *J. Appl. Crystallogr.* **2007**, *40*, 658-674.
94. Adams, P. D.; Afonine, P. V.; Bunkoczi, G.; Chen, V. B.; Davis, I. W.; Echols, N.; Headd, J. J.; Hung, L. W.; Kapral, G. J.; Grosse-Kunstleve, R. W.; McCoy, A. J.; Moriarty, N. W.; Oeffner, R.; Read, R. J.; Richardson, D. C.; Richardson, J. S.; Terwilliger, T. C.; Zwart, P. H. PHENIX: a comprehensive Python-based system for macromolecular structure solution. *Acta Crystallogr. D Biol. Crystallogr.* **2010**, *66*, 213-221.
95. Emsley, P.; Cowtan, K. Coot: model-building tools for molecular graphics. *Acta Crystallogr. D Biol. Crystallogr.* **2004**, *60*, 2126-2132.
96. Wang, Y.; Li, X.; Li, Y.; Pan, Y.; Cheng, K.; Wang, H. Simultaneous reduction of aldehyde group to hydroxymethyl group in palladium-catalyzed Suzuki cross-coupling reaction. *Chem. Res. Chin. Univ.* **2014**, *30*, 614-618.
97. Wenkert, E.; Angell, E. C. Preparation of Lactams Via Oxidation of Cyclic, Tertiary and Secondary Amines with Hg(II)-Edta Complex in Alkaline Medium. *Synth. Commun.* **1988**, *18*, 1331-1337.
98. Beuchet, P.; El kihel, L.; Dherbomez, M.; Charles, G.; Letourneux, Y. Synthesis of 6( $\alpha,\beta$ )-aminocholestanols as ergosterol biosynthesis inhibitors. *Bioorg. Med. Chem. Lett.* **1998**, *8*, 3627-3630.
99. Suginome, H.; Yabe, T.; Osawa, E. Photo-induced transformations. Part LXI. Syntheses of some six-membered and eight-membered lactams of the B-homo- and A-nor-B,B-dihomocholestane series by the photo-Beckmann rearrangement. *J. Chem. Soc. Perkin Trans. 1* **1982**, 931-938.
100. Bazin, M.-A.; Kihel, L. E.; Boulouard, M.; Bouët, V.; Rault, S. The effects of DHEA, 3 $\beta$ -hydroxy-5 $\alpha$ -androstane-6,17-dione, and 7-amino-DHEA analogues on short term and long term memory in the mouse. *Steroids* **2009**, *74*, 931-937.
101. Wilton, J. H.; Titus, M. A.; Efstathiou, E.; Fetterly, G. J.; Mohler, J. L. Androgenic biomarker profiling in human matrices and cell culture samples using high throughput, electrospray tandem mass spectrometry. *Prostate* **2014**, *74*, 722-731.

102. Gouveia, M. J.; Brindley, P. J.; Santos, L. L.; Correia da Costa, J. M.; Gomes, P.; Vale, N. Mass spectrometry techniques in the survey of steroid metabolites as potential disease biomarkers: a review. *Metabolism*. **2013**, *62*, 1206-1217.
103. Yamaoka, M.; Hara, T.; Hitaka, T.; Kaku, T.; Takeuchi, T.; Takahashi, J.; Asahi, S.; Miki, H.; Tasaka, A.; Kusaka, M. Orteronel (TAK-700), a novel non-steroidal 17,20-lyase inhibitor: Effects on steroid synthesis in human and monkey adrenal cells and serum steroid levels in cynomolgus monkeys. *The Journal of Steroid Biochemistry and Molecular Biology* **2012**, *129*, 115-128.
104. Cornish-Bowden, A. The origins of enzyme kinetics. *FEBS Lett.* **2013**, *587*, 2725-2730.
105. Moon, J. Y.; Kang, S. M.; Lee, J.; Cho, J. Y.; Moon, M. H.; Jang, I. J.; Chung, B. C.; Choi, M. H. GC-MS-based quantitative signatures of cytochrome P450-mediated steroid oxidation induced by rifampicin. *Ther. Drug Monit.* **2013**, *35*, 473-484.
106. Halket, J.; Zaikin, V. Review: Derivatization in mass spectrometry - 1. Silylation. *Eur. J. Mass Spectrom.* **2003**, *9*, 1-21.
107. Gomes, R. L.; Meredith, W.; Snape, C. E.; Sephton, M. A. Analysis of conjugated steroid androgens: deconjugation, derivatisation and associated issues. *J. Pharm. Biomed. Anal.* **2009**, *49*, 1133-1140.
108. Wlodawer, A.; Minor, W.; Dauter, Z.; Jaskolski, M. Protein crystallography for non-crystallographers, or how to get the best (but not more) from published macromolecular structures. *FEBS J.* **2008**, *275*, 1-21.
109. Carpenter, E. P.; Beis, K.; Cameron, A. D.; Iwata, S. Overcoming the challenges of membrane protein crystallography. *Curr. Opin. Struct. Biol.* **2008**, *18*, 581-586.
110. IUPAC-IUB Joint Commission on Biochemical Nomenclature (JCBN). The nomenclature of steroids. Recommendations 1989. *Eur. J. Biochem.* **1989**, *186*, 429-458.
111. Bazin, M.-A.; Travert, C.; Carreau, S.; Rault, S.; Kihel, L. E. First synthesis of 7 $\alpha$ - and 7 $\beta$ -amino-DHEA, dehydroepiandrosterone (DHEA) analogues and preliminary evaluation of their cytotoxicity on Leydig cells and TM4 Sertoli cells. *Bioorg. Med. Chem.* **2007**, *15*, 3152-3160.

112. Jana, N.; Nguyen, Q.; Driver, T. G. Development of a Suzuki Cross-Coupling Reaction between 2-Azidoarylboronic Pinacolate Esters and Vinyl Triflates To Enable the Synthesis of [2,3]-Fused Indole Heterocycles. *J. Org. Chem.* **2014**, *79*, 2781-2791.

113. Mori, K.; Nakayama, T.; Sakuma, M. Synthesis of some analogues of blattellastanoside A, the steroidal aggregation pheromone of the German cockroach. *Bioorg. Med. Chem.* **1996**, *4*, 401-408.

## 2. Spatiotemporal Control of Reactivity via Visible Light-Mediated C-H activation Creates Chemically Patterned Carbohydrate Surfaces

### Contributors

*University of Kansas, Department of Medicinal Chemistry:*

- Charlie Fehl: design and synthesis of initial coumarin library; developed immobilization on glass, cellulose, and paper; preliminary photopatterning conditions.

*Universität Regensburg, Institut für Organische Chemie:*

- Peter Schroll: optimized photopatterning conditions; generated data for manuscript.
- Stephan Dankesreiter: UV/Vis characterization of surfaces.
- Prof. Burkhard König: principal investigator.

➤ Published Aug. 2, 2013: *Org. Biomol. Chem.*, **2013**, *11*, 6510-6514.

### 2.1 Introduction

Photochemistry has been utilized for over a century as a renewable and environmentally benign form of chemical activation.<sup>114</sup> Recent advances in photochemical methodology have promoted the continued development of light as “reagent” in organic synthesis.<sup>115</sup> In particular, photocatalysis has enjoyed a renaissance in modern chemistry.<sup>116</sup> These reactions utilize a light-activated catalyst to transduce electromagnetic energy into reactive chemical intermediates.

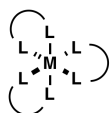
Photocatalysts are often highly conjugated systems that can absorb ultraviolet (UV) or visible light (Scheme 2-1 A).<sup>117</sup> When activated by light absorption, these molecules are able to generate several forms of reactive species, including radicals, radical ions, and triplet state molecules, depending on the substrates and conditions present (Scheme 2-1

B). Some of these species, such as triplet alkenes, are uniquely accessible through photochemical activation. Thus, the field of photocatalysis has promising synthetic utility.

## Scheme 2-1

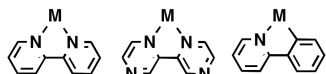
### A. Photocatalysts

Transition metal photocatalysts:



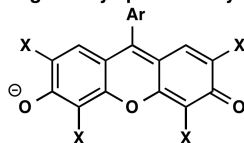
M = Ru, Ir, Cu, Au

L, L =



E.g. Ru(bpy)<sub>3</sub> Ir(bpz)<sub>3</sub> Ir(ppy)<sub>3</sub>

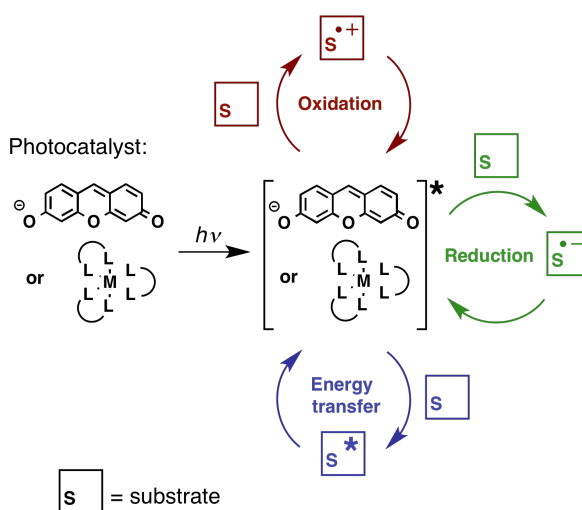
Organic dye photocatalysts:



Eosin Y: X = Br, Ar = 2-carboxyphenyl

Fluorescein: X = H, Ar = 2-carboxyphenyl

### B. photocatalytic reactivity



In contrast to UV light, which readily generates reactive species from organic and biological molecules, most organic molecules are not responsive to visible light. Thus, visible light photocatalysis can be a particularly gentle method of promoting organic reactivity. Some conditions are able to allow good to excellent control of the regio- and stereochemical outcomes of a reaction, as mediated by interactions between substrates and photocatalysts.<sup>118</sup>

When reactants are imprinted on a surface, only the areas of the surface irradiated by light are able to react, enabling techniques such as selective surface patterning. This concept, photolithography, has seen numerous applications in materials<sup>119</sup> and

electronics<sup>120</sup> research. However, drawbacks in many photolithographic technologies include a reliance on metal surfaces<sup>121</sup> and/or high energy radiation to deliver suitable reactivity.<sup>119</sup>

Surface patterning techniques have been recently applied to create interfaces between fabricated materials and biological molecules,<sup>122</sup> including cell surfaces.<sup>123</sup> Biomimetic surfaces can facilitate the study of cell membranes.<sup>124</sup> In another application, the adsorption of chemical cues on surfaces was shown to control cell behavior, particularly useful for the study of neurobiology.<sup>125</sup> Finally, surfaces can be linked with capture agents<sup>126</sup> to create sensors for biological molecules.<sup>127</sup> Thus, various patterned chemical surfaces can be utilized as tools in chemical biology.

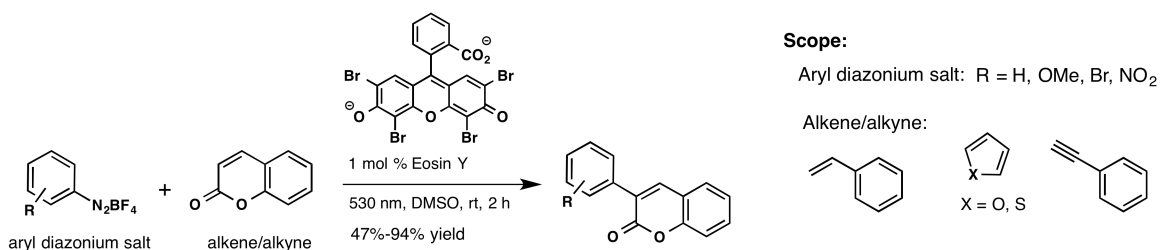
The project presented in this chapter sought to reformulate a visible light-photocatalyzed reaction as a photolithographic surface patterning technique. Specifically, the photo-Meerwein arylation reaction is especially suitable for this aim, as described in the next section.<sup>128</sup> Substrates for this reaction were linked to various surfaces, and in proof-of-concept studies were shown by a color change to afford successful reaction upon irradiation.

The overall goal in developing this technique was to enable a rapid, low-cost method for generating surfaces that could be selectively patterned with diverse chemical functionality. Potential uses for this methodology could follow some of the above examples toward the study of chemical biology.

### 2.1.1 The photo-Meerwein arylation and its potential for controlled surface functionalization

This work utilized the visible light-photocatalyzed photo-Meerwein arylation, which was recently developed by König *et al.* (Scheme 2-2).<sup>128</sup> The photo-Meerwein arylation reaction is akin to the copper-mediated Meerwein arylation reaction, which utilizes a transition metal to generate an aryl radical reactant able to functionalize olefins. The visible light-photocatalyzed generation of these radical species in the photo-Meerwein variant represents a substantial improvement over the traditional metal-catalyzed reaction, which suffers from low yields and the generation of heavy metal byproducts.<sup>129</sup>

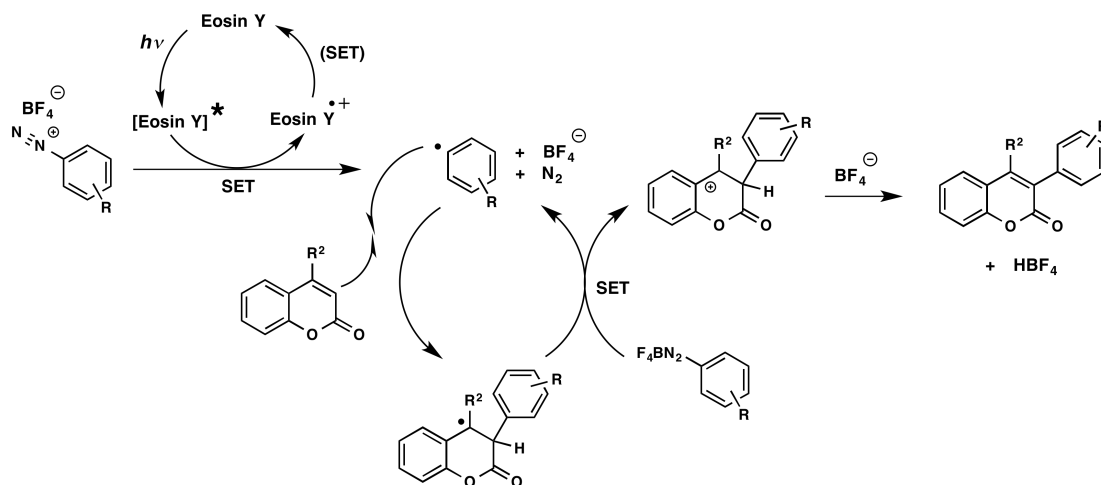
**Scheme 2-2**



The proposed mechanism and catalytic cycle of this reaction is given in Scheme 2-3. Upon visible light photoactivation of the catalyst, a radical reaction is initiated via single electron transfer (SET) to an aryl diazonium salt. This step liberates nitrogen (N<sub>2</sub>), a strong enthalpic driving force for the reaction, and a free aryl radical. This aryl radical species can then combine with a variety of olefins. To propagate the radical reaction, another molecule of the aryl diazonium salt can undergo SET to abstract the radical centered on this intermediate. Deprotonation of the resulting charged species leads to the

formation of the aryl-substituted olefin. The overall process represents a C-H functionalization reaction equivalent.

**Scheme 2-3**



### 2.1.2 Design strategy toward a surface-anchored photo-Meerwein reaction

Several features of the photo-Meerwein reaction were attractive for use in surface functionalization. Most importantly, the scope was broad, which was envisioned to provide flexibility in the design of a surface-anchored substrate. Additionally, this wide scope would increase the utility of surface patterning reactions resulting from this work.

The photo-Meerwein reaction proceeded in good to excellent yield at ambient temperatures, which would simplify the experimental setup. The 2 h reaction time that was originally reported could feasibly be improved by optimization of reaction conditions later in the project. Finally, all reagents were soluble when DMSO was used as the solvent. A homogenous reaction medium provided further flexibility when selecting which component could be anchored to a surface.

However, there were several challenges in formulating an anchored version of this reaction (Figure 2-1). Covalent surface functionalization was necessary to ensure utility. For this strategy to work, the surface localization feature could not hinder the reaction. Finally, a successful reaction would need to be readily detectable.

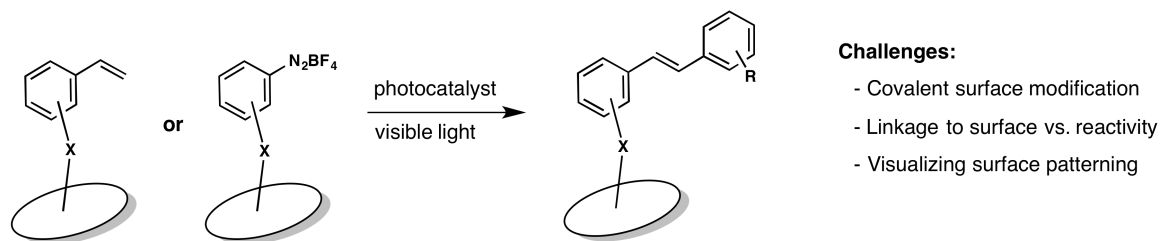
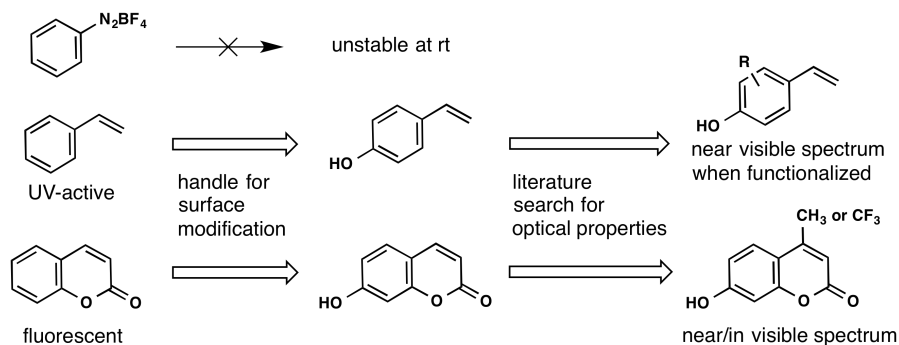


**Figure 2-1.** Schematic of a surface-anchored photo-Meerwein arylation, and the challenges we faced in this work.

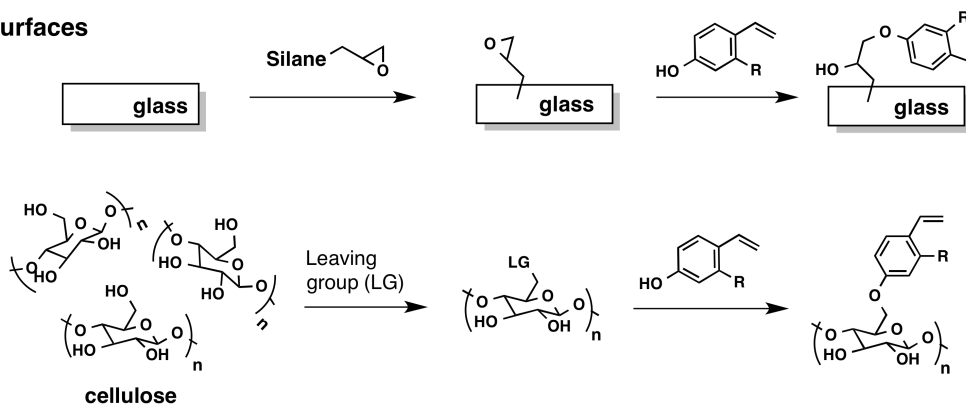
All of these factors were considered in the design aspects of this project (Scheme 2-4). The aryl diazonium salts were quickly discounted as the immobilization substrate since they are unstable to heat. From a scan of possible olefinic substrates for the photo-Meerwein arylation, substituted styrenes and coumarins appeared promising as they are readily functionalized with phenolic groups.<sup>130,131</sup> A phenol could serve as a handle for surface functionalization at a distal site from the reaction center. Coumarins in particular, which are fluorescent, additionally fit the goal of developing a surface reaction detectable using optical properties. Zhang *et al.* reported that methyl or trifluoromethyl substitution at the coumarin 4-position can shift absorbance properties into or near the visible spectrum.<sup>132</sup> Thus, this scaffold was chosen as the highest priority. As a backup, substituted styrenes and especially the stilbene products that would be generated by this reaction may also display visible photoproperties.<sup>133</sup>

## Scheme 2-4

### Substrates



### Surfaces



Glass was initially proposed for the surface medium, since it is readily functionalized through silylation.<sup>134</sup> However, other surfaces were considered. In particular, a previous student in the König group had reported immobilization of photocatalysts on cellulose polymers via tosylation and displacement of the C6-hydroxyl group of the glucose monomer.<sup>135</sup> Both glass and carbohydrate surfaces could form a platform for the study of biological systems.

## 2.2 Methods

### 2.2.1 Substrate synthesis and chromogenic scope of the photo-Meerwein arylation

Hydroxycoumarin substrates were synthesized via Pechmann condensation (Scheme 2-5 A).<sup>136</sup> Hydroxystyrene substrates were synthesized via Knoevenagel condensation of the corresponding benzaldehyde with malonic acid. Heat-mediated decarboxylation generated styrenes (Scheme 2-5 B).<sup>130</sup> Aryl diazonium salts were synthesized using a reported procedure (Scheme 2-5 C).<sup>128</sup> The synthetic procedures and compound characterization data is found in the Experimental Section of this chapter (2.5).

Scheme 2-5

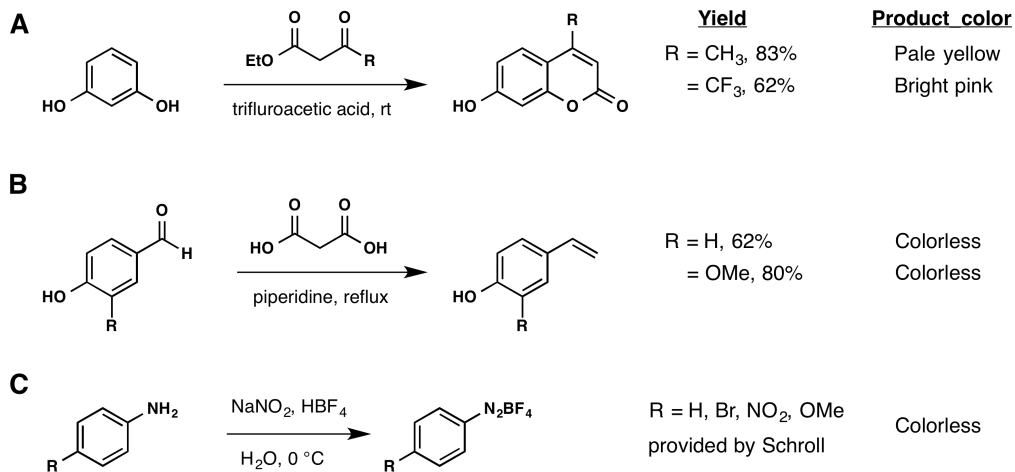
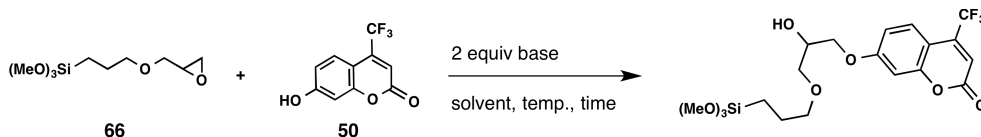


Photo-Meerwein reactions were performed on these substrates as previously reported.<sup>128</sup> Thus, eosin Y-catalyzed photoreactions were initiated with a green LED light source (Philips LUXEON<sup>®</sup> Rebel, P = 1.0 W, 700 mA,  $\lambda_{\text{max}}$  = 530 nm). These conditions were used to identify potential useful photo-Meerwein transformations for surface attachment.

### 2.2.2 Model reaction for glass resin epoxide-opening by coumarin substrates

Our strategy for covalent attachment of photo-Meerwein substrates to glass was based on two reactions. Glass surfaces would be functionalized by silanization, a known procedure.<sup>134</sup> One silane resin suitable for glass is 3-glycidoxypropyltrimethoxysilane (GOPS), which includes an epoxide for further modification. However, the epoxide ring opening of GOPS by these coumarin reactants was unknown. We used a model reaction to optimize these conditions (Scheme 2-6) before proceeding to glass silanization. Various bases and conditions were screened, listed in the Table 2-2 (Section 2.3.2).

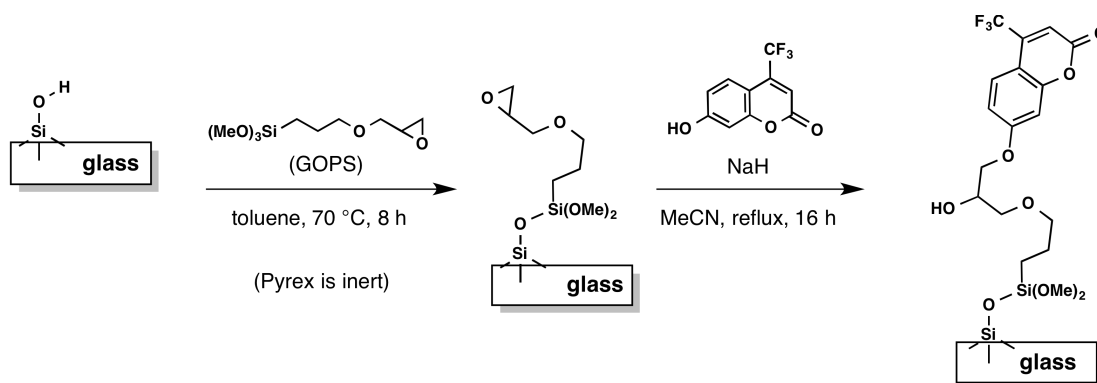
#### Scheme 2-6



### 2.2.3 Glass silylation with GOPS resin and functionalization with hydroxycoumarin substrate

Silica-based glass was cut into 20 mm x 50 mm plates and cleaned rigorously, as described in the Experimental section (2.5). These fit into a 100 mL round-bottomed sodium borosilicate (Pyrex) flask for silanization following a reported procedure.<sup>134</sup> Pyrex is inert to silanization using the conditions employed.<sup>137</sup> The best conditions for the epoxide ring opening reaction developed above were then adapted for reaction on glass plates (Scheme 2-7).

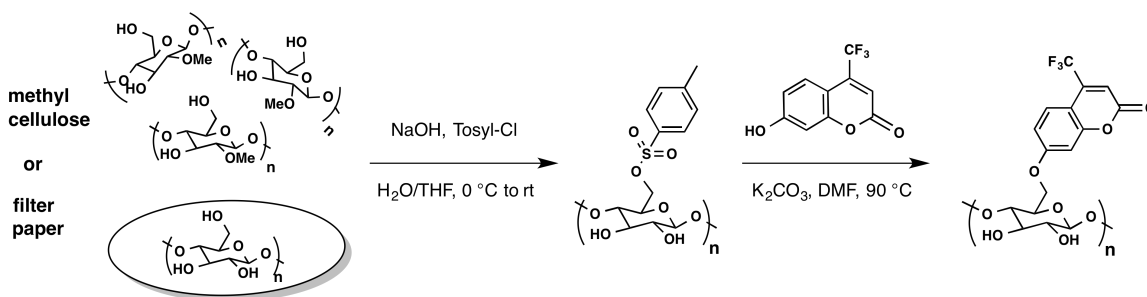
## Scheme 2-7



### 2.2.4 Cellulose polymer and filter paper functionalization

The glucose monomer of cellulose polymers can be modified with nucleophiles via activation of the C6 position with a leaving group (Scheme 2-8). This technique had been developed for methyl cellulose by a previous member of the König group.<sup>135</sup> We realized that filter paper would be a more convenient configuration of cellulose polymers for a membrane-anchored photoreaction, and hence adapted these conditions to paper sheets.

## Scheme 2-8



Thus, Whatman qualitative cellulose filter paper, Grade 1, 11  $\mu\text{m}$  thickness (GE Healthcare Life Sciences, UK) were functionalized under similar conditions as indicated above for methyl cellulose. Functionalized sheets are shown in Figure 2-2.



**Figure 2-2.** Coumarin-functionalized filter paper. A: unfunctionalized. B: 7-hydroxy-4-methylcoumarin-linked. C: 7-hydroxy-4-trifluoromethylcoumarin-linked.

### 2.2.5 Preliminary reactor setup for surface-anchored photo-Meerwein arylation

The coumarin-linked paper sheets were used for proof-of-concept photoreactions. These were placed on aluminum foil and soaked with a DMSO solution of aryl diazonium salt and photocatalyst. The photocatalyst was added to this mixture in the dark, and the solution was kept from ambient light until the reaction was ready. A foil photomask was placed over each sheet to isolate a selected area for the photoreaction. An LED array could be positioned directly over the paper, on cork rings (Figure 2-3).



**Figure 2-3.** Reactor setup. The LED array (left) could be positioned over coumarin-functionalized sheets on foil (middle). Photomasks (bottom) were also cut from foil.

## 2.3 Results and Discussion

### 2.3.1 Identification of a chromogenic photo-Meerwein transformation

Several substrates for the photo-Meerwein arylation were synthesized that incorporated a phenol handle for surface linkage (Figure 2-4 A). We sought to identify a transformation that drastically changed the absorbance or fluorescent properties over the substrate. In particular, **50** was promising insofar as it absorbed light in the visible spectrum, and was brightly colored in ambient light (Figure 2-4 B).

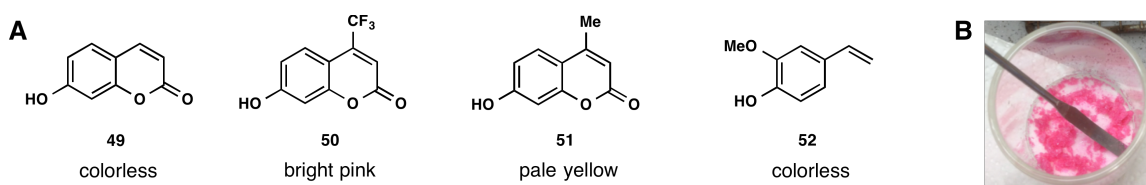


**Figure 2-4.** A: Substrates for photo-Meerwein arylation. B: crystals of **50**.

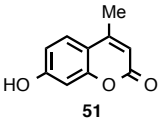
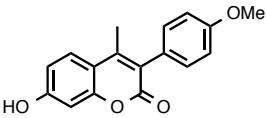
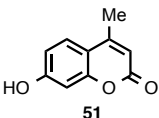
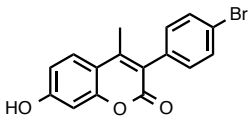
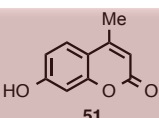
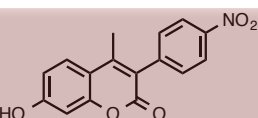
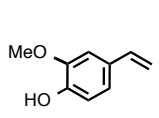
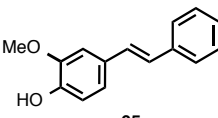
A screen of the eosin Y-photocatalyzed photo-Meerwein arylation of these substrates was performed with various aryl diazonium salts. These results are shown in Table 2-1. We utilized aryl diazonium salts with a range of neutral, electron-donating, electron-withdrawing, and inductive (halogen) substituents. This screen was designed to identify substrates that provided both high yield and useful photoproperties, ideally a strong color change. Colors were determined by visual inspection in ambient light.

**Table 2-1.** Chromogenic scope of the photo-Meerwein reaction

Entry	Substrate	Aryl R	Product	Yield <sup>a</sup>	Color <sup>b</sup>
1		<i>para</i> -H		48	Pale orange
2		<i>para</i> -OMe		25	Yellow
3		<i>para</i> -Br		24	Reddish-orange
4		<i>para</i> -NO <sub>2</sub>		23	yellow
5		<i>para</i> -H		85	Pale yellow
6		<i>para</i> -OMe		67	Dark green
7		<i>para</i> -Br		77	Bright yellow
8		<i>para</i> -NO <sub>2</sub>		56	Very bright yellow
9		<i>para</i> -H		28	Brown

(continued)

Table 2-1, continued

Entry	Substrate	Aryl R	Product	Yield <sup>a</sup>	Color <sup>b</sup>
10		<i>para</i> -OMe		23	Pale orange
11		<i>para</i> -Br		53	Orange-brown
12		<i>para</i> -NO <sub>2</sub>		56	Deep red
13		<i>para</i> -H		49	Pale yellow

<sup>a</sup>Isolated by preparative thin-layer chromatography and recrystallized from ethyl acetate/petroleum ether.

<sup>b</sup>Characterized by visual inspection.

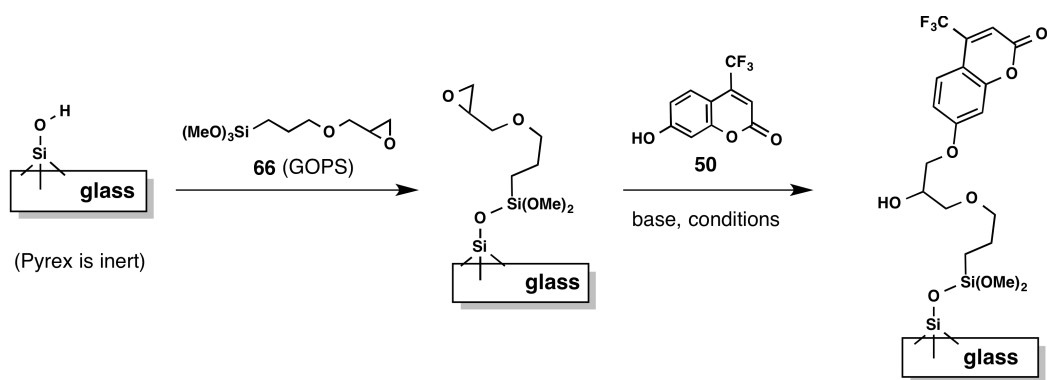
This screen identified several candidate substrate pairs to use in a chromogenic proof-of-concept experiment. The reactions highlighted by their respective colors in Table 2-1 had moderate to good yields, which suggested that sufficient reactivity could be demonstrated in less than 2 h of light exposure. The transformation of styrene **52** to stilbene **65** did not provide promising results, so we did not follow up on this scaffold.

### 2.3.2 Creation of glass surfaces for coumarin-anchored photo-Meerwein arylation

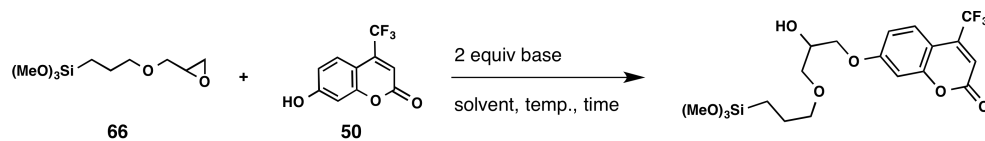
Glass surfaces can be readily functionalized with silane groups bearing various chemical handles, such as aldehydes,<sup>138</sup> amines,<sup>139</sup> and epoxides.<sup>134</sup> These functionalized glass surfaces have found utility in both DNA and protein based microarrays, and as such are compatible with organic and biological molecules.<sup>140</sup>

The least complex form of glass, silica, is readily silanized by alkoxy silanes such as 3-glycidoxypropyltrimethylsilane (GOPS, **66**).<sup>134</sup> In contrast, sodium borosilicate (Pyrex) requires significantly higher temperatures for silanization by these reagents.<sup>137</sup> Thus, we could perform selective silica-based glass silanization reactions in Pyrex flasks. The proposed silanization and functionalization process is shown in Scheme 2-9.

**Scheme 2-9**



To verify whether this strategy could potentially work with substrate **50**, we performed a model study of the ring-opening reaction. Thus, **66** was reacted with **50** under various conditions to identify suitable functionalization conditions. These results are listed in Table 2-2.

**Table 2-2.** Model reaction for GOPS epoxide ring-opening by hydroxycoumarin **50**

Entry	Base	Solvent	Temp. (°C)	Time (h)	Product Formation <sup>a</sup>
1	NaOH	EtOH/H <sub>2</sub> O (1:1)	100	2	none
2	NaOH	EtOH/H <sub>2</sub> O (1:1)	100	16	none
3	K <sub>2</sub> CO <sub>3</sub>	EtOH	80	16	none
4	K <sub>2</sub> CO <sub>3</sub>	DMF	120	16	none
5	NaH	EtOH	80	16	yes
6	NaH	DMSO	100	16	yes
7	NaH	MeCN	80	16	yes <sup>b</sup>

<sup>a</sup>Determined by thin-layer chromatography. The coumarin ether product was green.

<sup>b</sup>Purified via column for analysis by nuclear magnetic resonance (NMR).

With suitable resin functionalization conditions in hand, we turned to glass silanization. We attempted several reported procedures to attach **66** to glass surfaces. These did not give suitable results, as judged roughly by looking at the hydrophobicity of the glass with drops of water. When glass surfaces are silanized by an alkyl silane, a drop of water should form a characteristic round droplet, in comparison to an untreated glass surface.<sup>141</sup>

Professor Michael Schäferling at the University of Regensburg, who had experience in creating silanized glass surfaces, suggested a vigorous cleaning of the glass surfaces. We utilized a “piranha solution” (H<sub>2</sub>SO<sub>4</sub>/H<sub>2</sub>O<sub>2</sub>/H<sub>2</sub>O) to remove organic contaminants and regenerate the free hydroxyl groups on the silica surface for silanization reaction.

Subsequent reaction with **66** led to candidate surfaces for the ring opening reaction. The conditions from Table 2-2, Entry 7 were utilized to install **50** on the glass surfaces. However, upon washing, the glass only acquired a barely detectable green hue through functionalization with **50** (Figure 2-5).

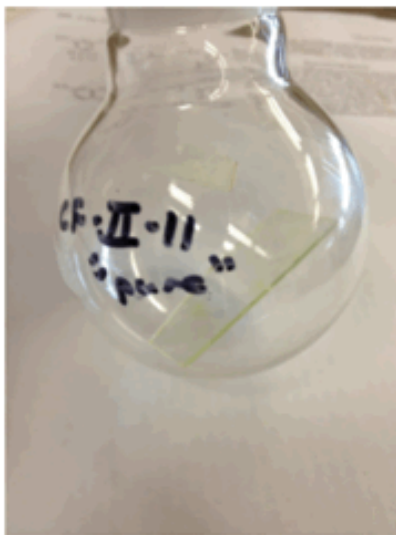


**Figure 2-5.** Glass slide silanized with **66** and functionalized with **50**. The faint green hue was barely detectable by eye.

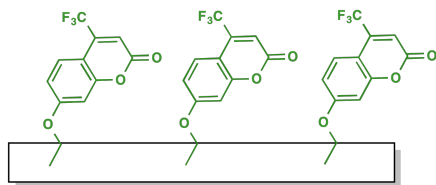
Since silanization only creates a molecular monolayer on the glass surface, this result revealed that **50** did not possess sufficient photoproperties for the determination of successful reactivity by eye. Though we did not characterize the absorbance spectrum of **50** or its products, we hypothesized that creating a thicker layer of this compound could ensure sufficient visibility. Thus, we turned to an alternative surface for functionalization.

### **2.3.3 Creation of functionalized cellulose sheets for anchored photo-Meerwein arylation**

Alternative surfaces for patterned surfaces include various hard materials such as plastics or metals. However, these would presumably also provide monolayers of reagent (Figure 2-6 A), which was unsuitable in the case of glass. Other possible surfaces could include polymer gels,<sup>142</sup> fabrics,<sup>143</sup> or paper.<sup>144</sup> These could provide thicker layers of substrates suitable for visualization (Figure 2-6 B).

### A. Hard surfaces

i.e. Glass, metal, plastic



### B. Porous material

i.e. gel polymers, fabric, paper

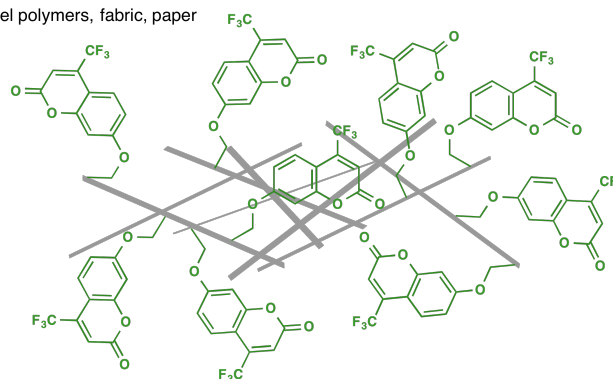
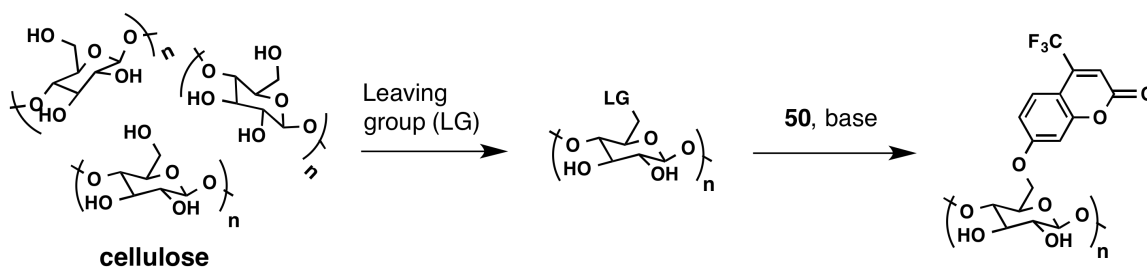


**Figure 2-6.** Various materials for functionalization. A: Hard surfaces present monolayers of material. B: Porous matrices could allow thicker layers of substrate.

In particular, cellulose can be configured as both a polymeric gel or as paper sheets. A previous student in the König lab, Katharina Limm, had immobilized several photocatalysts onto methyl cellulose. Her thesis contained conditions to tosylate the C6-hydroxyl of the glucose monomer for displacement by weak nucleophiles.<sup>135</sup> This concept is illustrated in Scheme 2-10.

### Scheme 2-10



Attempting this sequence on pure methyl cellulose was messy and resulted in a pulp that was difficult to ensure was mixed homogeneously. However, this concept would be readily extended to paper sheets, which are composed primarily of cellulose. To accomplish such a modification, we applied these conditions to standard laboratory filter

paper of 11  $\mu\text{m}$  thickness. Upon drying, this sequence provided colored sheets ready for the photoreaction (Figure 2-7). Peter Schroll later determined the yield of coumarin loading to be  $21\% \pm 3\%$  for **51**.

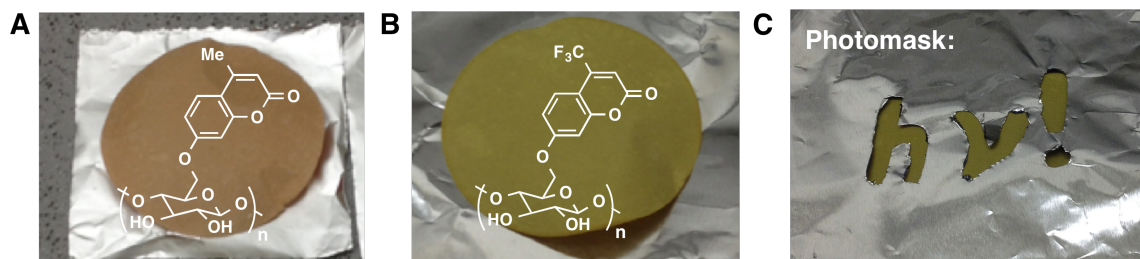


**Figure 2-7.** Coumarin-modified filter paper sheets. A: linked with **51**. B: linked with **50**. C: substrate-linked paper sheet under a photomask.

With suitable substrate-linked surfaces in hand, we were ready to test these in the photo-Meerwein reaction. To ensure control of the reactive conditions, a photomask was used to restrict the area exposed to light (Figure 2-7 C).

### 2.3.4 Preliminary conditions for surface-anchored photoreaction

These paper sheets were readily handled, which simplified the potential photoreactor design. We constructed a simple photoreactor configuration by placing the paper substrates on foil sheets under an LED array mounted on cork rings. This is shown in Figure 2-3 (Section 2.2.5).

The paper sheets used for the substrate immobilization were also absorbent. Thus, we were able to soak a mixture of aryl diazonium salt and catalyst directly onto the sheet, and react upon exposure to light. These conditions worked strikingly well the first time they were attempted, under a 2 h exposure (Figure 2-8). Alternate exposure times were

also briefly screened. These are presented in Table 2-3. Shorter reaction times generated faint images. The residual red color of the sheets is due to residual eosin Y not removed by the wash.

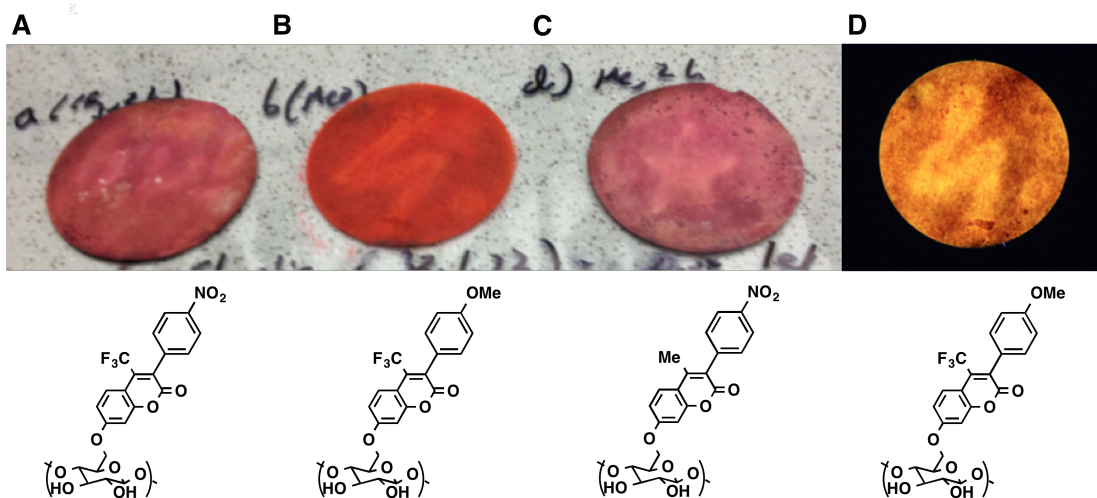
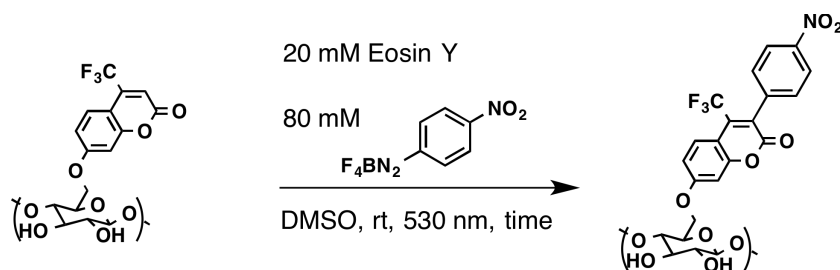


**Figure 2-8.** Photoreaction with coumarin-functionalized sheets. The patterns in the center were created by the photomask. A: Substrate **50** to product **60**. B **50** to **58**. C: **51** to **64**. D: Condition B with UV-excitation.

**Table 2-3.** Reaction time of the surface-anchored photo-Meerwein arylation



Entry	Substrate	Product	Time	Lightsource	Pattern Strength <sup>a</sup>
1	<b>50</b>	<b>60</b>	120 min	LED	Strongly visible
2	<b>50</b>	<b>60</b>	60 min	LED	Visible
3	<b>50</b>	<b>60</b>	15 min	LED	Faintly visible
4	<b>50</b>	<b>60</b>	5 s	Green laser pointer	Undetectable

<sup>a</sup>Determined by visual inspection.

Thus, proof-of-concept and preliminary conditions for a surface-anchored variant of the photo-Meerwein arylation were discovered. This was the end of my involvement on the project, which was completed by Peter Schroll and Stephan Dankesreiter.<sup>145</sup> These students in the König lab performed the necessary reaction controls. In addition, they characterized the surface by absorbance and fluorescence spectroscopy.

The optimized conditions worked out by Schroll utilized Ru(bpy)<sub>3</sub> as the photocatalyst. This improved the reaction time as well as resolution of the work, since this dye could be used in lower amounts and was readily removed from the paper sheets. These results are shown in Figure 2-9. The resolution of this technique is approximately 0.2 mm.

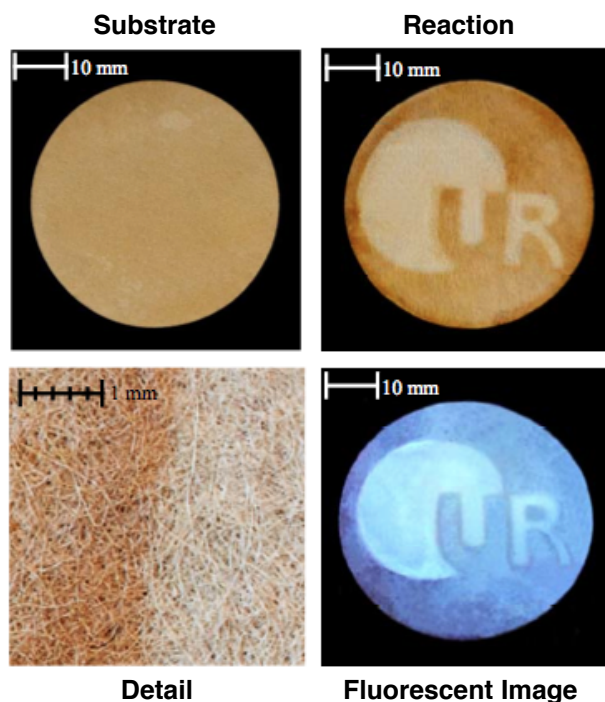


**Figure 2-9.** Optimized surface patterning photo-Meerwein arylation. The surface transformation **51** to **62** provided the best contrast between substrate and product.

## 2.4 Conclusion

This proof-of-concept study entailed the development of a chromogenic version of the photo-Meerwein reaction reported by König *et al.*<sup>128</sup> toward application as a novel method for surface patterning. Coumarins proved especially suitable for this purpose, exhibiting efficient reactivity under the mild conditions that were used, the ability to be linked to various surfaces, and especially a color change that could be detected by eye.

With the identification of suitable substrates, extension of the photo-Meerwein reaction to light-patterned surface functionalization proceeded rapidly, and took the form of covalent, coumarin-linked paper sheets. Use of a photomask gave the desired level of control over which parts of the surface reacted, easily seen by the naked eye, though enhanced by fluorescence upon UV excitation

This project was continued by Peter Schroll, who was able to demonstrate that the absence of photocatalyst, diazonium reactant, or light precluded surface patterning. This suggested that the proposed photocatalyzed reaction was taking place. Further confirmation of this mechanism came from absorbance measurements characterizing the reactants/products in solution phase, which gave analogous photochemical shifts to the surface-linked reactants/products.<sup>145</sup>

This work represents a novel form of chemical surface functionalization, spatially controlled by light. Other substrates can thus be linked to cellulose polymers or paper sheets, providing a simple and cost-effective surface patterning technique. Such applications include the generation of biosensors,<sup>140</sup> surfaces for protein linkage,<sup>122</sup> or model systems for biological membranes,<sup>126,124</sup> with controllable geometry and features.

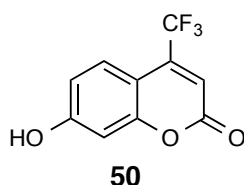
## 2.5 Experimental Section

Nuclear magnetic resonance (NMR) spectra were recorded on a Bruker Avance 300 ( $^1\text{H}$ : 300 MHz,  $^{13}\text{C}$ : 75 MHz,  $T = 295\text{ K}$ ) and a Bruker Avance 400 ( $^1\text{H}$ : 400 MHz,  $^{13}\text{C}$ : 100 MHz,  $T = 295\text{ K}$ ) spectrometer) equipped with a robotic sampler. Unless otherwise noted, all samples were dissolved in MeOD and the shifts expressed in parts per million ( $\delta$ ) relative to residual MeOH as an internal standard ( $\delta$  3.34 ppm  $^1\text{H}$  NMR). Abbreviations are: s, singlet; d, doublet; t, triplet; q, quartet; m, multiplet; dd, doublet of doublets; qd, quartet of doublets; td, triplet of doublets. Preparative thin layer chromatography (PTLC) was carried out on homemade glass plates (20 x 20 cm) coated with silica gel 60 GF254 with ca. 15% calcium sulfate and fluorescent indicator (20 g, Fluka). Column chromatography was performed on silica gel (Merck silica gel Si 40 – 63  $\mu\text{m}$ ). Visible light irradiation was performed with high-power LEDs. Blue light: OSRAM<sup>®</sup> Oslon SSL 80 LD H9GP-3T3U-35 royal-blue LED lamp ( $P = 1.12\text{ W}$ , 700 mA,  $I_{\text{max}} = 455\text{ nm}$ ). Green light: Philips LUXEON<sup>®</sup> Rebel ( $P = 1.0\text{ W}$ , 700 mA,  $I_{\text{max}} = 530\text{ nm}$ ). Solvents were used as analytical grade or dried by standard methods<sup>146</sup> and distilled prior to use if required by the experimental procedure. All reagents and starting materials were purchased from Aldrich, Fluka, VWR, Acros or Schleicher & Schüll and used without further purification.

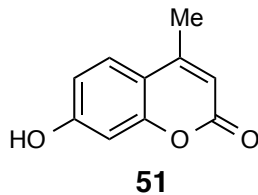
*Synthesis of compounds:*



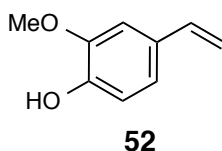
**Aryl diazonium salts.** These reagents were synthesized as previously reported.<sup>128</sup>



**7-Hydroxy-4-(trifluoromethyl)-2H-chromen-2-one (50).** Resorcinol (1 g, 9.1 mmol) and ethyl trifluoroacetoacetate (1.33 mL, 9.1 mmol) were added to a dry round-bottomed flask. Trifluoroacetic acid (4.5 mL, to make a 2 M solution of reagents) was added at room temperature, and the solution stirred overnight. The solution changed from clear to yellow to bright pink. This product is fluorescent on TLC. After completion, product was precipitated by the addition of 20 mL ice water. The solution was stored at 0 °C for 1 hour to facilitate precipitation. Crystals were collected on a sintered filter, washed with ice-cold water, and lyophilized overnight. Bright pink, cube-shaped crystals were isolated, 1.3 g (62%). <sup>1</sup>H-NMR (300 MHz, MeOD): δ 10.98 (s, 1H), 7.57 (d, 1H), 6.92 (d, 1H), 6.84 (s, 1H), 6.76 (s, 1H).

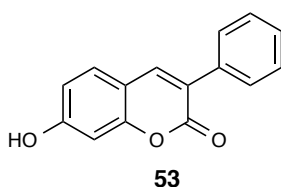


**7-Hydroxy-4-(methyl)-2H-chromen-2-one (51).** The reaction was performed as described for **50**. Resorcinol (1 g, 9.1 mmol) was reacted with ethyl acetoacetate (1.16 mL, 9.1 mmol). Faintly yellow crystals formed to yield 1.32 g (83 %) as a faint yellow solid. <sup>1</sup>H-NMR (300 MHz, MeOD): δ 10.53 (s, 1H), 7.58 (d, 1H), 6.81 (d, 1H), 6.71 (s, 1H), 6.13 (s, 1H), 2.36 (s, 3H).

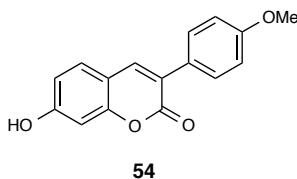


**2-Methoxy-4-vinylphenol (52).** Vanillin (2.5 g, 20.5 mmol) was dissolved in pyridine (80 mL, 0.25 M) and malonic acid (8.55 g, 82 mmol) was added. Piperidine (3.0 mL, 30.8 mmol) was added, and a condenser was attached. The reaction was refluxed for 4 hours. Toluene (100 mL) was added and removed along with the pyridine *in vacuo*. This was repeated, and the crude oil loaded directly onto a silica column. The mixture was purified (30 g silica, 10% to 20% ethyl acetate:petroleum ether) to obtain 2.01 g (80%) of a white solid. <sup>1</sup>H-NMR (300 MHz, MeOD): δ 9.10 (s, 1H), 7.04 (s, 1H), 6.83 (d, 1H), 6.75 (d, 1H), 6.56 (dd, 1H), 5.66 (d, 1H), 5.06 (d, 1H), 3.79 (s, 3H).

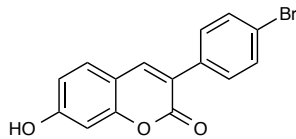
**General procedure for photo-Meerwein arylation.**<sup>128</sup> Eosin Y (7 mg, 0.05 mmol), aryl diazonium tetrafluoroborate (0.2 mmol), and olefin (0.2 mmol) were added to a 5 mL reaction vial. DMSO (to 1 M) was added and the solution immediately de-gassed with three cycles of vacuum (50 mbar) and N<sub>2</sub> atmosphere. The photoreaction was initiated with green high-power LED Lightsource (Philips LUXEON<sup>®</sup> Rebel, P = 1.0 W, 700 mA,  $\lambda_{\text{max}} = 530 \text{ nm}$ ) and allowed to react for 2 hours, jacketed in a water-cooled manifold to maintain ambient temperatures. These reactions were purified by preparative thin-layer crystallography (20% or 33% ethyl acetate:petroleum ether). All products readily crystallized from ethyl acetate/petroleum ether upon standing.



**7-Hydroxy-3-phenyl-2H-chromen-2-one (53).** Isolated 23 mg (48%) as a pale orange solid. <sup>1</sup>H-NMR (300 MHz, MeOD):  $\delta$  7.87 (s, 1H), 7.73 (d, 1H), 7.58 (d, 2H), 7.32 (m, 5H), 6.08 (d, 1H). Matched reported.<sup>147</sup>

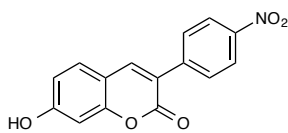


**7-Hydroxy-3-(4-methoxyphenyl)-2H-chromen-2-one (54).** Isolated 13 mg as a yellow solid. <sup>1</sup>H-NMR (300 MHz, MeOD):  $\delta$  7.85 (s, 1H), 7.65 (d, 2H), 7.47 (d, 1H), 7.15 (d, 1H), 6.96 (d, 1H), 6.81 (t, 1H), 6.72 (d, 1H), 3.83 (s, 3H). Matched reported.<sup>148</sup>



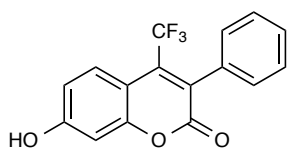
55

**7-Hydroxy-3-(4-bromophenyl)-2H-chromen-2-one (55).** Isolated 15 mg (24%) as a reddish-orange solid.  $^1\text{H-NMR}$  (300 MHz, MeOD):  $\delta$  8.00 (s, 1H), 7.74 (d, 1H), 7.62 (m, 4H), 6.80 (t, 1H), 6.72 (d, 1H). Matched reported.<sup>132</sup>



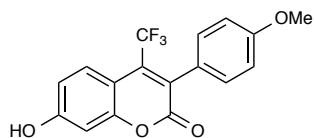
56

**7-Hydroxy-3-(4-nitrophenyl)-2H-chromen-2-one (56).** Isolated 13 mg (23%) as a yellow solid.  $^1\text{H-NMR}$  (300 MHz, MeOD):  $\delta$  8.29 (d, 2H), 7.98 (d, 1H), 7.86 (d, 1H), 7.44 (d, 1H), 6.76 (d, 2H), 6.19 (d, 1H). Matched reported.<sup>149</sup>



57

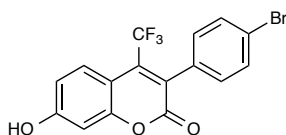
**7-Hydroxy-3-phenyl-4-(trifluoromethyl)-2H-chromen-2-one (57).** Isolated 52 mg (85%) of a pale yellow solid.  $^1\text{H-NMR}$  (300 MHz, MeOD):  $\delta$  7.54 (dd, 1H), 7.43 (dd, 1H), 7.30 (t, 2H), 7.14 (d, 1H), 6.74 (d, 1H), 6.64 (t, 1H), 6.46 (s, 1H). Matched reported.<sup>150</sup>



58

**7-Hydroxy-3-(4-methoxyphenyl)-4-(trifluoromethyl)-2H-chromen-2-one (58).**

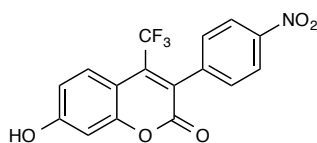
Isolated 45 mg (67%) of a dark green solid.  $^1\text{H-NMR}$  (300 MHz, MeOD):  $\delta$  7.67 (d, 1H), 7.18 (d, 2H), 6.98 (d, 2H), 6.88 (d, 1H), 6.78 (s, 1H), 3.81 (s, 3H). Matched reported.<sup>150</sup>



59

**7-Hydroxy-3-(4-bromophenyl)-4-(trifluoromethyl)-2H-chromen-2-one (59).** Isolated

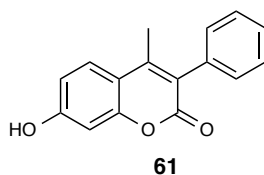
59 mg (77%) of a bright yellow solid.  $^1\text{H-NMR}$  (300 MHz, MeOD):  $\delta$  7.70 (d, 1H), 7.59 (d, 2H), 7.19 (d, 2H), 6.85 (d, 1H), 6.78 (s, 1H).  $^{13}\text{C-NMR}$  not determined.



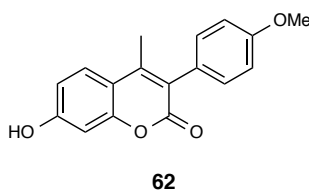
60

**7-Hydroxy-3-(4-nitrophenyl)-4-(trifluoromethyl)-2H-chromen-2-one (60).** Isolated 39

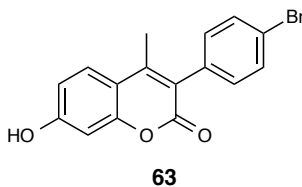
mg (56%) of a very bright yellow solid.  $^1\text{H-NMR}$  (300 MHz, MeOD):  $\delta$  8.28 (d, 2H), 7.67 (d, 1H), 7.55 (d, 2H), 6.90(d, 1H), 6.81 (s, 1H).  $^{13}\text{C-NMR}$  not determined.



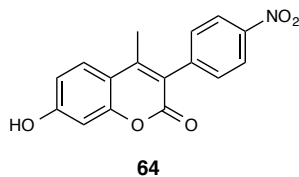
**7-Hydroxy-4-methyl-3-phenyl-2H-chromen-2-one (61).** Isolated 14 mg (28%) of a brown solid. <sup>1</sup>H-NMR (300 MHz, MeOD): δ 7.63 (m, 2H), 7.40 (m, 2H), 7.26 (t, 1H), 6.75 (m, 2H), 6.09 (s, 1H), 2.35 (s, 3H). Matches reported.<sup>151</sup>



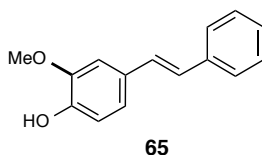
**7-Hydroxy-3-(4-methoxyphenyl)-4-methyl-2H-chromen-2-one (62).** Isolated 11 mg (23%) of a pale orange solid. <sup>1</sup>H-NMR (300 MHz, MeOD): δ 7.58 (m, 2H), 7.19 (d, 1H), 7.10 (d, 1H), 7.00 (d, 1H), 6.84 (t, 1H), 6.73 (d, 1H), 3.83 (s, 3H), 2.69 (s, 3H). Matches reported.<sup>152</sup>



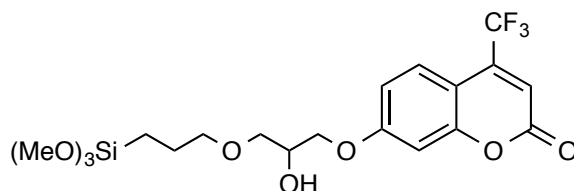
**7-Hydroxy-3-(4-bromophenyl)-4-methyl-2H-chromen-2-one (63).** Isolated 35 mg (53%) of an orange-brown solid. <sup>1</sup>H-NMR (300 MHz, MeOD): δ 7.59 (m, 4H), 7.18 (m, 2H), 6.81 (t, 1H), 6.68 (d, 1H), 2.25 (s, 3H). Matches reported.<sup>153</sup>



**7-Hydroxy-3-(4-nitrophenyl)-4-methyl-2H-chromen-2-one (64).** Isolated 33 mg (56%) of a deep red solid. <sup>1</sup>H-NMR (300 MHz, MeOD): δ 8.29 (d, 1H), 7.65 (d, 1H), 7.56 (d, 1H), 6.81 (t, 1H), 6.66 (d, 1H), 6.05 (s, 1H), 2.36 (s, 3H). Matches reported.<sup>131</sup>



**(E)-2-Methoxy-4-styrylphenol (65).** Isolated 22 mg (49%) of a pale yellow solid. <sup>1</sup>H-NMR (300 MHz, MeOD): δ 7.41-6.66 (m, 11H); matches reported.<sup>154</sup>



*3-Glycidyloxypropyltrimethoxysilane (GOPS, 66) epoxide ring opening model reactions:* A base (1.74 mmol) was added to a dry round-bottomed flask. Dry solvent (5 mL) was added, followed by **50** (0.87 mmol). This mixture was allowed to stir for 5 min at room temperature, and 50 min at 50 °C. A condenser was attached, **66** was added (0.87 mmol), and the solution was brought to the temperature listed in Table 2-2. The mixture was stirred overnight. The solvent was removed and the crude mixture was adsorbed directly onto silica gel for purification and characterization. <sup>1</sup>H-NMR (300 MHz, MeOD): δ 7.53

(d, 1H), 6.91 (d, 1H), 6.82 (s, 1H), 6.74 (s, 1H), 2.5 (s, 9H), 1.96-1 (m, 3H), 1.77 (s, 2H), 1.37 (s, 2H), 1.72-1.23 (m, 3H).

*Silylation of glass plates using GOPS:* Silica-based glass was cut into 20 mm x 50 mm plates and placed into a 100 mL round-bottomed Pyrex flask. The glass was stripped of organic contaminants using a 3:1 mixture of concentrated H<sub>2</sub>SO<sub>4</sub> and 30% H<sub>2</sub>O<sub>2</sub>. This solution was stirred for 2 h at ambient temperature. The plates were then sonicated for 10 min each in acetone, ethanol, and Millipore-filtered water. The plates were submerged in dry toluene and 20 mM of GOPS was added. The solution was heated to 70 °C for 8 h with stirring. The plates were washed with dry toluene and dried under vacuum overnight.

*Conditions for the epoxide ring opening reaction on functionalized glass plates:* Sodium hydride (1.74 mmol) was added to a dry round-bottomed flask as a 60% dispersion in mineral oil. The oil was removed with three petroleum ether washes. Dry acetonitrile (5 mL) was added, followed by 7-hydroxy-4-trifluoromethylcoumarin (0.87 mmol). This mixture was stirred for 5 min at room temperature, then warmed to 50 °C and stirred for 50 min. The silylized glass plate was added, a condenser was attached, and the solution was brought to reflux. The mixture was stirred overnight. The solvent was removed, the plate washed thrice with dry acetonitrile, and dried under vacuum overnight. The plate changed from clear to an almost undetectable green tint.

*Tosylation of methyl cellulose:* Methyl cellulose (13.9 mmol) was dissolved in minimal water. Tetrahydrofuran (THF, 15 mL) and 30 mL of 20% NaOH<sub>aq</sub> were added, and the mixture cooled to 0 °C. A solution of tosyl chloride (16.7 mmol in 15 mL THF) was added dropwise at 0 °C. The mixture was stirred and allowed to slowly rise to ambient temperatures overnight. The gray solid was filtered off and washed with acetone. This was redissolved in minimal water and then precipitated again with acetone. The white solid was filtered again, washed with acetone, and dried under vacuum at 60 °C.

*Tosylation of filter paper:* A stack of filter paper sheets (2.5 g, about 13.9 mmol with respect to glucose) were reacted as for methyl cellulose. However, these were simply placed in a Büchner funnel and rinsed with several washes of acetone before drying.

*Coumarin-linked filter paper:* A solution of hydroxycoumarin **50** or **51** (50 mM) and potassium carbonate (100 mM) was made in dimethylformamide (DMF, 35 mL). Tosylated filter paper was added and the mixture heated to 90 °C. This mixture was gently stirred overnight. The solution was cooled, and the paper was washed several times with water and ethanol. The sheets were dried under vacuum overnight. These sheets turned faintly red when substituted with 7-hydroxy-4-methylcoumarin (Figure 2-2 B) and bright green when substituted with 7-hydroxy-4-trifluoromethylcoumarin (Figure 2-2 C).

*General procedure for paper-linked photo-Meerwein arylation:* A dry, coumarin-substituted paper sheet was laid onto a foil backing. A photomask was cut from another

foil sheet. A DMSO stock solution of 40 mM aryl diazonium, 20 mM Eosin Y was made in the dark. Just enough solution to soak the paper, ca. 0.7 mL, was added via syringe. The photomask was fit over the paper, and the surface was irradiated with a high-power LED (530 nm) at rt for the specified time in Table 2-3. When the reaction was stopped, the paper was kept from light and washed with methanol, water, and acetone. This was air-dried for further characterization. Images were taken with an iPhone camera (ambient light) or a digital camera (UV-light cabinet).

## 2.6 References

114. Emma, E. C. Solar Photochemistry from the Beginnings of Organic Photochemistry to the Solar Production of Chemicals. In *CRC Handbook of Organic Photochemistry and Photobiology, Third Edition - Two Volume Set*, CRC Press: 2012; pp 237-247.
115. Bochet, C. G. 9.13 Organic Photochemistry. In *Comprehensive Organic Synthesis II (Second Edition)*, Knochel, P., Ed. Elsevier: Amsterdam, 2014; pp 330-350.
116. Ravelli, D.; Dondi, D.; Fagnoni, M.; Albini, A. Photocatalysis. A multi-faceted concept for green chemistry. *Chem. Soc. Rev.* **2009**, *38*, 1999-2011.
117. Schultz, D. M.; Yoon, T. P. Solar Synthesis: Prospects in Visible Light Photocatalysis. *Science* **2014**, *343*.
118. Prier, C. K.; Rankic, D. A.; MacMillan, D. W. C. Visible Light Photoredox Catalysis with Transition Metal Complexes: Applications in Organic Synthesis. *Chem. Rev.* **2013**, *113*, 5322-5363.
119. Stehlin, F.; Bourgin, Y.; Spangenberg, A.; Jurlin, Y.; Parriaux, O.; Reynaud, S.; Wieder, F.; Soppera, O. Direct nanopatterning of 100 nm metal oxide periodic structures by Deep-UV immersion lithography. *Opt. Lett.* **2012**, *37*, 4651-4653.
120. Singh, T. B.; Sariciftci, N. S. Progress in Plastic Electronics Devices. *Annu. Rev. Mater. Res.* **2006**, *36*, 199-230.
121. Ji, J.; Zhang, H.; Qiu, Y.; Wang, L.; Wang, Y.; Hu, L. Fabrication and photoelectrochemical properties of ordered Si nanohole arrays. *Appl. Surf. Sci.* **2014**, *292*, 86-92.
122. Ogaki, R.; Alexander, M.; Kingshott, P. Chemical patterning in biointerface science. *Mater. Today* **2010**, *13*, 22-35.
123. Zhao, W.; Teo, G. S. L.; Kumar, N.; Karp, J. M. Chemistry and material science at the cell surface. *Mater. Today* **2010**, *13*, 14-21.
124. Rahmany, M. B.; Van Dyke, M. Biomimetic approaches to modulate cellular adhesion in biomaterials: A review. *Acta Biomater.* **2013**, *9*, 5431-5437.

125. Diaz-Quijada, G. A.; Maynard, C.; Comas, T.; Monette, R.; Py, C.; Krantis, A.; Mealing, G. Surface Patterning with Chemisorbed Chemical Cues for Advancing Neurochip Applications. *Ind. Eng. Chem. Res.* **2011**, *50*, 10029-10035.
126. Jayasundara, D. R.; Duff, T.; Angione, M. D.; Bourke, J.; Murphy, D. M.; Scanlan, E. M.; Colavita, P. E. Carbohydrate Coatings via Aryldiazonium Chemistry for Surface Biomimicry. *Chem. Mater.* **2013**, *25*, 4122-4128.
127. Yoon, S.-J.; Chung, J. W.; Gierschner, J.; Kim, K. S.; Choi, M.-G.; Kim, D.; Park, S. Y. Multistimuli Two-Color Luminescence Switching via Different Slip-Stacking of Highly Fluorescent Molecular Sheets. *J. Am. Chem. Soc.* **2010**, *132*, 13675-13683.
128. Hari, D. P.; Schroll, P.; König, B. Metal-Free, Visible-Light-Mediated Direct C–H Arylation of Heteroarenes with Aryl Diazonium Salts. *J. Am. Chem. Soc.* **2012**, *134*, 2958-2961.
129. Hari, D. P.; König, B. The Photocatalyzed Meerwein Arylation: Classic Reaction of Aryl Diazonium Salts in a New Light. *Angew. Chem., Int. Ed.* **2013**, *52*, 4734-4743.
130. Simpson, C. J.; Fitzhenry, M. J.; Stamford, N. P. J. Preparation of vinylphenols from 2- and 4-hydroxybenzaldehydes. *Tetrahedron Lett.* **2005**, *46*, 6893-6896.
131. Gadre, J. N. K., R.A. Synthesis of 3-Aryl-4-Methyl-Hydroxy Coumarins. *Curr. Sci.* **1969**, *38*, 340.
132. Zhang, Y.-y. W., Xin-liang; Meng, Xian-mei, Xu, Long-he. Study on the synthesis and spectra characteristics of coumarins. *Ranliao Yu Ranse* **2003**, *40*, 68-70.
133. Li, Z.; Wu, K.; Su, G.; He, Y. Nonlinear optical properties of some derivatives of stilbene and vinyl cyanide. *Optical Materials* **2002**, *20*, 295-299.
134. Schüler, T.; Nykytenko, A.; Csaki, A.; Möller, R.; Fritzsche, W.; Popp, J. UV cross-linking of unmodified DNA on glass surfaces. *Anal. Bioanal. Chem.* **2009**, *395*, 1097-1105.
135. Limm, K. Immobilization of Triplet Sensitizers on Polymer Surfaces. University of Regensburg, 2011.

136. Woodruff, E. H. 4-methylcoumarin. *Organic Synthesis* **1944**, 1944, 69.
137. Deyhimi, F.; Coles, J. A. Rapid Silylation of a Glass Surface: Choice of Reagent and Effect of Experimental Parameters on Hydrophobicity. *Helv. Chim. Acta* **1982**, *65*, 1752-1759.
138. Song, J.; Chen, J.; Klapperich, C. M.; Eng, V.; Bertozzi, C. R. Functional glass slides for in vitro evaluation of interactions between osteosarcoma TE85 cells and mineral-binding ligands. *J. Mater. Chem.* **2004**, *14*, 2643-2648.
139. Oh, S. J.; Cho, S. J.; Kim, C. O.; Park, J. W. Characteristics of DNA Microarrays Fabricated on Various Aminosilane Layers. *Langmuir* **2002**, *18*, 1764-1769.
140. Oh, S. J.; Hong, B. J.; Choi, K. Y.; Park, J. W. Surface modification for DNA and protein microarrays. *OMICS* **2006**, *10*, 327-343.
141. Labit, H.; Goldar, A.; Guilbaud, G.; Douarche, C.; Hyrien, O.; Marheineke, K. A simple and optimized method of producing silanized surfaces for FISH and replication mapping on combed DNA fibers. *Biotechniques* **2008**, *45*, 649-652, 654, 656-648.
142. Patil, Y. B.; Toti, U. S.; Khair, A.; Ma, L.; Panyam, J. Single-step surface functionalization of polymeric nanoparticles for targeted drug delivery. *Biomaterials* **2009**, *30*, 859-866.
143. Abidi, N.; Cabrales, L.; Hequet, E. Functionalization of a cotton fabric surface with titania nanosols: applications for self-cleaning and UV-protection properties. *ACS Appl. Mater. Interfaces* **2009**, *1*, 2141-2146.
144. Ngo, Y. H.; Li, D.; Simon, G. P.; Garnier, G. Paper surfaces functionalized by nanoparticles. *Adv. Colloid Interface Sci.* **2011**, *163*, 23-38.
145. Schroll, P.; Fehl, C.; Dankesreiter, S.; Konig, B. Photocatalytic surface patterning of cellulose using diazonium salts and visible light. *Org. Biomol. Chem.* **2013**, *11*, 6510-6514.
146. Schwetlick, K. *Organikum*. Wiley-VCH: 2009.

147. Yang, J.; Liu, G.-Y.; Dai, F.; Cao, X.-Y.; Kang, Y.-f.; Hu, L.-M.; Tang, J.-J.; Li, X.-Z.; Li, Y.; Jin, X.-L.; Zhou, B. Synthesis and biological evaluation of hydroxylated 3-phenylcoumarins as antioxidants and antiproliferative agents. *Bioorg. Med. Chem. Lett.* **2011**, *21*, 6420-6425.
148. Bondarenko, S.; Frasinuk, M.; Vinogradova, V.; Khilya, V. Synthesis of flavonoid derivatives of cytosine. 1. aminomethylation of 7-hydroxy-3-arylcoumarins. *Chem. Nat. Compd.* **2010**, *46*, 771-773.
149. Buu-Hoi, N. P.; Saint-Ruf, G.; Lobert, B. Oxygen heterocycles. Part XIV. Hydroxylated 3-aryl- and 3-pyridyl-coumarins. *J. Chem. Soc. C* **1969**, 2069-2070.
150. Nishiwaki, T. K., Hirofumi. 3-Oxo-4,4,4-trifluorobutyronitriles as building blocks of trifluoromethyl substituted heterocycles Heterocyclization to 3-aryl-4-trifluoromethyl-2 -1-benzopyran-2-ones under hoesch reaction conditions. *J. Heterocycl. Chem.* **1994**, *31*, 889-892.
151. Liu, J.; Nguyen, T. T.; Dupart, P. S.; Sridhar, J.; Zhang, X.; Zhu, N.; Stevens, C. L. K.; Foroozesh, M. 7-Ethynylcoumarins: Selective Inhibitors of Human Cytochrome P450s 1A1 and 1A2. *Chem. Res. Toxicol.* **2012**, *25*, 1047-1057.
152. Bondarenko, S.; Frasinuk, M.; Khilya, V. Aminomethylation of 3-aryl-7-hydroxycoumarins. *Chem. Heterocycl. Compd. (N. Y., NY, U. S.)* **2010**, *46*, 529-535.
153. Raj, H. G.; Parmar, V. S.; Jain, S. C.; Goel, S.; Himanshu, P.; Malhotra, S.; Singh, A.; Olsen, C. E.; Wengel, J. Mechanism of Biochemical Action of Substituted 4-Methylbenzopyran-2-ones. Part I: Dioxygenated 4-Methyl Coumarins as Superb Antioxidant and Radical Scavenging Agents. *Bioorg. Med. Chem.* **1998**, *6*, 833-839.
154. Sinha, A. K.; Kumar, V.; Sharma, A.; Sharma, A.; Kumar, R. An unusual, mild and convenient one-pot two-step access to (E)-stilbenes from hydroxy-substituted benzaldehydes and phenylacetic acids under microwave activation: a new facet of the classical Perkin reaction. *Tetrahedron* **2007**, *63*, 11070-11077.

### 3. Studies Toward Overcoming Product Inhibition in Catalysis of the Intramolecular Schmidt Reaction

#### Contributors

*University of Kansas, Department of Medicinal Chemistry:*

- Dr. Sze-Wan Li: initial screen of catalyst/conditions for Schmidt chemistry.
- Dr. Erin Hirt: began optimizing Sc(OTf)<sub>3</sub> catalyst conditions.
- Charlie Fehl: finalized Sc(OTf)<sub>3</sub> conditions, characterization of reaction kinetics.
- Patrick Porubsky: assay development for product formation and selectivity.
- Dr. Hashim Motiwala: additional screening that led to improved conditions
- Prof. Jeffrey Aubé: principal investigator.

➤ Published May. 20, 2013: *J. Am. Chem. Soc.*, **2013**, *135*, 9000-9009.

#### 3.1 Introduction

The amide bond appears commonly in biological molecules.<sup>1</sup> Its strength, stability, and planarity have contributed to its utility in the inorganic,<sup>155</sup> material,<sup>156</sup> and medicinal<sup>157</sup> sciences. Reviewing an issue of the *Journal of Natural Products* will inevitably yield a rich display of amide- or peptide bond-containing targets, the syntheses of which often require efficient construction of this bond type.

Numerous chemical methods in amide bond formation have been described, many of which are based on coupling an activated acid derivative with a free amine (Scheme 3-1, A).<sup>158</sup> There are several drawbacks to this approach, including the need for protecting groups to ensure regiochemical control and the generation of byproducts resulting from stoichiometric amounts of coupling agents. Despite these limitations, this technique is by

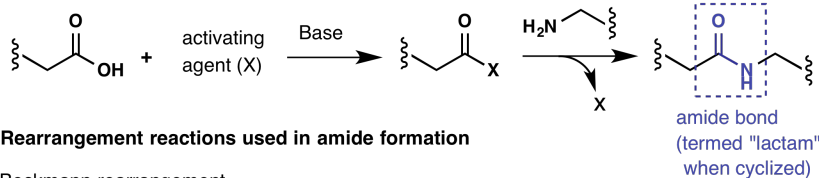
far the most extensively utilized for amide generation in medicinal chemistry, polymer synthesis, and total synthetic applications.<sup>159</sup>

Several rearrangement reactions can also be used to synthesize amide and lactam bonds. The Beckmann, Curtius, and Schmidt reactions are the most commonly applied of these rearrangements (Scheme 3-1 B).<sup>160</sup> Such operations allow additional flexibility in the syntheses of amides and lactams by offering alternative bond disconnections. These reactions also enjoy relatively widespread use, and are featured as key steps in the total syntheses of several natural products.<sup>161, 162,162,163</sup>

The Schmidt reaction in particular can efficiently generate primary, secondary, and tertiary amides and lactams. This reaction has been studied extensively in our laboratory.<sup>164</sup> The following section presents an overview of the Schmidt reaction relevant to the present project.

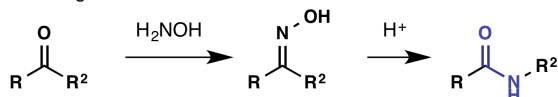
### Scheme 3-1

#### A - Acid and peptide coupling sequence for amide formation

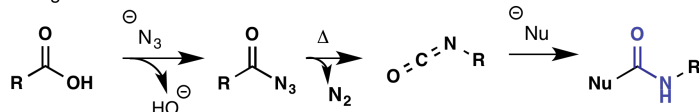


#### B - Rearrangement reactions used in amide formation

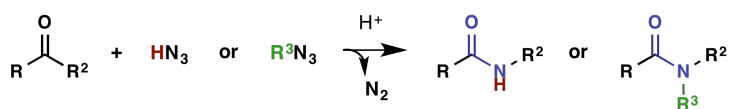
##### Beckmann rearrangement



##### Curtius rearrangement



##### Schmidt reaction

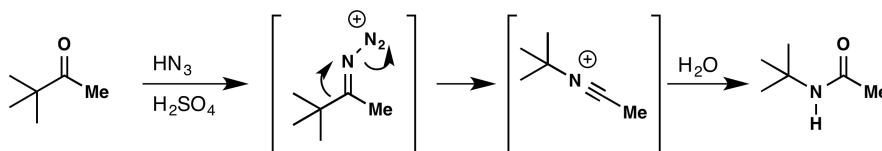


### 3.1.1 The Schmidt reaction, and the discovery of its intramolecular variant

The term “Schmidt reaction” denotes a class of reactions in which an electrophile is functionalized with a nucleophilic azide-containing reactant. These reactions are thermodynamically favored by the expulsion of nitrogen ( $N_2$ ), a strong enthalpic driving force.<sup>165</sup> The first such reaction was discovered in 1924 by K. F. Schmidt<sup>166</sup> and subsequently developed by P. A. S. Smith.<sup>167</sup> Schmidt discovered that carbonyl groups could be converted into primary and secondary amides upon treatment with hydrazoic acid ( $HN_3$ ) under acidic conditions (Scheme 3-2).<sup>166</sup> This reaction has been well studied and has seen regular use.<sup>168</sup> However, the reaction was found to fail under the original conditions when  $HN_3$  was substituted by an alkyl azide ( $RN_3$ ).<sup>169,167</sup>

#### Scheme 3-2

The classical Schmidt reaction (Schmidt, 1924)



#### Limitation

· Alkyl substituted azides do not react

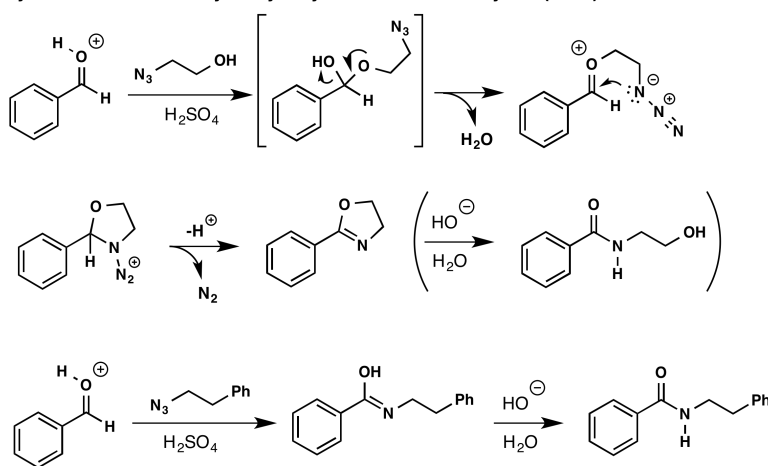
Three decades later, the work of Boyer established that hydrazoic acid could be replaced by select alkyl azides but only when an aromatic aldehyde was the electrophilic partner (Scheme 3-3, below).<sup>170</sup> In this work, Boyer also showed that superior yields could be obtained when hydroxyalkyl azides were reacted with aldehydes, resulting in the formation of oxazolines.

The efficiency of hydroxyalkyl azides in this reaction was initially attributed by Boyer to superior stability of the reagents under acidic conditions, but this mechanistic picture was substantially revised several decades later.<sup>171</sup> Thus, Milligan and Aubé proposed the

first step of the reaction to be carbonyl attack by the alcohol.<sup>172</sup> Dehydration of the resulting hemiacetal subsequently activates intramolecular azide addition. Loss of a proton and nitrogen ( $N_2$ ) finally affords the oxazoline. It was later shown by Aubé and coworkers that these oxazoline products could be hydrolyzed to the secondary amide under alkaline aqueous conditions (Scheme 3-3).<sup>173</sup>

### Scheme 3-3

Boyer's contribution - hydroxylalkyl azides and aldehydes (1955)



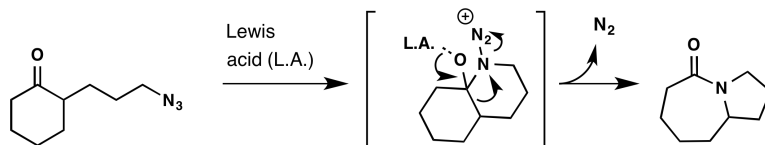
#### Limitation

- Ketones do not react
- Requires  $\beta$ -alcohol for good yield (77%)
- (Amide formation later demonstrated by Aubé)
- Aliphatic azides provide poor yield (10%)

In 1991, Aubé and Milligan further extended the utility of the Schmidt reaction by engineering a different intramolecular reaction pair. By tethering the azide to the carbonyl group, upon acidic activation even substituted alkyl azides could efficiently react with ketones (Scheme 3-4).<sup>164</sup> Heretofore, neither of these less-reactive components had been successfully reacted. This finding greatly extended the scope of the reaction, in particular facilitating the synthesis of bicyclic lactams from keto azides.

### Scheme 3-4

Aubé's contribution - the intramolecular Schmidt reaction (1991)



#### Limitation

- Requires excess acid due to product inhibition (discussed below)

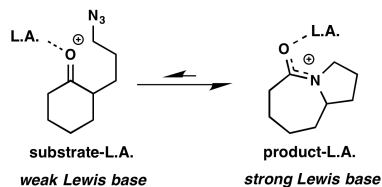
Despite these advances, when we undertook this project there were no existing reports of a substoichiometric catalytic system to promote the reaction.<sup>174</sup> In developing catalytic conditions for the intramolecular Schmidt reaction, we envisioned a reduction in waste and harshly acidic conditions. Improving these aspects could extend the scope and industrial capabilities of this transformation. The specific issues surrounding the identification of a suitable catalyst for the Schmidt reaction and related transformations are discussed in the next section.

#### 3.1.2 Product inhibition hinders acid turnover for a catalytic Schmidt reaction

The classical Schmidt reactions, which use carbonyl compounds as the electrophile, require strongly acidic conditions. These promote the initial attack on the carbonyl by the weakly nucleophilic azide group. As described above, these transformations generate amide and lactam products. Such amide product species are stronger Lewis bases, i.e. better able to sequester Lewis acids (including protons), than their aldehyde or ketone precursors. This is illustrated in Scheme 3-5 A. Extending this concept, a proposed catalytic cycle for the intramolecular Schmidt reaction under general conditions is drawn in Scheme 3-5 B. This scheme highlights the acid dissociation step as rate-limiting in the proposed cycle.

## Scheme 3-5

### A. Product inhibition: L.A. does not dissociate

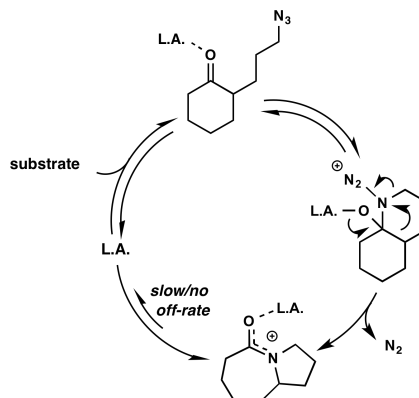


### C. Project overview:

Goal: Develop general conditions that use substoichiometric acids over a wide scope

- Approach:
- Screen catalysts and/or conditions that turn over
  - or
  - Screen additives and co-catalysts to displace L.A.

### B. Proposed cycle:



The related Beckmann rearrangement is also susceptible to identical product inhibition. However, catalyst systems have recently been developed for this transformation (Scheme 3-6).<sup>175,176</sup> These conditions required prolonged heating, and were strongly dependent on the reported solvent system for efficient conversion. However, the catalyst loading could be quite low, especially when the reaction is carried out in hexafluoroisopropanol (HFIP).

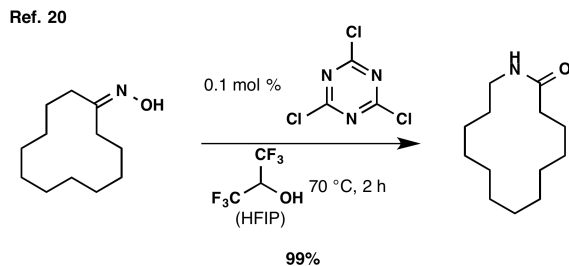
## Scheme 3-6

### Catalysis in the Beckmann rearrangement (late-2000s)



#### Other solvents: < 6% conversion

THF, DMF, acetone, DMA, 1,4-dioxane  
DMSO, hexane, DCE, toluene



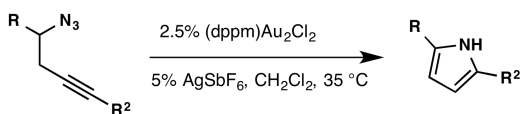
#### Other solvents: < 22% conversion

MeCN, AcOH, *tert*-BuOH

A variant of the Schmidt reaction, the acetylenic Schmidt reaction, has also been successfully catalyzed by gold (I) complexes (Scheme 3-7 A).<sup>177</sup> This reaction proceeds through the alternative mechanism depicted in Scheme 3-7 B. The catalytic gold (I) complex is generated by the silver co-catalyst, a halide scavenger.<sup>178</sup> In contrast to the classical or azide-mediated Schmidt reactions, this method does not generate an amide bond, and the reported substrates did not include any amide-containing species. Thus, it is unlikely that this reaction would suffer similar product inhibition as discussed above.

### Scheme 3-7

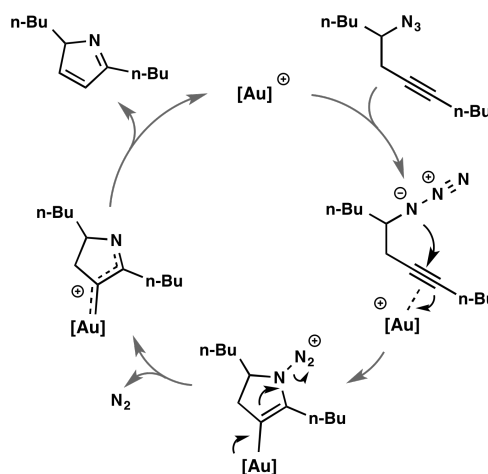
#### A. Gold-catalyzed acetylenic Schmidt reaction (2005)



#### Key factors in this catalyst system:

- Au-alkyne is a soft-soft interaction
- Ag salt is a co-catalyst; generates [Au] *in situ*
- Lack of strong Lewis bases in substrate scope (i.e. no amides) precludes the product inhibition observed in carbonyl-Schmidt reactions

#### B. Hypothetical cycle:



Another key difference between the acetylenic Schmidt reaction and Schmidt reactions that proceed through carbonyl electrophiles is the nature of the interaction between the activator and the electrophile. The acetylenic Schmidt reaction is promoted by a soft base-soft acid interaction between the alkyne and the gold Lewis acid. Such complexes are often highly reactive and labile,<sup>179</sup> as is the case in this reaction. In contrast, the Lewis acids often used for the carbonyl-based Schmidt reaction include

titanium (IV) tetrachloride (TiCl<sub>4</sub>), boron trifluoride diethyl etherate (BF<sub>3</sub>•OEt<sub>2</sub>), and strong protic acids like trifluoroacetic acid (TFA).<sup>174</sup> These are hard acid species, and their interaction with the amide carbonyl, a hard base species, can form stable complexes.<sup>179</sup> Thus, the classical Schmidt reactions of azides with carbonyls had resisted all attempts at acid-based catalysis when we began this work.<sup>174</sup>

The aim of this project was to take this common feature of the Schmidt reaction – its dependence on excess strong, hard acids – and develop a substoichiometric acid catalyst system for the intramolecular Schmidt reaction of carbonyls with azides (Scheme 3-5, C). The overall goal of this work was to reduce the waste and caustic conditions of the Schmidt reaction by reducing the amount of acid necessary for completion. We looked to thereby make the intramolecular Schmidt reaction more efficient, which could improve the scalability of this transformation.

### **3.1.3 Previous work in our laboratory toward overcoming product inhibition**

Prior to my involvement in the project, two researchers in our laboratory had carried out preliminary work to identify substoichiometric catalyst systems for the intramolecular Schmidt reaction. Dr. Sze-Wan Li conducted a screen of acids at substoichiometric loading levels in search of a system that revealed catalyst turnover. Selected results of this work are summarized in Table 3-1. Nuclear magnetic resonance (NMR) was used to detect percent conversion.

**Table 3-1.** Selected substoichiometric Schmidt conditions screened by Li

Entry	Conditions	Conversion to product <sup>a</sup>	Isolated yield <sup>b</sup>
1	5 mol % CuSO <sub>4</sub> , H <sub>2</sub> O, 180 °C, 4 h	37%	ND
2	5 mol % CuSO <sub>4</sub> , THF, 120 °C, 4 h	No Reaction	ND
3	5% TiCl <sub>4</sub> , CH <sub>2</sub> Cl <sub>2</sub> , rt, 16 h	8%	ND
4	10 mol % Sc(OTf) <sub>3</sub> , CH <sub>2</sub> Cl <sub>2</sub> , rt, 16 h	10%	ND
5	5 mol % Sc(OTf) <sub>3</sub> , C <sub>2</sub> H <sub>4</sub> Cl <sub>2</sub> , reflux, 2 h	17%	ND
6	5 mol % Sc(OTf) <sub>3</sub> , <i>t</i> -BuOH, 140 °C, 4 h	26%	ND
7	10 mol % Sc(OTf) <sub>3</sub> , MeCN, 80 °C, 16 h	47%	ND
8	5 mol % Sc(OTf) <sub>3</sub> , THF/H <sub>2</sub> O, 180 °C, 4 h	59%	ND
9	5 mol % Sc(OTf) <sub>3</sub> , H <sub>2</sub> O, 160 °C, 16 h	80%	ND
10	5 mol % Sc(OTf) <sub>3</sub> , H <sub>2</sub> O, 180 °C, 16 h	> 95%	78%

<sup>a</sup>Determined by NMR.

<sup>b</sup>ND – not determined.

In this work, Li found that a few Lewis acids were indeed able to proceed through a catalytic cycle, although all successful substoichiometric reactions required strong heating conditions to allow turnover. In addition, increased solvent polarity seemed to correlate with increased reactivity. One condition afforded full conversion, namely 5% Sc(OTf)<sub>3</sub> in water at 180 °C.

This result was further explored by Erin Hirt in her dissertation research.<sup>180</sup> Hirt investigated several aspects of these aqueous conditions. Selected results are summarized in Table 3-2, below. Other solvents were screened, such as methylene chloride, alcohols, and mixtures of water with dichloroethane, but these were found to be inferior or failed entirely to promote turnover. Hirt also reported that including the phase transfer catalyst tetrabutylammonium hydroxide (*n*-Bu<sub>4</sub>NOH) in water could expand the reaction scope beyond the cyclohexanone substrate (Table 3-2, Entry 6).

Despite these endeavors, several substrates that readily underwent Schmidt reactions in excess acid failed to react under Hirt's optimized conditions. In addition, several other lanthanide triflate Lewis acids beyond Scandium were screened, but all were less effective than the original Sc(OTf)<sub>3</sub> hit.

The above studies by Li and Hirt demonstrated that the Lewis acid Sc(OTf)<sub>3</sub> could act as a suitable catalyst toward some substrates for the intramolecular Schmidt reaction under conditions with strong heating. The unsuccessful screens for other solvents, as well as other lanthanide Lewis acids, suggested that there was either something special about Sc(OTf)<sub>3</sub> or that its reactivity in the Schmidt reaction was strictly limited to certain conditions and substrates. It was clear that further improvements would be necessary to render these conditions useful and general.

**Table 3-2.** Preliminary catalyst and substrate screening in H<sub>2</sub>O by Hirt<sup>180</sup>

Entry	Substrate	Conditions	Product	% Yield (conversion) <sup>a</sup>
1		5 mol % Sc(OTf) <sub>3</sub> , H <sub>2</sub> O, 180 °C, 4 h		(50)
2		10 mol % Sc(OTf) <sub>3</sub> , H <sub>2</sub> O, 180 °C, 4 h		73 (> 95)
3		25 mol % AuCl, H <sub>2</sub> O, 180 °C, 4 h		41 (> 95)
4		10 mol % Sc(OTf) <sub>3</sub> , H <sub>2</sub> O, 180 °C, 4 h		No reaction
5		25 mol % Sc(OTf) <sub>3</sub> , H <sub>2</sub> O, 180 °C, 4 h		No reaction
6		<b>25 mol % Sc(OTf)<sub>3</sub>, 10% <i>n</i>-Bu<sub>4</sub>NOH, H<sub>2</sub>O, 180 °C, 4 h</b>		<b>54 (&gt; 95)</b>
7		25 mol % Yb(OTf) <sub>3</sub> , 10% <i>n</i> -Bu <sub>4</sub> NOH, H <sub>2</sub> O, 180 °C, 4 h		(38)
8		25 mol % Eu(OTf) <sub>3</sub> , 10% <i>n</i> -Bu <sub>4</sub> NOH, H <sub>2</sub> O, 180 °C, 4 h		(31)
9		25 mol % Pr(OTf) <sub>3</sub> , 10% <i>n</i> -Bu <sub>4</sub> NOH, H <sub>2</sub> O, 180 °C, 4 h		(20)
10		25 mol % Nd(OTf) <sub>3</sub> , 10% <i>n</i> -Bu <sub>4</sub> NOH, H <sub>2</sub> O, 180 °C, 4 h		(24)
11		25 mol % Sc(OTf) <sub>3</sub> , 10% <i>n</i> -Bu <sub>4</sub> NOH, H <sub>2</sub> O, 180 °C, 4 h		60
12		25 mol % Sc(OTf) <sub>3</sub> , 10% <i>n</i> -Bu <sub>4</sub> NOH, H <sub>2</sub> O, 180 °C, 4 h		45
13		25 mol % Sc(OTf) <sub>3</sub> , 10% <i>n</i> -Bu <sub>4</sub> NOH, H <sub>2</sub> O, 180 °C, 4 h		55 <sup>b</sup>
14		25 mol % Sc(OTf) <sub>3</sub> , 10% <i>n</i> -Bu <sub>4</sub> NOH, H <sub>2</sub> O, 180 °C, 4 h		31
15		25 mol % Sc(OTf) <sub>3</sub> , 10% <i>n</i> -Bu <sub>4</sub> NOH, H <sub>2</sub> O, 180 °C, 4 h		No reaction <sup>c</sup>
16		25 mol % Sc(OTf) <sub>3</sub> , 10% <i>n</i> -Bu <sub>4</sub> NOH, H <sub>2</sub> O, 180 °C, 4 h		No reaction <sup>b,d</sup>
17		25 mol % Sc(OTf) <sub>3</sub> , 10% <i>n</i> -Bu <sub>4</sub> NOH, H <sub>2</sub> O, 180 °C, 4 h		No reaction <sup>b,e</sup>
18		25 mol % Sc(OTf) <sub>3</sub> , 10% <i>n</i> -Bu <sub>4</sub> NOH, H <sub>2</sub> O, 180 °C, 4 h		No reaction <sup>b,f</sup>

<sup>a</sup>Isolated yield. % Conversion determined by NMR.

<sup>b</sup>Stereochemistry not characterized.

<sup>c</sup>Reported 75% yield with excess TFA.<sup>172</sup>

<sup>d</sup>Reported 82% yield with excess TiCl<sub>4</sub>.<sup>181</sup>

<sup>e</sup>Reported 55% yield with excess triflic acid.<sup>182</sup>

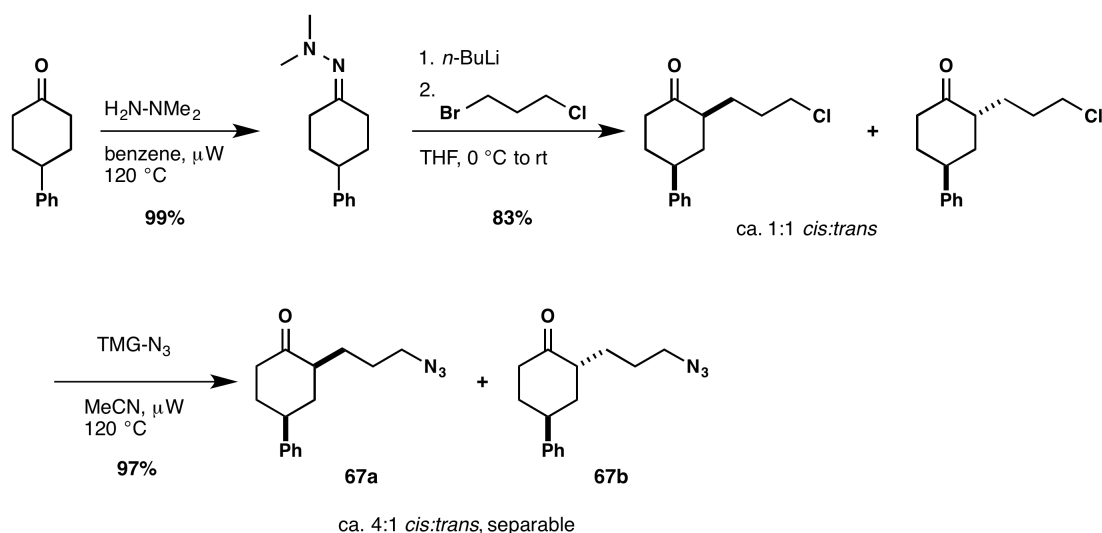
<sup>f</sup>Reported 93% yield with excess TFA.<sup>172</sup>

## 3.2 Methods

### 3.2.1 Substrate synthesis for intramolecular Schmidt reaction development

The substrates used in this study had been reported previously.<sup>164,180,172,182,181,183</sup> A representative synthetic route from a ketone is shown in Scheme 3-8. The *cis* isomer of **67a** was formed preferentially under the heating conditions of the azidation reaction, which used tetramethylguanidinium azide (TMG-N<sub>3</sub>) as a soluble azide source. Due to this rapid equilibration, **67a** was purified for use in the reaction condition screening and kinetic studies. This separation was performed to simplify analysis by preempting this ready epimerization toward the *cis* isomer during heated reactions. This substrate was chosen for reaction screening due to its UV-vis absorbance properties, which simplified analysis as described below. Additional details for the synthesis and characterization of substrates are provided in the Experimental Section of this chapter (3.5).

Scheme 3-8



The known substrates in Figure 3-1 were chosen to survey the reactivity of various ketones: 2-(3'-azidopropyl)cyclohexanone (**67c**),<sup>164</sup> 2-(3'-azidopropyl)cyclobutanone (**67d**),<sup>180</sup> 2-(3'-azidopropyl)cyclopentanone (**67e**),<sup>164</sup> 2-(3'-azidopropyl)cycloheptanone (**67f**),<sup>172</sup> (2*S*,4*S*)-2-(3'-azidopropyl)-4-*tert*-butylcyclohexanone (*cis*, **67g**),<sup>172</sup> (2*R*,4*S*)-2-(3'-azidopropyl)-4-*tert*-butylcyclohexanone (**67h**),<sup>172</sup> 2-(3'-azidopropyl)-2,6-dimethylcyclohexanone (**67i**),<sup>182</sup> 3-(3'-azidopropyl)bicyclo[2.2.1]heptan-2-one (**67j**),<sup>181</sup> 6-azidohexan-2-one (**67k**),<sup>172</sup> ethyl 1-(3'-azidopropyl)-2-oxocyclohexanecarboxylate (**67l**),<sup>172</sup> and 2-(3'-azidopropyl)-2-methylcyclohexane-1,3-dione (**67m**).<sup>183</sup>

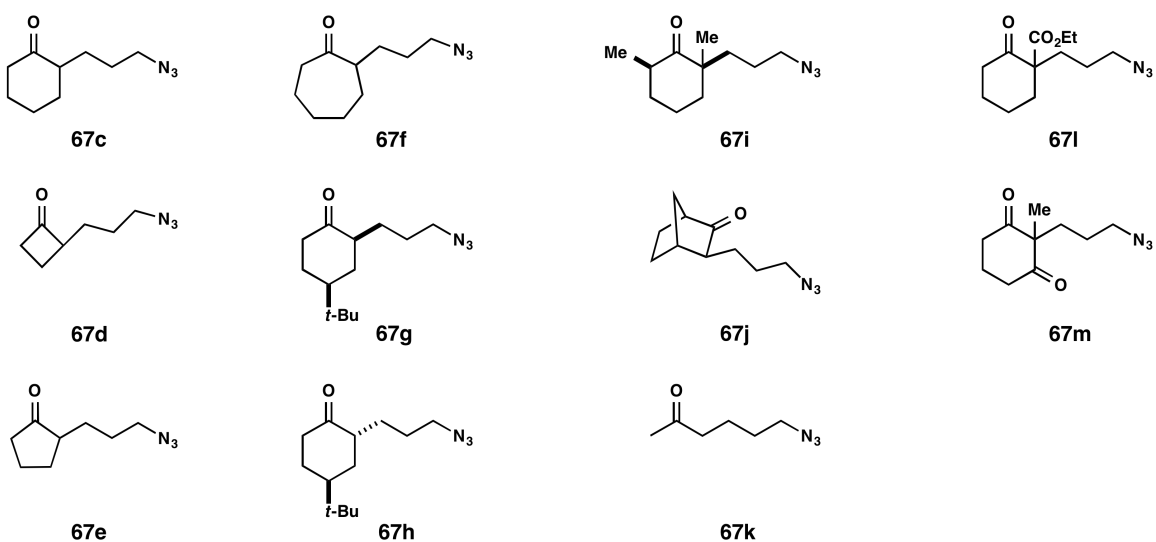


**Figure 3-1.** Substrates to examine the scope of the Sc(OTf)<sub>3</sub>-catalyzed intramolecular Schmidt reaction.

### 3.2.2 Reaction condition screening

To expedite condition screening, relative conversion was assessed based on ultra high performance liquid chromatography (UPLC) separation with mass spectrometric (MS) and ultraviolet-visible (UV-vis) absorbance detection. Samples were processed on a

Waters Acquity System (Waters LCT premier with ESI and PDA detector) employed with a Waters Acquity BEH C18 column (2.1 x 50 mm, 1.7  $\mu\text{m}$ ) with a “standard base” method (linear gradient elution of 95:5 water:MeCN, pH 9.8 to 0:100 water:MeCN; flow rate 0.6 mL/min for 2.7 min). The Waters MassLynx software with peak integration was utilized to compare the relative percent conversion based on the substrate and product areas of the chromatograms. Microwave conditions were performed with a mono-mode microwave ( $\mu\text{W}$ ) reactor (Biotage Initiator, Biotage USA, NC).

*General procedure for catalyst/condition screening:* Conditions were arranged as specified in Table 3-3 and performed as described in the Experimental Section (3.5). After cooling, 10  $\mu\text{L}$  of the reaction mixture was diluted to 1.0 mL of acetonitrile for analysis by UPLC. The Waters MassLynx software with peak integration was utilized to compare the relative percent conversion based on the substrate and product areas of the chromatograms.

### **3.2.3 Determination of the reaction substrate scope under optimized conditions**

Substrates **67a-67m** were used in the final conditions, as specified in the Experimental Section (3.5). Once cooled, these reactions were purified by silica column. The yields from three experiments were averaged for each substrate, presented in Table 3-4.

### **3.2.4 Further catalyst screening under optimized conditions**

UPLC analysis was performed as in section 3.2.2 to reinvestigate alternate acids in the optimized conditions for improved activity. Catalysts were utilized as specified in Table 3-5 (Section 3.2.3). The Waters MassLynx software with peak integration was utilized to

compare the relative percent conversion based on the substrate and product areas of the chromatograms.

### **3.2.5 Additive/co-catalyst screening under ambient conditions**

UPLC analysis was performed as in section 3.2.2 to investigate the effect of added co-catalysts, ligands, or salts to potentially lower the temperature required for catalyst turnover. Additives were added as listed in Table 3-9 (Section 3.5). The Waters MassLynx software with peak integration was utilized to compare the relative percent conversion based on the substrate and product areas of the chromatograms.

### **3.2.6 Standardized measurements of conversion for reaction characterization**

For more detailed studies on the kinetics of  $\text{Sc}(\text{OTf})_3$  in the Schmidt reaction, a more accurate assay was necessary. This was accomplished by adding a known amount of internal standard (**IS**) to the above screening setup. *N*-Benzyl-2-pyrrolidinone was chosen based on its similar elution properties to the substrate and product (Figure 3-2, below).

*General procedure for quantitative measurements of conversion:* Conditions were arranged for the substrate **67a** as specified. After cooling, 10  $\mu\text{L}$  of the reaction mixture was diluted to 1.0 mL in MeCN containing 0.01 M **IS** for analysis by UPLC-MS. The Waters MassLynx software with peak integration was utilized to compare the relative percent conversion between remaining substrate and product. A sample chromatogram is provided in Figure 3-2.

Sample Report:

ID cf-6-219\_100deg-25percent File cf-6-219\_100deg-25percent Date 07-May-2014 Time 18:25:23 Description

3: UV Detector: 214

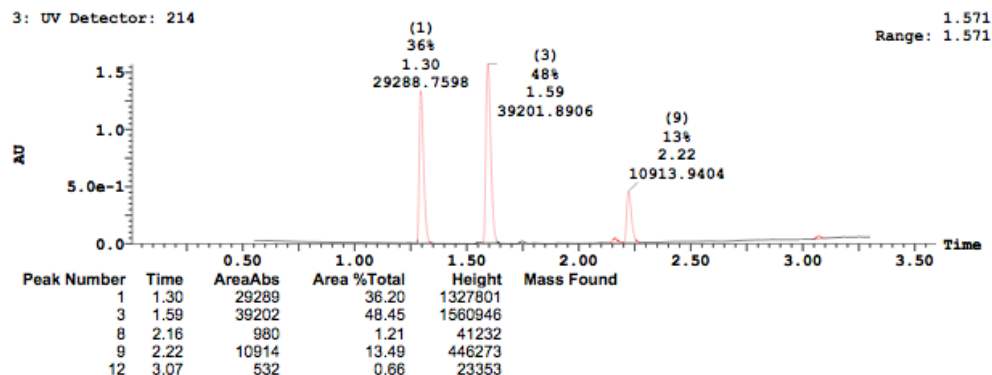


**Figure 3-2.** Quantitation of IS ( $R_T$  1.3 min), product **68a** ( $R_T$  1.59 min) and substrate **67a** ( $R_T$  2.22 min).

To calibrate the assay, normalization factors (NFs) of the IS with pure substrate **67a** and product **68a** were calculated (Equations 1 and 2). A solution of 0.2 M **68a** or **67a** in MeCN was created, and 10  $\mu$ L of these mixtures were withdrawn by calibrated micropipettors with siliconized tips (VWR Inc.), then added to 990  $\mu$ L aliquots of MeCN-IS (in the same manner as the actual samples).

$$NF_{\text{product}} = AUC_{\text{product}}/AUC_{\text{IS}} \quad (1)$$

$$NF_{\text{substrate}} = AUC_{\text{substrate}}/AUC_{\text{IS}} \quad (2)$$

Product **68a** conversion was then calculated as % product conversion (Equation 3):

$$\% \text{ product conversion} = (100 \times AUC_{\text{product}})/(AUC_{\text{IS}} \times NF_{\text{product}}) \quad (3)$$

Unreacted substrate **67a** could be similarly quantified (Equation 4):

$$\% \text{ substrate remaining} = (100 \times AUC_{\text{substrate}})/(AUC_{\text{IS}} \times NF_{\text{substrate}}) \quad (4)$$

### 3.2.7 Catalyst loading study of Sc(OTf)<sub>3</sub> in MeCN

Following the general procedure outlined in section 3.2.6, increasing amounts of Sc(OTf)<sub>3</sub> were reacted with **67a** according to Table 3-10 (Section 3.5). Product formation (% product conversion) was calculated over three trials, and the results analyzed using GraphPad Prism.

### 3.2.8 Microwave intensity study of Sc(OTf)<sub>3</sub> in MeCN

Following the general procedure outlined in section 3.2.6, this experiment was run holding mol % Sc(OTf)<sub>3</sub> constant and increasing the microwave temperature, according to Table 3-11 (Section 3.5). Product formation (% product conversion) was calculated over two trials, and the results analyzed using GraphPad Prism.

### 3.2.9 Turnover number and turnover frequency of Sc(OTf)<sub>3</sub> in MeCN

*Experimental procedure for turnover number and frequency study:* Following the general procedure outlined in section 3.2.6, the turnover kinetics were assessed by increasing mol % Sc(OTf)<sub>3</sub> at several temperatures. These conditions are listed in Table 3-12 (Section 3.5). Product formation (% product conversion) was calculated using Equation 3. These results were averaged to give the turnover number (ToN) at each temperature, as calculated by Equation 5.<sup>184</sup>

$$\text{ToN} = \text{mol product/mol catalyst} \quad (5)$$

The turnover frequency (ToF) was calculated by incorporating the reaction times, as calculated by Equation 6.<sup>184</sup>

$$\text{ToF} = \text{ToN/time of reaction} \quad (6)$$

These results were analyzed in Microsoft Excel and GraphPad Prism.

### 3.3 Results and Discussion

#### 3.3.1 Verification of preliminary substoichiometric catalytic conditions

First, a brief re-screen of the conditions identified by Li and Hirt was performed, which looked to identify factors that could be improved in these conditions. These results aligned with the previous studies, and are presented below in Table 3-3. This study used the more hydrophobic, UV-active substrate **67a** was to study conversion by UPLC screen.

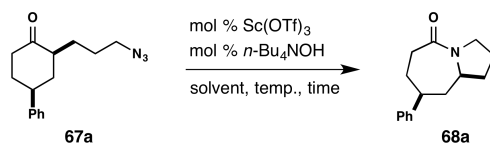
In each case, a relatively high catalyst loading was required. Thus, greater than 5 mol % Sc(OTf)<sub>3</sub> was necessary for full conversion under 5 h of conventional heating conditions (oil bath). The phase-transfer catalyst (PTC) *n*-Bu<sub>4</sub>NOH also aided conversion of **67a** to **68a**. The isolated yields were much lower than the conversion ratio suggested, possibly due the high solubility of amides in water, especially in the presence of a PTC.

Switching to the nonpolar but high boiling organic solvent xylene provided no turnover. However, acetonitrile (MeCN) was more promising. This polar, aprotic organic solvent precluded the need for the PTC with hydrophobic substrates such as **67a**. Similar conversion rates to the aqueous reactions were observed upon raising the temperature to 180 °C in a sealed tube. Full conversion could be obtained in less than an hour by slightly raising the temperature to 200 °C (Entry 15). For other substrates, discussed below, the switch from H<sub>2</sub>O to MeCN also greatly enhanced conversion.

In both solvent systems, the conversion time could be lowered using microwave heating ( $\mu$ W) conditions. Similar conditions were undergoing preliminary investigation by Hirt as she completed her preliminary work.<sup>180</sup> The need for shorter reaction times became especially relevant in terms of isolated yield. Shortened exposure to heat led to

the highest isolated yields, as seen in Entries 12, 13, and 15, possibly by reducing degradation.

**Table 3-3.** Preliminary condition screening with Sc(OTf)<sub>3</sub>



Entry	Solvent	Mol % Sc(OTf) <sub>3</sub>	Temp. (°C) <sup>a</sup>	Time	Mol % <i>n</i> -Bu <sub>4</sub> NOH	% Conversion <sup>b</sup> (isolated yield)
1	H <sub>2</sub> O	50	180	5 h	10	> 95
2	H <sub>2</sub> O	25	180	5 h	10	> 95
3	H <sub>2</sub> O	10	180	5 h	10	> 95 (33)
4	H <sub>2</sub> O	5	180	5 h	10	ca. 75
5	H <sub>2</sub> O	0	180	5 h	10	0
6	H <sub>2</sub> O	10	180	5 h	0	ca. 50 (28)
7	H <sub>2</sub> O	10	50	5 h	10	ca. 10
8	H <sub>2</sub> O	10	100	5 h	10	ca. 10
9	H <sub>2</sub> O	10	180, μW	1 h	10	ca. 85
10	H <sub>2</sub> O	10	180, μW	0.5 h	10	ca. 85
11	Xylenes	10	180	5 h	0	ca. 10
12	MeCN	10	180	5 h	0	> 95 (72)
13	MeCN	10	180, μW	1 h	0	> 95 (83)
14	MeCN	10	180, μW	0.5 h	0	ca. 85
15	MeCN	10	200, μW	0.5 h	0	> 95 (92)

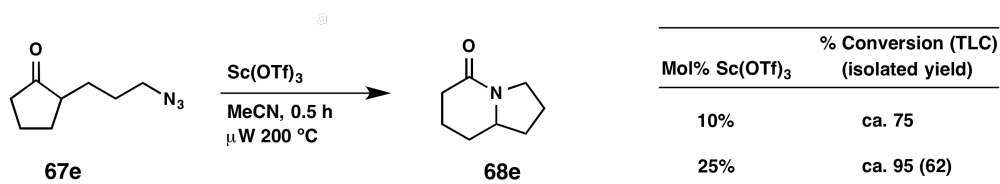
<sup>a</sup>Oil bath heating was applied unless designated as microwave irradiation (μW).

<sup>b</sup>Relative LC peak area of product to substrate; MassLynx software peak integration.

During the course of optimizing these conditions, other substrates were screened for conversion. In particular, the cyclopentanone substrate **67e** was used as a benchmark for reactivity. Cyclopentanone-based substrates have been reported to give lower yields in the Schmidt reaction than cyclohexanone-based substrates.<sup>164</sup> Lower reactivity of the 5-membered ketone has been attributed to an increased torsional strain encountered when a carbonyl substitution trajectory approaches its tetrahedral intermediate, a factor which raises the energetic barrier toward nucleophilic addition.<sup>185</sup>

Indeed, **67e** took longer to complete under the optimal conditions from Table 3-3, as shown in Scheme 3-9. However, by raising the catalyst loading to 25 mol %, we obtained complete conversion for this substrate. Thus, we confirmed Sc(OTf)<sub>3</sub> as a suitable catalyst for the intramolecular Schmidt reaction. The use of the polar, aprotic organic solvent acetonitrile notably improved the isolated yield and simplified the workup.

**Scheme 3-9**

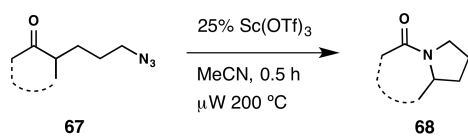


The less-desirable factors of high catalyst loading and strong heating requirements remained from the work of Li and Hirt. These factors were eventually further characterized (Section 3.2.3). However, the new conditions ensured full conversion, even for the recalcitrant substrate **67e**, and were carried forward to examine the substrate scope of this reaction variant.

### 3.2.2 Scope of the Sc(OTf)<sub>3</sub>-catalyzed intramolecular Schmidt reaction

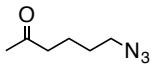
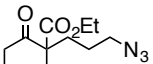
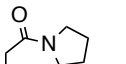
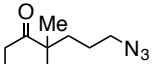
To study the scope of this version of the Schmidt reaction, we selected a representative number of substrates known to engage in Schmidt reactions when treated with excess acid.<sup>172</sup> These substrates included cyclic ketones of various ring sizes, the acyclic substrate **67k**, and several sterically-hindered ketones. The results from this study are shown in Table 3-4. All substrates were reacted under identical reaction conditions to test the generality of these conditions across this range of ketones.

**Table 3-4.** Substrate scope of improved catalytic Schmidt conditions



Entry	Substrate	Product	% Yield <sup>a</sup>
1	 <b>67a</b>	 <b>68a</b>	92
2	 <b>67b</b>	 <b>68b</b>	84
3	 <b>67c</b>	 <b>68c</b>	89
4	 <b>67d</b>	 <b>68d</b>	75
5	 <b>67e</b>	 <b>68e</b>	62
6	 <b>67f</b>	 <b>68f</b>	62
7	 <b>67g</b>	 <b>68g</b>	80
8	 <b>67h</b>	 <b>68h</b>	92
9	 <b>67i (plus isomer)</b>	 <b>68i (plus isomer)</b>	76 <sup>b</sup>
10	 <b>67j (plus isomer)</b>	 <b>68j (plus isomer)</b>	46 <sup>b</sup>

Table 3-4, continued

11	 <b>67k</b>	 <b>68k</b>	77
12	 <b>67l</b>	 <b>68l</b>	No reaction <sup>c</sup>
13	 <b>67m</b>	 <b>68m</b>	No reaction <sup>c</sup>

<sup>a</sup>Isolated yield, averaged from triplicate experiments.

<sup>b</sup>Stereochemistry not characterized.

<sup>c</sup>Proceeded in neat trifluoroacetic acid.

It is noteworthy that two substrates, **67l** and **67m**, did not react under  $\text{Sc}(\text{OTf})_3$  conditions, but proceed cleanly and in neat trifluoroacetic acid. Both of these substrates are 1,3-diketones. As  $\text{Sc}(\text{OTf})_3$  may accommodate up to 8 ligands,<sup>186</sup> it is possible that **67l** forms a bidentate complex with  $\text{Sc}(\text{OTf})_3$ . This could form a six-membered ring, sharing the electronic effect of the metal between the two ketones. A shared interaction may interrupt or preclude the intramolecular azide attack. However, a more detailed study incorporating the metal size and geometry would be required to confirm this hypothesis, in addition to the feasibility of bidentate complex formation with **67m**.

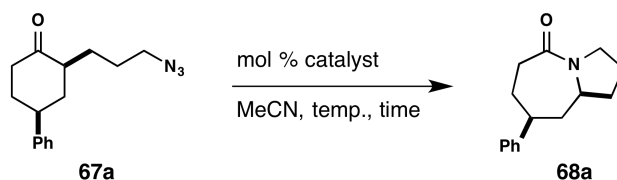
Despite the heating conditions that were applied, moderate to good yields were obtained over this small substrate scope with the exception of 1,3-diketone substrates. Here, the need for high temperatures seems to have been traded for the necessity of excess acid in previous incarnations of the Schmidt reaction. Given concerns about stability of azides, particularly low-molecular weight examples, an important goal was to reduce the temperature needed to carry out the reaction.

### 3.2.3 Screen of catalysts and co-catalysts to lower the temperature dependence

Alongside the optimization studies for the Sc(OTf)<sub>3</sub>-catalyzed intramolecular Schmidt reaction, additional screens were undertaken to improve the reaction conditions. In particular, we attempted to lower the high temperature requirement observed with Sc(OTf)<sub>3</sub> over the substrate scope tested.

*Selected alternative catalysts for the intramolecular Schmidt reaction in MeCN.* Other catalysts were also tested in the improved conditions identified above. The three most common stoichiometric reagents for the intramolecular Schmidt reaction were screened: trifluoroacetic acid (TFA), TiCl<sub>4</sub>, and BF<sub>3</sub>•OEt<sub>2</sub> (Table 3-5). Additionally, the similar lanthanide species Yb(OTf)<sub>3</sub> was examined to determine if Schmidt reactivity and turnover were a general property of this class of Lewis acids.

**Table 3-5.** Alternative catalysts in the improved conditions



Entry	Mol % catalyst	Temp (°C)	Time (h)	% Conversion <sup>a</sup>
1	25% TFA	rt	16	ca. 25
2	25% TFA	200	0.5	ca. 25 <sup>b</sup>
3	25% TiCl <sub>4</sub>	rt	16	ca. 25
4	25% TiCl <sub>4</sub>	200	0.5	ca. 60 <sup>b</sup>
5	25% BF <sub>3</sub> •OEt <sub>2</sub>	rt	16	ca. 25
6	25% BF <sub>3</sub> •OEt <sub>2</sub>	200	0.5	ca. 70
7	25% Yb(OTf) <sub>3</sub>	rt	16	ca. 25
8	25% Yb(OTf) <sub>3</sub>	200	0.5	ca. 80 <sup>b</sup>

<sup>a</sup>Relative LC peak area of product to substrate; MassLynx software peak integration.

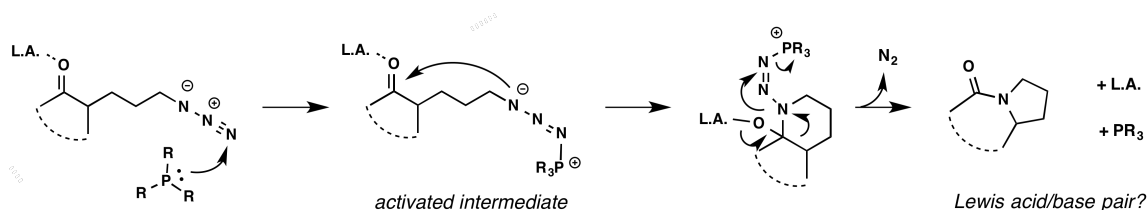
<sup>b</sup>Side peaks were observed in the chromatogram.

These results indicated that other catalysts known to promote the intramolecular Schmidt reaction were also able to turn over at high temperatures, but Yb(OTf)<sub>3</sub> and TiCl<sub>4</sub>

gave significant amounts of byproducts, and  $\text{BF}_3 \cdot \text{OEt}_2$  did not give full conversion after 0.5 hours at 200 °C. Therefore,  $\text{Sc}(\text{OTf})_3$  was reconfirmed as the best catalyst under these conditions.

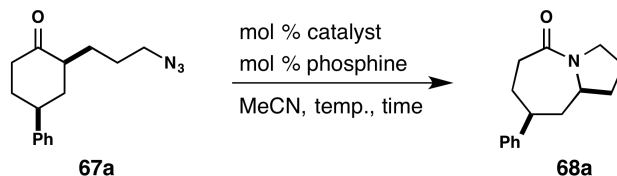
*Study of co-catalysts to lower the barrier toward successful reaction.* The next screen looked at the effect of Lewis basic phosphine reagents as activators of the nucleophilicity of the azide, in analogy to their role in the Staudinger ligation reaction.<sup>187</sup> Scheme 3-10 illustrates this concept as it would apply to the intramolecular Schmidt reaction. One concern was that phosphines are also Lewis bases, and can donate an electron pair to Lewis acids. Despite the propensity for Lewis acids to pair with Lewis bases, steric constraints can sometimes prevent this from occurring with some phosphines, notably tri(*tert*-butyl)phosphine.<sup>188</sup>

### Scheme 3-10



We set up a brief screen to investigate whether this strategy could lower the barrier for reaction. Alternatively, we were curious to see the effect of the additional Lewis base in the mixture. This could possibly facilitate the displacement of the catalyst to proceed at lower temperatures. The results from this study are shown in Table 3-6.

**Table 3-6.** Effect of phosphine additives on Sc(OTf)<sub>3</sub>-catalyzed intramolecular Schmidt reactivity



Entry	Mol % catalyst	Mol % additive	Temp (°C)	Time (h)	% Conversion <sup>a</sup>
1	25% Sc(OTf) <sub>3</sub>	100% triphenylphosphine	rt	16	ca. 18
2	25% Sc(OTf) <sub>3</sub>	100% triphenylphosphine	50	0.5	ca. 15
3	25% Sc(OTf) <sub>3</sub>	100% triphenylphosphine	100	0.5	ca. 16
4	25% Sc(OTf) <sub>3</sub>	100% triphenylphosphine	150	0.5	ca. 17
5	25% Sc(OTf) <sub>3</sub>	100 mol % tri( <i>t</i> -Bu)phosphine	rt	16	ca. 24
6	25% Sc(OTf) <sub>3</sub>	100 mol % tri( <i>t</i> -Bu)phosphine	50	0.5	ca. 24
7	25% Sc(OTf) <sub>3</sub>	100 mol % tri( <i>t</i> -Bu)phosphine	100	0.5	ca. 28
8	25% Sc(OTf) <sub>3</sub>	100 mol % tri( <i>t</i> -Bu)phosphine	150	0.5	ca. 21

<sup>a</sup>Relative LC peak area of product to substrate; MassLynx software peak integration.

Under these conditions, conversion was observed, albeit near the level of the mol % of Sc(OTf)<sub>3</sub> loading. Temperature did not increase turnover in these experiments. It is possible that strong Lewis bases may deactivate the Sc(OTf)<sub>3</sub> catalyst by forming an alternative Lewis acid-Lewis base pair that sequesters the catalytic species.

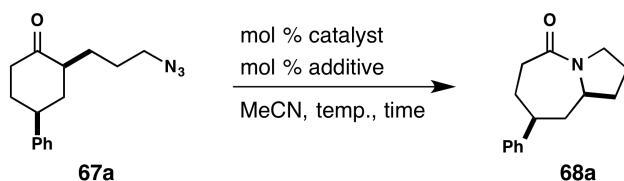
We also looked for the formation of the amine from the azide, through the related Staudinger reaction. However, no such species were suggested from the chromatogram, though an authentic sample was not prepared. Despite the lack of promising results, the measurable levels of conversion observed suggested that this strategy could perhaps be tuned using less reactive additives. This formed the basis for a more extensive additive screening campaign.

*Screen of other additives to displace the Lewis acid-amide complex at lower temperatures:* The last screen that was performed sought an alternative to heat for promoting a catalytic cycle. Since the presence of strong Lewis base species in the

previous experiment did not shut down the reaction entirely, we decided to screen a number of salts and organic species to potentially facilitate catalyst turnover.

Additionally, ligand/metal systems for  $\text{Sc}(\text{OTf})_3$  have been applied to similar rearrangement reactions. For example, a dioxide ligand activated  $\text{Sc}(\text{OTf})_3$  toward promoting a Baeyer–Villiger oxidation on ketones similar to our substrates.<sup>189</sup> Furthermore, enantioselectivity was observed when chiral ligands were used, which could eventually lead to utility in the catalytic Schmidt reaction.

To attempt to incorporate this approach into our study, we set up a screen of substoichiometric additives. The first screen was aimed at identifying any effects from small salts or charged organic species on the reaction (Table 3-7). These species could potentially coordinate the scandium metal, which could then change the strength of the metal interaction with the product amide. All reactions were performed at room temperature to readily identify an increase in turnover based on the effect of the additive.

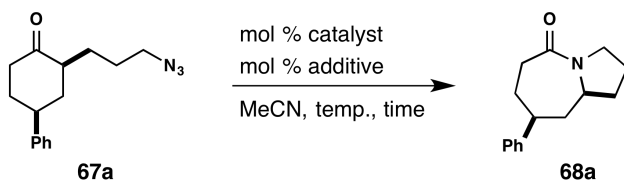
**Table 3-7.** Salt screen – potential ligands to destabilize the Lewis acid-product complex

Entry	Mol % catalyst	Mol % additive	Temp (°C)	Time (h)	% Conversion <sup>a</sup>
1	25% Sc(OTf) <sub>3</sub>	25% sodium acetate	rt	16	ca. 36
2	25% Sc(OTf) <sub>3</sub>	25% sodium benzoate	rt	16	ca. < 5
3	25% Sc(OTf) <sub>3</sub>	25% sodium carbonate	rt	16	ca. < 5
4	25% Sc(OTf) <sub>3</sub>	25% sodium citrate	rt	16	ca. < 5
5	25% Sc(OTf) <sub>3</sub>	25% sodium phenoxide	rt	16	ca. < 5
6	25% Sc(OTf) <sub>3</sub>	25% phenol	rt	16	ca. < 5
7	25% Sc(OTf) <sub>3</sub>	25% sodium tosylate	rt	16	ca. < 5
8	25% Sc(OTf) <sub>3</sub>	25% sodium bromide	rt	16	ca. < 5
9	25% Sc(OTf) <sub>3</sub>	25% sodium azide	rt	16	ca. < 5
10	25% Sc(OTf) <sub>3</sub>	25% sodium chloride	rt	16	ca. < 5
11	25% Sc(OTf) <sub>3</sub>	25% sodium iodide	rt	16	ca. < 5
12	25% Sc(OTf) <sub>3</sub>	25% potassium chloride	rt	16	ca. < 5
13	25% Sc(OTf) <sub>3</sub>	25% potassium fluoride	rt	16	ca. < 5
14	25% Sc(OTf) <sub>3</sub>	25% potassium phthalate	rt	16	ca. < 5
15	25% Sc(OTf) <sub>3</sub>	25% sodium tosylate	rt	16	ca. < 5
16	25% Sc(OTf) <sub>3</sub>	25% silver triflate	rt	16	ca. 35

<sup>a</sup>Relative LC peak area of product to substrate; MassLynx software peak integration.

Interestingly, reactivity was suppressed by many of these salt additives, even when added in 1:1 stoichiometry relative to the catalyst. This may indicate that Sc(OTf)<sub>3</sub> forms tight ionic interactions with these salts. The only species that promoted the Schmidt reaction with some degree of catalytic turnover, were the organic acetate and triflate counterions (Table 3-7, Entries 1 and 16). These data suggested that small organic species might make suitable ligands for Sc(OTf)<sub>3</sub> in this application. Thus, our final screen was designed to reduce the strength of potential ligand interactions by looking at neutral organic species. These might form readily reversible complexes that would not shut down catalyst activity.

**Table 3-8.** Organic additive screen – potential ligands to destabilize the Lewis acid-product complex



Entry	Mol % catalyst	Mol % additive	Temp (°C)	Time (h)	% Conversion <sup>a</sup>
1	25% Sc(OTf) <sub>3</sub>	25% dimethylhydrazine	rt	16	ca. < 5
2	25% Sc(OTf) <sub>3</sub>	25% methylamine	rt	16	ca. < 5
3	25% Sc(OTf) <sub>3</sub>	25% dimethylamine	rt	16	ca. < 5
4	25% Sc(OTf) <sub>3</sub>	25% trimethylamine	rt	16	ca. < 5
5	25% Sc(OTf) <sub>3</sub>	25% Hünig's base	rt	16	ca. < 5
6	25% Sc(OTf) <sub>3</sub>	25% DABCO <sup>b</sup>	rt	16	ca. < 5
7	25% Sc(OTf) <sub>3</sub>	25% trimethylamine <i>N</i> -oxide	rt	16	ca. < 5
8	25% Sc(OTf) <sub>3</sub>	25% dimethylaminopyridine	rt	16	ca. < 5
9	25% Sc(OTf) <sub>3</sub>	25% trimethylformamide	rt	16	ca. < 5
10	25% Sc(OTf) <sub>3</sub>	25% <i>N,N</i> -dimethylacetamide	rt	16	ca. < 5
11	25% Sc(OTf) <sub>3</sub>	25% <i>N</i> -methyl-2-pyrrolidone	rt	16	ca. < 5
12	25% Sc(OTf) <sub>3</sub>	25% tributylphosphine	rt	16	ca. 33
13	25% Sc(OTf) <sub>3</sub>	25% tri( <i>o</i> -tolyl)phosphine	rt	16	ca. < 5
14	25% Sc(OTf) <sub>3</sub>	25% tri(2-furyl)phosphine	rt	16	ca. 41

<sup>a</sup>Relative LC peak area of product to substrate; MassLynx software peak integration.

<sup>b</sup>DABCO: 1,4-Diazabicyclo[2.2.2]octane.

The data from this study were similar to the salt screen. There was a marginal increase in conversion with two of the phosphine reagents (Table 3-8, Entries 12 and 14). Since these additives did not increase turnover above 50%, this study was discontinued. Thus, the results from the additive studies suggested that a few weakly nucleophilic additives (sodium acetate, silver triflate, tributylphosphine, and tri(2-furyl)phosphine) were able to slightly increase turnover at room temperature. However, most additives shut down reactivity entirely, even at 1:1 additive:catalyst loading.

Altogether, several additional studies to further improve these conditions failed. Similar to the work of Li and Hirt, relatively high catalyst levels of Sc(OTf)<sub>3</sub> in heated polar solvent provided the best range of turnover and scope.

### 3.2.4 Further characterization of the Sc(OTf)<sub>3</sub>-catalyzed reaction

We noted during our initial studies on catalytic conditions for this intramolecular Schmidt reaction reactions did occur at temperatures below ca. 100 °C, but with no or little turnover. We were intrigued by this, and wondered if the ability of the Sc(OTf)<sub>3</sub> catalyst to dissociate from the product and turn over into its catalytic cycle was temperature-dependent.

Turnover frequency is a normalized parameter that quantitates the rate in which a catalyst can complete its catalytic cycle. In 1999, Van der Wiel *et al.* reported that the turnover frequency of a heterogeneous catalyst increased nearly two orders of magnitude over a 100 °C temperature range.<sup>190</sup> Based on this report, we decided to probe the dependence of temperature on Sc(OTf)<sub>3</sub> kinetics to tell us more about how this reaction behaves.

To study the reaction kinetics of the Sc(OTf)<sub>3</sub>-catalyzed intramolecular Schmidt reaction, we required a more accurate version of the UPLC-based screen used in the experiments described above. The use of a known amount of an internal standard was a straightforward way to accomplish this. *N*-Benzyl-2-pyrrolidinone was chosen as an internal standard based on its similar structural features and absorption coefficient to **67a** and **68a** (Figure 3-2 in Section 3.2.6).

A known concentration of internal standard was added in bulk to the UPLC analytical matrix for quantitation. The signal from internal standard was normalized to product and starting material for each experiment. Thus, our results could be quantitatively compared between experimental conditions.

*Catalyst loading experiment under ambient conditions.* Since reactivity was observed at lower temperatures, we needed to record a baseline turnover frequency to be able to identify potential temperature dependence in this reaction. We used ambient conditions to study this baseline. The catalyst loading was increased from 0 mol % Sc(OTf)<sub>3</sub> to 100 mol % Sc(OTf)<sub>3</sub> and reactions were stirred at room temperature. These were sampled at various time points out to 1 week.

The 24 h time point revealed a slow, but measurable, turnover rate when no heating was applied (Figure 3-3). The highest turnover frequency (ToF, from Equation 6 in Section 3.2.9) in the series was 0.089 h<sup>-1</sup>. This indicated that Sc(OTf)<sub>3</sub> could indeed dissociate from the lactam **68a** to complete a catalytic cycle, although the rate was slow.

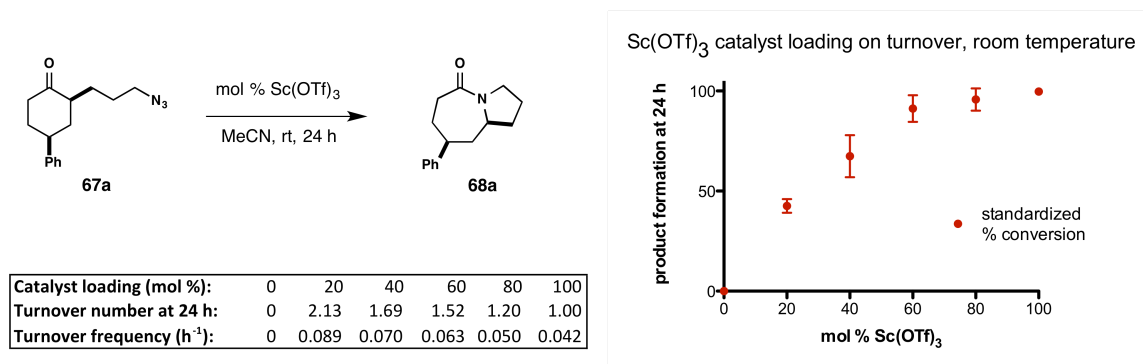


**Figure 3-3.** The effect of Sc(OTf)<sub>3</sub> loading on ambient turnover of the intramolecular Schmidt reaction.

However, when these reactions were sampled again, no further change was observed after 48 h, even extending out to 168 h (1 week). These results suggested that substoichiometric amounts of Sc(OTf)<sub>3</sub> may reach an equilibrium when amide products

are generated, halting further reaction at lower temperatures. Thus, our next goal was to look at the effect of temperature on product conversion, and thus turnover.

*Effect of temperature the on Sc(OTf)<sub>3</sub>-catalyzed intramolecular Schmidt reaction:* The preceding study suggested that while reactivity occurred at lower temperatures, catalyst turnover halted after a certain level of conversion had occurred. A comparison of these results with the full conversion we had observed when heating these reactions suggested a temperature dependence on turnover and reaction completion. In the literature, increased turnover with microwave heating has also been reported for a catalytic transfer hydrogenation reaction.<sup>191</sup> Thus, we characterized the effect of temperature on conversion in this system.

For this experiment, the amount of catalyst was held at 20 mol %, and the reactions were analyzed after 0.5 h (Figure 3-4). At temperatures above 100 °C, the reaction had completed within 0.5 h, so these results were excluded when fitting the conversion data.

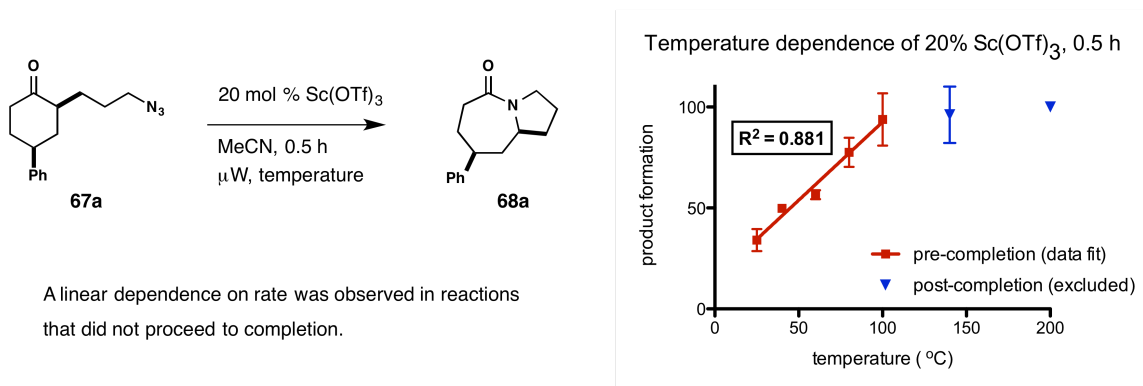
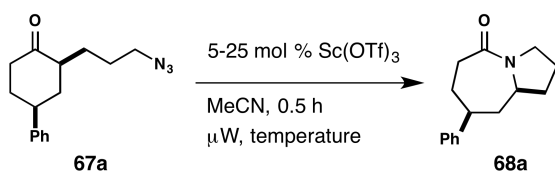


**Figure 3-4.** The temperature dependence of turnover is linear for Sc(OTf)<sub>3</sub> in this reaction.

When analyzed, a linear temperature dependence of conversion was observed. This aligned with the data we measured during the development of these conditions (refer to Table 3-3). Though this finding was not surprising, it did provide insight into this reaction. Since the catalyst loading was held constant, this data indicated that increasing the reaction temperature could stimulate catalyst turnover. Thus, our final study in this vein was to rigorously characterize the turnover parameters of  $\text{Sc}(\text{OTf})_3$ , to determine the effect temperature had in overriding product inhibition in this reaction.

*Determination of catalyst kinetics for  $\text{Sc}(\text{OTf})_3$ :* The previous study provided rough estimates of turnover parameters at 20 mol %  $\text{Sc}(\text{OTf})_3$  catalyst loading under various temperature conditions. We designed a study to fully characterize the turnover number (ToN) and turnover frequency (ToF) of this reaction. These parameters were defined in Section 3.2.9.

Catalyst levels were set at 5, 10, 15, 20, and 25 mol %. Each of these conditions were reacted at temperatures of rt, 75 °C, 100 °C, 150 °C, and 200 °C. The turnover numbers at each temperature did not appreciably vary over the range of catalyst loading studied, and thus were averaged to provide a comprehensive turnover number at each of these temperatures (Figure 3-5). This full data is provided in the Experimental Section (3.5).



Comprehensive ToN:

At each temperature, the turnover numbers for 5, 10, 15, 20, and 25 mol % Sc(OTf)<sub>3</sub> were averaged

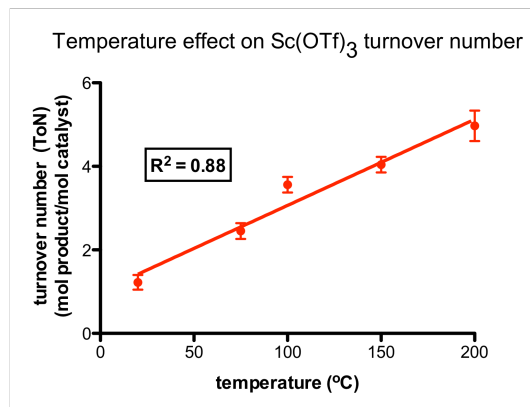


**Figure 3-5.** Kinetic characterization of Sc(OTf)<sub>3</sub> turnover number in the intramolecular Schmidt reaction.

As in the previous study, ToN increased in a linear relationship to temperature. The more useful parameter ToF was calculated by incorporating the reaction time. This is plotted in Figure 3-6. From ambient temperature to 200 °C, ToF increased 48-fold.

Turnover frequency (ToF):

ToN / time

Temp ( °C)	ToF (h <sup>-1</sup> ):
25	0.20
75	2.45
100	3.56
150	8.08
200	9.94

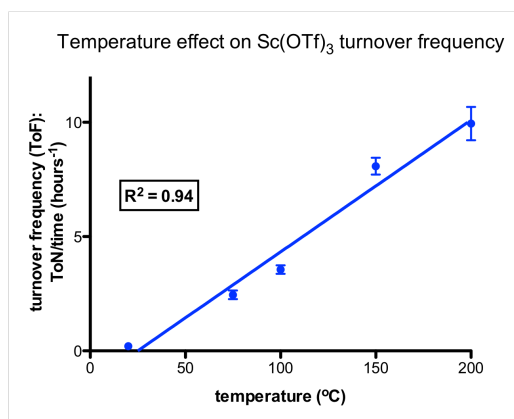


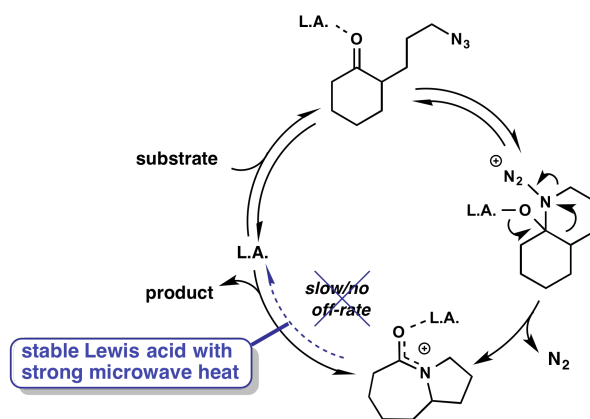
**Figure 3-6.** Kinetic characterization of Sc(OTf)<sub>3</sub> turnover frequency in the intramolecular Schmidt reaction.

Thus, turnover frequency in the Sc(OTf)<sub>3</sub>-catalyzed intramolecular Schmidt reaction increased with temperature. Sc(OTf)<sub>3</sub> has been reported to be stable, even at high

temperatures in polar media.<sup>186</sup> This thermal stability may explain why this catalyst is more suitable under these conditions than the other catalysts screened in earlier stages of this project (refer to Tables 3-1 to 3-3).

These results provided evidence for an updated mechanism of the catalytic cycle. As proposed in Scheme 3-11, heat can facilitate the dissociation of the Lewis acid-amide complex to facilitate movement through the catalytic cycle.

**Scheme 3-11**



### 3.4 Conclusions

The development of catalytic methodology for diverse organic transformations remains an important goal, both in augmenting our ability to synthesize essential molecules and in reducing the impact excesses of harmful solvents and reagents have on the environment.<sup>192</sup> Hitherto, the Schmidt reaction of alkyl azides and carbonyls has presented considerable difficulty in the discovery of a suitable substoichiometric catalytic system, which was the target of this work.

We confirmed the Lewis acid  $\text{Sc}(\text{OTf})_3$  to be a general catalyst for the intramolecular Schmidt reaction, with the caveat of requiring high temperatures for turnover. Alternative means for increasing reactivity were also screened. The dependence of turnover on strong heating conditions was characterized, revealing a ca. 50-fold increase over the studied temperature range. This result provided evidence for a mechanism of the catalytic cycle.

Though this work was an important first step toward developing a catalytic system for this reaction, the conditions and substrate scope studied herein were considered to be too limited to represent a useful, general platform for this goal. This project was later taken up by Hashim Motiwala, who carried out a more extensive solvent and catalyst screening campaign.<sup>193, 194</sup> Alternative conditions were found that allowed turnover under ambient conditions with an improved substrate scope.<sup>193, 194</sup>

Together, both of these studies open the door for the development of asymmetric variants of this transformation, an exciting prospect that has seen limited application.<sup>195,196</sup> Additionally, the published gentle methodology may show utility in the late-stage functionalization of ketone-containing molecular targets with an increased degree of pre-existing complexity.

### 3.5 Experimental Section

$^1\text{H}$  and  $^{13}\text{C}$  NMR spectra were collected on a Bruker DRX-400 (400 MHz and 100 MHz, respectively) or a Bruker AM-500 (500 MHz and 125 MHz, respectively) instrument. Unless otherwise noted, all samples were dissolved in  $\text{CDCl}_3$  and the shifts expressed in parts per million ( $\delta$ ) relative to residual  $\text{CHCl}_3$  as an internal standard.  $^{13}\text{C}$  NMR multiplicities were determined with the aid of an APT pulse sequence, differentiating the signals for methyl and methine carbons as “d” from methylene and quaternary carbons as “u”. Abbreviations are: s, singlet; d, doublet; t, triplet, q, quartet; m, multiplet; dd, doublet of doublets; qd, quartet of doublets; td, triplet of doublets. The infrared (IR) spectra were recorded on Perkin-Elmer 1420 spectrometer or a Perkin-Elmer Spectrum One FT-IR and the absorption frequencies are reported in  $\text{cm}^{-1}$ . All flash chromatography was performed using Sorbent technologies silica gel (32-63 mesh) with the reported eluent system. Acetonitrile, methylene chloride and THF were dried by passing through two packed columns of neutral alumina using the PurSolv solvent purification system (Innovative Technology Inc.) prior to use. All chemicals were used as purchased from commercial suppliers. Dry flasks (noted) were baked in an oven overnight or were flame dried under vacuum and then placed under a positive pressure of argon. Microwave vials (noted) were purchased from commercial suppliers (Biotage part numbers: 355458 (0.2-0.5 mL), 352016 (0.5-2mL), 351521 (2-5 mL), 354833 (10-20 mL)). Mono-mode microwave conditions were performed using a Biotage Initiator instrument (Biotage USA, Charlotte, NC). Fixed hold time is a microwave parameter in which time is not counted until the reaction reaches the desired temperature. UPLC-MS experiments were conducted using a Waters LCT Premier Mass Spectrometer, equipped

with a Waters Acquity Ultra Performance Liquid Chromatograph and a Waters 2998 Photodiode Array Detector. Tetramethylguanidinium azide was prepared according to literature precedent.<sup>197</sup>

### List of Known Compounds

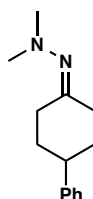
The following substrates are known; their preparation and spectra matched uneventfully to the corresponding reference: 2-(3'-azidopropyl)cyclohexanone (**67c**),<sup>164</sup> 2-(3'-azidopropyl)cyclobutanone (**67d**),<sup>180</sup> 2-(3'-azidopropyl)cyclopentanone (**67e**),<sup>164</sup> 2-(3'-azidopropyl)cycloheptanone (**67f**),<sup>172</sup> *cis*-2-(3'-azidopropyl)-4-*tert*-butylcyclohexanone (**67g**),<sup>172</sup> *trans*-2-(3'-azidopropyl)-4-*tert*-butylcyclohexanone (*trans*, **67h**),<sup>172</sup> 2-(3'-azidopropyl)-2,6-dimethylcyclohexanone (**67i**),<sup>182</sup> 3-(3'-azidopropyl)bicyclo[2.2.1]heptan-2-one (**67j**),<sup>181</sup> 6-azidohexan-2-one (**67k**),<sup>172</sup> ethyl 1-(3'-azidopropyl)-2-oxocyclohexanecarboxylate (**67l**),<sup>172</sup> and 2-(3'-azidopropyl)-2-methylcyclohexane-1,3-dione (**67m**).<sup>183</sup>

The spectral characterization of lactams resulting from Sc(OTf)<sub>3</sub>-catalyzed Schmidt reaction similarly matched those reported in the noted literature:

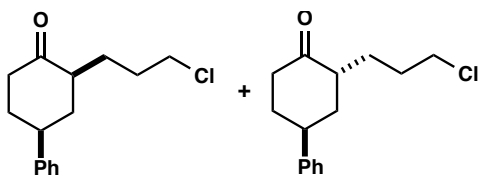
hexahydro-1*H*-pyrrolo[1,2-*a*]azepin-5(6*H*)-one (**68c**),<sup>164</sup> tetrahydro-1*H*-pyrrolizin-3(2*H*)-one (**68d**),<sup>172</sup> hexahydroindolizin-5(1*H*)-one (**68e**),<sup>164</sup> octahydropyrrolo[1,2-*a*]azocin-5(1*H*)-one (**68f**),<sup>172</sup> *cis*-8-*tert*-butylhexahydro-1*H*-pyrrolo[1,2-*a*]azepin-5(6*H*)-one (**68g**),<sup>172</sup> *trans*-8-*tert*-butylhexahydro-1*H*-pyrrolo[1,2-*a*]azepin-5(6*H*)-one (**68h**),<sup>172</sup> dimethyl-octahydro-pyrrolo[1,2-*a*]azepin-5-one (**68i**),<sup>182</sup> octahydro-7,10-methanopyrrolo[1,2-*a*]azepin-6(2*H*)-one (**68j**),<sup>181</sup> 1-(pyrrolidin-1-yl)ethanone (**68k**),<sup>182</sup>

ethyl 5-oxooctahydro-1H-pyrrolo[1,2-a]azepine-9a-carboxylate (**68l**),<sup>172</sup> 9-methyltetrahydro-1*H*-pyrrolo[1,2-a]azepine-5,9(6*H*,9*H*)-dione (**68m**).<sup>183</sup>

*General Procedure for the synthesis of starting azidoketones:*



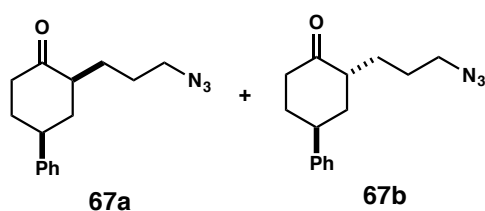
**1,1-Dimethyl-2-(4-phenylcyclohexylidene)hydrazine.** 4-Phenylcyclohexanone (7.0 g, 40.0 mmol) was dissolved in 10 mL benzene in a dry microwave vial. To this mixture was added *N,N*-dimethylhydrazine (3 mL, 40.0 mmol) at room temperature and the vial capped for. Heating conditions were set for 20 min at 120 °C, at which point conversion was complete by TLC analysis ( $R_f$  product = 0.1,  $R_f$  starting material = 0.38 at 20% EtOAc/hex). The reaction was diluted with DCM (100 mL), dried over sodium sulfate, concentrated, and the crude mixture was used in the next reaction, 8.42 g (99%) of a white solid. IR (neat) 2928, 1716  $\text{cm}^{-1}$ ;  $^1\text{H}$  NMR (400 MHz,  $\text{CDCl}_3$ )  $\delta$  1.62-1.82 (m, 2H), 1.94-2.03 (td,  $J = 5.2, 13.6$  Hz, 1H), 2.07-2.14 (m, 2H), 2.31-2.39 (m, 1H), 2.51 (s, 6H), 2.54-2.60 (m, 1H), 2.80-2.89 (m, 1H), 3.40-3.47 (m, 1H), 7.23-7.25 (m, 3H), 7.29-7.33 (m, 2H);  $^{13}\text{C}$  NMR (100.65 MHz,  $\text{CDCl}_3$ )  $\delta$  28.2, 33.8, 34.4, 35.7, 43.8, 126.3, 126.7, 128.5, 145.8, 169.0; HRMS calculated for  $\text{C}_{14}\text{H}_{21}\text{N}_2$ : 217.1705, found 217.1706.



***Cis-* and *trans*-2-(3'-chloropropyl)-4-phenylcyclohexanone.** 1,1-Dimethyl-2-(4-phenylcyclohexylidene)hydrazine (8.42 g, 40.0 mmol) was dissolved in 120 mL dry THF in a dry flask and the mixture cooled to 0 °C. *n*-Butyllithium (16.5 mL of a 2.52 M solution in hexanes, 41.6 mmol) was added dropwise over a period of 5 min. The reaction was allowed to stir for 30 min at 0 °C, then 3-bromo-1-chloropropane (5.9 mL, 60.0 mmol) was added dropwise over 5 min. The reaction was allowed to stir for 30 min at 0 °C, then allowed to warm to room temperature and continue stirring for 30 min. The reaction was poured into a mixture of 100 mL 2N aqueous HCl and 300 mL diethyl ether and was allowed to stir vigorously for 20 min at room temperature. The organic layer was separated and the aqueous layer extracted three times with 50 mL diethyl ether. The combined organic layers were washed with 250 mL of brine, dried over sodium sulfate, and concentrated. The residue was purified by flash chromatography (100% hexanes to 2% ethyl acetate/hexanes) to yield a ~ 1:1 (*cis:trans*) mixture of diastereomers as 8.0 g (83%) of a pale yellow oil. The diastereomers could be separated for characterization by preparative TLC (80% CH<sub>2</sub>Cl<sub>2</sub>/20% hexanes).

*Trans*-2-(3'-chloropropyl)-4-phenylcyclohexanone:  $R_f = 0.48$  (80% CH<sub>2</sub>Cl<sub>2</sub>/20% hexanes). <sup>1</sup>H NMR (CDCl<sub>3</sub>, 400 MHz)  $\delta$  1.68-1.81 (complex, 3H), 1.91-2.06 (complex, 3H), 2.11-2.20 (m, 2H), 2.33-2.39 (m, 1H), 2.44 (m, 1H), 2.59-2.78 (m, 1H), 3.20-3.24 (m, 1H), 3.57-3.61 (m, 2H). <sup>13</sup>C NMR (CDCl<sub>3</sub>, 100.62 MHz)  $\delta$  28.6, 30.2, 33.3, 37.4, 38.4, 38.6, 44.7, 48.6, 126.6, 126.8, 128.7, 144.3, 213.7.

*Cis*-2-(3'-chloropropyl)-4-phenylcyclohexanone:  $R_f = 0.49$  (80%  $\text{CH}_2\text{Cl}_2$ /20% hexanes).  $^1\text{H}$  NMR ( $\text{CDCl}_3$ , 400 MHz)  $\delta$  1.38-1.49 (m, 1H), 1.65-1.72 (m, 1H), 1.77-1.98 (complex, 4H), 2.25-2.36 (m, 2H), 2.50-2.63 (m, 3H), 3.11-3.20 (m, 1H), 3.52-3.61 (m, 2H), 7.24-7.29 (m, 3H), 7.33-7.38 (m, 2H).  $^{13}\text{C}$  NMR ( $\text{CDCl}_3$ , 100.62 MHz)  $\delta$  26.7, 30.3, 35.0, 41.4, 41.9, 43.5, 45.1, 49.4, 126.7, 126.7, 144.5, 211.7. IR 1710, 2932  $\text{cm}^{-1}$ . HRMS calculated for  $\text{C}_{15}\text{H}_{20}\text{OCl}$ : 251.1203, found 251.1204.



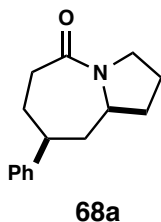
***Cis*- and *trans*-2-(3'-azidopropyl)-4-phenylcyclohexanone (67a and 67b).** The diastereomeric mixture of 2-(3'-chloropropyl)-4-phenylcyclohexanone (1.50 g, 6.00 mmol) was dissolved in dry acetonitrile (3.0 mL) in a dry microwave vial. Dry, solid tetramethylguanidinium azide (1.42 g, 9.00 mmol) was added and the vial capped. The solution was thoroughly shaken to dissolve any solid azide, and microwave conditions were set for 30 min at 120 °C. The reaction was poured into a beaker and the residual tetramethylguanidinium azide/halide salts were precipitated with ether (20 mL). The ether layer was decanted, washed with  $\text{H}_2\text{O}$  and brine, dried over sodium sulfate, and concentrated. The resulting oil was purified using flash chromatography (100% hexanes  $\rightarrow$  10% EtOAc/hexane) to afford 1.5 g (97%) of a 4:1 mixture of diastereomers as a clear oil. Preparative TLC was utilized to separate the diastereomers for characterization (70%  $\text{CH}_2\text{Cl}_2$ /20% hexanes/10% toluene). The mixture could be separated, up to 4 g scale,

using silica flash column chromatography (98% hexanes/2% ethyl acetate) for use in characterizing the Schmidt reaction.

*Trans*-2-(3'-Azidopropyl)-4-phenylcyclohexanone:  $R_f = 0.48$  (70%  $\text{CH}_2\text{Cl}_2$ /20% hexanes/10% toluene); IR (neat) 2095, 1710  $\text{cm}^{-1}$ ;  $^1\text{H}$  (400.23 MHz)  $\delta$  1.60-1.70 (m, 3H), 1.93-1.99 (m, 1H), 2.02-2.16 (m, 2H), 2.17-2.29 (m, 2H), 2.40-2.55 (m, 2H), 2.57-2.67 (m, 1H), 3.17-3.27 (m, 1H), 3.31-3.39 (t,  $J = 6.4$  Hz, 2H), 7.25-7.32 (m, 3H), 7.35-7.40 (m, 2H).  $^{13}\text{C}$  NMR ( $\text{CDCl}_3$ , 100.62 MHz)  $\delta$  26.7, 28.4, 33.3, 37.4, 38.4, 38.5, 48.8, 51.1, 126.6, 126.7, 128.7, 144.2, 213.7.

*Cis*-2-(3'-azidopropyl)-4-phenylcyclohexanone: TLC:  $R_f = 0.49$  (70%  $\text{CH}_2\text{Cl}_2$ /20% hexanes/10% toluene); IR (neat) 2095, 1710  $\text{cm}^{-1}$ ;  $^1\text{H}$  (400.23 MHz)  $\delta$  1.35-1.39 (m, 1H), 1.60-1.75 (m, 3H), 1.88-2.02 (m, 2H), 2.25-2.34 (m, 2H), 2.50-2.59 (m, 3H), 3.11-3.20 (m, 1H), 3.25-3.36 (m, 2H), 7.24-7.27 (m, 3H), 7.33-7.38 (m, 2H).  $^{13}\text{C}$  NMR ( $\text{CDCl}_3$ , 100.65 MHz)  $\delta$  26.4, 26.5, 35.0, 41.5, 41.9, 43.5, 49.6, 51.6, 126.7, 126.7, 128.6, 144.5, 211.7.

This azide group extruded  $\text{N}_2$  under all mass spectrometric techniques tried. HRMS calculated for  $\text{C}_{15}\text{H}_{20}\text{ON}$ : 230.1546, found 230.1526. The characteristic IR peak at 2095  $\text{cm}^{-1}$  indicated that azide was present.



***Cis*-8-Phenylhexahydro-1*H*-pyrrolo[1,2-*a*]azepin-5-one (2a).** *Cis*-2-(3'-azidopropyl)-4-phenylcyclohexanone, (50 mg, 0.194 mmol) was dissolved in acetonitrile (1 mL) in a

small microwave vial. Sc(OTf)<sub>3</sub> (23.9 mg, 0.049 mmol) was added and the vial capped for use. Microwave conditions were set for 30 min at 200 °C. Once cooled, the crude mixture was concentrated onto Celite and loaded onto a silica column (100% DCM to 2% MeOH/DCM). (40.6 mg, 90.7%). *Cis*-8-phenylhexahydro-1*H*-pyrrolo[1,2-*a*]azepin-5-one: TLC: R<sub>f</sub> = 0.31 (EtOAc); IR (neat) 1632 cm<sup>-1</sup>; <sup>1</sup>H NMR (400.23 MHz) δ 1.67-2.10 (m, 7H), 2.3-2.45 (m, 1H), 2.61-2.82 (m, 2H), 2.82-2.96 (t, *J* = 6.4 Hz, 1*H*), 3.48-3.61 (m, 1H), 3.76-3.89 (m, 1H), 3.90-4.03 (m, 1H), 7.17-7.35 (m, 3H), 7.35-7.48 (m, 2H). <sup>13</sup>C NMR (CDCl<sub>3</sub>, 100.57 MHz) δ 23.5, 30.6, 34.9, 37.5, 43.6, 46.9, 48.1, 58.0, 126.5, 126.6, 128.6, 146.4, 173.5; HRMS calculated for C<sub>15</sub>H<sub>20</sub>NO: 230.1545, found 230.1525.

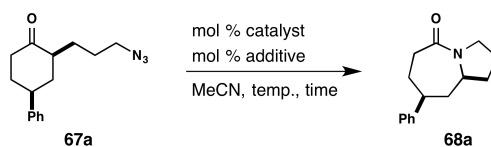
## Condition Screening

*General procedure for catalyst/condition screening:* To a mixture of substrate **67a** (25.7 mg, 0.100 mmol, 1.0 equiv) and solvent (0.5 mL, reaction concentration 0.2 M) in a microwave vial, the specified catalyst was added to the stated mol % in Table 3-3. The mixture was capped, then stirred for the listed time and temperature. Heat was applied by oil bath or Biotage microwave ( $\mu$ W), or stirred at ambient (room temperature, rt) as specified.

After cooling, the cap was removed and one 10  $\mu$ L of the mixture was diluted with 1.0 mL of acetonitrile for analysis by UPLC-MS. Samples were run on a Waters Acquity System (Waters LCT premier with ESI and PDA detector) employed with a Waters Acquity BEH C18 column (2.1 x 50 mm, 1.7  $\mu$ m) with a “standard base” method (linear gradient elution of 95:5 water:MeCN, pH 9.8 to 0:100 water:MeCN; flow rate 0.6 mL/min for 2.7 min). The Waters MassLynx software with peak integration was utilized to compare the relative % conversion between remaining substrate and product.

## Additive Screening

The general procedures outlined above were used to further investigate conditions using Sc(OTf)<sub>3</sub> as the catalyst and MeCN as solvent. Table 3-9 lists these results.

**Table 3-9.** Additive screen to increase turnover of Sc(OTf)<sub>3</sub> at room temperature

Entry	mol% additive	% conversion <sup>a</sup>
1	100% triphenylphosphine, rt, 16 h	18%
2	100% triphenylphosphine, $\mu$ W, 50 °C, 0.5 h	15%
3	100% triphenylphosphine, $\mu$ W, 100 °C, 0.5 h	16%
4	100% triphenylphosphine, $\mu$ W, 150 °C, 0.5 h	17%
5	100 mol % tri( <i>t</i> -Bu)phosphine, rt, 16 h	24%
6	100 mol % tri( <i>t</i> -Bu)phosphine, $\mu$ W, 50 °C, 0.5 h	24%
7	100 mol % tri( <i>t</i> -Bu)phosphine, $\mu$ W, 100 °C, 0.5 h	28%
8	100 mol % tri( <i>t</i> -Bu)phosphine, $\mu$ W, 150 °C, 0.5 h	21%
9	25 mol% tributylphosphine, rt, 16 h	33%
10	25 mol% tri( <i>o</i> -tolyl)phosphine, rt, 16 h	< 5%
11	25 mol% tri(2-furyl)phosphine, rt, 16 h	41%
12	25 mol% sodium acetate, rt, 16 h	36%
13	25 mol% sodium benzoate, rt, 16 h	< 5%
14	25 mol% sodium carbonate, rt, 16 h	< 5%
15	25 mol% sodium citrate, rt, 16 h	< 5%
16	25 mol% sodium phenoxide, rt, 16 h	< 5%
17	25 mol% phenol, rt, 16 h	< 5%
18	25 mol% sodium bromide, rt, 16 h	< 5%
19	25 mol% sodium azide, rt, 16 h	< 5%
20	25 mol% sodium chloride, rt, 16 h	< 5%
21	25 mol% sodium iodide	< 5%
22	25 mol% potassium chloride, rt, 16 h	< 5%
23	25 mol% potassium fluoride, rt, 16 h	< 5%
24	25 mol% potassium phthalate, rt, 16 h	< 5%
25	25 mol% sodium sulfite, rt, 16 h	< 5%
26	25 mol% sodium tosylate, rt, 16 h	< 5%
27	25 mol% silver triflate, rt, 16 h	35%
28	25 mol% dimethylhydrazine, rt, 16 h	< 5%
29	25 mol% methylamine, rt, 16 h	< 5%
30	25 mol% dimethylamine, rt, 16 h	< 5%
31	25 mol% trimethylamine, rt, 16 h	< 5%
32	25 mol% Hünig's base, rt, 16 h	< 5%
33	25 mol% DABCO, rt, 16 h	< 5%
34	25 mol% trimethylamine <i>N</i> -oxide, rt, 16 h	< 5%
35	25 mol% dimethylaminopyridine, rt, 16 h	< 5%
36	25 mol% trimethylformamide, rt, 16 h	< 5%
37	25 mol% <i>N,N</i> -dimethylacetamide, rt, 16 h	< 5%
38	25 mol% <i>N</i> -methyl-2-pyrrolidone, rt, 16 h	< 5%

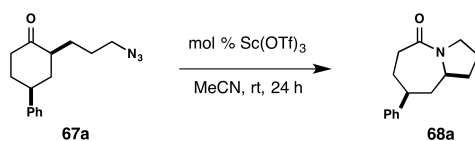
<sup>a</sup>Determined by UPLC-MS with MassLynx peak integration.

### **Experimental procedure for characterizing Sc(OTf)<sub>3</sub> catalyst activity:**

*General procedure for quantitative measurements of conversion:* To the listed amount (in mol %) of Sc(OTf)<sub>3</sub> in a dry 0.5-2.0 mL microwave vial was added 0.5 mL of an 0.2 M solution of **67a** in MeCN. The vial was capped, even for reactions run at ambient temperature (room temperature, rt). Heat was applied by Biotage Initiator microwave ( $\mu$ W) reactor or stirred at rt, as specified. *N*-Benzyl-2-pyrrolidinone was used as an internal standard (**IS**).

After cooling to rt, the cap was removed and 10  $\mu$ L of the reaction mixture was diluted to 1.0 mL in MeCN containing 0.01 M **IS** (**MeCN-IS**), for analysis by UPLC-MS. Samples were run on a Waters Acquity System (Waters LCT premier with ESI and PDA detector) employed with a Waters Acquity BEH C18 column (2.1 x 50 mm, 1.7  $\mu$ m) with a “standard base” method (linear gradient elution of 95:5 water:MeCN, pH 9.8 to 0:100 water:MeCN; flow rate 0.6 mL/min for 2.7 min). The Waters MassLynx software with peak integration was utilized to compare the relative percent conversion between remaining substrate and product.

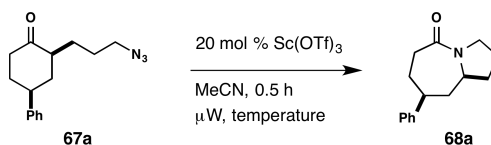
*Catalyst loading experiment:* The general procedure for quantitative measurements of conversion was followed using the conditions specified in Table 3-10. These results were analyzed using GraphPad Prism, and are plotted in Figure 3-3.

**Table 3-10.** Catalyst loading at room temperature (plotted in Figure 3-3)

Entry	mol%	% conversion – Trial 1 <sup>a</sup>	% conversion – Trial 2 <sup>a</sup>	% conversion – Trial 3 <sup>a</sup>
1	0	0.00	0.00	0.00
2	20	46.1	39.3	42.2
3	40	77.7	68.0	56.7
4	60	97.8	84.5	91.3
5	80	101	96.2	90.0
6	100	99.1	100	100

<sup>a</sup>Determined using UPLC-MS with MassLynx peak integration and Equation 3.

*Microwave intensity experiment:* The general procedure for quantitative measurements of conversion was followed using the conditions specified in Table 3-11. These results were analyzed using GraphPad Prism, and are plotted in Figure 3-4.

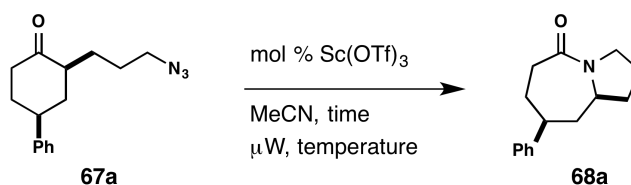
**Table 3-11.** Microwave intensity effect on turnover

Entry	μW temperature	% conversion- Trial 1 <sup>a</sup>	% conversion- Trial 2 <sup>a</sup>
1	None (rt)	28.6	39.6
2	40 °C	50.3	49.3
3	60 °C	58.8	54.3
4	80 °C	84.7	70.3
5	100 °C	80.9	107
6	140 °C	82.2	110
7	200 °C	100	100

<sup>a</sup>Determined using UPLC-MS with MassLynx peak integration and Equation 3.

*Turnover number and turnover frequency study:* The general procedure for quantitative measurements of conversion was followed using the conditions specified in Table 3-12. These results were analyzed using Microsoft Excel and GraphPad Prism, and are plotted in Figure 3-5 and Figure 3-6. Turnover frequency (ToF) could be calculated by taking into account the reaction time.<sup>184</sup>

**Table 3-12.** Measuring catalyst turnover by increasing temperature and catalyst loading



Entry	temp.	mol%	time	%conv. <sup>a</sup>	Turnover Number (ToN) [%conv. / %catalyst]	Turnover (ToF) [ToN / time] (h <sup>-1</sup> )	Frequency
1	rt	10	6 h	9.60	0.96	0.16	
2	rt	15	6 h	21.8	1.46	0.24	
3	rt	20	6 h	31.7	1.59	0.26	
4	rt	25	6 h	22.2	0.89	0.15	<b>Avg. 0.20 ± 0.029</b>
5	75 °C	10	1 h	25.8	2.58	2.58	
6	75 °C	15	1 h	28.3	1.89	1.89	
7	75 °C	20	1 h	53.7	2.69	2.69	
8	75 °C	25	1 h	66.2	2.65	2.65	<b>Avg. 2.45 ± 0.189</b>
9	100 °C	10	1 h	40.2	4.02	4.01	
10	100 °C	15	1 h	54.1	3.61	3.61	
11	100 °C	20	1 h	70.1	3.50	3.51	
12	100 °C	25	1 h	77.8	3.11	3.11	<b>Avg. 3.56 ± 0.186</b>
13	150 °C	10	0.5 h	44.5	4.44	8.89	
14	150 °C	15	0.5 h	61.2	4.07	8.16	
15	150 °C	20	0.5 h	81.7	4.08	8.17	
16	150 °C	25	0.5 h	88.7	3.54	7.10	<b>Avg. 8.08 ± 0.370</b>
17	200 °C	5	0.5 h	27.5	5.50	11.0	
18	200 °C	10	0.5 h	42.7	4.27	8.54	
19	200 °C	15	0.5 h	85.4	5.69	11.4	
20	200 °C	20	0.5 h	88.4	4.42	8.84	<b>Avg. 9.94 ± 0.723</b>

<sup>a</sup>Determined using UPLC-MS with MassLynx peak integration and Equation 3.

<sup>b</sup>Avg. = average ± standard error of the mean.

### 3.6 References

1. Donald Voet, J. G. V. *Biochemistry, 4th Edition*. John Wiley & Sons, Inc.: 2010.
155. Sigel, H.; Martin, R. B. Coordinating properties of the amide bond. Stability and structure of metal ion complexes of peptides and related ligands. *Chem. Rev.* **1982**, *82*, 385-426.
156. Martina, M.; Hutmacher, D. W. Biodegradable polymers applied in tissue engineering research: a review. *Polym. Int.* **2007**, *56*, 145-157.
157. Roughley, S. D.; Jordan, A. M. The Medicinal Chemist's Toolbox: An Analysis of Reactions Used in the Pursuit of Drug Candidates. *J. Med. Chem.* **2011**, *54*, 3451-3479.
158. Montalbetti, C. A. G. N.; Falque, V. Amide bond formation and peptide coupling. *Tetrahedron* **2005**, *61*, 10827-10852.
159. Pattabiraman, V. R.; Bode, J. W. Rethinking amide bond synthesis. *Nature* **2011**, *480*, 471-479.
160. Aubé, J.; Fehl, C.; Liu, R.; McLeod, M. C.; Motiwala, H. F. 6.15 Hofmann, Curtius, Schmidt, Lossen, and Related Reactions. In *Comprehensive Organic Synthesis II (Second Edition)*, Knochel, P., Ed. Elsevier: Amsterdam, 2014; pp 598-635.
161. Meyer, A. M.; Katz, C. E.; Li, S.-W.; Vander Velde, D.; Aubé, J. A Tandem Prins/Schmidt Reaction Approach to Marine Alkaloids: Formal and Total Syntheses of Lepadiformines A and C. *Org. Lett.* **2010**, *12*, 1244-1247.
162. Nyfeler, E.; Renaud, P. Intramolecular Schmidt Reaction: Applications in Natural Product Synthesis. *CHIMIA International Journal for Chemistry* **2006**, *60*, 276-284.
163. Frankowski, K. J.; Golden, J. E.; Zeng, Y.; Lei, Y.; Aubé, J. Syntheses of the Stemona Alkaloids (±)-Stenine, (±)-Neostenine, and (±)-13-Epineostenine Using a Stereodivergent Diels–Alder/Azido-Schmidt Reaction. *J. Am. Chem. Soc.* **2008**, *130*, 6018-6024.
164. Aubé, J.; Milligan, G. L. Intramolecular Schmidt reaction of alkyl azides. *J. Am. Chem. Soc.* **1991**, *113*, 8965-8966.

165. Engel, P. S.; Hayes, R. A.; Keifer, L.; Szilagyi, S.; Timberlake, J. W. Extrusion of nitrogen from cyclic and bicyclic azo compounds. *J. Am. Chem. Soc.* **1978**, *100*, 1876-1882.
166. Schmidt, K. F. Über den Imin-Rest. *Berichte der deutschen chemischen Gesellschaft (A and B Series)* **1924**, *57*, 704-706.
167. Smith, P. A. S. The Schmidt Reaction: Experimental Conditions and Mechanism. *J. Am. Chem. Soc.* **1948**, *70*, 320-323.
168. Smith, P. A. S.; Horwitz, J. P. The Effect of Structure on the Course of the Schmidt Reaction on Unsymmetrical Ketones<sup>1</sup>. *J. Am. Chem. Soc.* **1950**, *72*, 3718-3722.
169. Briggs, L. H.; De Ath, G. C.; Ellis, S. R. 16. Reactions of hydrazoic acid. Part I. *J. Chem. Soc.* **1942**, 61-63.
170. Boyer, J. H.; Hamer, J. The Acid-catalyzed Reaction of Alkyl Azides upon Carbonyl Compounds<sup>1</sup>. *J. Am. Chem. Soc.* **1955**, *77*, 951-954.
171. Grecian, S.; Aubé, J. Schmidt Rearrangement Reactions with Alkyl Azides. In *Organic Azides*, John Wiley & Sons, Ltd: 2010; pp 191-237.
172. Milligan, G. L.; Mossman, C. J.; Aubé, J. Intramolecular Schmidt Reactions of Alkyl Azides with Ketones: Scope and Stereochemical Studies. *J. Am. Chem. Soc.* **1995**, *117*, 10449-10459.
173. Gracias, V.; Milligan, G. L.; Aubé, J. Efficient Nitrogen Ring-Expansion Process Facilitated by in Situ Hemiketal Formation. An Asymmetric Schmidt Reaction. *J. Am. Chem. Soc.* **1995**, *117*, 8047-8048.
174. Wroblewski, A.; Coombs, T. C.; Huh, C. W.; Li, S.-W.; Aubé, J. The Schmidt Reaction. In *Organic Reactions*, John Wiley & Sons, Inc.: 2012.
175. Ramalingan, C.; Park, Y.-T. Mercury-Catalyzed Rearrangement of Ketoximes into Amides and Lactams in Acetonitrile. *J. Org. Chem.* **2007**, *72*, 4536-4538.
176. Hashimoto, M.; Obora, Y.; Sakaguchi, S.; Ishii, Y. Beckmann Rearrangement of Ketoximes to Lactams by Triphosphazene Catalyst†. *J. Org. Chem.* **2008**, *73*, 2894-2897.

177. Gorin, D. J.; Davis, N. R.; Toste, F. D. Gold(I)-Catalyzed Intramolecular Acetylenic Schmidt Reaction. *J. Am. Chem. Soc.* **2005**, *127*, 11260-11261.
178. Fang, W.; Presset, M.; Guérinot, A.; Bour, C.; Bezzenine-Lafollée, S.; Gandon, V. Silver-Free Two-Component Approach in Gold Catalysis: Activation of [LAuCl] Complexes with Derivatives of Copper, Zinc, Indium, Bismuth, and Other Lewis Acids. *Chemistry – A European Journal* **2014**, *20*, 5439-5446.
179. Ho, T.-L. Hard soft acids bases (HSAB) principle and organic chemistry. *Chem. Rev.* **1975**, *75*, 1-20.
180. Hirt, E. E.; Aubé, J. Development of Three Reaction Methodologies En Route to Nitrogen Containing Heterocycles: a Diels-Alder/Schmidt, a Diels-Alder/Acylation and a Catalytic Intramolecular Schmidt. University of Kansas, 2009.
181. Wendt, J. A.; Aubé, J. Toward the synthesis of sparteine: Intramolecular Schmidt reactions on a norbornanone platform. *Tetrahedron Lett.* **1996**, *37*, 1531-1534.
182. Lei, Y.; Wroblewski, A. D.; Golden, J. E.; Powell, D. R.; Aubé, J. Facile C–N Cleavage in a Series of Bridged Lactams. *J. Am. Chem. Soc.* **2005**, *127*, 4552-4553.
183. Lertpibulpanya, D.; Marsden, S. P. Concise access to indolizidine and pyrroloazepine skeleta via intramolecular Schmidt reactions of azido 1,3-diketones. *Org. Biomol. Chem.* **2006**, *4*.
184. Boudart, M. Turnover Rates in Heterogeneous Catalysis. *Chem. Rev.* **1995**, *95*, 661-666.
185. Finiels, A.; Geneste, P. Correlation of the reactivity of ketones relative to different nucleophiles. *J. Org. Chem.* **1979**, *44*, 1577-1578.
186. Kobayashi, S. Scandium Triflate in Organic Synthesis. *Eur. J. Org. Chem.* **1999**, *1999*, 15-27.
187. Köhn, M.; Breinbauer, R. The Staudinger Ligation—A Gift to Chemical Biology. *Angew. Chem., Int. Ed.* **2004**, *43*, 3106-3116.

188. Mömming, C. M.; Otten, E.; Kehr, G.; Fröhlich, R.; Grimme, S.; Stephan, D. W.; Erker, G. Reversible Metal-Free Carbon Dioxide Binding by Frustrated Lewis Pairs. *Angew. Chem., Int. Ed.* **2009**, *48*, 6643-6646.
189. Zhou, L.; Liu, X.; Ji, J.; Zhang, Y.; Hu, X.; Lin, L.; Feng, X. Enantioselective Baeyer–Villiger Oxidation: Desymmetrization of Meso Cyclic Ketones and Kinetic Resolution of Racemic 2-Arylcyclohexanones. *J. Am. Chem. Soc.* **2012**, *134*, 17023-17026.
190. Van der Wiel, D. P.; Pruski, M.; King, T. S. A Kinetic Study on the Adsorption and Reaction of Hydrogen over Silica-Supported Ruthenium and Silver–Ruthenium Catalysts during the Hydrogenation of Carbon Monoxide. *J. Catal.* **1999**, *188*, 186-202.
191. Gordon, E. M.; Gaba, D. C.; Jebber, K. A.; Zacharias, D. M. Catalytic transfer hydrogenation of benzaldehyde in a microwave oven. *Organometallics* **1993**, *12*, 5020-5022.
192. Kobayashi, S.; Manabe, K. Development of Novel Lewis Acid Catalysts for Selective Organic Reactions in Aqueous Media. *Acc. Chem. Res.* **2002**, *35*, 209-217.
193. Motiwala, H. F. A., Jeffrey. Catalysis of Intra- and Intermolecular Schmidt Reactions; Copper-Catalyzed Oxaziridine-Mediated C–H Bond Oxidation; Synthesis and Cytotoxic Evaluation of Withalongolide A Analogues. University of Kansas, Lawrence, KS, 2014.
194. Motiwala, H. F.; Fehl, C.; Li, S.-W.; Hirt, E.; Porubsky, P.; Aubé, J. Overcoming Product Inhibition in Catalysis of the Intramolecular Schmidt Reaction. *J. Am. Chem. Soc.* **2013**, *135*, 9000-9009.
195. Sahasrabudhe, K.; Gracias, V.; Furness, K.; Smith, B. T.; Katz, C. E.; Reddy, D. S.; Aubé, J. Asymmetric Schmidt Reaction of Hydroxyalkyl Azides with Ketones. *J. Am. Chem. Soc.* **2003**, *125*, 7914-7922.
196. Yang, M.; Zhao, Y.-M.; Zhang, S.-Y.; Tu, Y.-Q.; Zhang, F.-M. Chiral Brønsted Acid-Promoted Enantioselective Desymmetrization in an Intramolecular Schmidt Reaction of Symmetric Azido 1,3-Hexanediones: Asymmetric Synthesis of Azaquaternary Pyrroloazepine Skeletons. *Chem. Asian J.* **2011**, *6*, 1344-1347.
197. Papa, A. J. Synthesis and Azidolysis of 2-Chlorotetramethylguanidine. Synthetic Utility of Hexa- and Tetramethylguanidinium Azide. *J. Org. Chem.* **1966**, *31*, 1426-1430.

